TECHNISCHE UNIVERSITÄT MÜNCHEN

MAX-PLANCK-INSTITUT

FÜR

ASTROPHYSIK

Aspects of Nucleosynthesis in Core-Collapse Supernovae

Else Pllumbi

Vollständiger Abdruck der von der Fakultät für Physik der Technischen Universität München zur Erlangung des akademischen Grades eines

Doktors der Naturwissenschaften (Dr. rer. nat.)

genehmigten Dissertation.

Vorsitzender: Univ.-Prof. Dr. Lothar Oberauer
Prüfer der Dissertation: 1. Priv.-Doz. Dr. Hans-Thomas Janka
                          2. Univ.-Prof. Dr. Björn Garbrecht

Die Dissertation wurde am 16.04.2015 bei der Technischen Universität München eingereicht und durch die Fakultät für Physik am 07.07.2015 angenommen.

Contents

1 Introduction

Understanding the origin of the elements, as well as of ourselves, is a very fascinating and exciting question. Finding the answer is challenging. It requires to deeply dig simultaneously into nuclear physics and astrophysics, also called *nuclear astrophysics*. The former tells us how nuclei form, while the latter where they form. Nowadays, we know that we are all made of stars, but we do not exactly know which ones!

The aim of this thesis is to address some of the opened questions of this research field.

1.1 Where do the chemical elements come from?

Most of the matter which we see in the Universe is made of protons and neutrons, also called nucleons. These nucleons combine with each other giving rise to the heavier chemical elements, such as He, C, O etc. The way and under which conditions these nucleons combine together are still a very active research field. In order to answer some questions about the origin of the chemical elements, we start by having a look at the mass fraction of the chemical elements (X) which we observe in our Solar System (see Fig. 1.1) as a function of mass number A. In Fig. 1.1, we clearly see that the most abundant element in Nature is hydrogen, followed by helium. After helium, we can see a rapid drop of the mass fractions of the elements until the most stable element (iron) is reached, and around iron (mass number $A = 56$) there is a big peak. After the Fe-peak, we notice a slow decline of the mass fractions and, in particular, there is a certain regular pattern which is repeated, namely there are peaks in the mass fraction distribution of the elements corresponding to very stable nuclei and some "bumps" on their left side.

All these features in the element distribution of our Solar System brought Hoyle, Fowler, Burbidge G. R. and Burbidge E. M. with their pioneering works to the conclusion that, while hydrogen and partially He are produced during the Big Bang nucleosynthesis, the elements heavier than He (the so-called *metals*) are produced inside stars (Hoyle et al. 1956, Burbidge et al. 1957).

A star is, at the beginning of its life, a kind of "ball" of gas made almost entirely of H and He. The star contacts due to the force of gravity and as soon as the temperature in its center is high enough, H starts to fuse into He producing energy, and the pressure which is consequently created acts against gravity and holds the stellar structure from collapsing.

The more massive the star is, the more these fusion reactions proceed, so that heavier and heavier elements are produced. In order for a fusion reaction to occur, the reacting nuclei have to overcome the Coulomb barrier, which significantly increases as their charges increase. This is the reason why the mass fractions of the elements decrease in the range $A = 1 - 50$.

Furthermore, the binding energy per nucleon of the nuclei increases with mass number and reaches its maximum for ^{56}Fe (8.8 MeV/nucleon), causing the iron-peak formation in the element distribution, as we can clearly see in Fig. 1.1. This is also the reason why the fusion reactions do not go beyond iron, since they would be endothermic (absorb energy) and not exothermic (release energy) like the

Element distribution of the Solar System
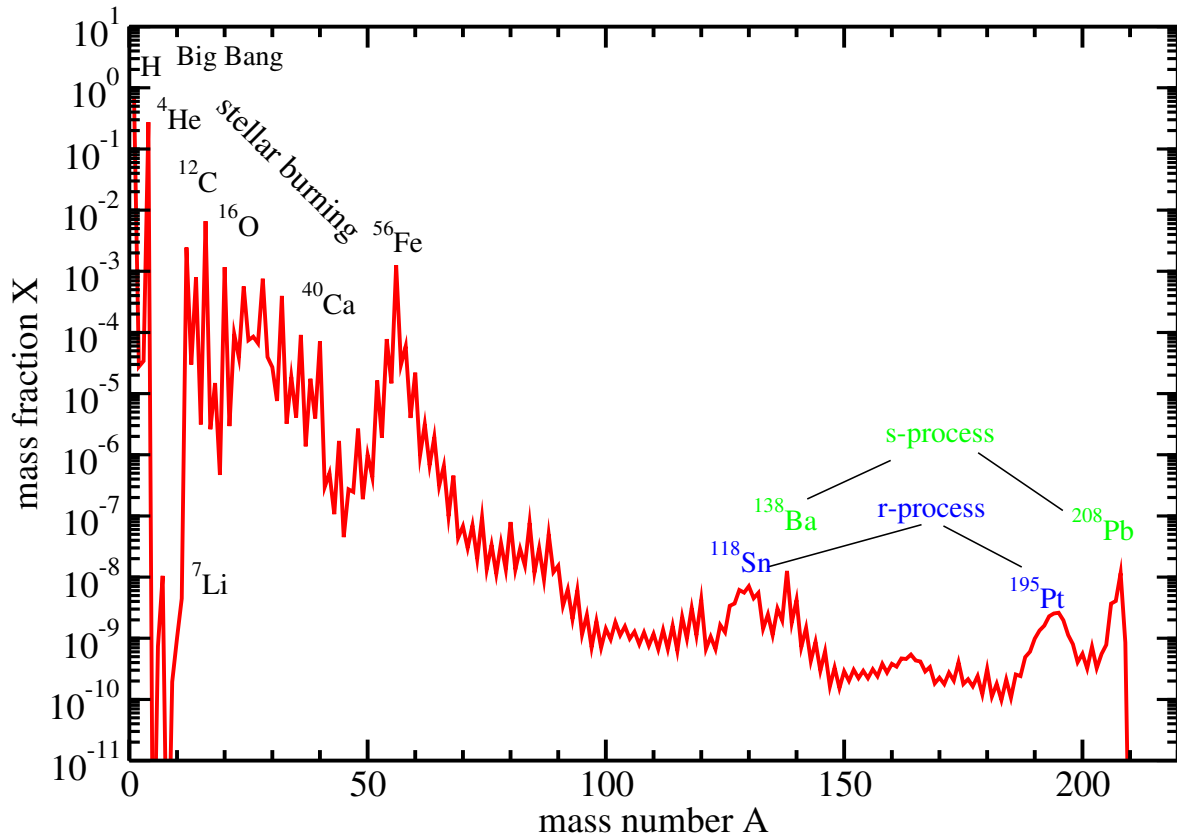
Figure 1.1 Distribution of mass fractions *X* of chemical elements of our Solar System as functions of mass number *A* (Lodders 2003). The lightest elements H and some He are produced during the Big-Bang nucleosynthesis, while the elements from C to Fe are produced through fusion reactions during the different burning stages in the stellar interiors. The heavy elements beyond Fe are produced through the s-process (peaks corresponding to very stable or magic nuclei, with Z or N=50, 82, 126) or r-process (bumps on the left side of the magic nuclei).

fusion reactions involving lighter nuclei. The above considerations led to the conclusion that only the metals which are lighter than Fe can be produced inside stars through fusion reactions.

Let us now focus on the distribution of the elements heavier than Fe. The first thing we notice is that the decrease of the mass fraction of the element distribution beyond iron is much less steeper than the one of the lighter elements. This means that nuclei beyond Fe cannot be produced through charge-reactions, since the probability for these reactions to occur is very low (the Coulomb barrier is extremely high), and therefore the observed distribution of the elements should decrease much faster as it does with increasing A.

In 1957, Burbidge et al. (1957) suggested the *neutron capture* reactions as the main mechanism to produce the elements beyond iron. This means that, starting from a "seed" nucleus, this nucleus can capture free neutrons, and therefore become bigger and bigger. Eventually, the neutrons inside the nucleus can decay β, transforming neutrons into protons, and therefore change the "identity" of the nucleus by increasing its charge number (*Z*).

Thus, in order for neutron captures to occur, we need an astrophysical environment where a significant number of *free neutrons* is available. If a lot of free neutrons are available, namely the neutron number density is $N_n \simeq (10^{20} - 10^{30}) \cdot cm^{-3}$, then the time a seed nucleus needs to capture a neutron (τ_n) is much lower than the time it needs to decay β (τ_β), therefore the so-called rapid-process (or *r-process*) can occur. On the other hand, if $N_n \simeq (10^7 - 10^{10}) \cdot cm^{-3}$, then $\tau_n \ll \tau_\beta$ and so-called slow-process (*s-process*) can take place. The s-process can explain the production of the elements which are very stable (also called *magic nuclei*), since they have a closed shell configuration of protons or neutrons (Z or neutron number N=50, 82, 126). These elements correspond to the peaks observed in the solar distribution of the elements in Fig.1.1. On the other hand, the r-process explains the formation of the "bumps" on the left side of these peaks.

Due to the very different conditions required for the s-process and the r-process, at least two different astrophysical sites are required for them to take place. The s-process is thought to be produced through neutron captures on silicon-iron seed nuclei during the helium-burning core of massive stars and in the thermally pulsing helium stages of asymptotic giant branch stars (see José & Iliadis 2011 for a review on the origin of the elements). On the contrary, the sites for the r-process have not yet been unambiguously discovered (for a review on the r-process see Arnould et al. 2007, José & Iliadis 2011), although the candidate sites are either core-collapse supernovae (CCSNe) and/or mergers involving neutron stars (NS) or black holes (BH) (e.g., Goriely et al. 2013, Bauswein et al. 2013, Just et al. 2015). In particular, among CCSNe models, magneto-rotational SNe explosions seem to have favorable conditions for the r-process, although they are not favored to be the main source of the galactic r-process elements since they are rare events (Nishimura et al. 2015) and, as yet, they only work if extremely high pre-collapse magnetic fields are assumed. On the other side, NS-NS as well as NS-BH mergers seem to be the most promising site for r-process. In particular, very recently, Just et al. (2015) showed that the ejecta expelled during NS-NS and NS-BH mergers can have suitable conditions for the production of r-process elements heavier than $A \gtrsim 90$, whose distribution matches the one of our solar system. However, besides the aforementioned sites, there is another possible astrophysical environment in the CCSNe context, the so-called *neutrino-driven wind* (*v-driven wind*), in which at least some r-process elements can be produced.

It is the aim of this work to focus on the production of the elements in CCSNe (both in the explosion itself as well as in the *v*-driven wind). Before discussing the details of nucleosynthesis, let us briefly have a look at the theory which lies behind the formation of CCSNe in the next section.

1.2 Core-collapse supernovae: delayed neutrino-driven explosion mechanism

Massive stars (with a mass $M > 10 \ M_\odot$, $M_\odot \simeq 2 \cdot 10^{30}$ kg being the mass of our sun) end their lives either as black holes or as one of the most powerful explosions of the Universe, the so-called core-collapse supernovae (CCSNe). For a detailed discussion of the underlying mechanism of CCSNe we refer to reviews by Bethe (1990), Janka et al. (2012), Burrows (2013) and Foglizzo et al. (2015). In the following we only give a brief summary of the general picture.

All along the life of a massive star, fusion burning reactions occur (releasing energy) until the final formation of an iron core. Consequently, at the end of their lives, massive stars have the so-called "onion-shell" structure (see Fig. 1.2): The core is made of Fe and, going towards the surface, the shells are made of the lighter products of the fusion reactions, namely Si, O, Ne, C, He, and H.

Due to the fusion of Si in the shell surrounding the Fe core, the mass of the Fe core increases and as

soon as the Fe core reaches a critical mass, which is about the Chandrasekhar mass ($M_{\text{Ch}} \simeq 1.3 \; M_\odot$), the core becomes gravitationally unstable. At this stage, electrons are captured on nuclei and nuclei photodisintegrate. This means that the degeneracy and thermal pressure significantly decrease and they cannot counterbalance the force of gravity anymore. Therefore, the core collapses. During the collapse, the gravitational energy is converted into internal energy which is in large part radiated away by neutrinos. As soon as the density of the core reaches about $\rho \simeq 10^{12} \text{g/cm}^3$, neutrinos are trapped inside the stellar core, since their diffusion time becomes larger than the collapse time.

From this point on, the inner stellar core collapses adiabatically until the saturation density of nuclei ($\rho \simeq 10^{14} \text{g/cm}^3$) is reached. Then, the collapse stops because of the stiffening of the equation of state due to the short range repulsive interaction of the nucleons. This leads to the bounce of the inner core and the formation of a shock wave, which travels outwards and collides with the in-falling matter of the outer stellar core of the progenitor.

However, this shock wave is not energetic enough to directly trigger a supernova explosion, since it loses energy through the dissociation of Fe peak nuclei into free nucleons. Furthermore, as it reaches densities below $\simeq 10^{11} \text{g/cm}^3$, the shock wave loses further energy, because the region behind the shock front becomes transparent to neutrinos. Shortly after, the shock wave stalls at a typical distance from the center of the nascent proto-neutron star (PNS) of $r \simeq 100-200$ km. Since the matter behind the shock is falling inwards, i.e. has negative velocities, the shock is called an accretion shock.

According to the so-called "delayed neutrino-driven explosion mechanism", the shock wave can be revived again thanks to the energy which is deposited by neutrinos emitted from the PNS. In fact, most of the gravitational energy released during the collapse of inner stellar core is carried away by neutrinos. These neutrinos can heat up the matter by depositing a fraction of their energy in the region between the nascent PNS and the shock surface by means of the following charged-current neutrino capture reactions on free nucleons:

$$\nu_e + n \longrightarrow p + e^-, \tag{1.1}$$

$$\bar{\nu}_e + p \longrightarrow n + e^+. \tag{1.2}$$

On the other hand, the matter is also cooled by the corresponding inverse reactions:

$$p + e^- \longrightarrow \nu_e + n, \tag{1.3}$$

$$n + e^+ \longrightarrow \bar{\nu}_e + p. \tag{1.4}$$

Since the neutrino heating rate is $\propto r^{-2}$, while the cooling rate is much steeper $\propto r^{-6}$ (Janka et al. 2012), there exists a radius, the so-called gain radius, at which the cooling and heating processes balance each other. This means that in the region between the gain radius and the shock front neutrinos effectively heat the matter and, if this heating is strong enough, then the shock can be revived again and, finally, the SN explosion can occur.

Besides the energy deposition due to neutrino interaction, improved numerical simulations show also that hydrodynamic instabilities can help as well in reviving the shock, and therefore trigger the explosion (Janka et al. 2012).

The SN 1987A event was a great opportunity to better understand the mechanism of CCSNe, also because it showed that the mass distribution of the ejecta was anisotropic (e.g., Hillebrandt et al. 1989; Arnett et al. 1989; Müller 1998). These features in the SN explosion can be explained only if hydrodynamic instabilities take place shortly after the bounce of the core (Kifonidis et al. 2006; Hammer et al. 2010).

Furthermore, stars heavier than 10 $M_\odot$ do not explode if spherical symmetry (1D) is assumed in simulations with a self-consistent treatment of neutrinos (e.g., Rampp & Janka 2000; Liebendörfer et al.

"Onion-shell" structure of pre-supernova
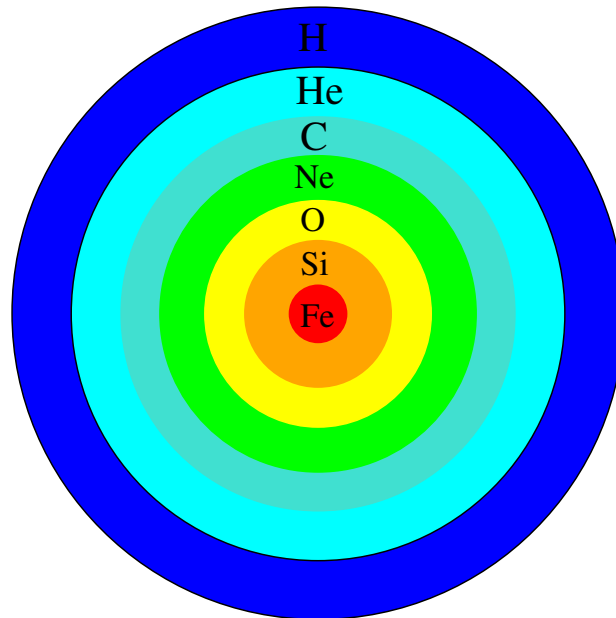
Figure 1.2 Schematic representation of the so-called "onion-shell" structure of a massive star ($M >$ 10 $M_\odot$), as predicted by stellar evolution models, shortly before the core-collapse. In each shell, the main element coming from the different burning stages of the star is shown.

2001). This means that multi-dimensional effects play a crucial role in helping the neutrino-driven mechanism to launch the SN explosion. In particular, two important hydrodynamic instabilities have been identified which can play an important role in the region between the stalled SN shock and the nascent PNS:

(i) The neutrino hot-bubble convection (e.g., Herant et al. 1992; Mueller & Janka 1997), which is due to the fact that the heating of the matter due to neutrino interactions is stronger close to the gain radius and decreases with increasing radius, and thus going towards the shock front. This causes the matter to be unstable against buoyancy-driven convection (Bethe 1990), and therefore high-entropy bubbles are produced which transport heated material from the gain radius to the shock front, helping the shock front to move out;

(ii) The "standing-accretion-shock-instability" (SASI) (Blondin et al. 2003) which can show up in large-scale sloshing motions of the shock front with strongly pulsating expansions and contractions. In 3D, it can also develop spiral modes (Blondin & Mezzacappa 2007).

In summary, it is expected that both convection and SASI sufficiently contribute to the energy deposition in the gain layer so that the shock wave can be revived and the SN explosion can occur.

Once the explosion is launched, the shock wave passes through the different layers above the core and the so-called "explosive nucleosynthesis" takes place, as it will be discussed in the next section. Then, the matter which is processed by the shock wave, together with the layers which are not affected by

explosive nucleosynthesis (the outermost H and He layers), is ejected into the interstellar medium, making CCSNe one of the major sources of nuclei with $A > 12$ in our Galaxy.

Furthermore, shortly after the explosion has been launched, there is a flow of matter driven by the energy deposited on the surface of the PNS by neutrinos, the already mentioned ν-driven wind, which has been considered for a long time as a site for the νp-process (Fröhlich et al. 2006b) and the r-process (see Sect. 1.3).

1.2.1 Explosive nucleosynthesis in core-collapse supernovae

Here, we give a short summary of the explosive nucleosynthesis associated with the passage of the SN shock wave through the layers above the PNS, for a review see Woosley et al. (2002) and José & Iliadis (2011).

Once the shock wave has been launched from the core, it first encounters the ^{28}Si shell (see Fig. 1.2), leading to an increase of the peak temperature $T_{\text{peak}} \gtrsim 5$ GK and of the peak density $\rho_{\text{peak}} \gtrsim 10^7 - 10^8$ g/cm^3. At such high densities and temperatures, the matter reaches the so-called *"nuclear statistical equilibrium (NSE)"*. In NSE, the rates of all forward and reverse electromagnetic and strong interactions are in a *global equilibrium*, i.e. there is a global balance between the nuclear reactions which produce nuclei and the photodisintegration reactions which disintegrate the existing nuclei into nucleons. In NSE, the mass fraction X of a nucleus with charge number Z and mass number A is given by (Meyer et al. 1992):

$$X(Z,A) = G(Z,A)[\zeta(3)^{A-1}\pi^{(1-A)/2}2^{(3A-5)/2}]A^{5/2}\left(\frac{kT}{m_N c^2}\right)^{3(A-1)/2}\phi^{1-A}X_p^Z X_n^{A-Z}\exp\left[\frac{B(Z,A)}{k_B T}\right], \quad (1.5)$$

where $G(Z,A)$ is the nuclear partition function, ζ is the Riemann function, T is the temperature, m_N is the nucleon mass, ϕ is the photon-to-baryon ration, X_p and X_n are the mass fractions of free protons and neutrons, respectively, $B(Z,A)$ is the nuclear binding energy, and k_B is the Boltzmann constant. Furthermore, ϕ can be expressed in terms of temperature and density as:

$$\phi = \frac{n_\gamma}{\rho N_A} = \frac{1}{\pi^2}\frac{g_\gamma}{(\hbar c)^3}\frac{\zeta(3)(k_B T)^3}{\rho N_A} \quad (1.6)$$

where n_γ is the number density of the photons, ρ is the mass density, N_A is Avogadro's number, and g_γ is the helicity for photons. We can also write Eq. (1.6) in terms of the temperature in units of 10^9 K (T_9) and of density in units of 10^5g/cm^3 (ρ_5):

$$\phi = 0.39\frac{T_9^3}{\rho_5}. \quad (1.7)$$

From Eqs. (1.5), (1.6) and (1.7), we can deduce that, once the nuclear properties of the nuclei are known (e.g., binding energy, mass, and spins), their *abundances*[1] in NSE are determined by temperature, density, and the electron fraction of the matter Y_e (or the *neutron excess* η[2]), which can change only because of the weak interactions. Furthermore, because of the strong dependence of $X(Z,A)$ on ϕ and on $B(Z,A)/k_B T$, the outcome of the nucleosynthesis in NSE depends on the competition between these terms:

---

[1]The abundance Y of a nucleus with mass number A and mass fraction X is defined as $Y = X/A$.

[2]The neutron excess is defined as $\eta = 1 - 2Y_e$.

- If ϕ is large, then a lot of photons are available per baryon, therefore NSE favors a composition mainly made of nucleons and α particles, because the production of heavier nuclei is hampered by the photodisintegration reactions.

- On the other hand, if ϕ is of the order of unity or less, then iron-peak nuclei are favored in NSE, since they have the largest binding energy $B(Z,A)$.

For example, in the silicon layer, where ϕ is less than the order of unity, the main expected product of the explosive nucleosynthesis is ^{56}Ni, since it has the largest binding energy among all iron-peak nuclei and all species which have the same number of neutrons and protons .

The detailed outcome of the explosive Si burning depends basically on the peak density and expansion time scale (τ_{exp}) of the matter after reaching NSE:

i) if ρ_{peak} and τ_{exp} are large enough, then NSE produces very small amounts of light particles (p, n, and α). This regime, is also called *"normal freeze-out"*, and the main nucleosynthesis products are ^{56}Ni and other Fe-peak nuclei;

ii) if ρ_{peak} or τ_{exp} are small enough, then NSE leads to the production of a relatively large amount of light particles, especially α-particles, the so-called *"α-rich freeze out"*. In this case as well, if $\eta \sim 0$, the main product is ^{56}Ni, but, furthermore, the very important $\gamma-$ray emitter ^{44}Ti is produced (see chapter 5).

As the shock propagates further outwards through the Si layer, the matter is heated up to $T_{peak} \sim 4-5$ GK. In this case, the global equilibrium among all the nuclear species is not reached, but instead, a local equilibrium in two different mass ranges is reached, the one centered in the silicon and the other in the Fe-peak nuclei. For this reason, in this case, we talk about a *"quasi equilibrium"* (QSE), instead of NSE.

In QSE, the abundance of any nucleus is determined, besides by nuclear parameters, by the temperature, density, η, and the abundance of ^{28}Si. The major products of QSE are Fe-peak nuclei, intermediate-mass nuclei (with mass number $A = 40 - 44$) and ^{28}Si. Since, there is a lot of ^{28}Si which remains after the passage of the shock wave, this stage is called *"incomplete silicon burning"*.

After the Si layer, the shock wave passes through the oxygen shell (see Fig. 1.2). The peak temperature reached in the ^{16}O layer is in the range $T_{peak} \sim 3 - 4$ GK. In this case as well, two QSE clusters form in the region of Si and Fe-peak nuclei, but, since T_{peak} in this case is lower than in the case of incomplete Si burning, there is much more material around the Si mass region than around the Fe-peak region. The main products of explosive oxygen burning are ^{28}Si, ^{28}S, ^{36}Ar, and ^{40}Ca.

After the shell consisting mostly of ^{16}O, the shock wave passes through a layer made mainly of ^{16}O, ^{20}Ne and ^{12}C. In this layer, $T_{peak} \sim 2 - 3$ GK and ^{20}Ne and ^{12}C burn explosively. In this case the nuclear reactions proceed far from equilibrium conditions, since T_{peak} and τ_{exp} are too small for a QSE configuration to be reached. Therefore, the final abundances of the nuclear species are determined by the initial composition and the thermonuclear reaction rates (see chapter 2). In this case, the most abundantly produced nuclei are ^{16}O, ^{20}Ne, ^{24}Mg and ^{28}Si. Another important element which is produced during this burning stage is the γ-ray emitter ^{26}Al, which has been detected in the interstellar medium of our Galaxy (José & Iliadis 2011).

After the Ne/C layer, the peak temperature reached by the matter is too low ($T_{peak} \leq 2$ GK) for explosive nucleosynthesis to take place. Therefore, the composition of the layers above Ne/C layer remains as it was after the hydrostatic burning of the pre-supernova stage.

In Fig. 1.3, we show a schematic representation of the explosive nucleosynthesis occurring during the passage of the supernova shock wave through the different layers of the star.

We notice that the exact abundance distribution of the elements, which are produced during the explo-

Explosive nucleosynthesis
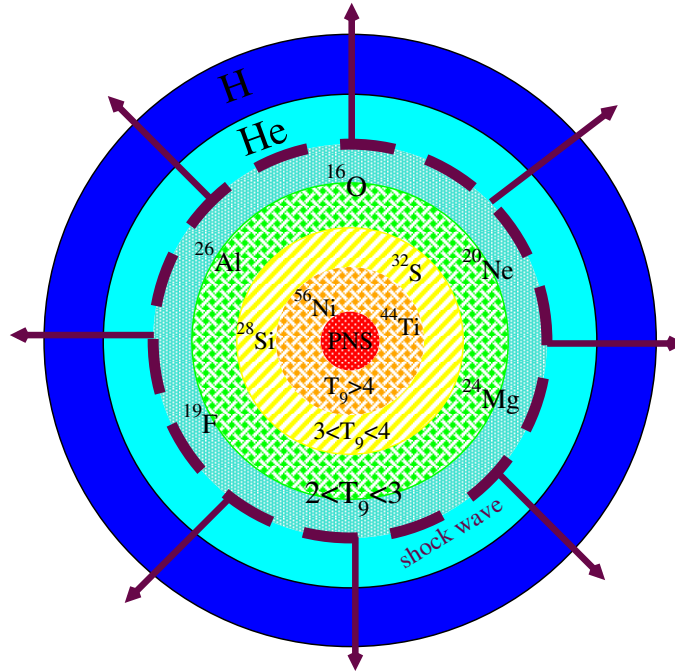
Figure 1.3 Schematic representation of the explosive nucleosynthesis due to the passage of the supernova shock wave through the different layers of the star (Si, O, C, He, H). The main elements produced during the explosive nucleosynthesis are also shown. If the peak temperature of the shock is $T_9 > 4$, then the burning of Si produces mostly ^{56}Ni, if $3 < T_9 < 4$ then the burning of O produces mainly ^{28}Si and ^{32}S, and if $3 < T_9 < 2$ then the burning of Ne and C produces especially ^{16}O, ^{20}Ne, ^{24}Mg and ^{26}Al. If $T_9 < 2$ the explosive nucleosynthesis stops, therefore the layers above C are almost not affected by the explosive nucleosynthesis, since the peak temperature reached during the passage of the shock is too low.

sive nucleosynthesis, depends on the details of the pre-supernova stellar structure, since it determines the amount of matter which is exposed to the different explosive nucleosynthesis stages. Furthermore, the electron fraction (Y_e) profile of the pre-supernova stage, strongly influences the outcome of the explosive nucleosynthesis which occurs in NSE or QSE.

While the shock wave is propagating outwards through the different layers above the stellar core, another interesting site for the nucleosynthesis (the neutrino-driven wind) starts blowing away from the surface of the PNS, as it will be discussed in the next section.

1.3 Neutrino-driven wind

Shortly after the supernova has occurred, the PNS is left behind by the explosion at the center of the massive star. After its formation, the PNS can heat up to temperatures of 10 MeV or higher. At such high temperatures, neutrinos are copiously produced, which carry away the gravitational binding energy of the PNS. As a consequence of the emission of neutrinos, the hot PNS cools down.

The emitted neutrinos can also be reabsorbed by the matter close to the surface of the PNS, and therefore deposit enough energy so that the matter can escape the huge gravitational field of the PNS. For this reason, this flow of matter which blows away from the PNS is called *neutrino-driven wind* (or ν-driven wind), as schematically shown in Fig 1.4 (for a review on this topic we refer to Qian & Woosley 1996 and Arcones & Thielemann 2013). The mass loss of the PNS due to the ν-driven wind continues until the PNS is transparent to neutrinos (until about 10 s after the bounce of the core).

Very close to the surface of the PNS the matter is so hot that it is basically made of free neutrons and protons, but, as the ν-driven wind blows away from the PNS surface, the matter cools down, allowing for α particles, and later on heavier nuclei, to form.

The ν-driven wind has been considered as an interesting site for the nucleosynthesis and, in particular, a candidate for the r-process. However, the exact outcome of the nucleosynthesis in the ν-driven wind depends on different physical conditions, as it will be discussed in the next section.

1.3.1 Nucleosynthesis in the neutrino-driven wind

As we already mentioned in Sect. 1.1, the sites for the r-process have not yet unambiguously been identified. Among the possible candidates, there is also the ν-driven wind, since it is a rapidly expanding and cooling high-entropy environment. These conditions can lead to the production of the elements beyond iron (Takahashi et al. 1994).

Very close to the surface of the PNS, the temperature and density are so high ($T \geq 10$ GK) that the matter is in NSE (see Sect. 1.2.1). In particular, the matter is mainly made of free neutrons and protons. As the matter expands, the temperature decreases and the nuclear composition changes. At $T \simeq 9$ GK, α-particles start forming. As the matters continues to expand, the temperature keeps decreasing and the nuclear reactions proceed more slowly, and finally the reaction rates become smaller than the expansion rate. Therefore, the reactions first fall out of equilibrium and finally "freeze out". When $T \simeq 6$ GK, the triple-α reaction ($3\alpha \longrightarrow {}^{12}$C) starts, which is followed by other reactions, such as captures of neutrons and protons on ^{12}C. In particular, after the formation of ^{12}C, depending on the neutron to proton ratio of the matter, two main different nucleosynthesis processes in the ν-driven wind can be distinguished:

- If the matter is *proton-rich* ($Y_e > 0.5$), then the νp-process could occur (Fröhlich et al. 2006b). In this process, ^{12}C acts as a seed nucleus for the capture reaction such as (p, γ), (α, γ) and (α, p) which proceed until the formation of seed nuclei with $N = Z$, up to ^{64}Ge. After the formation of ^{64}Ge, nuclear reactions can proceed thanks to the electron antineutrino fluxes streaming from the surface of the PNS. In fact, in proton-rich conditions, $\bar{\nu}_e$ can be absorbed by free protons which produce a continuous supply of free neutrons which can be captured by the seed nuclei through (n, p) reactions. Then, the subsequent (p, γ) reactions allow for the production of nuclei with $A > 64$ on the proton-rich side of the nuclear chart. The name of this process is related to the crucial role played by neutrinos and protons;

Neutrino-driven wind nucleosynthesis

Figure 1.4 Schematic representation of the ν-driven wind, namely the flow of matter which, shortly after the SN explosion has been launched, escapes the huge gravitational field of the PNS thanks to the energy deposited by neutrinos and antineutrinos. Close to the PNS surface the temperature is so high that the matter is almost made of free neutrons and protons. As the matter expands and cools down, α particles start forming. As it propagates even further out, the "seed" nuclei can form. After the seed nuclei have formed, eventually the r-process can occur (in neutron-rich conditions) or the νp-process (in proton-rich conditions).

- On the other hand, if the ν-driven wind matter is *neutron-rich* ($Y_e > 0.5$), then, after a sequence of reactions such as (α, n), $(\alpha n, \gamma)$ (Witti et al. 1994), the matter is made of seed nuclei and *free* neutrons. This means that the r-process could occur, namely the free neutrons can be captured into the seed nuclei, leading to the formation of heavy nuclei, which then decay β. In order for the production of very heavy nuclei ($A \sim 240$) to occur, starting from seed nuclei with $A \sim 50 - 100$, the free neutron-to-seed nuclei ratio has to be $Y_n/Y_{\text{seed}} > 100$. This means that only a relatively small number of seed nuclei should be formed, so that, when the r-process occurs, a sufficiently large number of free neutrons is available to be captured by the seed nuclei. In order for the r-process to occur, the neutron richness of the matter is not enough, but two other conditions have also to be fulfilled:
  i) The entropy has to be high enough so that the photodisintegration of heavier nuclei allows for the presence of much more neutron than seed nuclei;
  ii) The expansion time scale has to be short enough (about few milliseconds) so that the efficiency of the α-process, which leads to the formation of the seed nuclei, is damped. In such a

way, the ratio of neutrons-to-seed nuclei remains high, as the r-process requires.

The ν-driven wind parameters, which determine the production of the elements, depend on the structure of the neutron star (e.g., on its gravitational field) and on the properties of the emitted neutrinos (i.e., luminosities and spectra). The latter play a crucial role in determining the neutron-to-proton ratio through β-reaction, and hence the outcome of the nucleosynthesis. Therefore, in order to predict which elements are produced in the ν-driven wind, we have to accurately investigate the properties of ν_e and $\bar{\nu}_e$.

1.4 Aim and structure of this thesis

The aim of this thesis is to investigate certain aspects of the nucleosynthesis in CCSNe, both of the explosive nucleosynthesis associated with the explosion of the supernova itself and of the outcome of the nucleosynthesis in the ν-driven wind.

After describing the nuclear reaction network which we use for our nucleosynthesis calculations in chapter 2, we will focus on the impact of the neutrino properties on the ν-driven wind nucleosynthesis in chapters 3 and 4, since, as we already mentioned, they play a crucial role in determining the production of the elements. In particular, in chapter 3, using sophisticated supernova simulations of an 8.8 $M_\odot$ progenitor, we will present a parametric study about the neutrino and antineutrino properties and their impact on the electron fraction. This study is motivated by recent works on nucleon potential corrections on the neutrino opacities (Martínez-Pinedo et al. 2012; Roberts et al. 2012), which shift the mean energies of neutrinos and antineutrinos compared to the uncorrected case. We will also investigate the validity of equilibrium assumptions about Y_e in the different evolution phases of our ν-driven wind.

In chapter 4, we will focus on the impact of neutrino flavor oscillations on the ν-driven wind nucleosynthesis for the same progenitor as considered in chapter 3. In one case, we will consider only oscillations among active flavors (e, μ, and τ) and, in the other case, we will consider what would happen if sterile neutrinos existed, and therefore active flavors could convert to sterile ones.

In chapter 5, we will present our results concerning the explosive nucleosynthesis of a 15 $M_\odot$ and a 20 $M_\odot$ progenitor, whose SN explosions were simulated in 3D and 1D. We will focus on the produced amounts and spatial distributions of ^{44}Ti and ^{56}Ni, since these two radioactive elements have been observed in supernova explosions, and therefore allow us to test the modeling which is used to perform our supernova simulations. In particular, we will pay a special attention to the role played by the asymmetries in setting the SN explosion.

Finally, in chapter 6, we will give a summary of our main results shown in chapters 3, 4 and 5, and present our conclusions and perspectives.

2 Nuclear Reaction Rates and Nuclear Reaction Network

2.1 Introduction

Nuclear astrophysics deals with the description of the nuclear reactions which take place in astrophysical environments, and therefore change the energy and composition of the system.

In this chapter, some notions concerning the nuclear reaction rates and the nuclear reaction networks are presented. A nuclear reaction network describes the evolution of the nuclear composition of a physical system. In order to follow this evolution, one has to solve the coupled first order differential equations, which describe each nuclear species. Their evolution is dependent on the nuclear reaction rates which produce or destroy them. These reaction rates include fusion reactions, photodisintegration of nuclei, and weak interactions like absorption or emission of neutrinos, electrons etc. Therefore, three of the four fundamental forces have to be taken into account in order to describe the reaction rates: The strong force, which concerns the emission or absorption of nucleons and nuclei; The weak interaction, which concerns all processes involving leptons, such as electrons, positrons, neutrinos, and antineutrinos; The electromagnetic interaction, which concerns the emission and absorption of photons.

In the following, we start by summarizing the different kinds of reaction rates involved in the astrophysical plasma and we will conclude by showing a method which is used to solve nuclear reaction networks.

2.2 Cross-sections and thermonuclear reaction rates

Let us consider a reaction between a projectile a and a target b, whose final products are c and d[1]:

$$a + b \longrightarrow c + d. \tag{2.1}$$

The cross-section of the reaction (2.1) is then defined as:

$$\sigma = \frac{\dot{N}_{\text{reac}}}{F_{\text{proj}}}, \tag{2.2}$$

where $\dot{N}_{\text{reac}}$ is the number of reactions per target per second and F_{proj} is the flux of incoming projectiles. If the projectile and the target follow the same distribution, that is generally isotropic and depends only on the momenta p of the reactants, and if the particles are in thermal equilibrium, then

---

[1] We follow the notation of Martínez-Pinedo (2008).

the system can be characterized by the temperature T and by the chemical potential μ. If the projectiles and the targets follow a distribution $n_a(p)$ and $n_b(p)$, respectively, then for a constant relative velocity v between a and b, the number of reactions per cm^3 and per second for the reaction (2.1) can be written as (Martínez-Pinedo 2008):

$$r_{ab} = \int \sigma(v) v n_a(p) n_b(p) dp_a dp_b. \tag{2.3}$$

In a typical astrophysical plasma, the nuclei follow a Maxwell-Boltzmann distribution. Therefore, their normalized distribution is:

$$n = \frac{G(T)}{(2\pi\hbar)^3} \int e^{\left(\frac{E-\mu}{kT}\right)} 4\pi p^2 dp, \tag{2.4}$$

where $G(T)$ is the partition function of the considered nuclei and is given by:

$$G(T) = \sum_i (2J_i + 1) e^{-E_i/(kT)}, \tag{2.5}$$

and the sum runs over all excited states with angular momentum J_i and energy E_i (Tubbs & Koonin 1979).
Using Eq. (2.4), the thermonuclear reaction rate (2.3) can be written as:

$$r_{ab} = \langle \sigma v \rangle_{a,b} n_a n_b, \tag{2.6}$$

where $\langle \sigma v \rangle$ is the average value of σv over the energy distribution, namely:

$$\langle \sigma v \rangle_{a,b} = \left(\frac{8}{\pi m_u}\right)^{1/2} \frac{1}{(kT)^{3/2}} \int e^{-\frac{E}{kT}} \sigma(E) E dE, \tag{2.7}$$

and m_u is the reduced mass. In the same way, we can also define the mean lifetime of a nucleus b against destruction due to the nucleus a:

$$\tau(b) \equiv \frac{1}{\langle \sigma v \rangle_{a,b} n_a}. \tag{2.8}$$

Nuclear reaction rates are enhanced in astrophysical environments of high temperatures or low densities, since the reacting nuclei are surrounded by electrons which shield the repulsive Coulomb force felt by charged nuclei. In order to account for this effect, which is called *electron screening*, we can write Eq. (2.7) as (Itoh et al. 1979):

$$\langle \sigma v \rangle_{a,b}^{scr} = \langle \sigma v \rangle_{a,b} \cdot f_{scr}(Z_a, Z_b, \rho, T, Y_a), \tag{2.9}$$

where the screening factor $f_{scr}(Z_a, Z_b, \rho, T, Y_a)$ is a function of the charges of the reacting nuclei, the density, the temperature and the composition of the plasma.
Whenever it is possible, the cross-sections σ of the thermonuclear reactions are determined experimentally, and if the particles which are involved in the reaction follow a Maxwell-Boltzmann distribution, the value of $\langle \sigma v \rangle$ can be determined. However, it is not always necessary to directly find (experimentally or theoretically) the reaction rates of all reactions. In fact, if the cross-section of a reaction $\sigma_{ab \to cd}$ is known, then, thanks to the *detailed balance theorem*, we can straight forward find the

cross-section of its inverse reaction $\sigma_{cd\to ab}$, because they are linked by the following relation (Blatt & Weisskopf 1952):

$$\frac{\sigma_{cd\to ab}}{\sigma_{ab\to cd}} = \frac{(2j_a + 1)(2j_b + 1)k_{ab}^2(1 + \delta_{cd})}{(2j_c + 1)(2j_d + 1)k_{cd}^2(1 + \delta_{ab})}, \tag{2.10}$$

where $2j_i + 1$ are the states of orientation available for a particle with spin j_i, k_i are the wave numbers and the factors $1 + \delta_{cd}$ (δ_{cd} is the Kronecker delta) account for the fact that cross-sections between identical particles in the entrance channel are twice those between different particles, the other factors being equal. Eq. (2.10) applies to particles with rest mass as well as to photons. The symbols a, b, c and d do not only refer to specific nuclei, but to specific nuclear states. This means that the detailed balance theorem connects the same nuclear levels in the forward as in the inverse reaction. For example, in an astrophysical plasma the excited states of a nucleus are thermally populated and the term $2j_i + 1$ has to be replaced by $G(T)$ (see Eq. 2.5). Therefore, knowing the value of $\sigma_{ab\to cd}v$ for a thermonuclear reaction, thanks to Eqs. (2.5), (2.7) and (2.10), we can find for the inverse reaction:

$$\sigma_{cd\to ab} = \frac{1 + \delta_{cd}}{1 + \delta_{ab}} \frac{G_a G_b}{G_c G d} \left(\frac{m_{u_{cd}}}{m_{u_{ab}}}\right)^{3/2} e^{-Q/kT} \sigma_{ab\to cd}, \tag{2.11}$$

where m_u is the reduced mass and Q is the Q-value of the reaction.

2.3 Reactions with light or massless particles

If we consider reactions where one of the particles is much lighter (projectile) than the other (target) (e.g., the electron is 2000 times lighter than neutrons and protons), then we can assume that the relative velocity of the particles is just the one of the lightest one.
In this case the integration of Eq. (2.3) over the target nucleus gives just the density of the targets n_b. Therefore, Eq. (2.3) becomes:

$$r_{ab} = n_b\lambda_b(T, \rho_a, \mu_a), \tag{2.12}$$

where

$$\lambda_b = \int \sigma v_a n p_a dp_a \tag{2.13}$$

is an effective decay rate of the target nucleus, which depends on the temperature, on the density, and on the chemical potential of the projectile.
In particular, in reactions involving nuclei and photons we can assume that the relative velocity is the speed of light c. In this case, the target nuclei follow a Maxwell-Boltzmann distribution and the photons follow a Bose-Einstein distribution with temperature T and chemical potential zero:

$$n_\gamma(p) = \frac{1}{\pi^2\hbar^3} \frac{p^2}{e^{pc/kT} - 1}. \tag{2.14}$$

Using Eq. (2.13) and Eq. (2.14), we can write the effective photodisintegration rate as:

$$\lambda_\gamma(T) = \frac{1}{\pi^2\hbar^3 c^3} \int \frac{\sigma(E)cE^2}{e^{E/kT} - 1} dE, \tag{2.15}$$

which depends only on the temperature. If we know the photodisintegration cross-section, then we can find λ_γ through the integral in Eq. (2.15). Otherwise, we can use the detailed balance theorem in order to determine the photodisintegration rates, once we know the term $\langle \sigma_{a,b}v \rangle$ of the inverse reaction:

$$a + b \longrightarrow c + \gamma, \tag{2.16}$$

having a reaction Q-value $Q = m_a c^2 + m_b c^2 - m_c c^2$ and each species having a atomic weight A_i. Then, making use of $k_\gamma = E_\gamma/(c\hbar)$, $G_\gamma = 2$ (for photons), and substituting Q and A_i in Eqs. (2.15, 2.10), it follows that:

$$\lambda_\gamma(T) = \left(\frac{m_u kT}{2\pi\hbar^2}\right)^{3/2} \frac{1}{1+\delta_{a,b}} \frac{G_a G_b}{G_c} \left(\frac{A_a A_b}{A_c}\right)^{3/2} e^{-Q/kT} \langle\sigma v\rangle_{a,b}. \tag{2.17}$$

2.4 Decay reactions

For reactions involving the decay of nuclei with mass number A and charge number Z, e.g. α decays:

$$(A, Z) \longrightarrow (A - 4, Z - 2) + \alpha, \tag{2.18}$$

with a half-life $\tau_{1/2}$, the number of reactions per second is:

$$r = \lambda_A n, \tag{2.19}$$

where λ_A is the decay constant. If we consider the ground state, with a constant half-life $\tau_{1/2}$, then $\lambda_A = \ln 2/\tau_{1/2}$. If the temperature T is high enough, then the excited states can be thermally populated and they have individual constant decays $\lambda_{A,i}(T)$. In this case, the total decay constant of the nucleus, which depends on T, is:

$$\lambda_A = \frac{\sum_i \lambda_{A,i}(2J_i + 1)e^{-E_i/kT}}{G_A(T)}, \tag{2.20}$$

where $G_A(T) = \sum_i \lambda_{A,i}(2J_i + 1)e^{-E_i/kT}$.

2.5 Reactions involving leptons: Electron and positron captures

Reactions involving electron e^- or positron e^+ captures on nuclei can formally be treated as photodisintegration reactions, since the mass of the electron ($m_e = 0.511\text{MeV/cm}^2$) is much smaller than those of the nucleons ($m_n = 931\text{MeV/cm}^2$). Therefore, we can assume that the relative velocity between nuclei and electrons is just the velocity of electrons.

Let us consider the following e^- capture reaction into a nucleus with mass number A and charge number Z:

$$e^- + (A, Z) \longrightarrow (A, Z - 1) + \nu, \tag{2.21}$$

then, following the same procedure as for photodisintegration reactions, the number of reactions per cm^3 per second is given by:

$$r_e = n_A \int \sigma_e(v_e) v_e dn_e, \tag{2.22}$$

with n_A being the number density of the nuclei with mass number A. In an astrophysical plasma electrons follow a Fermi-Dirac distribution and, depending on the density and temperature conditions, they can have any degree of degeneracy, be relativistic or non-relativistic. At very high temperature the reaction of electron and positron pairs must be taken into account as well.

For reactions involving positron captures into nuclei:

$$e^+ + (A, Z) \longrightarrow (A, Z + 1) + \bar{\nu}, \tag{2.23}$$

a formalism very similar to the one used for electron captures can be adopted in order to calculate the capture rates. We refer to chapter 3 for a detailed discussion of the electron and positron capture rates into nucleons.

2.5.1 Neutrino and antineutrino captures

Neutrinos are weakly interacting particles, and therefore have a very small cross-section, but if the density of the astrophysical plasma is high enough, then the electron neutrinos and antineutrinos can be captured into nuclei:

$$\nu_e + (A, Z) \longrightarrow (A, Z + 1) + e^- \tag{2.24}$$

$$\bar{\nu}_e + (A, Z) \longrightarrow (A, Z + 1) + e^+. \tag{2.25}$$

Neutrinos usually are not in thermal equilibrium and their distribution has to be computed by solving the Boltzmann transport equation. Once we know the neutrino distribution, we can use the same formalism as done for the electrons and positron captures into nuclei and calculate the rates of the reactions (2.24) and (2.25):

$$r_\nu = n_A \int \sigma_\nu(E_\nu) E_\nu dE_\nu = n_A \lambda_\nu, \tag{2.26}$$

where n_A is the number density of the capturing nucleus and λ_ν is the decay constant.
We refer to chapters 3 and 4 for a discussion of the capture reactions of electron neutrino and antineutrinos into free neutron and protons, which are among the most relevant reactions in our study.

2.6 Nuclear reaction network

Nuclear network calculations allow us to simulate the change of composition, namely the nucleosynthesis, in astrophysical environments, once we know the evolution of their densities ρ and temperatures T. The way the number density n_i of a nuclear species changes depends not only on the nuclear reactions which produce or destroy this species, but also on hydrodynamic effects. In fact, the expansion and contraction of the environment can change the volume of the stellar plasma. In order to separate the changes in composition due to hydrodynamic effects and to nuclear reactions, we can define for a certain species i its *nuclear abundance*[2]:

$$Y_i = \frac{n_i}{n} = \frac{n_i}{\rho N_A}, \tag{2.27}$$

where N_A is the Avogadro number and $n = \sum_j n_j A_j \simeq \rho/m_b$ is the total number of nucleons (or baryons) in the stellar environment. The abundance of a nucleus Y_i is related to its *mass fraction* by $Y_i = X_i/A_i$. The conservation of the baryon number implies that $\sum_i Y_i A_i = 1$ (or $\sum_i X_i = 1$) and from the conservation of the charge number, it follows that $\sum_i Y_i Z_i = Y_e$, where $Y_e = n_e/n$ is the electron

---

[2]The formalism we use here is similar to the one of Martínez-Pinedo (2008).

fraction.

The time evolution of the abundance Y_i of a species i can be expressed as (Martínez-Pinedo 2008):

$$\frac{dY_i}{dt} = \sum_j N_j^i \lambda_j Y_j + \sum_{j,k} N_{j,k}^i \frac{\rho}{m_b} \langle \sigma v \rangle_{j,k} Y_j Y_k + \sum_{j,k,l} N_{j,k,l}^i \left(\frac{\rho}{m_b}\right)^2 \langle \sigma v \rangle_{j,k,l} Y_j Y_k Y_l, \qquad (2.28)$$

where the sum runs over all the reaction terms which change the composition of the species i:

- the first term refers to the *one-body reactions* (decays, photodisintegration, lepton captures);

- the second sum describes the reactions involving two nuclei, or *two-body reactions*, such as fusion reactions;

- the last term takes into account composition changes due to reactions involving three particles, or *three-body reactions*, which generally describe two successive captures with an intermediate phase of the formation of an unstable nucleus. For example, the triple-alpha reaction is a typical three-body reaction.

The terms with N account for the right number of nuclei participating in the considered reaction and also avoid double counting whenever two identical particles react together. Therefore, we have: $N_j^i = N_i$, $N_{j,k}^i = N_i/(|N_j|!|N_k|!)$ and $N_{j,k,l}^i = N_i/(|N_j|!|N_k|!|N_l|!)$. Since the N factors specify how many particles are created or destroyed during the nuclear reactions, they can be either positive or negative.

2.6.1 Implicit method to solve the nuclear reaction network

In order to find the solutions of the nuclear reaction network we have to solve the coupled non-linear differential equations in Eq. (2.28) (for more details see Hashimoto et al. 1985 and Timmes 1999). For this purpose, we can write Eq. (2.28) as:

$$\frac{dY_j}{dt} = f_j(\mathbf{Y}), \qquad (2.29)$$

where j refers to a nuclear species. In terms of the ith- time step we can write the implicit expression:

$$\frac{Y^{(i)}_j - Y^{(i-1)}_j}{\Delta t^{(i)}} = f_j(\mathbf{Y}^{(i)}), \qquad (2.30)$$

with

$$Y_j^{(i)} = Y_j^{'(i-1)} + \delta Y_j^{'(i-1)}, \qquad (2.31)$$

$$Y_j^{'(i-1)} = Y_j^{(i-1)} + \Delta Y_j^{'(i-1)}, \qquad (2.32)$$

where $Y_j^{'(i-1)}$ is the trivial value of the ith time step, $\delta Y_j^{'(i-1)}$ is the error of the actual value and $\Delta Y_j^{'(i-1)}$ is given by:

$$\Delta Y_j^{(i-1)} = \left(Y_j^{(i-1)} - Y_j^{(i-2)}\right) \frac{\Delta t^{(i)}}{\Delta t^{(i-1)}}. \qquad (2.33)$$

Combining the Eqs. (2.31) and (2.32), we get:

$$Y_j^{(i)} - Y_j^{(i-1)} = \delta Y_j^{'(i-1)} + \Delta Y_j^{(i-1)}. \qquad (2.34)$$

If we substitute Eq. (2.34) into Eq. (2.30) and make a Taylor expansion of the first order for f_j, we get:

$$\frac{\delta Y_j^{'(i-1)} + \Delta Y_j^{(i-1)}}{\Delta t^{(i)}} = f_j\left(\mathbf{Y}^{'(i-1)} + \delta \mathbf{Y}^{'(i-1)}\right) \simeq f_j\left(\mathbf{Y}^{'(i-1)}\right) + \sum_k^N \frac{\partial f_j}{\partial Y_k^{'(i-1)}} \delta Y_k^{'(i-1)}. \qquad (2.35)$$

Therefore, from Eq. (2.35), we obtain the following linear equation:

$$\sum_k^N \left(\frac{\delta_{jk}}{\Delta t^{(i)}} - \frac{\partial f_j}{\partial Y_k^{'(i-1)}} \delta Y_k^{'(i-1)} \right) \simeq f_j\left(\mathbf{Y}^{'(i-1)}\right) - \frac{\Delta Y_j^{(i-1)}}{\Delta t^{(i)}}. \qquad (2.36)$$

The above expression (Eq. 2.36) can be written in the matrix form as:

$$\begin{pmatrix} \frac{1}{\Delta t^{(i)}} - \frac{\partial f_0}{\partial Y_0^{'(i-1)}} & \cdots & -\frac{\partial f_0}{\partial Y_N^{'(i-1)}} \\ \vdots & & \vdots \\ -\frac{\partial f_N}{\partial Y_0^{'(i-1)}} & \cdots & \frac{1}{\Delta t^{(i)}} - \frac{\partial f_N}{\partial Y_N^{'(i-1)}} \end{pmatrix} \begin{pmatrix} \delta Y_0^{'(i-1)} \\ \vdots \\ \delta Y_N^{'(i-1)} \end{pmatrix} = \begin{pmatrix} f_0\left(\mathbf{Y}^{'(i-1)}\right) - \frac{\Delta Y_0^{(i-1)}}{\Delta t^{(i)}} \\ \vdots \\ f_N\left(\mathbf{Y}^{'(i-1)}\right) - \frac{\Delta Y_N^{(i-1)}}{\Delta t^{(i)}}. \end{pmatrix} \qquad (2.37)$$

In order to find the abundances Y_j for each of the $j = 1, ..., N$ nuclear species, we can invert this matrix and the iteration is done until the following criterion is satisfied:

$$\max \left| \frac{\delta Y_j^{'(i-1)}}{Y_j^{(i-1)}} \right| < \epsilon, \qquad (2.38)$$

and for ϵ we can take a value of 10^{-6}.

In theory, we can include in our reaction network as many nuclear species as we want, as far as we have the corresponding nuclear reaction rates. Furthermore, each nucleus can, at least theoretically speaking, interact with every other nucleus present in the plasma. This makes it computationally expensive to find the network solution. However, in most cases, the majority of reactions can be neglected, since usually the most important reactions for each nucleus are capture reactions involving nucleons, or photons and their inverse reactions. This means that the resulting matrix which has to be inverted is sparse and band diagonal.

3 Dynamical Study of the Electron Fraction in the Supernovae Neutrino-Driven Wind

Recent works (Martínez-Pinedo et al. 2012, Roberts 2012, and Roberts et al. 2012) have shown that the nucleon potential corrections on the electron neutrino and antineutrino spectra in core-collapse supernovae (CCSNe), especially in the deleptonization phase of the newly born proto-neutron-star (PNS), can have an important impact on the nucleosynthesis yields in the neutrino-driven wind (ν-driven wind). This was the motivation to perform this study, in which we use the trajectories of the ν-driven wind of an 8.8 $M_\odot$ progenitor electron-capture supernova (ECSN) simulated self-consistently using a sophisticated treatment of the neutrino transport (Hüdepohl et al. 2010). However, in our simulations, the aforementioned nucleon potential corrections on the neutrino opacities were not included. Therefore, in order to mimic their impact on the neutrino spectra from our simulations, we vary the electron neutrino and antineutrino properties (mean energy and luminosity) and investigate how they impact the electron fraction Y_e in the ν-driven wind.

We even consider different cross-sections for the β-processes (with or without the inclusion of recoil and weak magnetism corrections) and test their impact on Y_e. Furthermore, we calculate Y_e in different ways (with or without nuclear reaction network), in order to check the validity of equilibrium assumptions about its evolution.

We conclude that both weak magnetism corrections as well as a proper inclusion of the dynamical effects, and in particular the formation of the alpha particles, can significantly impact the electron fraction in the ν-driven wind. The formation of a very neutron-rich environment, which is required for the r-process to occur, is foreseen only for neutrino parameters which are far from the values given by the current most sophisticated supernovae simulations (Fischer et al. 2010; Hüdepohl et al. 2010).

3.1 Introduction

The question of the origin of the chemical elements heavier than Fe, in particular of the r-process elements, is still under debate (see chapter 1). Although it looks like the most promising sites for their production are systems involving neutron star mergers, core-collapse supernovae (CCSNe) are still thought to play an important role. In particular, the so-called electron-capture supernovae (ECSNe) are interesting for the production of the chemical elements, because they represent about 30% of all CCSNe, and therefore they could significantly contribute to the chemical enrichment of our Galaxy (Ishimaru & Wanajo 1999). ECSNe originate from a progenitor star having a mass between 8 and 10 $M_\odot$ and an O-Ne-Mg core. The collapse of an ECSN is triggered by the capture of electrons into the nuclei in the core of the star, so that the degeneracy pressure of the electrons is decreased. Shortly after the ECSN explosion, the ν-driven wind starts blowing away from the PNS surface. As the ν-driven wind blows away from the surface of the PNS, it cools down and the nucleons combine producing heavier and heavier nuclei. The neutrino-driven wind has historically been considered, and is still

considered, as a potential site for the production of heavy elements. However, the production of the very heavy elements seems to be excluded by the most recent sophisticated and long-term supernovae simulations, which produce proton-rich matter (Fischer et al. 2010; Hüdepohl et al. 2010), rather than neutron-rich, as it would be required for the r-process to occur (see chapter 1). In any case, there are some neutrino properties which have not yet been properly taken into account in the above mentioned long-term supernova simulations. For example, they assume neutrino opacities based on a non-interacting gas of nucleons and nuclei. This simplification is inconsistent with the equation of state (EOS) itself (Shen et al. 1998) which was used in the aforementioned simulations for the thermodynamic quantities. This assumption is valid only for the early evolution phases of CCSNe, such as the collapse of the core, the accretion phase and the onset of the SN explosion (Martínez-Pinedo et al. 2012), since the densities at which neutrinos decouple are relatively low ($\sim 10^{11}$g/cm^3). However, as the time after the explosion (the postbounce time) increases, neutrinos decouple from the matter at higher and higher densities and the non-interacting gas approximation is not valid anymore. Therefore, one has to take into account this effect, with the help of nucleon potential corrections (Reddy et al. 1998), which have been shown to significantly reduce Y_e in the ν-driven wind from initially proton-rich values down to ~ 0.42–0.45 (Roberts 2012; Roberts et al. 2012).

In this work, we aim to study the impact of nucleon potential corrections (with or without weak-magnetism corrections) on Y_e in the ν-driven wind of an 8.8 $M_\odot$ progenitor electron-capture supernova (Hüdepohl et al. 2010). To this aim, we analyze the ν-driven wind trajectories at three different representative postbounce times (t_0=0.5 s, 2.9 s and 6.5 s), corresponding to the early, intermediate, and late cooling phase of the PNS, respectively. In particular, we artificially vary the luminosities and mean energies of electron neutrinos and antineutrinos, while using the ν-driven wind hydrodynamic trajectories of the above mentioned ECSN, which was simulated using a full neutrino transport in 1D. The goal is to explore the range of the neutrino parameters which determine the boundary between the neutron-rich ($Y_e < 0.5$) and the proton-rich matter ($Y_e > 0.5$).

Furthermore, we also study the difference between Y_e given by full network calculations where the dynamical effects are properly taken into account, and Y_e calculated making some assumptions about the nuclear composition and the β-reactions in the ν-driven wind, as it will be better specified in what follows.

This chapter is structured in the following way: In Sect. 3.2, we describe our ν-driven wind model as well as our reaction network; In Sect. 3.3 we discuss in detail the evolution of the electron fraction in the ν-driven wind; In Sect. 3.4, we present the methodology which we use in order to investigate the impact of nucleon potential corrections on Y_e; In Sect. 3.5, we show the first part of our results on Y_e using different physical approaches. Namely, we explore the difference between dynamical and equilibrium effects, impact of weak magnetism and recoil correction and the influence of different neutrino parameters assumptions on Y_e; In Sect. 3.6, we discuss the time dependence of the evolution of Y_e. Finally, in Sect. 3.7, we present our conclusions and perspectives.

3.2 Neutrino-driven wind and nuclear reaction network

In order to explore the impact of the mean field nucleon potential corrections on the electron fraction in the ν-driven wind of supernovae, we use one-dimensional (1D) long-term simulations of an 8.8 $M_\odot$ progenitor (Hüdepohl et al. 2010), computed using the Shen et al. (1998) equation of state. For
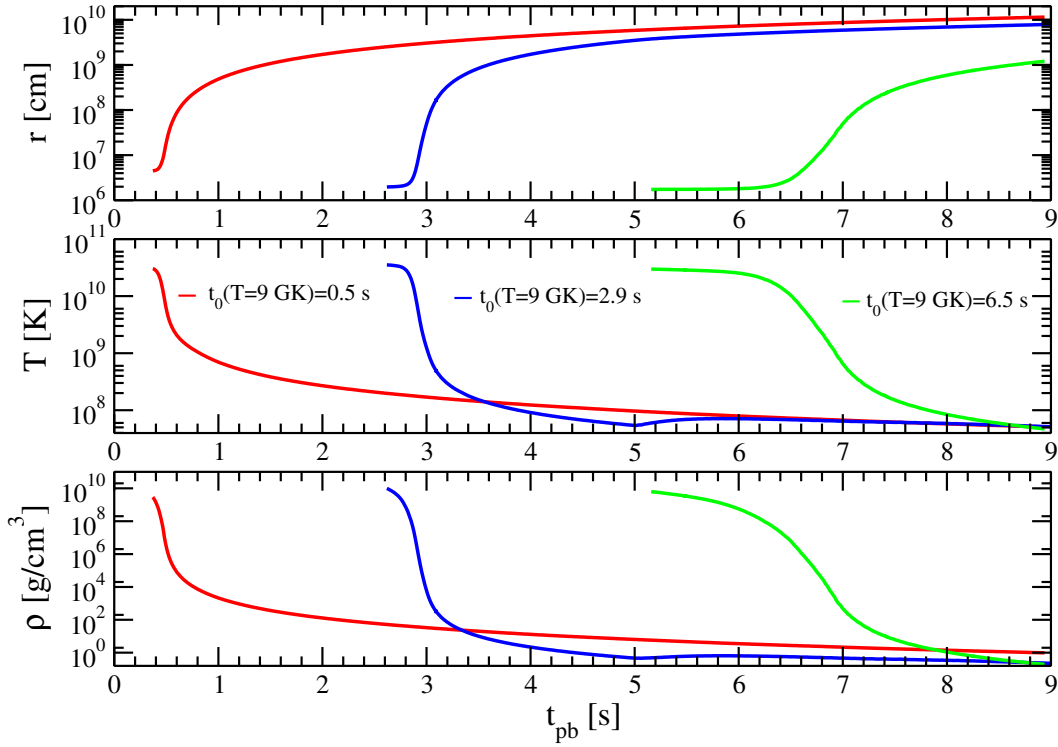
Figure 3.1 Mass-shell trajectories of the neutrino-driven wind as functions of the postbounce time (t_{pb}) at three representative initial ejection times (t_0 = 0.5 s, 2.9 s and 6.5 s): Radial distance from the PNS center (top), temperature (middle), and density (bottom) along the ejecta trajectories. The kinks visible in the temperature and density evolution of the trajectories at t_0 = 2.9 s indicate the existence of a weak reverse shock.

this study we adopt the Model Sf 21 (see Hüdepohl et al. 2010 for more details). In this model, the accretion phase ends at a postbounce time $t_{pb} \sim 0.2$ s, and the subsequent deleptonization and cooling phase of the PNS due to the escape of neutrinos last ~ 10 s.

In order to perform our calculations, we use three trajectories (at t_0 = 0.5 s, 2.9 s, and 6.5 s) taken from Hüdepohl et al. (2010), which are representative of the early, intermediate, and late phase evolution of the ν-driven wind, respectively. In Fig. 3.1, we show the distance r from the center of the PNS (top panel), the temperature T (middle panel), and the matter density ρ (bottom panel) profiles of the three representative mass-shell ν−driven wind trajectories as functions of t_{pb}.

We use a nuclear reaction network in which 6300 species are included between the proton and the neutron-drip lines, up to the $Z = 110$ isotopes (for more details, see Wanajo 2006). In our calculations, we include all relevant reactions such as (n, γ), (p, γ), (α, γ), (p, n), (α, n), (α, p), and their inverse reactions. The reactions involving the capture of ν_e and $\bar{\nu}_e$ on free neutrons and protons play a crucial role, since they determine Y_e in the ν-driven wind (see next section). Therefore, we use two different sets for the neutrino opacities, namely without or with the inclusion of weak magnetism and recoil corrections (Horowitz & Li 1999). Furthermore, we do not include neutrino-induced reactions on heavy nuclei, because they have negligible effects (Meyer et al. 1998). Since the matter blowing away from the PNS is (at the beginning) in NSE, we assume an initial composition of $1 - Y_e$ and Y_e for free neutrons and protons, respectively. Finally, the nucleosynthesis calculations are started when the

mass-shell temperature decreases to 9 GK.

3.3 Electron fraction evolution

Together with the entropy and the expansion timescale, a basic quantity defining the conditions for element formation (and eventually an r-process) in the ν-driven wind is the excess of initially free n or p expressed by the electron fraction Y_e. It is locally defined as the ratio of the net electron (electrons minus positrons) number density (N_e) to the sum of the proton number density (N_p) and of the neutron number density (N_n):

$$Y_e(r) = \frac{N_e(r)}{N_p(r) + N_n(r)} = X_p(r) + \frac{X_\alpha(r)}{2} + \sum_{Z_A > 2} \frac{Z_A(r)}{A(r)} X_A(r) \,, \tag{3.1}$$

where X_p, X_α, and X_A are the mass fractions of free protons (p), α particles, and heavy elements ($Z_A > 2$) as functions of the radius. The charge and the mass numbers of the heavy nuclear species are Z_A and A, respectively. In all neutral media, $Y_e = Y_p$ and $Y_n = 1 - Y_e$, with Y_j being the number density of free or bound particle species j relative to baryons. The lower Y_e, the more the environment is neutron rich, and thus the more favorable it is for the r-process to occur (e.g. Hoffman et al. 1997). On the other hand, $Y_e > 0.5$ implies that the matter is proton-rich and p-rich nuclei could be formed through the νp−process (Fröhlich et al. 2006b; Pruet et al. 2006; Wanajo 2006).

Having in mind the overall evolution of abundances with radius and time and assuming that the reactions of neutrinos on nuclei are negligible, the n/p ratio in the wind ejecta is set by β-interactions of electron neutrinos (ν_e) and electron antineutrinos ($\bar{\nu}_e$) with free n and p and their inverse reactions:

$$\nu_e + n \;\; \rightleftharpoons \;\; p + e^- \,, \tag{3.2}$$

$$\bar{\nu}_e + p \;\; \rightleftharpoons \;\; n + e^+. \tag{3.3}$$

The Y_e evolution therefore depends on the spectra and luminosities of ν_e and $\bar{\nu}_e$. Modifications of the neutrino emission properties, for example due to nucleon potential corrections or to neutrino flavor oscillations, could significantly change the n/p ratio and thus Y_e in the ν-driven wind.

Because of slow time variations of the outflow conditions during the PNS cooling phase, a near steady-state situation applies (Qian & Woosley 1996) and the rate-of-change of Y_e within an out-flowing mass element can be written as in McLaughlin et al. (1996):

$$\frac{dY_e}{dt} = v(r)\frac{dY_e}{dr} \simeq (\lambda_{\nu_e} + \lambda_{e^+})Y_n^{\mathrm{f}} - (\lambda_{\bar{\nu}_e} + \lambda_{e^-})Y_p^{\mathrm{f}} \,, \tag{3.4}$$

where $v(r)$ is the velocity of the out-flowing mass element, the λ_i are the reaction rates, and Y_n^{f} and Y_p^{f} are the abundances of free nucleons.

In the free streaming limit with neutrinos propagating radially, the forward reaction rates of Eqs. (3.2,3.3) can be written in terms of the electron (anti)neutrino emission properties as:

$$\lambda_{\nu_e} \;\; \simeq \;\; \frac{L_{\nu_e}}{4\pi r^2 \langle E_{\nu_e} \rangle} \langle \sigma_{\nu_e} \rangle \,, \tag{3.5}$$

$$\lambda_{\bar{\nu}_e} \;\; \simeq \;\; \frac{L_{\bar{\nu}_e}}{4\pi r^2 \langle E_{\bar{\nu}_e} \rangle} \langle \sigma_{\bar{\nu}_e} \rangle \,, \tag{3.6}$$

where L_{ν_e} and $L_{\bar{\nu}_e}$ are the luminosities of ν_e and $\bar{\nu}_e$ respectively, $\langle E_{\nu_e} \rangle$ and $\langle E_{\bar{\nu}_e} \rangle$ the mean spectral energies. The ν_e and $\bar{\nu}_e$ capture cross-sections of the forward reactions (3.2,3.3), averaged over the corresponding ν_e and $\bar{\nu}_e$ energy spectra, are $\langle \sigma_{\nu_e} \rangle$ and $\langle \sigma_{\bar{\nu}_e} \rangle$, respectively. Including the weak magnetism and recoil corrections, the average neutrino capture cross-sections are (Horowitz & Li 1999):

$$\langle \sigma_{\nu_e} \rangle \simeq k \langle E_{\nu_e} \rangle \varepsilon_{\nu_e} \left[1 + 2\frac{\Delta}{\varepsilon_{\nu_e}} + a_{\nu_e} \left(\frac{\Delta}{\varepsilon_{\nu_e}} \right)^2 \right] W_{\nu_e}, \tag{3.7}$$

$$\langle \sigma_{\bar{\nu}_e} \rangle \simeq k \langle E_{\bar{\nu}_e} \rangle \varepsilon_{\bar{\nu}_e} \left[1 - 2\frac{\Delta}{\varepsilon_{\bar{\nu}_e}} + a_{\bar{\nu}_e} \left(\frac{\Delta}{\varepsilon_{\bar{\nu}_e}} \right)^2 \right] W_{\bar{\nu}_e}, \tag{3.8}$$

where $k \simeq 9.3 \cdot 10^{-44}$ cm^2/MeV^2, $\varepsilon_\nu = \langle E_\nu^2 \rangle / \langle E_\nu \rangle$ ($\nu = \nu_e, \bar{\nu}_e$), $a_\nu = \langle E_\nu^2 \rangle / \langle E_\nu \rangle^2$, M is the nucleon mass in MeV and $\Delta = 1.293$ MeV is the neutron-proton mass difference. The weak magnetism and recoil correction factors are given by $W_{\nu_e} = [1 + 1.02 b_{\nu_e} \varepsilon_{\nu_e} / M]$ and $W_{\bar{\nu}_e} = [1 - 7.22 b_{\bar{\nu}_e} \varepsilon_{\bar{\nu}_e} / M]$, where $b_\nu = \langle E_\nu^3 \rangle \langle E_\nu \rangle / \langle E_\nu^2 \rangle^2$ represents the spectral shape factor for ν_e or $\bar{\nu}_e$. For simplicity, in this study, we adopt the following approximations, which are valid for a moderately degenerate Fermi-Dirac distribution (Horowitz & Li 1999): $\varepsilon_\nu = 1.2 \langle E_\nu \rangle$ and $a_\nu = b_\nu = 1.2$[1] (Horowitz & Li 1999). In this approximation the above corrections become:

$$W_{\nu_e} = \left[1 + 1.47 \frac{\langle E_{\nu_e} \rangle}{M} \right], \tag{3.9}$$

$$W_{\bar{\nu}_e} = \left[1 - 10.39 \frac{\langle E_{\bar{\nu}_e} \rangle}{M} \right]. \tag{3.10}$$

We also point out that in Eq. (3.8) the spectral integration was approximated by integrating over the interval $[0, \infty)$ instead of $[\Delta, \infty)$. Since the rates λ_{ν_e} and $\lambda_{\bar{\nu}_e}$ are functions of the neutrino fluxes, they can be affected by nucleon potential corrections which influence $\langle E_{\nu_e} \rangle$ and $\langle E_{\bar{\nu}_e} \rangle$ (see Sect. 3.4).

The inverse reaction rates λ_{e^-} and λ_{e^+} of the reactions (3.2,3.3), are given, in analogy to the forward reaction rates, by:

$$\lambda_{e^-} = c \cdot \widetilde{n}_{e^-} \cdot \langle \sigma_{e^-} \rangle, \tag{3.11}$$

$$\lambda_{e^+} = c \cdot n_{e^+} \cdot \langle \sigma_{e^+} \rangle, \tag{3.12}$$

where c is the speed of light. In Eq. (3.11), $\widetilde{n}_{e^-}$ is slightly modified compared to the electron number density and is given by:

$$\widetilde{n}_{e^-} = \frac{8\pi}{(2\pi\hbar c)^3} \cdot \int_0^\infty \frac{\epsilon^2}{1 + \exp[\frac{\epsilon - \widetilde{\mu}_e}{k_B T}]} \, d\epsilon, \tag{3.13}$$

where $\widetilde{\mu}_e = \mu_e - \Delta$ and μ_e is the electron chemical potential. The average cross section $\langle \sigma_{e^-} \rangle$ of the inverse reaction (3.2) is:

$$\langle \sigma_{e^-} \rangle \simeq \frac{1}{2} k \langle \widetilde{E}_{e^-} \rangle \varepsilon_{e^-} \left[1 + 2\frac{\Delta}{\varepsilon_{e^-}} + a_{e^-} \left(\frac{\Delta}{\varepsilon_{e^-}} \right)^2 \right] W_{\nu_e}, \tag{3.14}$$

---

[1] These values are similar to the ones of our adopted model and our results are insensitive to their small variations.

where $\varepsilon_{e^-} = \langle \widetilde{E}_{e^-}^2 \rangle / \langle \widetilde{E}_{e^-} \rangle$ and $a_{e^-} = \langle \widetilde{E}_{e^-}^2 \rangle / \langle \widetilde{E}_{e^-} \rangle^2$. In analogy to $\langle E_\nu^n \rangle$, $\langle \widetilde{E}_{e^-}^n \rangle$ is defined by using $\widetilde{f}_{e^-}(E) = \frac{\widetilde{\xi} \cdot E^2}{1 + \exp{[(E - \widetilde{\mu}_e)/k_B T]}}$ for the electron distribution function with $\widetilde{\xi}$ being the normalization factor such that $\int \widetilde{f}_e(E)\,\mathrm{d}E = 1$. In Eq. (3.12), the positron number density is given by:

$$n_{e^+} = \frac{8\pi}{(2\pi\hbar c)^3} \cdot \int_0^\infty \frac{\epsilon^2}{1 + \exp[\frac{\epsilon + \mu_e}{k_B T}]}\, \mathrm{d}\epsilon, \qquad (3.15)$$

and the positron average capture cross section is given by:

$$\langle \sigma_{e^+} \rangle \simeq \frac{1}{2} k \langle E_{e^+} \rangle \varepsilon_{e^+} \left[1 + 2\frac{\Delta}{\varepsilon_{e^+}} + a_{e^+} \left(\frac{\Delta}{\varepsilon_{e^+}} \right)^2 \right] W_{\bar{\nu}_e}, \qquad (3.16)$$

where $\varepsilon_{e^+} = \langle E_{e^+}^2 \rangle / \langle E_{e^+} \rangle$ and $a_{e^+} = \langle E_{e^+}^2 \rangle / \langle E_{e^+} \rangle^2$. The energy moments are calculated using the positron distribution function $f_{e^+}(E) = \frac{\xi_{e^+} \cdot E^2}{1 + \exp{[(E - \mu_{e^+})/k_B T]}}$, where ξ_{e^+} is the normalization factor such that $\int f_{e^+}(E)\,\mathrm{d}E = 1$.

We approximate the weak magnetism and recoil corrections in Eqs. (3.14,3.16) by using W_{ν_e} and $W_{\bar{\nu}_e}$ of Eqs. (3.7,3.8) with the energy moments of the emitted neutrinos in the β-reactions, fulfilling the detailed balance theorem. We notice that in Eqs. (3.14,3.16) and Eqs. (3.7,3.8) we have neglected the mass of the electron, m_e, since it does not make any difference in our calculations ($m_e \ll E \pm \Delta$). We also point out that λ_{e^-} and λ_{e^+}, neglecting weak magnetism and recoil corrections (i.e. for $W_{\nu_e} = W_{\bar{\nu}_e} = 1$), but including m_e-dependent terms, are given in Bruenn (1985).

The nucleons involved in the β-reactions of Eq. (3.4) are free. Accounting for the nucleons bound in α particles, the number fractions of free protons and neutrons can be written as functions of Y_e as:

$$Y_p^f = Y_e - \frac{X_\alpha}{2} - \sum_{Z_A > 2} \frac{Z_A}{A} X_A, \qquad (3.17)$$

$$Y_n^f = 1 - Y_e - \frac{X_\alpha}{2} - \sum_{Z_A > 2} \frac{N_A}{A} X_A, \qquad (3.18)$$

where X_α (X_A) is the mass fraction of α particles (heavy nuclei). The recombination of free nucleons to α-particles affects Y_p^f and Y_n^f according to Eqs. (3.17) and (3.18) and via Eq. (3.4) influences the evolution of Y_e. Since the formation of α-particles binds equal numbers of neutrons and protons, the remaining free nucleons will be dominated by the more abundant nucleonic species, either n or p. The corresponding capture reactions of ν_e (and e^+) on neutrons in the case of neutron excess or of $\bar{\nu}_e$ (and e^-) on protons for proton-rich conditions will drive Y_e closer to 0.5, which is the so-called "α-effect" first pointed out by McLaughlin et al. (1996) and Meyer et al. (1998).

If Y_e is always in an instantaneous equilibrium (i.e., $dY_e/dt = 0$) and the capture rates of the reactions (3.2,3.3) are known, then we can calculate Y_e without performing full network calculations. In fact, in this case, assuming that the matter is only made of free neutrons ($Y_n^f = 1 - Y_e$) and protons ($Y_p^f = Y_e$), as it happens in NSE conditions, Eq. (3.4) becomes:

$$Y_e = \frac{1}{1 + \frac{\lambda_2}{\lambda_1}}, \qquad (3.19)$$

where $\lambda_1 = \lambda_{\nu_e} + \lambda_{e^+}$ and $\lambda_2 = \lambda_{\bar{\nu}_e} + \lambda_{e^-}$. Therefore, this approximation for Y_e is only valid if the β-reactions are in equilibrium, which means that their reaction time τ_β has to be smaller than the

dynamical expansion timescale τ_{dyn} of the ν-driven wind[2]. In general, the condition $\tau_\beta < \tau_{\mathrm{dyn}}$ is more likely to be verified as the postbounce time increases (e.g., late phases of the cooling evolution of the PNS), because τ_{dyn} of the matter increases as well. However, especially at early phases of the ν-driven wind, it can happen that $\tau_\beta > \tau_{\mathrm{dyn}}$, so that Eq. (3.19) is not valid anymore.

From Eq. (3.19), it also follows that, if $\lambda_{e^-} \ll \lambda_{\bar{\nu}_e}$ (or $\lambda_{e^-} = 0$) and $\lambda_{e^+} \ll \lambda_{\nu_e}$ (or $\lambda_{e^+} = 0$), then Y_e can also be written as:

$$Y_e = \frac{1}{1 + \frac{\lambda_{\bar{\nu}_e}}{\lambda_{\nu_e}}}, \tag{3.20}$$

and it depends only on neutrino parameters according to Eqs. (3.5) and (3.6). In this case, Y_e including weak magnetism and recoil corrections is *higher* than without their inclusion, because the value of λ_{ν_e} increases (Eq. 3.7) while $\lambda_{\bar{\nu}_e}$ decreases (Eq. 3.8). This condition is especially verified for late phases of the ν-driven wind evolution. We notice that, this particular approximation of Y_e is broadly used in the literature to make predictions about Y_e in the ν-driven wind, once the properties of ν_e and $\bar{\nu}_e$ are known (e.g, Roberts et al. 2012).

On the other hand, in the early phases of the ν-driven wind evolution, due to the higher densities and temperatures of the matter than in the late phases, the electron and positron captures on free nucleons play an important role in determining Y_e, especially at small radii, where we may have $\lambda_{\bar{\nu}_e} \ll \lambda_{e^-}$ and $\lambda_{\nu_e} \ll \lambda_{e^+}$, since $\lambda_{e^-/e^+} \propto T^6 \propto r^{-6}$ while $\lambda_{\nu_e/\bar{\nu}_e} \propto r^{-2}$ (Janka 2012). In these conditions, Y_e in Eq. (3.19) is approximately given by:

$$Y_e = \frac{1}{1 + \frac{\lambda_{e^-}}{\lambda_{e^+}}}. \tag{3.21}$$

From Eq. (3.21), it follows that, if λ_{e^-} and λ_{e^+} play the dominant role in the β-reactions, then in the presence of weak magnetism and recoil corrections Y_e is *lower* than Y_e without their inclusion, because the value of λ_{e^-} increases (Eq. 3.11, 3.14) while λ_{e^+} decreases (Eq. 3.12, 3.16).

Summarizing, depending on the ν-driven wind conditions, Y_e has to be computed accurately solving the Eq. (3.4) or can be estimated with one of the above simplified formulae.

One of the goals of this work is also to test the validity of the different assumptions about Y_e in the different evolution phases of our ν-driven wind model. To this aim we calculate the electron fraction in three different ways:

1. It is computed using *full network* calculations (where X_α is accurately calculated) and the dynamical effects are properly taken into account as in Eq. (3.4), "Y_e case";

2. It is calculated solving Eq. (3.4), assuming $X_\alpha = 0$ and setting $\lambda_{e^-} = 0$ and $\lambda_{e^+} = 0$, "$\overline{Y}_e$ case";

3. It is calculated assuming instantaneous *equilibrium* ($dY_e/dt = 0$), $X_\alpha = 0$, $\lambda_{e^-} = 0$ and $\lambda_{e^+} = 0$, as in Eq. (3.20), "$\overline{Y}_{e,\nu}$ case".

The first case allows us to make accurate predictions about Y_e in the ν-driven wind, including the α-effect and all the dynamical properties of the matter. The second case allows us to investigate the competition between the α particle formation and the neutrinos properties in setting the value of Y_e by comparing $\overline{Y}_e$ with Y_e, while taking into account the dynamical properties of the ν-driven wind. The third case is a probe of the equilibrium assumption about Y_e. If $\overline{Y}_{e,\nu}$ is significantly different from $\overline{Y}_e$,

---

[2]The expansion timescale can be defined as $\tau_{\mathrm{dyn}} = r/v$ at $T = 0.5$ MeV (Qian & Woosley 1996), where v is the velocity of the matter.

then the dynamical effects play a crucial role in setting the value of Y_e. If $\overline{Y}_{e,\nu}$ is very different also from Y_e, then it means that not only the equilibrium assumption is not valid, but also that the α-effect plays an important role in setting the value of Y_e. On the contrary, if $\overline{Y}_{e,\nu} \simeq Y_e$ then the equilibrium assumption is valid and one can estimate Y_e by simply using Eq. (3.20).

After giving this overview about the electron fraction in the ν-driven wind, in the next section, we present our method to investigate the impact of the nucleon potential corrections on Y_e.

3.4 Methodology

The equation of state (EoS) used in our simulations (Shen et al. 1998) assumes that neutrons and protons form a gas of quasi-particles which move in a mean field single particle potential U. In very neutron-rich conditions the mean-field potentials of neutrons U_n and protons U_p can be very different and the difference $U_n - U_p$ is directly related to the symmetry energy [3] (Martínez-Pinedo et al. 2012; Roberts et al. 2012).

The impact of non-relativistic mean-field nucleon potential corrections in the β-reactions (3.2) and (3.3) can be expressed through the following relations[4](Martínez-Pinedo et al. 2012):

$$E_{\nu_e} = E_{e^-} - (m_n - m_p) - (U_n - U_p),   \tag{3.22}$$

$$E_{\bar{\nu}_e} = E_{e^+} + (m_n - m_p) + (U_n - U_p),   \tag{3.23}$$

where E_i is the energy of the particle i, m_n and m_p are the masses of neutron and proton, respectively. From Eqs. (3.22) and (3.23) we can see that the mean field nucleon potential corrections *reduce* the energy of emitted ν_e and *increase* the one of $\bar{\nu}_e$, so that the net energy difference between ν_e and $\bar{\nu}_e$ is $2(U_n - U_p)$. This means that, the opacities of ν_e (Eq. 3.7) and $\bar{\nu}_e$ (Eq. 3.8) change as well, and therefore Y_e changes consequently.

As we previously mentioned, these nucleon potential corrections are not included in our ECSN simulation and, in order to estimate their impact on Y_e, we parametrize the ν_e and $\bar{\nu}_e$ energy spectra by using three different methods:

(i) We discretize the mean energies of ν_e and $\bar{\nu}_e$ in the range [5-23] MeV, while keeping the same luminosities L_{ν_e} and $L_{\bar{\nu}_e}$ as given by the hydrodynamic simulations (see Fig. 3.2). The discretization is done by steps of 0.5 MeV in the energy range [5-10] MeV and by steps of 1 MeV in the range [11-23] MeV;

(ii) We keep the same number fluxes (i.e, $L/\langle E \rangle$) for ν_e and $\bar{\nu}_e$ as given by the hydrodynamic simulations (see Table 3.1). Namely, we vary the mean energies (as in (i)) and luminosities of ν_e and $\bar{\nu}_e$, so that their number fluxes remain constant.

(iii) We fix the luminosities L_{ν_e} and $L_{\bar{\nu}_e}$ as given in Table 3.1, and vary $\langle E_{\nu_e} \rangle$ and $\langle E_{\bar{\nu}_e} \rangle$ as in (i). This case is very similar to case (i), but it allows us to test the consequences of the variations (although small) in the evolution of L_{ν_e} and $L_{\bar{\nu}_e}$ on Y_e, by comparing Y_e in case (iii) and in case (i).

In Fig. 3.2, we show the luminosities of ν_e and $\bar{\nu}_e$ as given by the hydrodynamic simulation for each of the representative phases of the ν-driven wind as functions of $t_{\rm pb}$. The time t_0 corresponds to the time at which the temperature decreases to 9 GK, namely at the time where nucleosynthesis starts. We use these luminosities in order to perform our study using method (i). In Table 3.1, we

---

[3]There are different definitions of the symmetry energy of nuclear matter, which according to Lattimer (2014) can also be defined as the difference between the energies of pure neutron and symmetric nuclear matter as a function of density.

[4]In the elastic approximation, namely if the neutron and the proton have the same moment ($\mathbf{p}_n \simeq \mathbf{p}_p$).
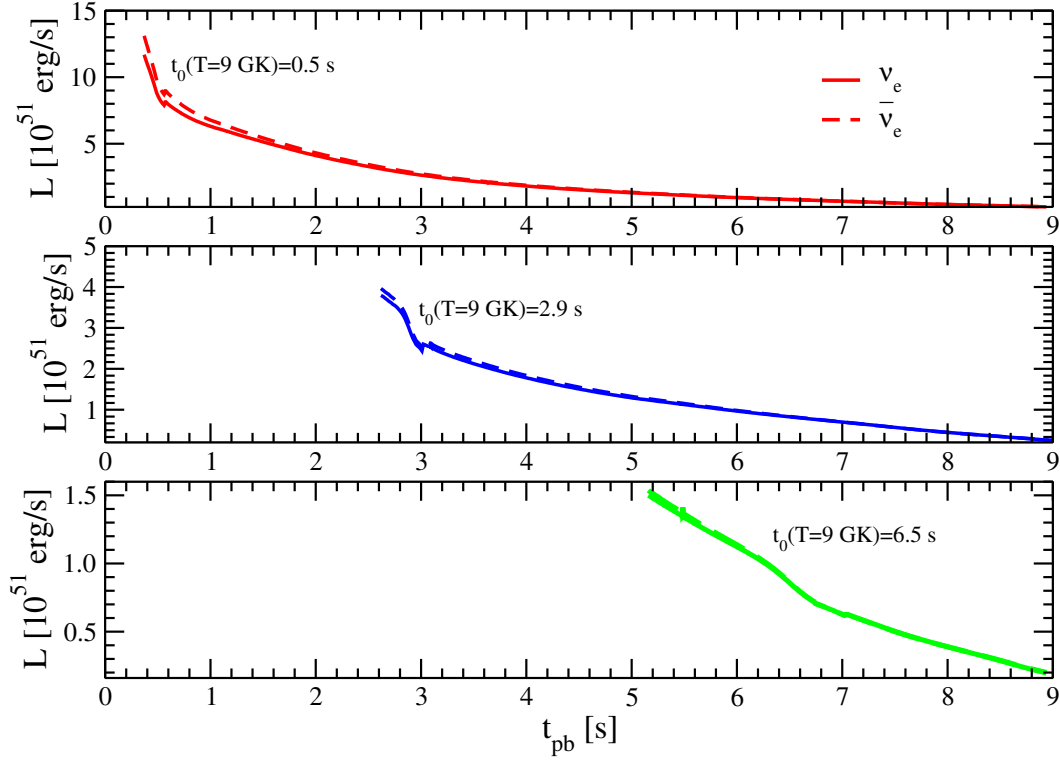
Figure 3.2 Luminosities of ν_e and $\bar{\nu}_e$ as functions of the postbounce time (t_{pb}). The time t_0 corresponds to the postbounce time at which the temperature of the ν-driven wind decreases to 9 GK: Upper panel, $t_0 = 0.5$ s (early phase of the ν-driven wind evolution), middle panel $t_0 = 2.9$ s (intermediate phase), lower panel $t_0 = 6.5$ s (late phase). As the time increases, L_{ν_e} and $L_{\bar{\nu}_e}$ become always more similar to each other.

report the initial conditions given by the hydrodynamic simulation at the neutrinosphere[5]. We even report the values of the ν_e and $\bar{\nu}_e$ number fluxes which we use to perform our study using the method described in (ii) and L_{ν_e} and $L_{\bar{\nu}_e}$ used in case (iii). Notice that, in case (ii) and (iii), we assume that the representative number fluxes and luminosities which we choose do not change as a function of t_{pb}. Therefore, in cases (ii) and (iii), we ignore the evolutionary changes due to remaining neutrino interactions in the external medium and general relativistic red-shift corrections, which are included in the hydrodynamic simulations. However, by comparing case (i) and (iii), we will see that these changes have only a small impact on Y_e.

3.5 Results I: Variation of the physical treatment

In this section, we discuss our results concerning the evolution of Y_e in the ν-driven wind with respect to the different physical assumptions. First, we will focus on the comparison between the evolution of Y_e while performing full network calculations (case 1, Y_e in Sect. 3.3), Y_e in the case where $X_\alpha = 0$,

---

[5]The neutrinosphere is defined as the region at which the neutrinos or antineutrinos escape from the PNS. We assume that the neutrinosphere is equal for all neutrino flavors, and that their properties (luminosities and mean energies) do not change anymore as ν_e and $\bar{\nu}_e$ propagate outwards the surface of the PNS.

Table 3.1 At each representative postbounce time t_0 (corresponding to the time at which the temperature decreases to 9 GK) we show the values of the initial radius R_i and the initial electron fraction $Y_{e,i}$. We even show the representative luminosities L, the mean energies $\langle E \rangle$ in MeV, and the corresponding neutrino number fluxes $L/\langle E \rangle$ of ν_e and $\bar{\nu}_e$ as given by hydrodynamic simulations which we use for our study, according to the procedure (ii) and (iii).

t_0 [s]	R_i[a] [km]	$Y_{e,i}$	L_{ν_e} [10^{51}erg/s]	$L_{\bar{\nu}_e}$ [10^{51}erg/s]	$\langle E_{\nu_e} \rangle$ [MeV]	$\langle E_{\bar{\nu}_e} \rangle$ [MeV]	$L_{\nu_e}/\langle E_{\nu_e} \rangle$ [10^{56}s^{-1}]	$L_{\bar{\nu}_e}/\langle E_{\bar{\nu}_e} \rangle$ [10^{56}s^{-1}]
0.5	45.1	0.360	9.5	10.1	16.8	18.1	3.526	3.482
2.9	19.7	0.270	3.3	3.4	15.8	16.3	1.303	1.302
6.5	17.4	0.280	1.0	0.99	12.4	11.9	0.499	0.518

---

[a]We start our calculations slightly outside the surface of the PNS (or the neutrinosphere), but close enough so that all important effects due to β-reactions and α particle formation are taken into account.

$\lambda_{e^-} = 0$ and $\lambda_{e^+} = 0$ (case 2, $\overline{Y}_e$ in Sect. 3.3) and in the case were equilibrium is assumed (case 3, $\overline{Y}_{e,\nu}$ in Sect 3.3). Secondly, we will discuss the impact of weak magnetism and recoil correction on Y_e, $\overline{Y}_e$ and $\overline{Y}_{e,\nu}$. Thirdly, we will consider the impact of different assumptions about the neutrino parameters on Y_e, namely the difference between Y_e in the case where we assume the luminosities as given by the hydrodynamic simulations (case (i) in Sect. 3.4) and the case where we fix the neutrino number fluxes (case (ii) in Sect. 3.4) or the luminosity (case (iii) in Sect. 3.4).

3.5.1 Dynamical and equilibrium assumptions on the Y_e evolution

The accurate treatment of the evolution of the electron fraction in the ν-driven wind requires detailed network calculations. However, in certain cases (see Sect. 3.3), even an approximate treatment of the physics determining the evolution of Y_e could be enough in order to have an idea about its value.
In Fig. 3.3, we show the contour plots of Y_e (left), $\overline{Y}_e$ (right, solid lines) and $\overline{Y}_{e,\nu}$ (right, dashed lines) as functions of $\langle E_{\nu_e} \rangle$ and $\langle E_{\bar{\nu}_e} \rangle$ for the early phase evolution of the ν-driven wind ($t_0 = 0.5$ s), assuming that the luminosities of ν_e and $\bar{\nu}_e$ are the same as in the hydrodynamic simulations (see case (i) for Y_e and $\overline{Y}_e$, and case (iii) for $\overline{Y}_{e,\nu}$ in Sect. 3.4). The panels at the top refer to the cases without including weak magnetism and recoil corrections on the β-reactions which determine the electron fraction (see Eqs. 3.2 and 3.3). The green star symbol corresponds to the electron fraction using the hydrodynamic values of $\langle E_{\nu_e} \rangle$ and $\langle E_{\bar{\nu}_e} \rangle$ (see Tab. 3.1). The values of $\overline{Y}_e$ and $\overline{Y}_{e,\nu}$ are determined by the forward reactions (3.2) and (3.3) and, therefore, they only depend on the neutrino properties (see Eq. 3.20). By comparing the left and the right panels, we see that the values of Y_e are smaller than the corresponding ones of $\overline{Y}_e$ (and $\overline{Y}_{e,\nu}$) for $Y_e > 0.5$ and larger for $Y_e < 0.5$. This is mainly due to the α-effect (McLaughlin et al. 1996 and Sect. 3.3), namely to the interplay between the formation of α particles and the β-reactions which drive $Y_e \longrightarrow 0.5$, compared to the case where $X_\alpha = 0$, as in the $\overline{Y}_e$ and $\overline{Y}_{e,\nu}$ cases. The impact of the α-effect can also easily be seen by comparing the number of lines of Y_e and $\overline{Y}_e$ (or $\overline{Y}_{e,\nu}$) in the same range of $\langle E_{\nu_e} \rangle$ and $\langle E_{\bar{\nu}_e} \rangle$ values. In fact, we notice that their
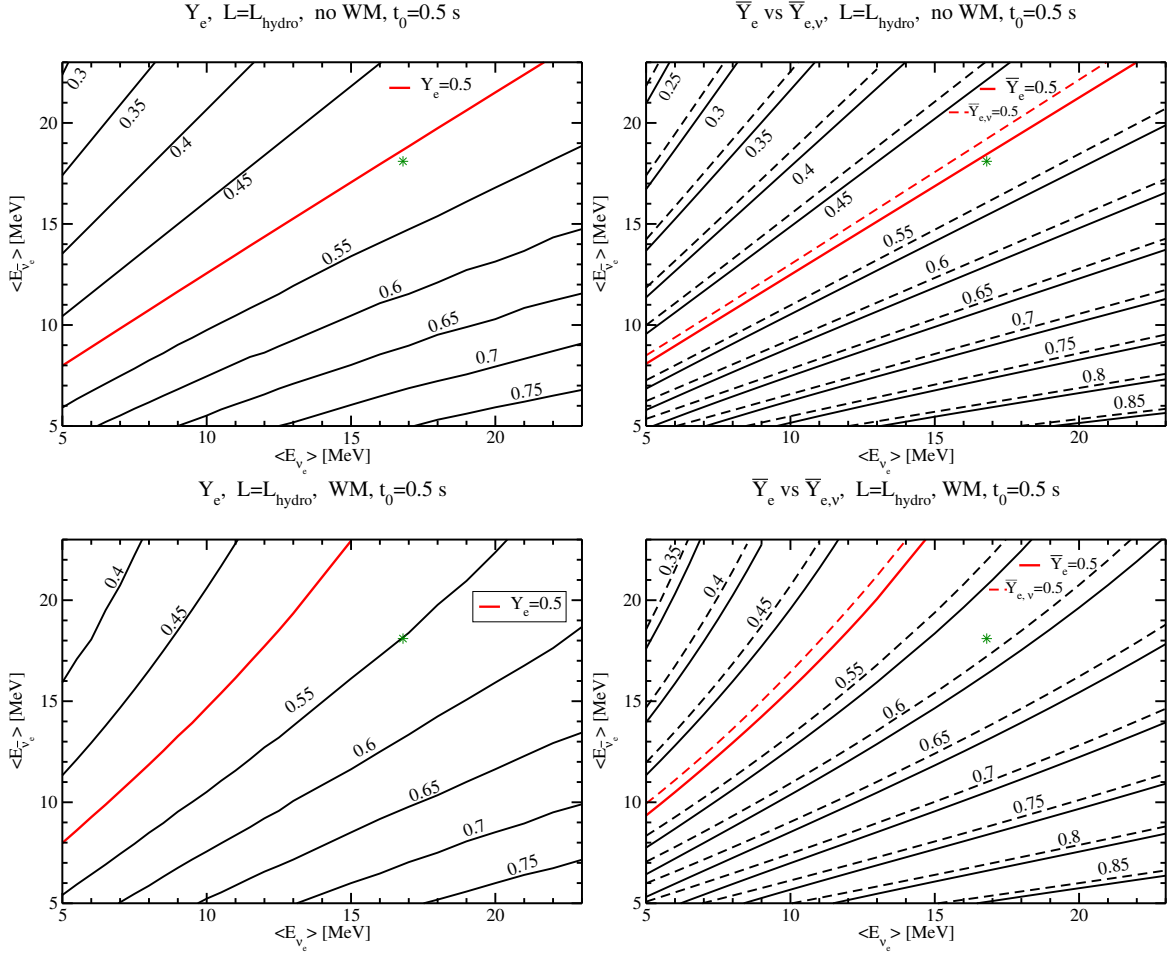
Figure 3.3 The upper panel on the left shows contour plots of the electron fraction Y_e as functions of the mean energy of ν_e ($\langle E_{\nu_e} \rangle$) and $\bar{\nu}_e$ ($\langle E_{\bar{\nu}_e} \rangle$) at postbounce time $t_0 = 0.5$ s, while keeping the luminosities of ν_e (L_{ν_e}) and $\bar{\nu}_e$ ($L_{\bar{\nu}_e}$) as given by the hydrodynamic simulations (case (i) for Y_e and $\overline{Y}_e$ and case (iii) for $\overline{Y}_{e,\nu}$, see Sect. 3.4). The weak magnetism corrections are not taken into account ("no WM" case). The upper panel on the right shows the electron fraction at $t_0 = 0.5$ s, as on the left, but with $X_\alpha = 0$ and switching off the electron and positron capture rates: $\overline{Y}_e$ takes into account dynamical effects, while $\overline{Y}_{e,\nu}$ is the equilibrium value (i.e., assuming $dY_e/dt = 0$). The lower panels are the same as the corresponding upper ones, but in the case where weak magnetism corrections ("WM" case) are applied to the neutrino opacities. The green stars in each plot correspond to the values from the hydrodynamic simulations.

number in the Y_e case (the range of values which Y_e can span) is lower than the one in the $\overline{Y}_e$ (and $\overline{Y}_{e,\nu}$) case, although the difference between two adjacent Y_e and $\overline{Y}_e$ contour lines is always the same, namely $\Delta Y_e = \Delta \overline{Y}_e = \Delta \overline{Y}_{e,\nu} = 0.05$.

By comparing $\overline{Y}_e$ and $\overline{Y}_{e,\nu}$, we can see the difference between the pure dynamical effects ($dY_e/dt \neq 0$) and the equilibrium assumption ($dY_e/dt = 0$), in the case the luminosities are fixed as described in Sect. 3.4. We notice that this difference is not as big as the one between Y_e and $\overline{Y}_e$ (or $\overline{Y}_{e,\nu}$).

Therefore, at $t_0 = 0.5$ s, in the case where the neutrino luminosities are kept constant as in case (i) or (iii) of Sect. 3.4, the value of Y_e strongly depends on the α-effect and on the electron and
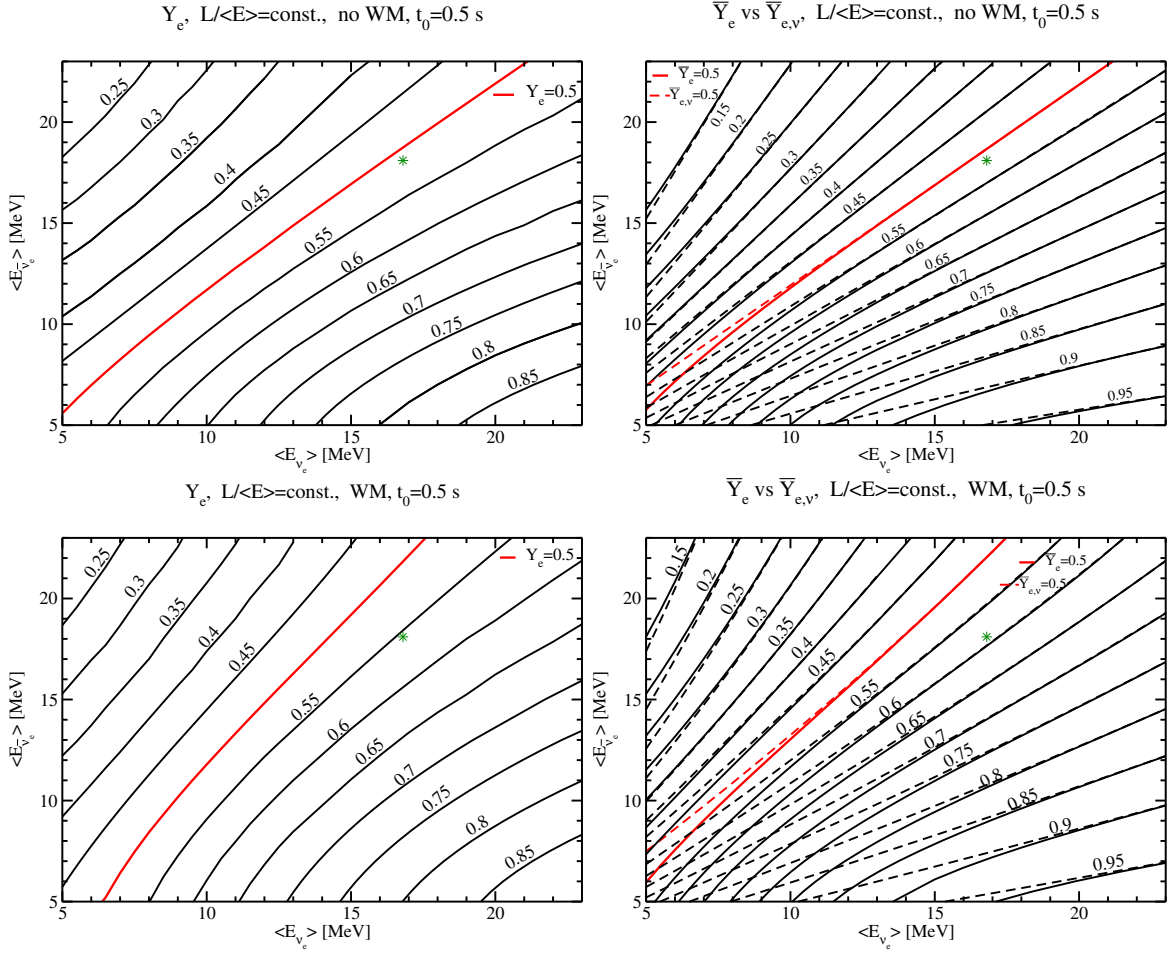
Figure 3.4 Same as Fig. 3.3, but keeping the number fluxes of ν_e ($L_{\nu_e}/\langle E_{\nu_e}\rangle$) and $\bar{\nu}_e$ ($L_{\bar{\nu}_e}/\langle E_{\bar{\nu}_e}\rangle$) as given by the hydrodynamic simulations (see Tab. 3.1 and case (ii) in Sect. 3.4).

positron captures. In particular, since the difference between Y_e and $\overline{Y}_{e,\nu}$ is significantly large, we can conclude that the equilibrium assumption about Y_e at early evolution stages of the ν-driven wind, in the "$L = L_{\text{hydro}}$" case, is not valid. This means that, in this case, the condition $\tau_\beta < \tau_{\text{dyn}}$ is not fulfilled (see Sect. 3.3).

Besides the nuclear composition and the dynamical effects, the physics involved in the β-reactions themselves also is of great importance in setting the value of Y_e in the ν-driven wind, as we will discuss in the next section.

3.5.2 Impact of weak magnetism and recoil corrections on Y_e

In this section, we discuss the influence of weak magnetism and recoil corrections on the evolution of Y_e (Horowitz & Li 1999). The weak magnetism and recoil corrections increase the capture rates of ν_e and e^-, while they decrease the capture rates of $\bar{\nu}_e$ and e^+ (see Sect. 3.3). In particular, close to the surface of the proto-neutron star (or at smaller radii), the evolution of Y_e is mainly determined by λ_{e^-}

and λ_{e^+}, while far away from the PNS λ_{ν_e} and $\lambda_{\bar{\nu}_e}$ determine Y_e. This is due to the fact that the capture rates of e^- and e^+ are proportional to T^6 (r^{-6}), while those of ν_e and $\bar{\nu}_e$ are proportional to r^{-2} (Janka 2012). In Fig. 3.3 (lower panel), we show the contour plots of Y_e, $\overline{Y}_e$ and $\overline{Y}_{e,\nu}$ as functions of $\langle E_{\nu_e} \rangle$ and $\langle E_{\bar{\nu}_e} \rangle$ with weak magnetism and recoil corrections ("WM case"), at $t_0 = 0.5$ s. By comparing the "no WM" case with the "WM case", in the "$L = L_{\text{hydro}}$" case, we see that the main effect of these corrections is to *increase* Y_e, although this increase strongly depends on $\langle E_{\nu_e} \rangle$ and $\langle E_{\bar{\nu}_e} \rangle$. In particular, at low neutrino energies, the corrections due to weak magnetism and recoil are smaller than at high energies, as we expect from the correction factors W_{ν_e} and $W_{\bar{\nu}_e}$ (see Sect. 3.3). This can also be more easily seen by comparing $\overline{Y}_e$ (or $\overline{Y}_{e,\nu}$) in the "no WM" case with the one in the "WM" case, since $\overline{Y}_e$ and $\overline{Y}_{e,\nu}$ depend *only* on λ_{ν_e} and $\lambda_{\bar{\nu}_e}$ and in the "WM" case they are always higher than in the "no WM" case (see discussion in Sect. 3.3).

In all the above considerations, we assumed that L_{ν_e} and $L_{\bar{\nu}_e}$ are fixed according to the prescriptions in case (i) (for Y_e and $\overline{Y}_e$) or (iii) (for $\overline{Y}_{e,\nu}$) of Sect.3.4. Therefore, we have to wonder how do our results change if we use another prescription for the neutrino parameters themselves. This is the topic of our next section.

3.5.3 Influence of neutrino parameters on Y_e

In this section, we focus on the difference between the three assumptions (i), (ii) and (iii) made in Sect. 3.4. In Fig. 3.4, we show Y_e, $\overline{Y}_e$ and $\overline{Y}_{e,\nu}$ analogously to Fig. 3.3, but while keeping the number fluxes of neutrinos $L/\langle E \rangle$ constant as given in Table 3.1 (case (ii) in Sect. 3.4). The differences between Y_e and $\overline{Y}_e$ (or $\overline{Y}_{e,\nu}$) are similar to the case "$L = L_{\text{hydro}}$", namely the α-effect drives Y_e towards more symmetric conditions ($Y_e \longrightarrow 0.5$), therefore the Y_e contour plot lines are "less dense" than the $\overline{Y}_e$ ones (or the $\overline{Y}_{e,\nu}$ ones). On the other hand, there is an important difference concerning the impact of weak magnetism and recoil corrections between the "$L = L_{\text{hydro}}$" case and the "$L/\langle E \rangle =$ const." case. Namely, in the latter case, at low energies, Y_e in "WM" case is *lower* than in the "no WM" case. This is due to the fact that, at these energies and with constant neutrino and antineutrino fluxes, the evolution of Y_e is mainly driven by e^+ and e^- captures before α particles start forming. Therefore, these corrections decrease the value of Y_e compared to the "no WM" case, already before α-effect, λ_{ν_e} and $\lambda_{\bar{\nu}_e}$ start controlling the evolution of Y_e. Differently from the "$L = L_{\text{hydro}}$" case, in the "$L/\langle E \rangle =$ const." case, we "force" the number fluxes of ν_e and $\bar{\nu}_e$ to be constant, and this constant is lower than the corresponding neutrino number fluxes in the "$L = L_{\text{hydro}}$" case, especially at lower energies. Therefore, the neutrino capture rates in the "$L/\langle E \rangle =$ const." case are lower than the ones in the "$L = L_{\text{hydro}}$" case especially at smaller radii, where the evolution of Y_e is then mainly determined by e^+ and e^- captures.
Another important difference between the "$L = L_{\text{hydro}}$" and the "$L/\langle E \rangle =$ const." cases concerns the agreement between the values of $\overline{Y}_e$ and $\overline{Y}_{e,\nu}$.

In fact, in the "$L/\langle E \rangle =$ const." case, we notice that $\overline{Y}_e = \overline{Y}_{e,\nu}$ (i.e., the dynamical effects do not play the dominant role) at higher (anti)neutrino energies, while $\overline{Y}_e \neq \overline{Y}_{e,\nu}$ at lower energies. This suggests that at higher neutrino and antineutrino energies the equilibrium assumption $\tau_\beta < \tau_{\text{dyn}}$ may still be valid, even for early evolution phases of the ν-driven wind. In fact, $\tau_\beta \propto 1/(\lambda_\nu)$ and, if "$L/\langle E \rangle =$ const.", then $\tau_\beta \propto E_\nu^{-2}$. This means that, if E_ν is sufficiently high, then τ_β can become enough small so that the condition $\tau_\beta < \tau_{\text{dyn}}$ may be fulfilled. In the "$L = L_{\text{hydro}}$" case, $\tau_\beta \propto E_\nu^{-1}$, therefore the probability that the condition $\tau_\beta < \tau_{\text{dyn}}$ is achieved is much lower.
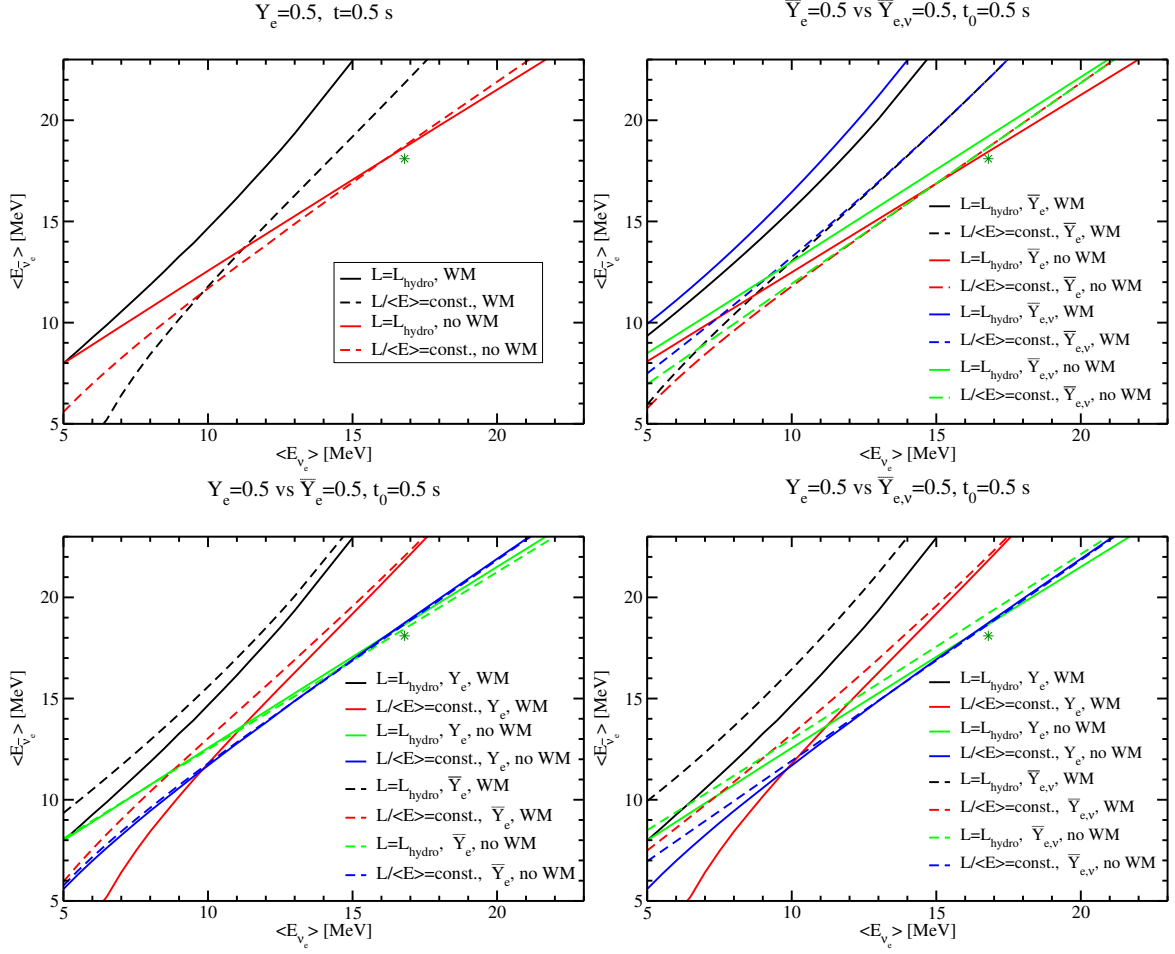
Figure 3.5 Upper panel (left): Electron fraction $Y_e = 0.5$ given by full network calculations as a function of $\langle E_{\nu_e} \rangle$ and $\langle E_{\bar{\nu}_e} \rangle$ at $t_0 = 0.5$ s in the "$L = L_{hydro}$" (case (i) in Sect. 3.4) and "$L/\langle E \rangle =$ const." cases (case (ii) in Sect. 3.4). In the "WM" case, weak magnetism and recoil corrections are taken into account while in the "no WM" case they are ignored. Upper panel (right): $\overline{Y}_e = 0.5$ in the case where $X_\alpha = 0$, $\lambda_{e^-} = 0$ and $\lambda_{e^+} = 0$ and $\overline{Y}_{e,\nu} = 0.5$ in the case where equilibrium is assumed (see also text for details). Lower panel: Comparison of $Y_e = 0.5$ and $\overline{Y}_e = 0.5$ (left) and $Y_e = 0.5$ and $\overline{Y}_{e,\nu} = 0.5$ (right) at $t_0 = 0.5$ s. Since $Y_e \neq \overline{Y}_{e,\nu}$, equilibrium conditions cannot be assumed for Y_e at $t_0 = 0.5$ s. The star symbols correspond to the hydrodynamic simulations values.

After having discussed the individual cases, in Fig. 3.5, we show a summary of the results at $t_0 = 0.5$ s concerning the different assumptions in determining the electron fraction. In the top panel, we show $Y_e = 0.5$ (left), $\overline{Y}_e = 0.5$ and $\overline{Y}_{e,\nu} = 0.5$ (right) as functions of $\langle E_{\nu_e} \rangle$ and $\langle E_{\bar{\nu}_e} \rangle$ in the cases "$L = L_{hydro}$" and "$L/\langle E \rangle =$ const.", as well as with or without weak magnetism and recoil corrections. We show with the symbol star the electron fraction corresponding to $\langle E_{\nu_e} \rangle$ and $\langle E_{\bar{\nu}_e} \rangle$ from the hydrodynamic simulations.

In the Y_e case, the weak magnetism and recoil corrections play an important role in both directions of the β-reactions determining Y_e. Therefore, in the "$L/\langle E \rangle =$ const." case, at $\langle E_{\nu_e} \rangle \simeq 10$ MeV and $\langle E_{\bar{\nu}_e} \rangle \simeq 12$ MeV, there is a crossing point between "WM" and "no WM" cases. This means that, for $\langle E_{\nu_e} \rangle \lesssim 10$ MeV, weak magnetism and recoil corrections *lower* Y_e compared to the "no WM" case. In

the "$L = L_{\text{hydro}}$" case, Y_e in the "WM" case is generally higher than in the "no WM" case, and at very low energies they achieve the same value.

$\overline{Y}_e$ and $\overline{Y}_{e,\nu}$ are in the "WM" case always higher or equal than the corresponding ones in the "no WM" case, because they only depend on the neutrino captures, and therefore weak magnetism and recoil corrections increase $\overline{Y}_e$, as expected. We can also see the impact of dynamical effects (without network calculations) on the electron fraction, by comparing $\overline{Y}_e$ and $\overline{Y}_{e,\nu}$. In general, in the "$L/\langle E \rangle = $ const." case, independently from "WM" or "no WM" case, at high $\langle E_{\nu_e} \rangle$ and $\langle E_{\bar{\nu}_e} \rangle$, $\overline{Y}_e = \overline{Y}_{e,\nu}$, while in all the other cases they are significantly different.

We also notice that the difference between the Y_e, $\overline{Y}_e$ and $\overline{Y}_{e,\nu}$ values in the "$L = L_{\text{hydro}}$" case and the corresponding ones in the "$L/\langle E \rangle = $ const." case is much bigger in the "WM" case than in the "no WM" case (compare solid and dashed lines in the upper panel of Fig. 3.5). In order to understand the reason, we can focus, for example, on the contour lines $\overline{Y}_{e,\nu} = 0.5$. From Eq. 3.20, it follows that, $\overline{Y}_{e,\nu} = 0.5$, if $\langle E_{\bar{\nu}_e} \rangle \propto \langle E_{\nu_e} \rangle \cdot (W_{\nu_e}/W_{\bar{\nu}_e})$, in the "$L = L_{\text{hydro}}$" case, and $\langle E_{\bar{\nu}_e} \rangle \propto \langle E_{\nu_e} \rangle \cdot \sqrt{W_{\nu_e}/W_{\bar{\nu}_e}}$ in the "$L/\langle E \rangle = $ const." case. Furthermore, in the "no WM" case, we simply have $W_{\nu_e}/W_{\bar{\nu}_e} = 1$. This means that, in the "no WM" case, independently from "$L = L_{\text{hydro}}$" case or "$L/\langle E \rangle = $ const.", $\overline{Y}_{e,\nu} = 0.5$, if $\langle E_{\bar{\nu}_e} \rangle \propto \langle E_{\nu_e} \rangle$. This simple linear relation between $\langle E_{\bar{\nu}_e} \rangle$ and $\langle E_{\nu_e} \rangle$ does not apply to the "WM" case, because of the energy dependence of W_{ν_e} and $W_{\bar{\nu}_e}$ terms. Therefore, in the WM case, the spacing between the contour lines in the "$L = L_{\text{hydro}}$" case is very different from the one in the "$L/\langle E \rangle = $ const." case. This is the reason why in the "no WM" case, independently from the assumptions about the neutrino parameters, the values of Y_e, $\overline{Y}_e$ and $\overline{Y}_{e,\nu}$ are more similar than in the "WM" case.

In the lower panel of Fig. 3.5, we compare $Y_e = 0.5$ and $\overline{Y}_e = 0.5$ (left) and $Y_e = 0.5$ and $\overline{Y}_{e,\nu} = 0.5$ (right) in order to directly see the difference between full dynamical network calculations and the approximated values of the electron fraction. The full network effects play a bigger role in the case where weak magnetism and recoil corrections are included, although these effects strongly depend on $\langle E_{\nu_e} \rangle$ and $\langle E_{\bar{\nu}_e} \rangle$. In particular, by comparing $Y_e = 0.5$ and $\overline{Y}_{e,\nu} = 0.5$, we can conclude that the equilibrium assumption for $Y_e = 0.5$ strongly depends on the neutrino parameters and the inclusion or absence of weak magnetism and recoil corrections.

Furthermore, taking into account the most complete calculation of Y_e, namely Y_e in the "WM" case, we can say that the matter is proton-rich rather than neutron-rich, if $\langle E_{\nu_e} \rangle$ and $\langle E_{\bar{\nu}_e} \rangle$ are not very different from the values given by hydrodynamic simulations (shown by the star symbol).
This means that if the shift of $\langle E_{\nu_e} \rangle$ and $\langle E_{\bar{\nu}_e} \rangle$ values due to nucleon potential corrections is not very big, then the matter in the ν-driven wind will still be proton-rich, precluding the possibility for the r-process to occur at least in the early phase of the ν-driven wind.

However, the competition between ν_e ($\bar{\nu}_e$) and e^- (e^+) capture rates in determining Y_e and the role played by the dynamical effects and full network calculations are sensitively time dependent. Therefore, the time dependence evolution of Y_e will be our next topic and leads us to the next section.

3.6 Results II: Time dependence evolution of Y_e

The evolution of Y_e in the ν-driven wind is time dependent, due to the time dependence of the hydrodynamic trajectories and of the neutrino properties (see Figs. 3.1 and 3.2). Therefore, we perform our

study of Y_e, analogously to what already shown at $t_0 = 0.5$ s (early ν-driven wind phase), at $t_0 = 2.9$ s (intermediate ν-driven wind phase) and $t_0 = 6.5$ s (late ν-driven wind phase). The consideration of these three representative times allows us to have a general overview about the time dependence of Y_e in the ν-driven wind.

In Figs. 3.6 and 3.7, we show the contour plots of Y_e, $\overline{Y}_e$ and $\overline{Y}_{e,\nu}$ at $t_0 = 2.9$ s, analogously to Fig. 3.3 and 3.4 at $t_0 = 0.5$ s, as functions of $\langle E_{\nu_e}\rangle$ and $\langle E_{\bar{\nu}_e}\rangle$. In this case as well, for the same energy range of $\langle E_{\nu_e}\rangle$ and $\langle E_{\bar{\nu}_e}\rangle$, Y_e is higher than $\overline{Y}_e$ ($\overline{Y}_{e,\nu}$) for $Y_e < 0.5$ and is lower than $\overline{Y}_e$ ($\overline{Y}_{e,\nu}$) for $Y_e > 0.5$. This is mainly due to the α-effect, which pushes Y_e towards 0.5. This effect is particularly evident at $t_0 = 6.5$ s, as we can see from Figs. 3.9 and 3.10, where Y_e is pushed towards 0.5 even more, although the details depend on the physical approximations which are used to describe the neutrino parameters and opacities.
In general, the impact of the α-effect is bigger at late times than at early times, since the wind entropy is higher and the expansion timescale longer, as a result of the more compact PNS with lower neutrino luminosities, resulting in a longer duration of the α-effect (see also next chapter for more details).

By comparing $\overline{Y}_e$ and $\overline{Y}_{e,\nu}$, we can also say that the pure dynamical effects do not play any important role on the evolution of Y_e, namely the assumption $dY_e/dt = 0$ is well justified at intermediate (compare solid and dashed lines in Fig. 3.6 (right) and 3.7 (right)) and late phases (see Fig. 3.9 (right)) of the ν-driven wind. Furthermore, the marginal difference between $\overline{Y}_e$ and $\overline{Y}_{e,\nu}$ in the "$L = L_{\text{hydro}}$" case, suggests that basically the variations of the neutrino luminosities as functions of the postbounce time (see Fig. 3.2) do not play any important role and that case (i) and (iii) in Sect. 3.4 essentially give the same value of the electron fraction.

In Figs. 3.8 and 3.11, analogously to Fig. 3.5 at $t_0 = 0.5$ s, we show the summary of $Y_e = 0.5$ and $\overline{Y}_e = 0.5$ in all the different considered cases, at $t_0 = 2.9$ s and at $t_0 = 6.5$ s, respectively. At $t_0 = 2.9$ s and at $t_0 = 6.5$ s, in the "$L = L_{\text{hydro}}$" case, Y_e in the "WM" case is always higher than the one in the "no WM" case. This means that the evolution of Y_e is mainly determined by the capture reactions involving neutrinos, and therefore weak magnetism and recoil corrections *increase* its value, analogously to what happens at $t_0 = 0.5$ s. In the "$L/\langle E\rangle = $ const." case instead, there is an interesting difference between the intermediate and late postbounce times, because at $t_0 = 2.9$ s the $Y_e = 0.5$ curves in the "WM" and "no WM" cases intersect at about $\langle E_{\nu_e}\rangle = 6.5$ MeV and $\langle E_{\bar{\nu}_e}\rangle \simeq 9.0$ MeV, differently from $t_0 = 6.5$ s case. This means that, at $t_0 = 2.9$ s, weak magnetism and recoil corrections *decrease* Y_e, and therefore the electron and positron captures play an important role in setting Y_e (see also the analogous discussion at $t_0 = 0.5$ s), while at late times the value of Y_e is in all cases mainly determined by the capture reactions of neutrinos as we can see from the fact that $Y_e(\text{WM}) > Y_e(\text{no WM})$, independently from the assumptions about the neutrino parameters.

In Fig. 3.12, we show a summary of the time evolution ($t_0 =0.5$ s, 2.9 s, and 6.5 s) of $Y_e = 0.5$, $\overline{Y}_e = 0.5$ and $\overline{Y}_{e,\nu} = 0.5$ in all the considered cases ("WM", "no WM", "$L = L_{\text{hydro}}$", and "$L/\langle E\rangle = $ const."). In the "$L = L_{\text{hydro}}$" case, Y_e and $\overline{Y}_e$ increase with time, independently from the physics involved in the β-reactions.

In the "$L/\langle E\rangle = $ const." case, instead, we cannot see a clear dependence of Y_e over time, since it can increase as well as decrease, according to the case.

Even more importantly, in the "WM" case, independently from the time, the matter in the ν-driven wind is proton-rich ($Y_e > 0.5$) for $\langle E_{\nu_e}\rangle$ and $\langle E_{\bar{\nu}_e}\rangle$ values close to the hydrodynamic ones (shown by star symbols). This suggests that, unless the mean-field nucleon potential corrections on $\langle E_{\nu_e}\rangle$ and
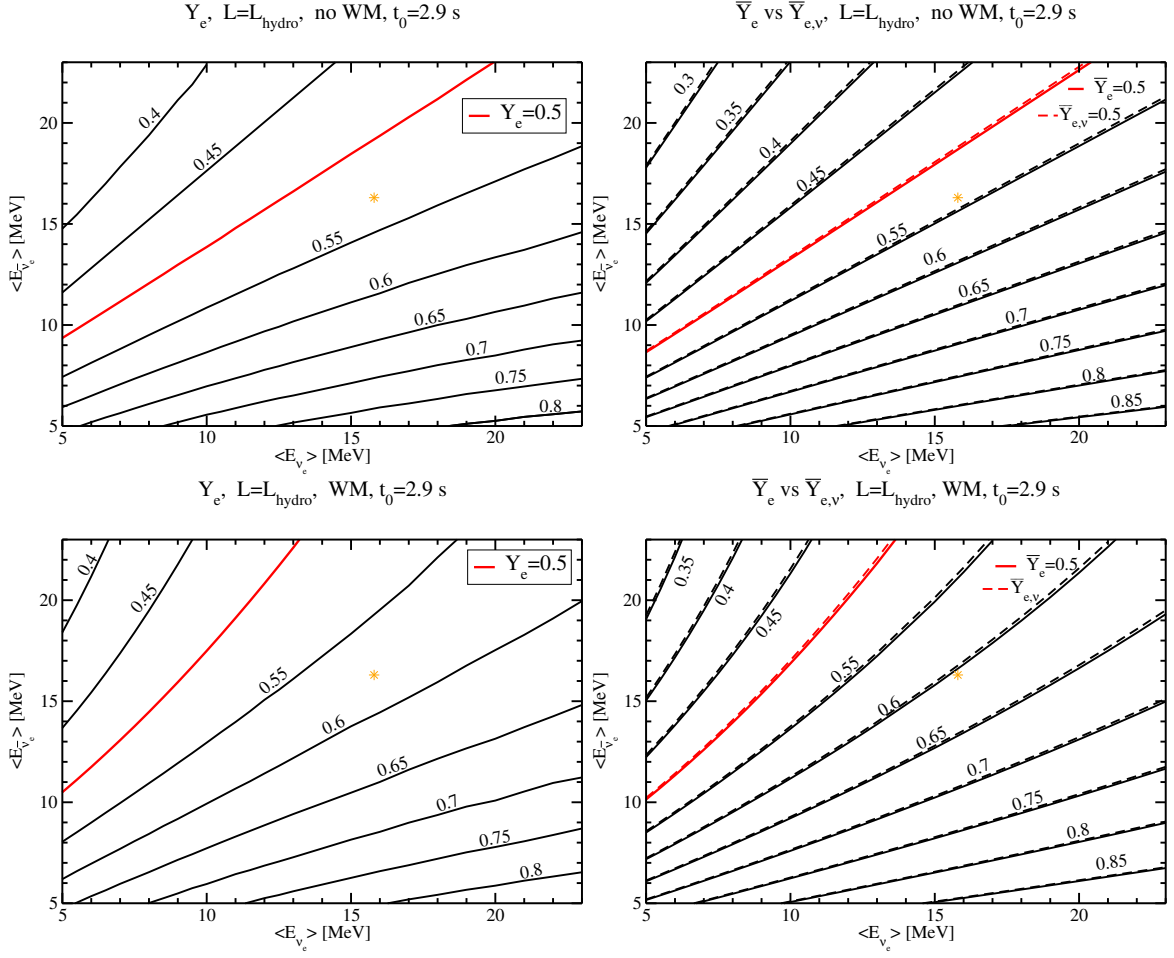
Figure 3.6 The same as Fig. 3.3, but at $t_0 = 2.9$ s.

$\langle E_{\bar{\nu}_e} \rangle$ values are extremely large (e.g, more than 3-4 MeV), the ν-driven wind of our ECSN model should remain proton-rich even if the aforementioned corrections were included.

In order to have a quantitative distinction between the space of neutrino parameters for which the ν-driven wind matter of our ECSN is proton-rich ($Y_e > 0.5$) or neutron-rich $Y_e < 0.5$, we fit $\langle E_{\bar{\nu}_e} \rangle$ as a function of $\langle E_{\nu_e} \rangle$ (or the other way around) in all the considered cases corresponding to the electron-fraction $Y_e = 0.5$ (in the full network calculations case).

We assume a polynomial relation between $\langle E_{\nu_e} \rangle$ and $\langle E_{\bar{\nu}_e} \rangle$ for $Y_e = 0.5$ (see red lines in Figs. 3.3, 3.4, 3.6, 3.7, 3.9 and 3.10):

$$\langle E_{\bar{\nu}_e} \rangle = a + b \cdot \langle E_{\nu_e} \rangle + c \cdot \langle E_{\nu_e} \rangle^2 + d \cdot \langle E_{\nu_e} \rangle^3 + e \cdot \langle E_{\nu_e} \rangle^4, \tag{3.24}$$

where a is given in MeV, b, c, d, and e are the fitting parameters, which are summarized in Table 3.2. Notice that the values in boldface in Table 3.2 correspond to the fitting parameters of $\langle E_{\nu_e} \rangle$ as a function of $\langle E_{\bar{\nu}_e} \rangle$:

$$\langle E_{\nu_e} \rangle = a + b \cdot \langle E_{\bar{\nu}_e} \rangle + c \cdot \langle E_{\bar{\nu}_e} \rangle^2 + d \cdot \langle E_{\bar{\nu}_e} \rangle^3 + e \cdot \langle E_{\bar{\nu}_e} \rangle^4. \tag{3.25}$$

From Table 3.2, we can see that the relation between $\langle E_{\nu_e} \rangle$ and $\langle E_{\bar{\nu}_e} \rangle$ (for $Y_e = 0.5$) is linear only in the "$L = L_{\text{hydro}}$, no WM" case.
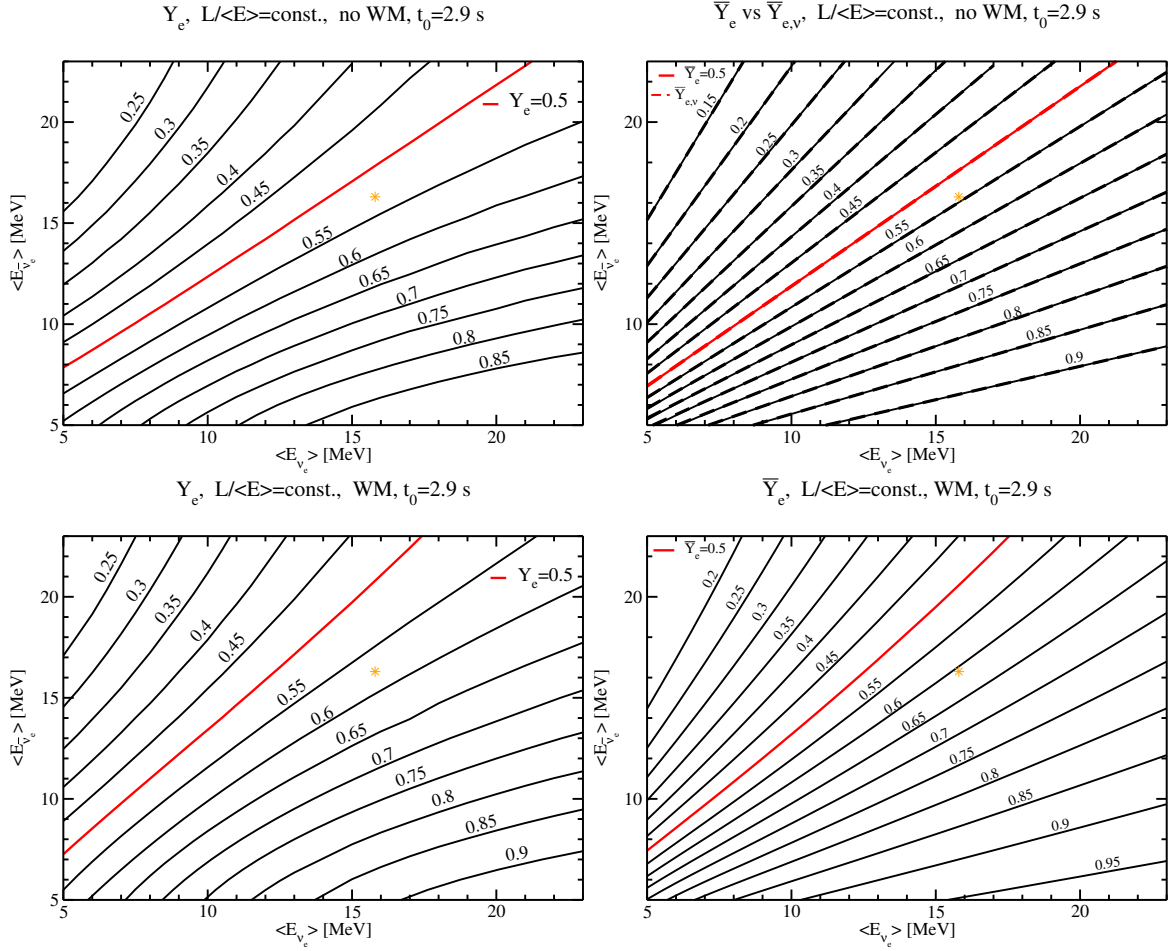
Figure 3.7 The same as Fig. 3.4, but at $t_0 = 2.9$ s. Notice that, in the lower panel (right), we do not show the contour lines of $\overline{Y}_{e,\nu}$, since they overlap with the ones of $\overline{Y}_e$.

3.7 Conclusions

In this chapter, we have investigated the impact of nucleon potential corrections on the electron fraction in the ν-driven wind of an 8.8 $M_\odot$ ECSN (Hüdepohl et al. 2010). These corrections can have important consequences for Y_e, and therefore for the nucleosynthesis in the ν-driven wind. In the hydrodynamical simulations of Hüdepohl et al. (2010), these corrections were not included. Therefore, we adopt some assumptions about the neutrino parameters in order to perform our study. In one case, we adopt the neutrinos and antineutrino luminosities of Hüdepohl et al. (2010) and vary the mean energies. In the other case, we fix the neutrino and antineutrino number fluxes as in Hüdepohl et al. (2010) and vary the mean energies. We also make different assumptions about the opacities involved in the β-reactions which determine Y_e in the ν-driven wind, namely we do include or omit weak magnetism and recoil corrections (Horowitz & Li 1999). Furthermore, we also consider different approximations about Y_e. First, we calculate Y_e using a full network, then we only consider the dynamical evolution of Y_e taking into account only neutrino reactions in the β-reactions ($X_\alpha = 0$, $\lambda_{e^+/e^-} = 0$). Finally, we assume an instantaneous equilibrium for Y_e (i.e., $dY_e/dt = 0$).

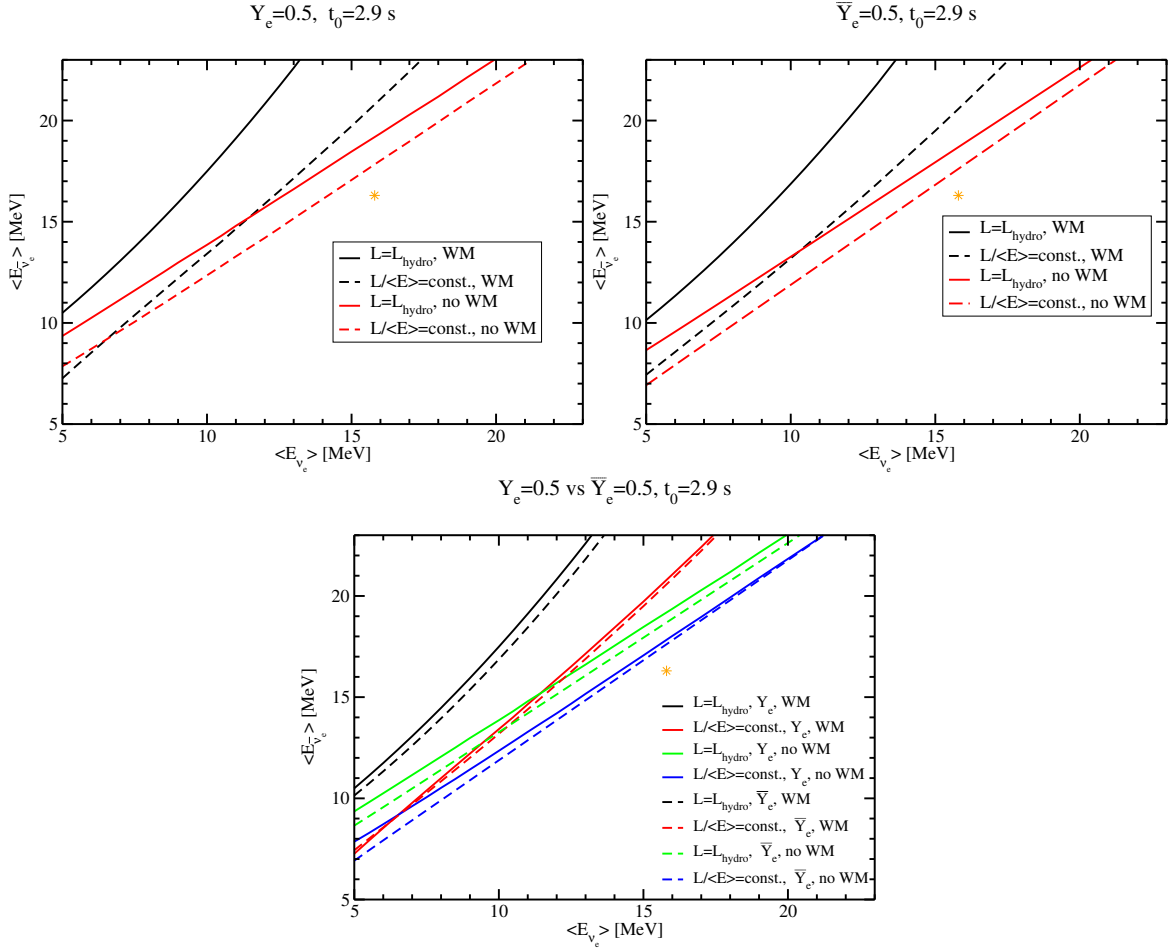These assumptions allow us to investigate the impact of the α-effect on Y_e and in which conditions the

Figure 3.8 Same as Fig. 3.5, but at $t_0 = 2.9$ s. Notice that, contrary to the $t_0 = 0.5$ s case, we do not show the contour lines of $\overline{Y}_{e,\nu}$ here, since they basically overlap with the ones of $\overline{Y}_e$.

equilibrium assumption for Y_e is valid.

Since the evolution of Y_e in the ν-driven wind is also time dependent, we study three trajectories which are representative for the early, intermediate and late phases of our ν-driven wind model.

At early times ($t_0 = 0.5$ s) and intermediate times ($t_0 = 2.9$ s), weak magnetism and recoil (WM) corrections can increase Y_e (at high neutrino and antineutrino energies) or lower it (at low neutrino and antineutrino energies) compared to the case where these corrections are not included. The details depend also on the assumed neutrino parameters. At late times ($t_0 = 6.5$ s), WM corrections always increase Y_e compared to the "no WM" case. The α-effect always pushes Y_e towards 0.5, but at later times this effect is even more evident due to the higher wind entropy and to the longer expansion timescale. This is a consequence of a more compact PNS with lower neutrino luminosities, and therefore the α-effect lasts longer.

The equilibrium conditions for Y_e are well fulfilled at intermediate and late times, but not at early times. Therefore, one has to apply full network calculations in order to predict accurate values for Y_e at early times, but can safely use the equilibrium formula for Y_e, which depends only on neutrinos parameters, at intermediate and late times.
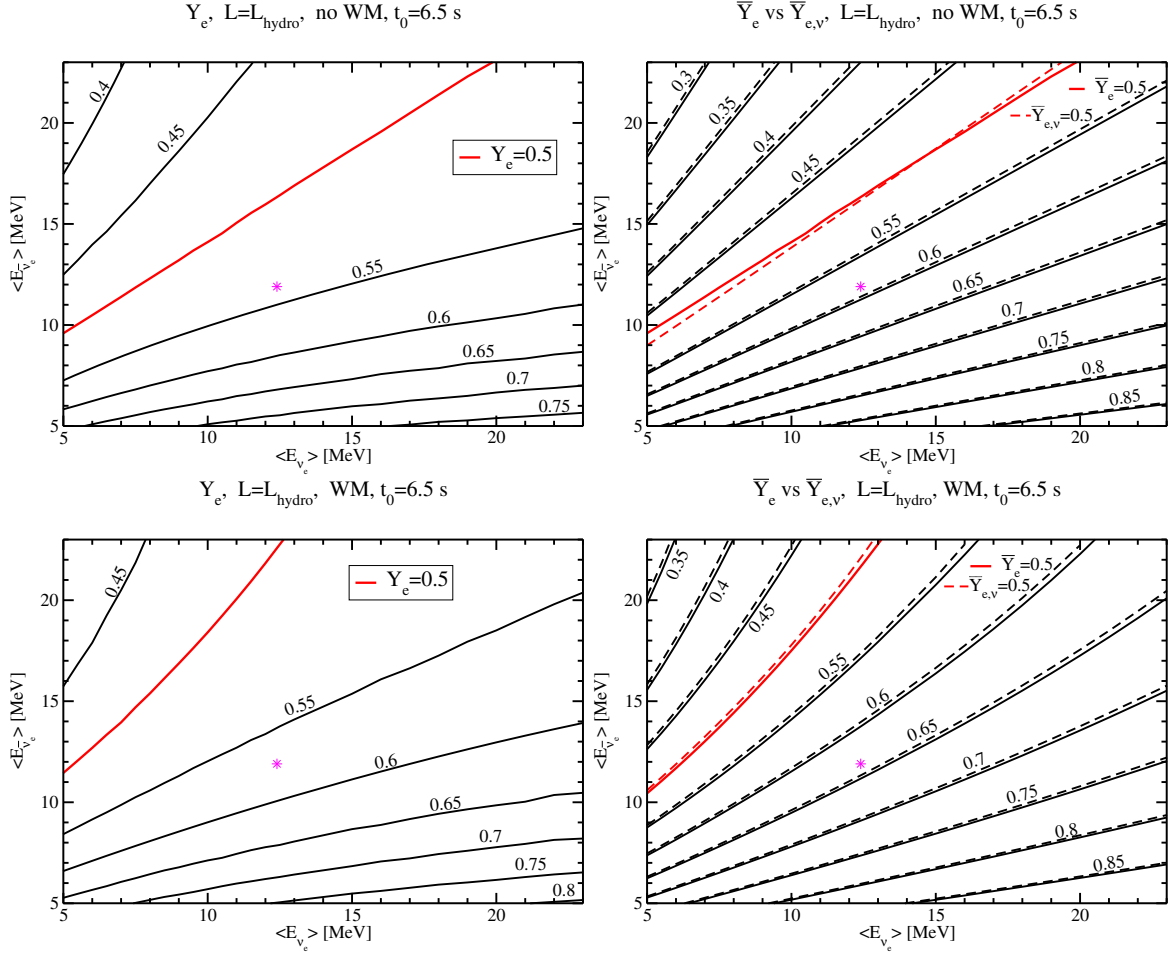
Figure 3.9 The same as Fig. 3.3, but at $t_0 = 6.5$ s.

In general, if we include the recoil and weak magnetism corrections and perform full network calculations, then Y_e tends to be in the proton-rich side, for neutrino parameters which are not very far from those of the most sophisticated ECSNe simulations.

However, a proper inclusion of mean-field nucleon potential corrections on neutrino opacities in the hydrodynamical simulations is necessary in order to accurately predict their impact on Y_e in the ν-driven wind, and therefore on the nucleosynthesis.

There is another property of neutrinos which can impact the nucleosynthesis outcome in SN and which has not been included in our adopted model of Hüdepohl et al. (2010), namely neutrino flavor oscillations. Therefore, one has to wonder how do neutrino flavor oscillations impact the nucleosynthesis in the ν-driven wind? An attempt to answer this question brings us to the next chapter.
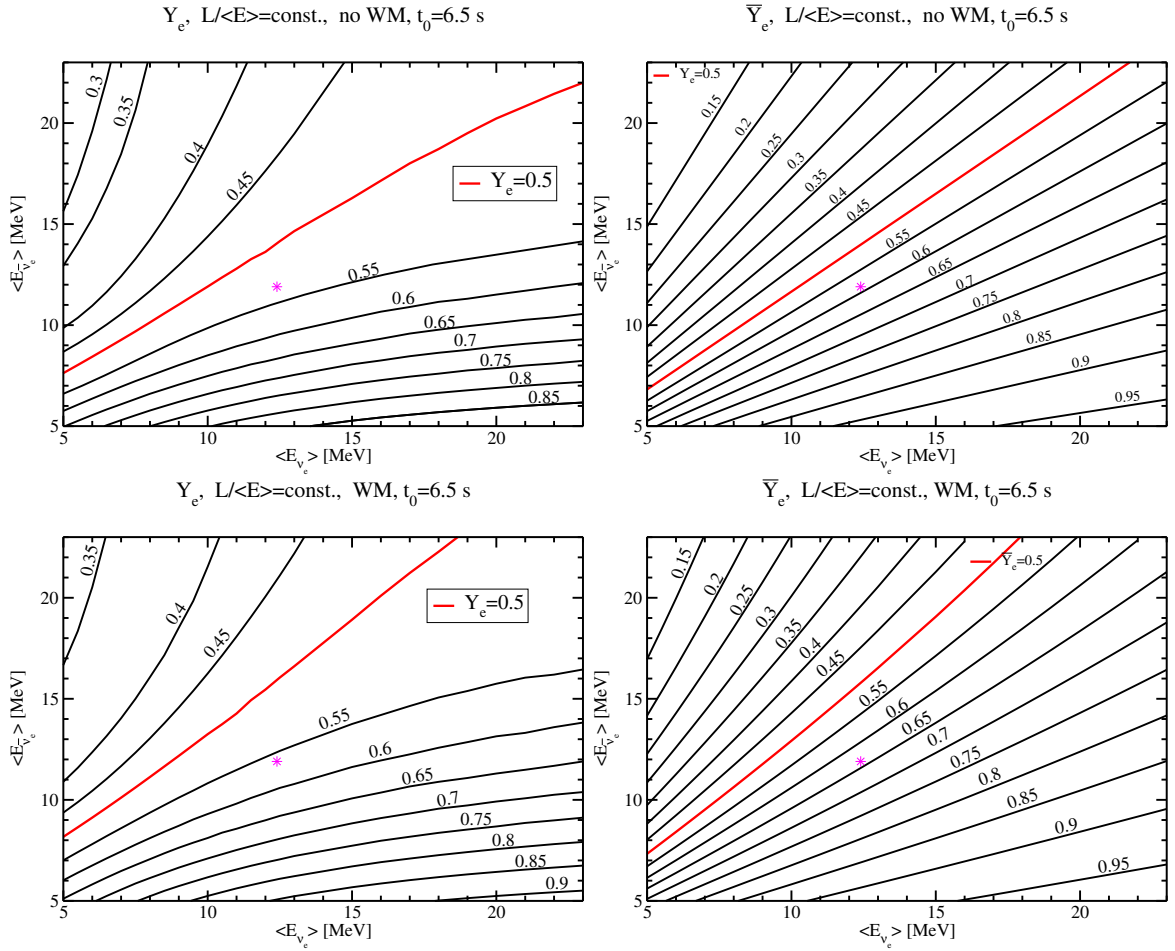
Figure 3.10 The same as Fig. 3.4, but at $t_0 = 6.5$ s. Notice that, contrary to the $t_0 = 0.5$ s case, we do not show the contour lines of $\overline{Y}_{e,\nu}$, since they overlap with the ones of $\overline{Y}_e$.
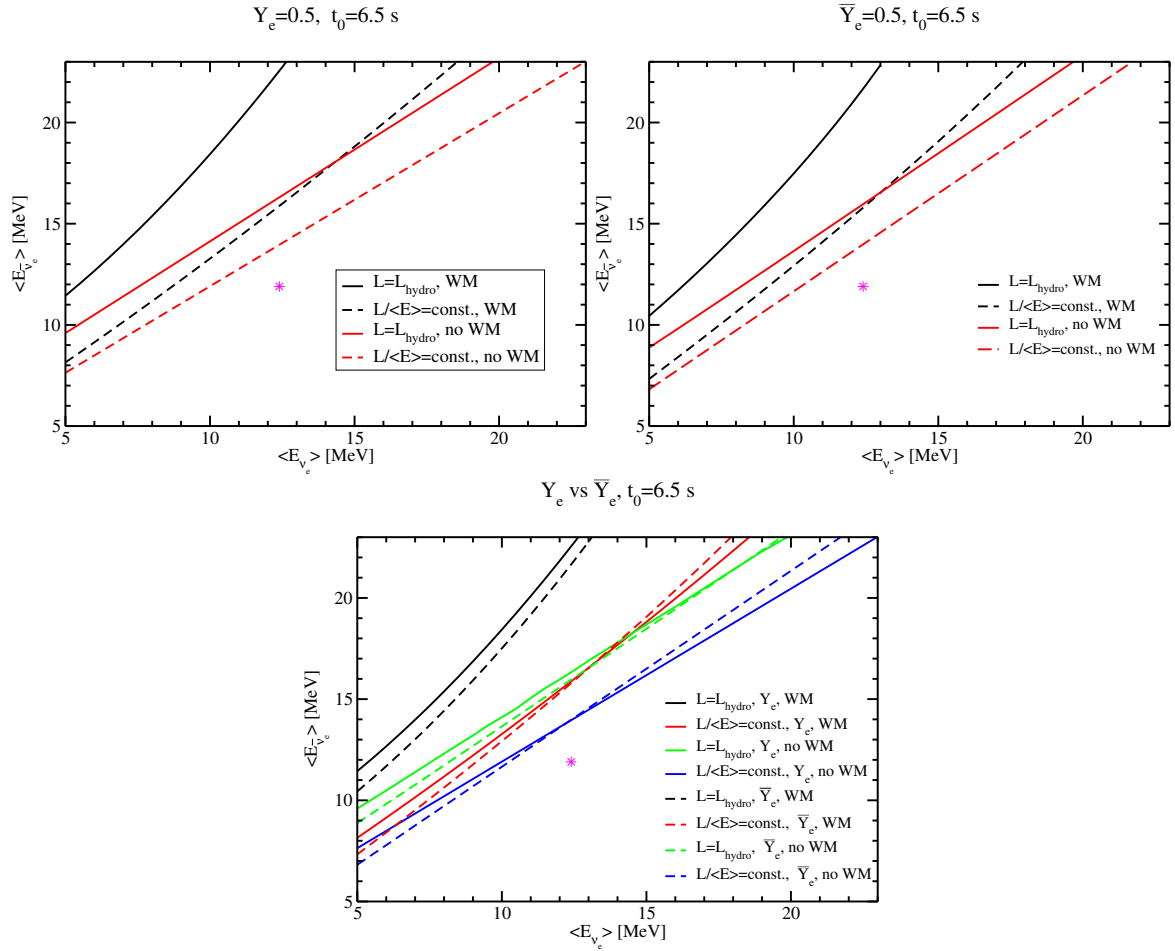
Figure 3.11 Same as Fig. 3.5, but at $t_0 = 6.5$ s. Notice that, contrary to the $t_0 = 0.5$ s case, we do not show the contour lines of $\overline{Y}_{e,\nu}$ here, since they basically overlap with the ones of $\overline{Y}_e$.
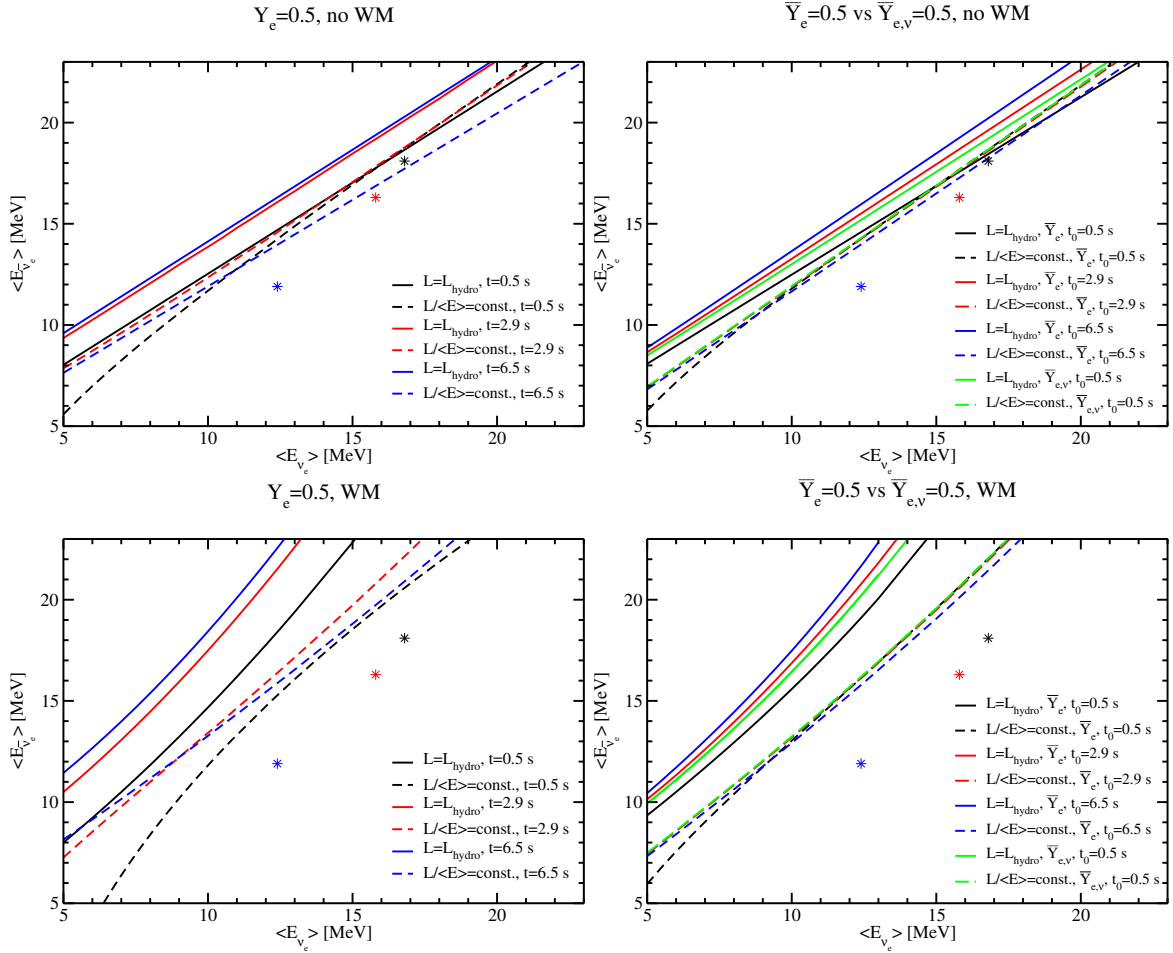
Figure 3.12 Upper panel (left): Electron fraction $Y_e = 0.5$ as given by full network calculations as a function of $\langle E_{\nu_e} \rangle$ and $\langle E_{\bar{\nu}_e} \rangle$ at $t_0 = 0.5$ s, 2.9 s, and 6.5 s, in the case where weak magnetism and recoil corrections are not taken into account in the β-reactions ("no WM" case), and in both $L = L_{hydro}$ and $L/\langle E \rangle = $ const. cases. The upper and lower panels on the right show, analogously to the corresponding panels on the left, the electron fraction $\overline{Y}_e = 0.5$ in the case where $X_\alpha = 0$, $\lambda_{e^-} = 0$ and $\lambda_{e^+} = 0$. In the same panels of $\overline{Y}_e = 0.5$, we even show the equilibrium solution $\overline{Y}_{e,\nu} = 0.5$ only at $t_0 = 0.5$, since at the other postbounce times it is essentially the same as $\overline{Y}_e = 0.5$. The star symbols correspond to the values of the hydrodynamic simulations of Hüdepohl et al. (2010).

Table 3.2 At each of the considered postbounce times (t_0 = 0.5 s, 2.9 s and 6.5 s), we show the parameters (*a* in MeV, *b*, *c*, *d* and *e*) used to fit $\langle E_{\bar{\nu}_e} \rangle$ as a function of $\langle E_{\nu_e} \rangle$, at Y_e = 0.5, in the case where no weak magnetism and recoil corrections are included ("no WM" case) and in the case where they are included ("WM" case) and both in the "$L = L_{\text{hydro}}$" and "$L/\langle E \rangle$ = const." cases (see Sect. 3.4). The numbers in boldface refer to the fitting of $\langle E_{\nu_e} \rangle$ as a function of $\langle E_{\bar{\nu}_e} \rangle$.

Y_e = 0.5	no WM	WM	no WM	WM
t_0 = 0.5 s	$L = L_{\text{hydro}}$	$L = L_{\text{hydro}}$	$L/\langle E \rangle$ = const.	$L/\langle E \rangle$ = const.
a	3.5270	2.7985	**2.5017**	**4.9198**
b	0.9000	0.8931	**0.1672**	**0.1547**
c	0	0.0295	**0.0613**	**0.0299**
d	0	0	**-0.00021**	$\mathbf{-5.5493 \cdot 10^{-4}}$
e	0	0	$\mathbf{2.8846 \cdot 10^{-5}}$	**0**
t_0 = 2.9 s				
a	4.7721	5.4000	3.4733	1.3490
b	0.9124	0.8299	0.8601	1.1625
c	0	0.0379	0.0029	0.0044
d	0	0	0	0
e	0	0	0	0
t_0 = 6.5 s				
a	5.0626	6.5939	4.2333	3.4330
b	0.9065	0.7547	0.5447	0.9019
c	0	0.0429	0.0317	0.0082
d	0	0	$-9.536 \cdot 10^{-4}$	0
e	0	0	0	0

4 Impact of Neutrino Flavor Oscillations on Neutrino-Driven Wind Nucleosynthesis

Neutrino oscillations, especially to light sterile states, can affect the nucleosynthesis yields because of their possible feedback effect on the electron fraction (Y_e). For the first time, we perform nucleosynthesis calculations for neutrino-driven wind trajectories from the neutrino-cooling phase of an 8.8 $M_\odot$ electron-capture supernova, whose hydrodynamic evolution was computed in spherical symmetry with sophisticated neutrino transport and whose Y_e evolution was post-processed by including neutrino oscillations both between active and active-sterile flavors. We also take into account the α-effect as well as weak magnetism and recoil corrections in the neutrino absorption and emission processes. We observe effects on the Y_e evolution which depend in a subtle way on the relative radial positions of the sterile MSW resonances, of collective flavor transformations, and on the formation of α-particles. For the adopted supernova progenitor, we find that neutrino oscillations, also to a sterile state with eV-mass, do not significantly affect the element formation and in particular cannot make the post-explosion wind outflow neutron rich enough to activate a strong r-process. Our conclusions become even more robust when, in order to mimic equation-of-state dependent corrections due to nucleon potential effects in the dense-medium neutrino opacities, six cases with reduced Y_e in the wind are considered. In these cases, despite the conversion of neutrinos to sterile neutrinos, Y_e increases or is not significantly lowered compared to the values obtained without oscillations and active flavor transformations. This is a consequence of a complicated interplay between sterile-neutrino production, neutrino-neutrino interactions, and α-effect[1].

4.1 Introduction

In the previous chapter, we discussed the evolution of the electron fraction in the electron-capture supernova (ECSN) neutrino-driven wind (ν-driven wind) simulated by Hüdepohl et al. (2010), paying attention to the impact of mean-field nucleon potential corrections on Y_e, and therefore on the nucleosynthesis. We came to the conclusion that the neutron-rich conditions, which are required for the r-process to occur, are foreseen only for ν_e and $\bar\nu_e$ luminosities far from the ones of supernovae simulations (Fischer et al. 2010; Hüdepohl et al. 2010).

However, there is another aspect of neutrino properties which we did not take into account, namely neutrinos flavor oscillations. In fact, neutrino flavor oscillations could modify the wind-Y_e, if they significantly alter the ν_e and $\bar\nu_e$ fluxes before Y_e reaches its asymptotic value. Therefore, the inclusion of neutrino flavor oscillations (with or without sterile neutrinos) may be important for determining the nucleosynthesis in the ν-driven wind and to clarify whether ECSNe could still be considered as candidate sites for the r-process.

---

[1]The work contained in this chapter is published in Pllumbi et al. (2015).

The nucleosynthesis yields (and the r-process) in supernovae might be affected by the existence of light sterile neutrinos, hypothetical gauge-singlet fermions that could mix with one or more of the active states and thus show up in active-sterile flavor oscillations (see Abazajian et al. 2012; Palazzo 2013 for recent reviews on the topic). In particular, eV-mass sterile neutrinos with large mixing imply that the ν_e flux would undergo Mikheyev-Smirnov-Wolfenstein (MSW) conversions (Mikheyev & Smirnov 1985; Wolfenstein 1978) to ν_s closer to the SN core than any other oscillation effect. We assume that the sterile state is heavier than the active ones because of cosmological neutrino mass limits (Abazajian et al. 2012). The idea that removing the ν_e flux by active-sterile oscillations could favor a neutron-rich outflow environment was proposed some time ago (Beun et al. 2006; Keränen et al. 2007; Fetter et al. 2003; Fetter 2000; McLaughlin et al. 1999; Hidaka & Fuller 2007; Nunokawa et al. 1997). However, the considered mass differences were larger and the possible impact of ν-ν interactions in the active sector (Duan et al. 2010) was not taken into account.

Recently, low-mass sterile neutrinos have been invoked to explain the excess $\bar{\nu}_e$ events in the LSND experiment (Aguilar et al. 2001; Strumia 2002; Gonzalez-Garcia & Maltoni 2008) as well as the MiniBooNE excess (Aguilar-Arevalo et al. 2009b,a; Karagiorgi et al. 2009; MiniBooNE Collaboration et al. 2012). Moreover an indication for the possible existence of eV-mass sterile neutrinos comes from a new analysis of reactor $\bar{\nu}_e$ spectra and short-baseline experiments (Kopp et al. 2011; Giunti & Laveder 2011a,b; Giunti et al. 2012; Donini et al. 2012; Giunti et al. 2013). The cosmic microwave background anisotropies (Reid et al. 2010; Hamann et al. 2010; Hou et al. 2013; Hinshaw et al. 2013; Planck Collaboration et al. 2013; Archidiacono et al. 2013) as well as big-bang nucleosynthesis (Pettini & Cooke 2012; Aver et al. 2012) point towards a cosmic excess radiation compatible with one family of fully thermalized sub-eV sterile neutrinos or one or even two partially thermalized sterile neutrino families with sub-eV/eV mass (Archidiacono et al. 2013; Giusarma et al. 2014).

Such intense activity triggered new interest in the role of neutrino oscillations with and without sterile neutrinos, and including ν-ν interactions, on nucleosynthesis processes like the r-process and the νp-process in SN outflows (Tamborra et al. 2012b; Duan et al. 2011a; Martínez-Pinedo et al. 2011). The role of active-sterile neutrino mixing for the ν-driven explosion mechanism and the nucleosynthesis in the early ($t \leq 100$ ms postbounce) ejecta of ECSNe was discussed by Wu et al. (2014). The authors found that active-sterile conversions can not only suppress neutrino heating considerably but can potentially enhance the neutron-richness of the ejecta allowing for the production of the elements from Sr, Y and Zr up to Cd. The conclusiveness of these results is unclear, however, because, besides approximate modeling of neutrino oscillations, only spherically symmetric models were considered, although multi-dimensional effects had been shown to be important during the onset of the explosion (cf. Wanajo et al. 2011). In contrast to spherical models, multi-dimensional ones provide sufficient neutron excess to yield interesting amounts of elements between the Fe-group and N = 50 nuclei even without involving sterile neutrino effects (Wanajo et al. 2011).

In this work, we explore the impact of neutrino flavor oscillations (with and without the inclusion of an extra eV-mass sterile neutrino) on the Y_e evolution of the ν-driven wind and on the corresponding nucleosynthesis yields of an ECSN, whose evolution can be well described in spherical symmetry and has been followed beyond the explosion continuously into the subsequent proto-neutron star cooling phase (Hüdepohl et al. 2010). The simulation of Hüdepohl et al. (2010) did not include the aforementioned nucleon mean-field effects in the charged-current neutrino-nucleon reactions (see also chapter 3) and resulted in the ejection of proton-rich matter throughout the wind phase. We still use this model to examine neutrino oscillation effects in the neutrino-driven wind, because the wind dynamics and thermodynamics conditions are only marginally changed despite the impact of the nucleon potentials

on the electron fraction (e.g. Martínez-Pinedo et al. 2012).

This chapter is structured in the following way. In Sect. 4.2, we describe the ν-driven wind trajectories adopted for the nucleosynthesis calculations, as well as our reaction network. In Sect. 4.3, the nucleosynthesis results are presented when no neutrino oscillations occur as fiducial case. After introducing the neutrino mass-mixing parameters in Sect. 4.4, we briefly discuss the oscillation physics[2] involved in the nucleosynthesis calculations in Sect. 4.5. Our results for Y_e and how it is affected by neutrino oscillations (with and without sterile neutrinos) including the corresponding nucleosynthesis are presented in Sect. 4.6. In Sect. 4.7, we introduce six toy model cases for the ν_e and $\bar{\nu}_e$ energy spectra in order to explore the possible consequences of nuclear mean-field effects in the neutrino opacities. In Sect. 4.8, we discuss our results and compare with other works. We present our conclusions and perspectives in Sect. 4.9. In the appendix A, we give more details about the feedback of neutrino self-interactions on Y_e.

4.2 Neutrino-driven wind and nuclear reaction network

In order to perform the network calculations for the nucleosynthesis in the neutrino-driven wind, we use 98 ejecta trajectories from Hüdepohl et al. (2010) (for more details we also refer to chapter 3). Figure 4.1 shows the time evolution of the distance r from the center of the PNS (top panel), temperature T (middle panel), and matter density ρ (bottom panel) for these mass-shell trajectories as functions of t_{pb}. The outflow evolution of 7 of the 98 trajectories, corresponding to initial times $t_0 = 0.5, 1, 2, 2.9, 4.5, 6.5, 7.5$ s (t_0 being measured when the temperature $T_0 = 9$ GK), is highlighted with different colors. We adopt these seven trajectories as representative of the cooling evolution of the PNS to discuss the impact of neutrino oscillations (with and without an additional light sterile neutrino) on the nucleosynthesis in the ν-driven wind. The total ejecta mass of the 98 mass-shell trajectories is $M_{98} = 1.1 \times 10^{-2} M_{\odot}$.

We perform our network calculations in the same way as already described in Sect. 3.2 in chapter 3. Furthermore, we refer to Sect. 3.3 in chapter 3 for a detailed discussion of the electron fraction evolution in the ν-driven wind. In the following, we will compute Y_e as described in Sect. 3.3, but without making any assumption about the spectral shape factors of neutrinos and antineutrinos, unless otherwise specified. The spectra which we use will be described in Sect. 4.4.

In Table 4.1, we list the Y_e values at the neutrinosphere radius R_ν for the selected seven postbounce times t_0, as obtained from the numerical simulation of Model Sf 21 of Hüdepohl et al. (2010). Notice the partial overlap of Table 4.1 and Table 3.1. Since we aim to discuss the role of neutrino oscillations and of the so-called "α-effect" (see chapter 3) on the electron fraction and on the nucleosynthesis in the ν-driven wind, we distinguish two cases with different X_α in what follows:

  (i) We compute X_α using the full network (labelled "incl. α-effect");

  (ii) We keep X_α constant at its value at $T = 9$ GK as given by Model Sf 21.

Since a proper inclusion of the α-effect always requires detailed network calculations as in our case (i), we consider case (ii), i.e. X_α constant for $T < 9$ G, for isolating the effect of the formation of α particles on Y_e, as we will elucidate in Sect. 4.6.

---

[2]All neutrino flavor oscillation calculations are done by Irene Tamborra. She gave me the neutrino oscillated spectra, which I then used as input to perform nucleosynthesis calculations.
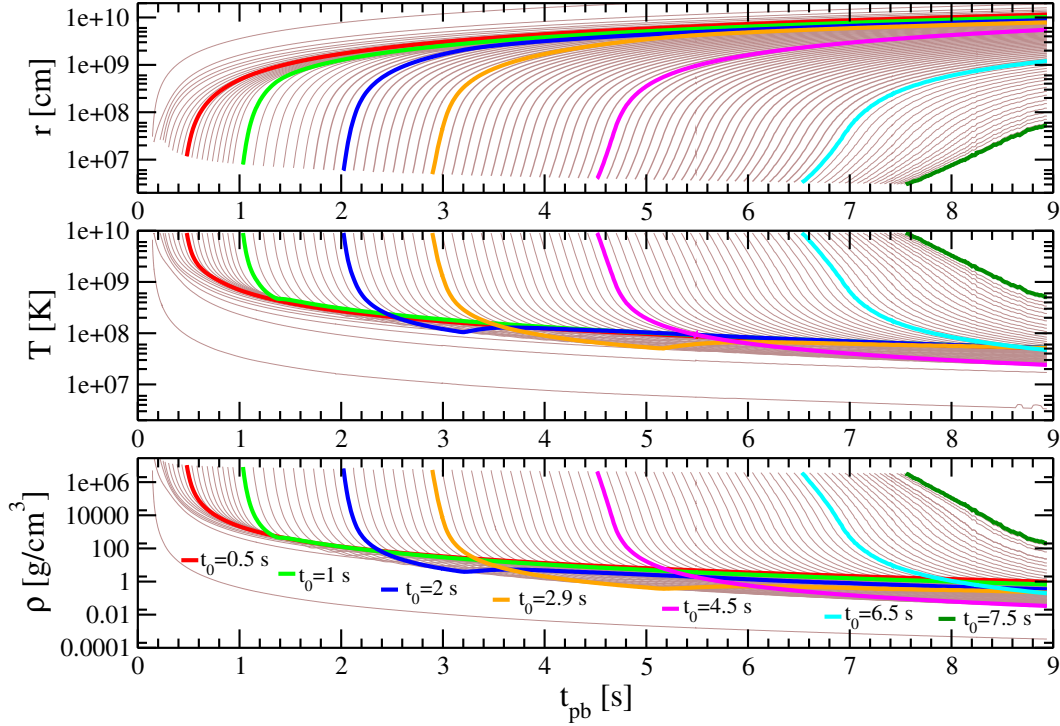
Figure 4.1 Mass-shell trajectories of the neutrino-driven wind as functions of postbounce time (t_{pb}): Radial distance from the PNS center (top), temperature (middle), and density (bottom) along the ejecta trajectories. The colored curves correspond to the selected 7 trajectories representative of the evolution of the ν-driven wind for initial times, $t_0 = 0.5, 1, 2, 2.9, 4.5, 6.5, 7.5$ s. The kinks visible in the temperature and density evolution of the trajectories for $t_0 = 2$ s and 2.9 s indicate the existence of a weak reverse shock.

4.3 Nucleosynthesis yields without neutrino oscillations

In this section, we discuss as our fiducial case the results of nucleosynthesis in the ν-driven wind ejecta of an 8.8 $M_\odot$ ECSN without taking into account neutrino oscillations (but including the α-effect). Note that nucleosynthesis computations were done in previous papers adopting semi-analytically (Wanajo et al. 2001; Wanajo 2006) or hydrodynamically (Fröhlich et al. 2006a; Takahashi et al. 1994; Pruet et al. 2006; Arcones & Montes 2011) computed neutrino-driven winds. With the exception of investigations by Meyer et al. (1992) and Woosley et al. (1994), who used the now outdated model of J. Wilson, however, the other existing calculations were based on a number of simplifications or considered only constrained periods of evolution (like Pruet et al. 2006). In this sense, our study is the first one in which the wind nucleosynthesis is explored in a self-consistently exploded progenitor, whose evolution was continuously followed from collapse to beyond the explosion through the complete subsequent proto-neutron star cooling phase. Nevertheless, the results should not be taken as firm nucleosynthetic prediction to be used for galactic chemical evolution studies because of the absence of dense-medium nucleon potential effects in the charged-current neutrino reactions of the hydrodynamic simulation. The inclusion of these nucleon-potential effects will cause nuclear equation-of-state dependent modifications of the neutrino emission and therefore of the Y_e evolution in the ν-driven wind (e.g Martínez-Pinedo et al. 2012; Roberts 2012; Roberts et al. 2012), whose investigation is beyond

Table 4.1. Neutrinospheric parameters and electron fractions Y_e as functions of postbounce time t_0.

t_0[a] [s]	R_ν[b] [10^5 cm]	Y_e[c]	$Y_{e,a}$[d]	$\Delta\overline{M}_j$[e] [10^{-3} M$_\odot$]	L_{ν_e}[f] [10^{51}erg/s]	$L_{\bar\nu_e}$[g] [10^{51}erg/s]	L_{ν_x}[h] [10^{51}erg/s]	$\langle E_{\nu_e}\rangle$[i] [MeV]	$\langle E_{\bar\nu_e}\rangle$[j] [MeV]	$\langle E_{\nu_x}\rangle$[k] [MeV]	α_{ν_e}[l]	$\alpha_{\bar\nu_e}$[m]	α_{ν_x}[n]
0.5	25.0	0.0547	0.554	9.640	9.5	10.10	10.80	16.8	18.1	18.3	2.9	3.0	2.8
1.0	20.5	0.0522	0.546	0.770	7.3	8.30	7.90	15.9	17.4	17.3	3.0	2.9	2.6
2.0	17.5	0.0445	0.564	0.380	4.7	4.90	5.30	15.3	16.5	16.1	3.2	2.7	2.3
2.9	16.0	0.0323	0.566	0.110	3.3	3.40	3.70	15.8	16.3	15.7	3.1	2.3	2.5
4.5	15.2	0.0268	0.574	0.060	1.9	1.90	2.00	13.8	13.4	12.9	3.0	2.3	2.1
6.5	14.5	0.0233	0.555	0.020	1.0	0.99	1.04	12.4	11.9	11.8	2.6	2.3	2.4
7.5	14.5	0.0223	0.549	0.002	0.6	0.60	0.60	9.9	9.6	9.5	2.4	2.3	2.5

[a]Postbounce time.

[b]Neutrinosphere radius.

[c]Electron fraction at R_ν.

[d]Asymptotic electron fraction (at $r = 3 \cdot 10^7$ cm).

[e]$\Delta\overline{M}$: ejecta mass of the 7 representative wind trajectories.

[f,g,h]Luminosities of ν_e, $\bar\nu_e$ and ν_x, respectively.

[i,j,k]Mean energies of ν_e, $\bar\nu_e$ and ν_x, respectively.

[l,m,n]Spectral fitting parameters of ν_e, $\bar\nu_e$ and ν_x, respectively (see Sect. 4.4).

the present work. Including 98 trajectories, X_A is given by

$$X_A = \frac{1}{M_{\text{tot}}} \sum_{i=1}^{98} X_{i,A}\, \Delta M_i \,, \tag{4.1}$$

where $X_{i,A}$ and ΔM_i are the mass fractions and the ejecta-shell masses respectively, while M_{tot} is the total mass of the ejecta, which we consider to be the sum of the ejected mass from the core plus the outer H/He-envelope (assumed to contain no heavy elements):

$$M_{\text{tot}} = (8.8\ M_\odot - 1.366\ M_\odot) + 0.0114\ M_\odot \simeq 7.44\ M_\odot \,.$$

Here $1.366\ M_\odot$ defines the initial mass cut between neutron star and ejecta and $M_{98} = 0.0114\ M_\odot$. In order to discuss the impact of neutrino oscillations[3] in the following sections, we replace the full set of 98 trajectories by 7 "representative" ν-driven wind trajectories (Fig. 4.1).

For the 7 representative wind trajectories, we define combined mass elements, $\Delta\overline{M}_j$ ($j = 1, ..., 7$), in such a way that $\Delta\overline{M}_j = \sum_{i=i_{j-1}+1}^{i_j} \Delta M_i$, where the summation includes all mass shells ejected between the representative shell i_{j-1} and the representative shell i_j (see Table 4.1). The first representative shell, for example, includes all the 10 trajectories of the full set which are ejected before $t_0 = 0.5$ s. Thus, for the 7 representative trajectories, we define

$$\overline{X}_A = \frac{1}{M_{\text{tot}}} \sum_{j=1}^{7} X_{j,A}\, \Delta\overline{M}_j \,, \tag{4.2}$$

with X_j being the mass fractions for the j-th trajectory.

[3]We assume that the ν_e and $\bar\nu_e$ luminosities and energy spectra do not change for $r \geq R_\nu$. This means that we do not only ignore small evolutionary changes due to remaining neutrino interactions in the external medium but we also disregard
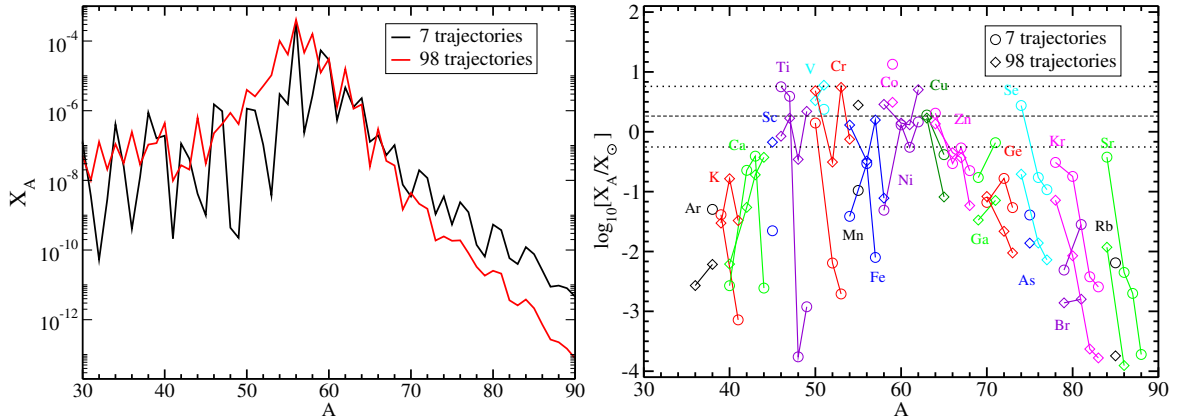
Figure 4.2 *Left:* Mass fractions X_A of the ejecta as a function of mass number A comparing the cases for 7 representative trajectories and for all the 98 trajectories. *Right:* Comparison of the isotopic ejecta mass fractions (X_A) relative to the solar ones ($X_\odot$). The horizontal upper dotted line passes through the most overproduced isotopes (^{51}V, ^{53}Cr, and ^{62}Ni) in the 98 trajectory case, and the horizontal lower dotted line lies a factor of ten below the level of the upper line. The dashed line represents the median value. Our 7 selected trajectories reproduce the case with the 98 trajectories satisfactorily well only for certain values of A (e.g. $58 \le A \le 69$).

Figure 4.2 shows the nucleosynthesis mass fractions, without taking into account neutrino oscillations, for the 98 trajectories and for the 7 trajectories after mass integration over the ejecta mass-shell range as given by Eqs. (4.1) and (4.2), respectively. In the left panel, the mass fractions X_A obtained for all of the 98 available ν-driven wind trajectories are compared to the ones obtained for the 7 selected trajectories. The right panel of Fig. 4.2 shows the isotopic mass fractions X_A relative to the solar ones $X_\odot$ (Lodders 2003, i.e. the production factors) for the 98 available ν-driven wind trajectories and for the 7 representative ones as functions of A. The dotted horizontal lines represent a "normalization band." The isotopes which fall into this band are considered to be the main nucleosynthetic products from the neutrino-driven wind phase of our fiducial ECSN model that could contribute to galactic chemical evolution. The upper dotted line passes through the most overproduced elements (^{51}V, ^{53}Cr, and ^{62}Ni), and the lower dotted line lies a factor of ten below that. The middle dashed line represents the median value.

We find that the nucleosynthesis yields of the 7 trajectories reproduce those obtained from all the 98 trajectories only very approximately because of the coarse time resolution of the wind history. Nevertheless, this will be qualitatively sufficient to discuss the effects of neutrino oscillations on the nucleosynthesis conditions. The right panel of Fig. 4.2 shows little production of isotopes with $A > 65$ in the 98 trajectory case as well as in the 7 trajectory case. This is a consequence of a weak νp-process[4] in this supernova environment because of the absence of a dense outer stellar envelope in ECSNe, which is crucial for an efficient νp-process (Wanajo et al. 2011). Many of the iron-group and light trans-iron isotopes still lie on the normalization band, but the greatest production factors (for ^{51}V, ^{53}Cr, and ^{62}Ni in the 98 trajectory case) are below 10. For example, the production factor of ^{62}Ni is several times smaller than the corresponding one in the early ($\lesssim 400$ ms) convective ejecta,

---

general relativistic redshift corrections, which depend on r, and which are included in the hydrodynamic simulations.

[4]In Table 4.1, we show the asymptotic values (indicated by subscript "a") of the electron fraction $Y_{e,a}$ for our 7 representative trajectories. Notice that since $Y_{e,a} > 0.5$ for all the considered cases, the νp-process may be enabled.

which are absent in 1D but found in the 2D counterpart of the ECSN explosion model (Wanajo et al. 2011, 2013a). It appears, therefore, that the nucleosynthetic contribution of the ν-driven wind to the Galactic chemical evolution is unimportant. It should be noted, however, that the effects of nucleon potential corrections might alter the Y_e history; thus the wind contribution could be more important for nucleosynthesis than found here.

4.4 Reference neutrino signal and flavor evolution equations

At radius $r > R_\nu$, the unoscillated spectral number fluxes for each flavor ν ($\nu = \nu_e, \bar{\nu}_e, \nu_x, \bar{\nu}_x$ with $x = \mu$ or τ) can be approximated by

$$F_\nu(E) \approx \frac{L_\nu}{4\pi r^2} \frac{f_\nu(E)}{\langle E_\nu \rangle} , \tag{4.3}$$

where L_ν is the luminosity for the flavor ν and $\langle E_\nu \rangle$ the mean spectral energy[5]. The neutrino spectrum $f_\nu(E)$ is well reproduced by a combined power-law and exponential fit (Keil et al. 2003; Tamborra et al. 2012a):

$$f_\nu(E) = \xi_\nu \left(\frac{E}{\langle E_\nu \rangle} \right)^{\alpha_\nu} e^{-(\alpha_\nu+1)E/\langle E_\nu \rangle} , \tag{4.4}$$

being the parameter α_ν defined by $\langle E_\nu^2 \rangle / \langle E_\nu \rangle^2 = (2 + \alpha_\nu)/(1 + \alpha_\nu)$ and ξ_ν a normalization factor such that $\int f_\nu(E)\, dE = 1$.

In order to incorporate neutrino oscillations in our nucleosynthesis computations, we consider the 7 selected postbounce times t_0 as representative of the changing wind conditions during the proto-neutron star cooling phase (note the partial overlap with data from the simulation by Hüdepohl et al. 2010 used for the analysis in Tamborra et al. 2012b). In Table 4.1 we list the neutrinosphere radius R_ν (assumed to be equal for all flavors), the luminosity L_ν, the mean energy $\langle E_\nu \rangle$, and the fit exponent α_ν for each neutrino flavor and for the seven representative wind trajectories.

In what follows, we neglect oscillations driven by the smallest mass difference between the active flavors, $\delta m_{\rm sol}$, and focus on neutrino oscillations in the active sector driven by the largest mass difference between ν_e and ν_x, $\delta m_{\rm atm}$, and by the mixing angle θ_{13}. The reduction to two effective active flavors is justified, since oscillations driven by the solar parameters tend to take place at a radius larger than the one at which oscillations driven by $\delta m_{\rm atm}^2$ occur. Flavor oscillations driven by the solar parameters are, therefore, unlikely to affect SN nucleosynthesis (see Dasgupta & Dighe 2008; Fogli et al. 2009a; Dasgupta et al. 2010 for details). Concerning active-sterile oscillations, we assume the mixing only of the electron neutrino flavor with a light sterile state for simplicity. Overall, we discuss a 2-flavor scenario (2 active flavors, ν_e and ν_x) as well as a 3-flavor one (2 active+1 sterile flavors, ν_e, ν_x and ν_s).

If interpreted in terms of sterile neutrinos ν_s, the reactor antineutrino anomaly requires a mass difference in the eV range, and cosmological hot dark matter limits imply that the sterile state would have to be heavier than the active flavors (Abazajian et al. 2012). We here adopt the following mass splittings (Capozzi et al. 2013; Mention et al. 2011):

$$\delta m_{\rm atm}^2 = -2.35 \times 10^{-3} \text{ eV}^2 \text{ and } \delta m_{\rm s}^2 = 2.35 \text{ eV}^2 , \tag{4.5}$$

---

[5]In Eq. (4.3), general relativistic redshift corrections, which depend on r, as well as a "flux factor" accounting for nonradial neutrino momenta close to the neutrinosphere, are ignored.

with δm^2_{atm} being the squared mass difference between the neutrino mass eigenstates ν_3 and the remaining two $\nu_{1,2}$ (Fogli et al. 2006) and δm^2_s the squared mass difference between the neutrino mass eigenstate ν_4 and ν_1, chosen to be representative of reactor-inspired values. We assume normal hierarchy for the sterile mass-squared difference, namely $\delta m^2_s > 0$ (i.e., the neutrino mass eigenstate ν_4 is heavier than the other mass eigenstates associated to the active neutrino flavors) and inverted mass hierarchy for the atmospheric difference, $\delta m^2_{\text{atm}} < 0$ (meaning that the neutrino mass eigenstate ν_3 is lighter than $\nu_{1,2}$, see Fogli et al. 2006). Note that current global fits of short-baseline neutrino experiments estimate $0.82 \leq \delta m^2_s \leq 2.19$ eV^2 at 3σ of confidence level (Giunti et al. 2013), which is lower than our adopted reference value (Mention et al. 2011). Our conservative choice favors a comparison with previous results discussed in Tamborra et al. (2012b) besides not qualitatively changing our conclusions. We choose to scan only the inverted hierarchy scenario in the active sector (i.e., $\delta m^2_{\text{atm}} < 0$), since this is the case where the largest impact due to collective flavor oscillations on nucleosynthesis is expected (Hannestad et al. 2006; Fogli et al. 2007, 2008; Dasgupta et al. 2010). The associated "high" (H) and "sterile" (S) vacuum oscillation frequencies are then

$$\omega_{\text{H}} = \frac{\delta m^2_{\text{atm}}}{2E} \ \text{ and } \ \omega_{\text{S}} = \frac{\delta m^2_s}{2E} \,, \tag{4.6}$$

with E being the neutrino energy. For the mixing angles we use (Capozzi et al. 2013; Mention et al. 2011)

$$\sin^2 2\theta_{14} = 10^{-1} \ \text{ and } \ \sin^2 \theta_{13} = 2 \times 10^{-2} \,. \tag{4.7}$$

We treat neutrino oscillations in terms of matrices of neutrino densities ρ_E for each energy mode E. The diagonal elements of the density matrices are related to the neutrino densities, while the off-diagonal ones encode phase information. The radial flavor evolution of the neutrino flux is given by the "Schrödinger equations,"

$$i\partial_r \rho_E = [\mathsf{H}_E, \rho_E] \ \text{ and } \ i\partial_r \bar{\rho}_E = [\bar{\mathsf{H}}_E, \bar{\rho}_E] \,, \tag{4.8}$$

where an overbar refers to antineutrinos and sans-serif letters denote 3×3 matrices in the (ν_e, ν_x, ν_s) flavor space. The initial conditions for the density matrices are $\rho_E = \text{diag}(n_{\nu_e}, n_{\nu_x}, 0)$ and $\bar{\rho}_E = \text{diag}(n_{\bar{\nu}_e}, n_{\bar{\nu}_x}, 0)$, i.e., we assume that sterile neutrinos are generated by flavor oscillations. The Hamiltonian matrix consists of the vacuum, matter and neutrino self-interaction terms:

$$\mathsf{H}_E = \mathsf{H}^{\text{vac}}_E + \mathsf{H}^{\text{m}}_E + \mathsf{H}^{\nu\nu}_E \,. \tag{4.9}$$

In the flavor basis, the vacuum term,

$$\mathsf{H}^{\text{vac}}_E = \mathsf{U} \,\text{diag}\!\left(-\frac{\omega_{\text{H}}}{2}, +\frac{\omega_{\text{H}}}{2}, \omega_{\text{S}}\right) \mathsf{U}^\dagger \,, \tag{4.10}$$

is a function of the mass-squared differences (with U being the unitary matrix transforming between the mass and the interaction basis) and of the mixing angles. The matter term spanned by (ν_e, ν_x, ν_s) is in the flavor basis

$$\mathsf{H}^{\text{m}} = \sqrt{2} G_{\text{F}} \,\text{diag}(N_e - \frac{N_n}{2}, -\frac{N_n}{2}, 0) \,, \tag{4.11}$$

with N_e the net electron number density and N_n the neutron density. Using Eq. (1), the matter term becomes

$$\mathsf{H}^{\text{m}} = \sqrt{2} G_{\text{F}} N_b \,\text{diag}\!\left(\frac{3}{2}Y_e - \frac{1}{2}, \frac{1}{2}Y_e - \frac{1}{2}, 0\right) \,, \tag{4.12}$$

being N_b the baryon density. Note that the matter potential can be positive or negative and for $Y_e > 1/3$ ($Y_e < 1/3$) a ν_e-ν_s ($\bar{\nu}_e$-$\bar{\nu}_s$) MSW resonance can occur (Mikheyev & Smirnov 1985; Nunokawa et al. 1997; McLaughlin et al. 1999; Fetter 2000). Because of Eq. (4.12), neutrinos feel a different matter potential as Y_e changes and, at the same time, Y_e is affected by neutrino oscillations via Eq. (3.4).

The $H^{\nu\nu}$ term describes ν-ν interactions and vanishes for all elements involving sterile neutrinos (Sigl & Raffelt 1993), i.e. $H^{\nu\nu}_{es} = H^{\nu\nu}_{xs} = H^{\nu\nu}_{ss} = 0$ (i.e., the only non-vanishing off-diagonal element of the 3×3 matrix is $H^{\nu\nu}_{ex}$). In the treatment of ν-ν interactions, we assume the so-called "single-angle approximation" for the sake of simplicity, i.e. we assume that all neutrinos feel the same average neutrino-neutrino refractive effect (Duan et al. 2006; Fogli et al. 2007; Duan et al. 2010). We will discuss in the following the limits of such approximation.

In what follows, we explore the impact of active-active and active-sterile neutrino conversions on the nucleosynthesis conditions and nucleosynthetic yields for the 7 representative trajectories corresponding to postbounce times t_0. We distinguish two scenarios:

1. "Active" case, referring to neutrino oscillations in the active sector (2 active states).

2. "Sterile" case, meaning neutrino oscillations in the active and sterile sectors (2 active states + 1 sterile state).

The coupled equations of the neutrino flavor evolution (Eqs. 4.8) were discretized in the energy range 1–60 MeV and solved by numerical integration together with Eq. (3.4) at each selected t_0 [6]. The initial conditions for the electron fraction and the neutrino spectral properties were assumed as given in Table 4.1.

4.5 Neutrino oscillations in the neutrino-driven wind and feedback on the electron fraction

In this section, we discuss the neutrino flavor oscillation physics during the neutrino-driven wind phase and the oscillation feedback on Y_e for scenarios 1 and 2 (see Sect. 4.4). After qualitatively describing the oscillation phenomenology, we will discuss in detail how the neutrino fluxes are affected by flavor oscillations at three representative times $t_0 = 0.5, 2.9$ and 6.5 s, representing the early, intermediate and late cooling phases, respectively. We will focus on the impact of flavor oscillations on Y_e, neglecting the α-effect for sake of simplicity (i.e., X_α is assumed to be as in case (ii) in Sect. 4.2); The role of the α-effect on the electron fraction and its interplay with neutrino oscillations will be described in Sect. 4.6.

4.5.1 Neutrino oscillation phenomenology

In the presence of only active neutrinos, the MSW resonance due to the atmospheric mass difference occurs at radii much larger than the ones considered here ($r \lesssim 3 \times 10^7$ cm), where Y_e has already

---

[6]Note that, for simplicity, in our computations we consider the effects of energy-dependent features of the oscillated neutrino spectra on the Y_e evolution in an integral sense by adopting neutrino spectral quantities averaged over energy in Eqs. (3.7, 3.8).
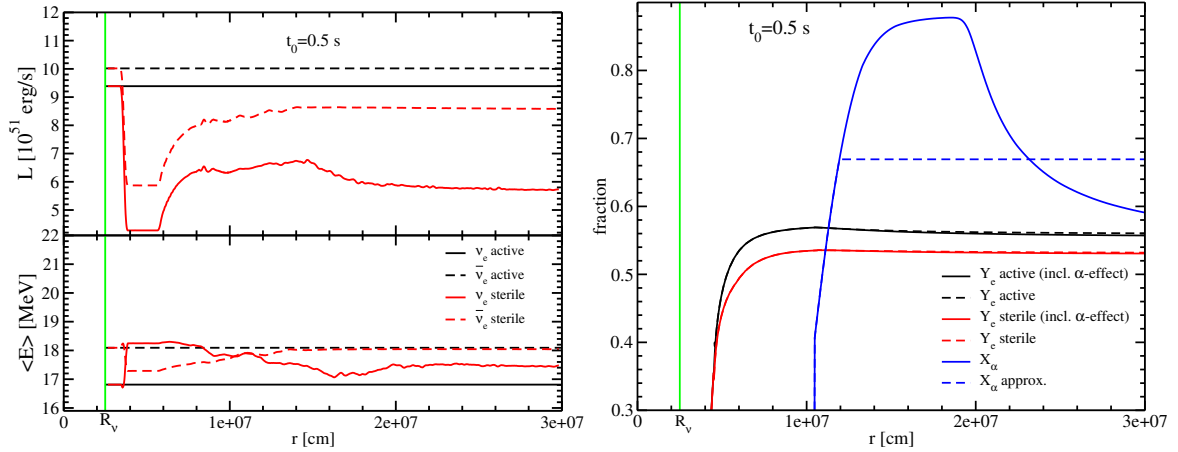
Figure 4.3 *Left:* Electron neutrino and antineutrino luminosities (L_{ν_e} and $L_{\bar{\nu}_e}$) in units of 10^{51} erg/s (upper panel) and mean energies (E_{ν_e} and $E_{\bar{\nu}_e}$, lower panel) as functions of distance (r) from the center of the PNS at $t_0 = 0.5$ s postbounce. (The solid red lines are computed as running averages over $\Delta r \simeq 3.5 \cdot 10^5$ cm.) In the "active" case the luminosities and mean energies of both ν_e and $\bar{\nu}_e$ are constant for $r \geq R_\nu$, which implies that the "active" case does not show any significant variations compared to the case without ν oscillations for the studied ECSN progenitor. In the "sterile" case, the inner active-sterile MSW resonance occurs for ν and $\bar{\nu}$ at $r \simeq 4 \times 10^6$ cm. Visible modifications of the neutrino spectral properties due to neutrino self-interactions occur at 6×10^6 cm, while the outer MSW resonance occurs at about 1.4×10^7 cm. *Right:* Electron fraction Y_e and α mass fraction X_α as functions of distance r from the center of the PNS at $t_0 = 0.5$ s. In the "active" scenario neutrino oscillations negligibly affect Y_e (the same as in the no oscillations case which is not shown here). The solid lines ("incl. α-effect" cases) refer to Y_e obtained when full network calculations are performed (the corresponding X_α is also shown with the solid blue line), while the dashed Y_e lines refer to calculations corresponding to case (ii) in Sect. 4.2 (the corresponding X_α is also shown by a dashed blue line). The vertical line shows the neutrinosphere radius R_ν.

reached its asymptotic value, and therefore the electron fraction is not affected. Because of ν-ν interactions, multiple spectral splits should occur in inverted hierarchy for the initial conditions of neutrinos and antineutrinos of the studied ECSN (i.e., $L_{\nu_e,\bar{\nu}_e}/\langle E_{\nu_e,\bar{\nu}_e}\rangle - L_{\nu_x}/\langle E_{\nu_x}\rangle < 0$, Fogli et al. 2009b). However, since the ν_e and $\bar{\nu}_e$ luminosities and mean energies are very similar to those of the heavy-lepton neutrinos, as shown in Table 1, and because of the total lepton-number conservation, we do not expect any appreciable variations in the oscillated luminosities and mean energies (see Fogli et al. 2009b for an extended discussion).

In the sterile scenario, while active neutrinos propagate away from the SN core, they interact with the matter background and convert to sterile states through MSW resonances in two different spatial regions (see also Appendix A). Close to the neutrinosphere, due to the steep growth of Y_e, and therefore of the matter potential via Eq. (4.12), the inner active-sterile MSW resonance occurs for both neutrinos and antineutrinos at about the same radius (r_{IR}). At larger radii (located closer to the neutrinosphere as the postbounce time increases), an outer active-sterile MSW resonance occurs and it mainly affects neutrinos.

Any modification of the neutrino energy spectra due to oscillations will affect the electron fraction via Eqs. (3.4), (3.5) and (3.6).
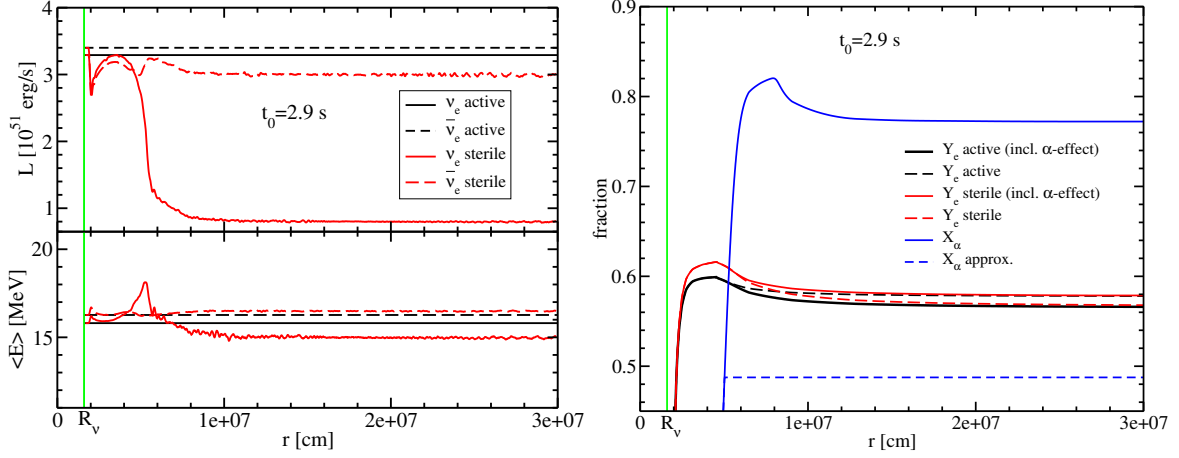
Figure 4.4 Same as Fig. 4.3, but at $t_0 = 2.9$ s. In the "sterile" case, the inner active-sterile MSW resonance occurs for ν and $\bar{\nu}$ at $r \simeq 2 \times 10^6$ cm triggering neutrino self-interactions. The outer MSW resonance occurs at about 5×10^6 cm. (The solid red lines are computed as running averages over $\Delta r \simeq 2.9 \cdot 10^5$ cm.)

At early postbounce times, the matter potential felt by neutrinos close to r_{IR} is slightly less steep than the one felt by antineutrinos (see Appendix A and left panel of Fig. 4.6), therefore the adiabaticity of the $\bar{\nu}$ conversions is slightly decreased and the one of ν slightly increased with a net conversion probability for neutrinos a bit larger than for antineutrinos, as pointed out by Nunokawa et al. (1997). This is particularly evident during the accretion phase as discussed in Wu et al. (2014) and, for our purposes, during the early-cooling phase ($t_0 = 0.5, 1$ s), where the difference in the conversion probabilities of ν_e and $\bar{\nu}_e$ is responsible for a plateau in the Y_e profile close to r_{IR} (Wu et al. 2014). As the postbounce time increases, the matter potential felt by neutrinos close to r_{IR} becomes steeper (see Fig. 4.6, left panel), and therefore the $\nu_e \rightarrow \nu_s$ and $\bar{\nu}_e \rightarrow \bar{\nu}_s$ resonant conversions are expected to have more or less the same degree of adiabaticity, with a resultant small feedback effect on Y_e (assuming that further flavor conversions due to ν-ν interactions are negligible).

The outer active-sterile MSW resonance is generally more adiabatic than the inner one: It occurs where the matter potential is shallow and the effective mixing angle is larger. Therefore, ν_e are abundantly converted to ν_s, lowering the wind Y_e (via Eqs. 3.4, 3.5, and 3.6).

Besides neutrino interactions with matter, neutrino self-interactions affect the neutrino oscillated fluxes, and therefore Y_e (see Appendix A for more details). As discussed in Tamborra et al. (2012b), $\nu_e \leftrightarrow \nu_x$ conversions, due to neutrino-neutrino interactions, partially repopulate the electron sector depleted by $\nu_e \rightarrow \nu_s$ MSW conversions. The net effect is that ν-ν interactions favor the repopulation of the ν_e sector (because of ν_x-ν_e conversions) and partially counterbalance the effect of ν_e-ν_s MSW resonances on the electron fraction. The role played by neutrino self-interactions becomes more and more evident as the time t_0 increases, since the matter background is lower.

4.5.2 Results: Neutrino oscillation and feedback on the electron fraction

In order to quantitatively describe the impact of oscillations on the Y_e evolution as t_0 increases, we select three representative postbounce times, $t_0 = 0.5$ s, 2.9 s, and 6.5 s, and discuss the oscillation
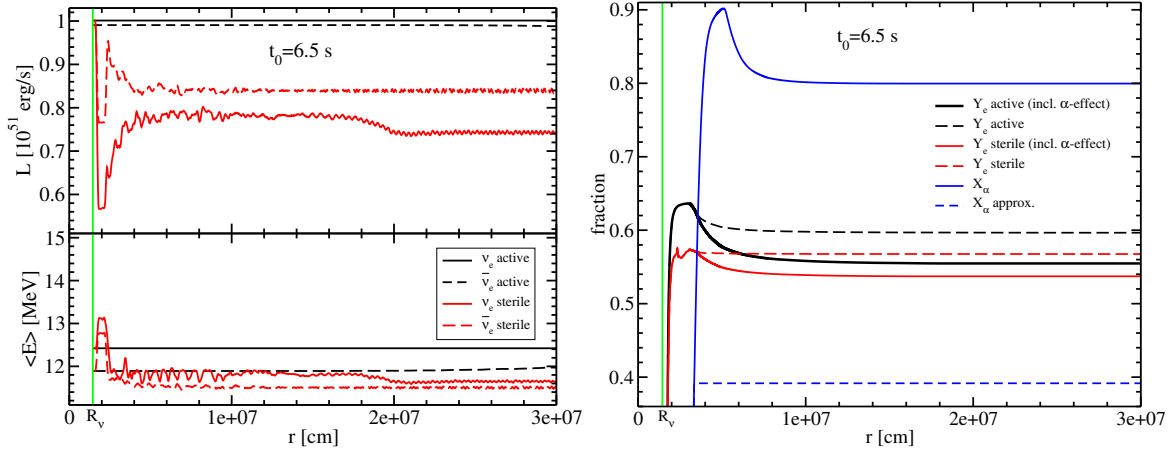
Figure 4.5 *Left:* Same as Fig. 4.3, but at $t_0 = 6.5$ s. In the "sterile" case the inner MSW resonance occurs for ν and $\bar{\nu}$ at $r \simeq 1.8 \times 10^6$ cm, triggering collective oscillations. The outer ν_e-ν_s MSW takes place at $r \simeq 2.5 \times 10^6$ cm. (The red lines display running averages over $\Delta r \simeq 2.1 \cdot 10^5$ cm.)

phenomenology in the active and sterile cases.

Figure 4.3 (left panel) shows the luminosities and mean energies for ν_e and $\bar{\nu}_e$ as functions of radius in the active and sterile cases at $t_0 = 0.5$ s. As expected, in the active case, neutrino oscillations do not visibly modify the mean energies and the luminosities in the radial regime where Y_e is still evolving (i.e., $r \lesssim 2 \times 10^7$ cm). To demonstrate the effect of neutrino oscillations on Y_e, we plot Y_e as a function of the radius at $t_0 = 0.5$ s in Fig. 4.3 (right panel); In the active case, the Y_e evolution does not differ from the case without neutrino oscillations. In the sterile case, instead, the inner active-sterile MSW resonance occurs at $r_{\mathrm{IR}} \simeq 4 \times 10^6$ cm and it is responsible for a $\nu_e \to \nu_s$ conversion probability larger than the $\bar{\nu}_e \to \bar{\nu}_s$ one, as expected (Fig. 4.3, left panel). Such active-sterile flavor conversion modifies the ν_e and $\bar{\nu}_e$ energy spectra, introducing non-zero off-diagonal terms in the neutrino density matrices. Neutrino self-interactions are therefore triggered at about 6×10^6 cm. The outer active-sterile MSW resonance occurs at $r_{\mathrm{OR}} \simeq 1.4 \times 10^7$ cm, converting ν_e to ν_s. The corresponding electron fraction (Fig. 4.3, right panel) remains lower than in the active case due to active-sterile flavor conversions.

Figure 4.4, analogously to Fig. 4.3, shows the luminosities and mean energies for ν_e and $\bar{\nu}_e$ as functions of radius at $t_0 = 2.9$ s (left panel) and the corresponding electron fraction (right panel). In the active case, neutrino oscillations do not visibly modify the neutrino spectral properties in the radial regime where Y_e is still evolving, as already discussed at $t_0 = 0.5$ s. In the sterile case, the inner active-sterile MSW resonance occurs at $r_{\mathrm{IR}} \simeq 2 \times 10^6$ cm. As discussed in Appendix A, the instability induced by the inner MSW resonance and the fact that the matter potential is lower than at earlier postbounce times trigger neutrino self-interactions converting slightly more $\bar{\nu}_e$ than ν_e, contrarily to what is expected. The outer active-sterile MSW resonance occurs at about $r_{OR} \simeq 5 \times 10^6$ cm converting a large number of ν_e to ν_s. Correspondingly, the Y_e profile (Fig. 4.4, right panel) is higher than the active one close to the neutrinosphere (because more $\bar{\nu}_e$ are converted to sterile states than ν_e). The depletion of the ν_e flux due to the outer MSW resonance is responsible for lowering the electron fraction below the active one (compare the black dashed line to the red dashed line).

Figure 4.5 shows the radial evolution of the ν_e and $\bar{\nu}_e$ spectral properties and the corresponding Y_e profile at $t_0 = 6.5$ s. In this case as well, active neutrino oscillations do not change the values of the

luminosities and mean energies, and therefore Y_e does not change compared to the case without oscillations. In the sterile case, instead, the inner MSW resonance already occurs at $r \simeq 1.8 \times 10^6$ cm for ν and $\bar{\nu}$, triggering at the same time neutrino collective oscillations, while the outer MSW resonance takes place at $r_{OR} \simeq 2.5 \times 10^6$ cm, (see Appendix A for more details). The MSW resonances together with ν-ν interactions significantly reduce the ν_e number flux (i.e. $L_{\nu_e}/\langle E_{\nu_e}\rangle$) compared to the $\bar{\nu}_e$ number flux. This means that a more neutron-rich environment (i.e., a lower Y_e) is favored compared to the active case (see Fig. 4.5, right panel).

4.6 Interplay of neutrino oscillations and α-effect on the electron fraction

In this section, we discuss the evolution of Y_e as a function of radius at our selected postbounce times ($t_0 = 0.5$ s, 1 s, 2 s, 2.9 s, 4.5 s, 6.5 s, and 7.5 s), for the scenarios 1 and 2 described in Sect. 4.4, and with the two different assumptions made in Sect. 4.2 about the evolution of the mass fraction of α particles. These assumptions allow us to disentangle between the role played by neutrino oscillations and α-effect in determining Y_e.

The evolution of the electron fraction is not just influenced by the ν_e and $\bar{\nu}_e$ properties, which are affected by neutrino oscillations, as discussed in the previous section, but also by the presence of α particles (see Eqs. 3.4). Therefore, the whole Y_e evolution is a complicated interplay between neutrino oscillations and α-effect associated with the formation of α particles and the outcome depends on the location of the region of active-sterile conversions relative to that of α particle formation. For this reason, we choose to analyze the evolution of Y_e in detail at three representative postbounce times, $t_0 = 0.5$ s, 2.9 s, and 6.5 s.

In Fig. 4.3 (right), we show the evolution of Y_e at $t_0 = 0.5$ s, in the active and sterile cases and with ("incl. α-effect" case) or without the inclusion of α-effect. In this case, the formation of α particles doesn't play any significant role in determining Y_e, because the formation of α particles (solid blue line) occurs when Y_e has almost reached its asymptotic value (compare the solid and dashed lines). At intermediate and late postbounce times, the results of simulations with and without α particle formation from free nucleons have to be distinguished, because the α-effect associated with the presence of large abundances of α particles has severe consequences for the Y_e evolution. In Fig. 4.4 (right), we show the evolution of Y_e at $t_0 = 2.9$ s, analogously to Fig. 4.3 (right). In this case, the formation of α particles occurs when Y_e is still evolving and it overlaps with the region where the outer MSW resonance, which converts ν_e to ν_s, takes place (see Fig. 4.4, left).

The results with α-effect (solid red and black lines in Fig. 4.4, right) show a counterintuitive behavior. While for active flavor oscillations the α-effect drives Y_e closer to 0.5 in the usual way (compare the black dashed and solid lines in Fig. 4.4, right), the sterile neutrino case exhibits the opposite behavior: In the presence of a higher abundance of α-particles, i.e. despite the α-effect, Y_e remains higher and the evolution towards $Y_e = 0.5$ is clearly damped (red solid line in comparison to red dashed line). The formation of a larger abundance of α particles thus obviously reduces the influence of the active-sterile ν_e-ν_s conversions on Y_e. This astonishing result is a consequence of the fact that the conversion to sterile neutrinos occurs slightly outside (or overlaps with) the region where the rapid recombination of neutrons and protons to α particles takes place. In such a situation the influence of the ν_e-ν_s conversion on the Y_e evolution is diminished by the lower number fractions of free neutrons and protons, which
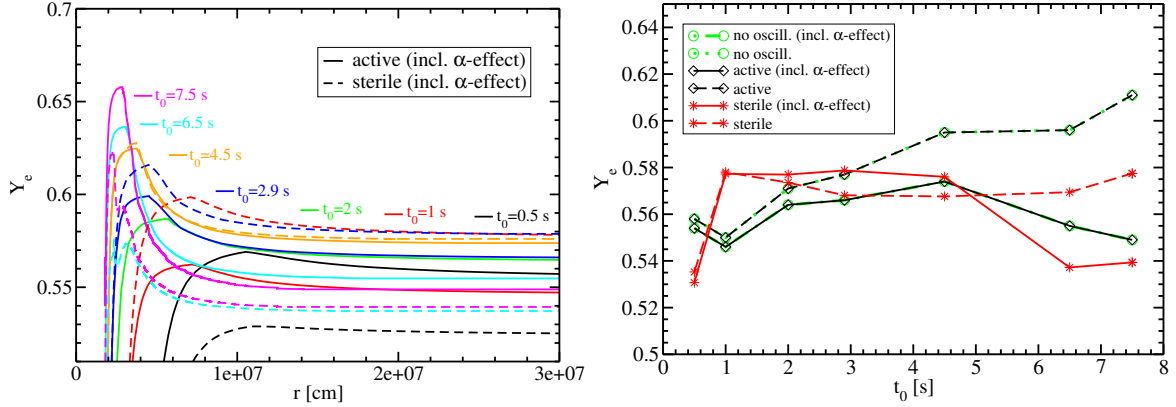
Figure 4.6 *Left:* Electron fraction (Y_e) as a function of distance r from the center of the PNS for all considered postbounce times (t_0), and in the active and sterile cases. The α-effect is included in all cases ("incl. α-effect"). Because of the near equality of the neutrino luminosities and mean energies of neutrinos of all flavors, Y_e in the active cases does not appreciably differ from the one obtained without neutrino oscillations. *Right:* Asymptotic electron fractions (Y_e) as functions of postbounce time (t_0) in the active and sterile as well as no oscillations cases. The dashed lines refer to Y_e calculated without the α-effect, while the solid lines refer to Y_e calculated with the full network. The α-effect is stronger especially at late times ($t_0 = 6.5$ and 7.5 s) when the neutron star is more compact and the neutrino luminosities are lower. The values in the cases without oscillations coincide with those in the active cases and cannot be distinguished.

lead to a lower rate of change of Y_e according to Eq. (3.4). Instead of undergoing reactions with ν_e or $\bar{\nu}_e$, the majority of free nucleons react to form α particles as we wind expands away from the ν_e-ν_s conversion radius.

The influence of α particle formation manifests itself differently in the late wind evolution, where ν_e conversions to sterile neutrinos take place closer to the neutrinosphere and, in particular, at a radius which is smaller than the one at which nucleon recombination begins to raise the α abundance.

In Fig. 4.5 (right), we display the evolution of the electron fraction Y_e at $t_0 = 6.5$ s, in the active and sterile cases, in analogy to Fig. 4.4 (right).

In the sterile case, Y_e is lower than in the active case already very close to the neutrinosphere where the matter is still in NSE (and thus no α particles are present). The dashed lines are again calculated without the $\alpha-$effect, while the solid lines include the α-effect.

When the $\alpha-$effect is included, the value of Y_e is, as expected, pushed towards 0.5 in both active (black solid line) and sterile cases (red solid line). We notice that at $t_0 = 6.5$ s, differently from $t_0 = 2.9$ s, neutrino oscillations, in particular both the inner and outer MSW resonances, take place *before* α particles start forming, and therefore they make the environment significantly less proton-rich (Y_e is lowered) before the $\alpha-$effect takes place and decreases Y_e even further towards more symmetric conditions ($Y_e = 0.5$) in the usual way.

Figure 4.6 gives an overview of the interplay between neutrino oscillations and α-effect by showing the evolution of the electron fraction Y_e at all considered postbounce times t_0. Figure 4.6 (left) shows Y_e as a function of the distance r from the center of the PNS at different postbounce times t_0 in both
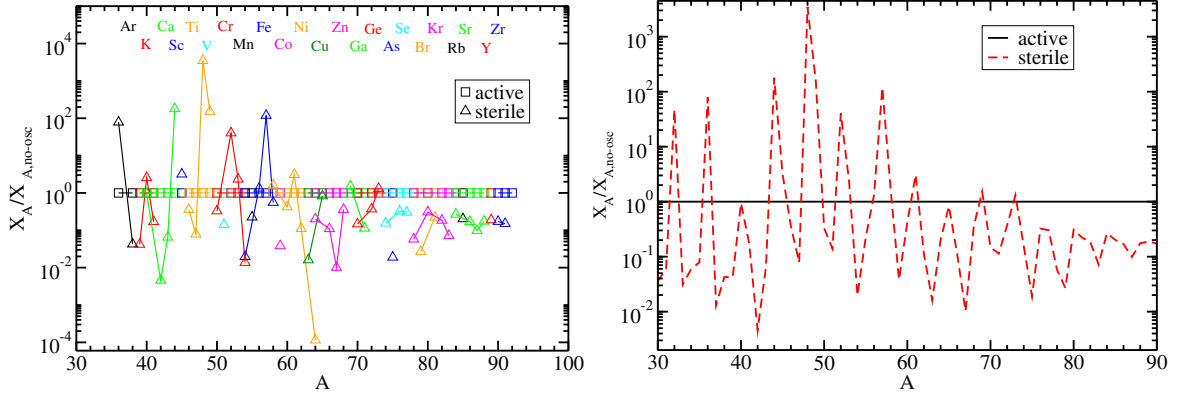
Figure 4.7 *Left:* Isotopic mass fractions in the active and sterile cases relative to those in the case without oscillations versus mass number *A* for all representative 7 trajectories. *Right:* Nucleosynthetic abundances in the active and sterile cases relative to those without oscillations for all the representative 7 trajectories. Since in our model active flavor oscillations do not change the neutrino properties and the wind Y_e at any significant level up to the radius of interest, the nucleosynthesis results are essentially identical for all the cases with active oscillations and no neutrino oscillations.

the active and sterile cases and including the α-effect.

In Fig. 4.6 (right) the asymptotic Y_e values (namely, Y_e at $r \simeq 3 \times 10^7$ cm) are plotted as functions of the postbounce time for each of the considered scenarios (active, sterile and no oscillations cases). Note that the values in the active case cannot be distinguished from those in the no oscillations case, suggesting essentially negligible roles of the active-active oscillations on the evolution of Y_e (see discussion in Sect. 4.5).

Furthermore, in the active case, Y_e is systematically pushed towards 0.5 by α-effect, as we can see by comparing the black dashed line with the black solid one ("incl. α-effect" cases). In the sterile case (red solid line), neutrino oscillations combined with the α-effect lead to Y_e being lower than in the active case (black solid line) at early postbounce times ($t_0 = 0.5$ s), higher than in the active case at intermediate postbounce times ($t_0 = 1$ s, 2 s, and 2.9 s) and again lower than in the active case at late postbounce times ($t_0 = 6.5$ s, and 7.5 s).

In particular, at late times, Y_e in the sterile case and including the α-effect becomes lower than Y_e in the active case and lower than Y_e in the case without full α recombination, because both MSW ν_e-ν_s conversions happens so close to the neutrinosphere that the α particle formation at larger radii further enhances the Y_e-reduction associated with the presence of sterile neutrinos, although Y_e remains always higher than 0.5.

Therefore, the α-effect plays an important role in lowering Y_e especially at late times ($t_0 = 6.5$ s and 7.5 s). This is due to the higher entropy and the longer expansion timescale as a result of the more compact PNS with the lower neutrino luminosities, resulting in a delay of the α recombination relative to both the MSW ν_e-ν_s conversions and to a longer duration of the α-effect (see also next section for more details). However, although the α-effect has a strong impact on Y_e and therefore on the element production, it plays only a sub-leading role for the neutrino oscillations and no detectable modifications are expected for the neutrino fluxes at the Earth (plots not shown here).

Because of the leading role of the α-effect relative to oscillations on Y_e, especially at late times (see
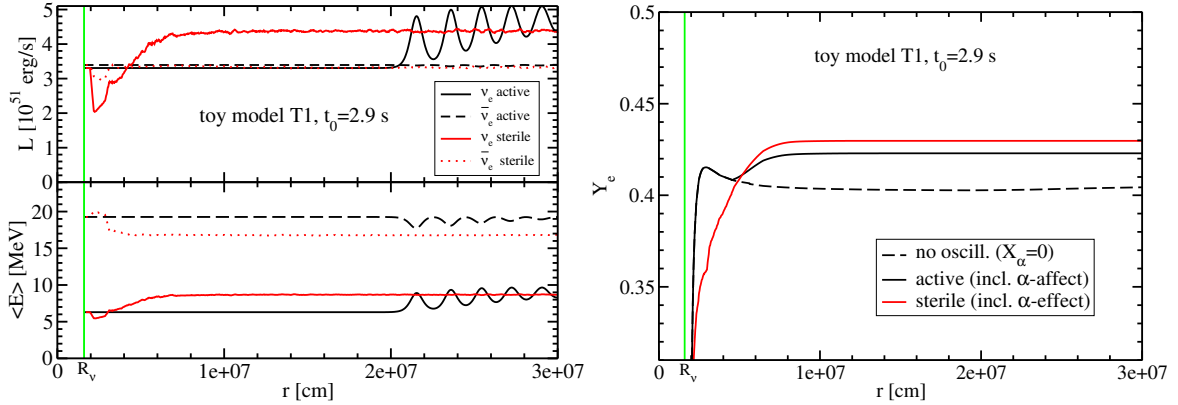
Figure 4.8 *Left:* Electron neutrino and antineutrino luminosities (L_{ν_e} and $L_{\bar{\nu}_e}$ in units of 10^{51} erg/s, upper panel) for toy model 1 (see Table 4.2 and text for details) as functions of distance r from the center of the PNS, at $t_0 = 2.9$ s, in the active and sterile cases. Lower panel: Similar to the upper panel, but for the mean energies $\langle E_{\nu_e} \rangle$ and $\langle E_{\bar{\nu}_e} \rangle$. (The red lines are running averages over $\Delta r \simeq 1.98 \cdot 10^5$ cm.) *Right:* Electron fraction Y_e as function of distance r from the center of the PNS for our toy model at $t_0 = 2.9$ s (see text for details) in the case without neutrino oscillations and setting $X_\alpha = 0$ ("no oscill. ($X_\alpha = 0$)" case, dashed black line), in the case with flavor conversions of active neutrinos (solid black line), and in the case of active-sterile conversions (solid red line). Both of the last two cases were computed with α particle recombination. Neutrino oscillations, jointly with the α-effect, drive Y_e towards 0.5, disfavoring the r-process.

Fig. 4.6, where Y_e in the active and sterile cases including α-effect is fairly similar), we expect that the nucleosynthesis yields in the presence of oscillations are not significantly different from the cases where oscillations are not considered (see Sect. 4.3). This can be seen in Fig. 4.7, where we show the nucleosynthesis yields obtained for the 7 representative trajectories in the active and sterile cases relative to those without neutrino oscillations. In Fig. 4.7 (left) we notice that most of the isotopic mass fraction ratios in the sterile case relative to the no oscillation case are lower than 2, with the exception of some isotopes (with $A < 60$) which have enhanced production factors.

The most abundantly produced isotope in the relative comparison is ^{49}Ti ($X^{49\text{Ti}}_{\text{sterile}}/X^{49\text{Ti}}_{\text{no-oscill.}} \simeq 3.57 \cdot 10^3$). This overproduction of the ^{49}Ti isotope in the sterile case compared to the case without oscillations, however, is still too small to have any significant impact on the production factor of this isotope (see Fig. 4.2, right). From Fig. 4.7, it is also clear that in the sterile case, there is less production of heavy elements (e.g. $A \geq 70$) than in the case without oscillations.

For all the reasons above, from Figs. 4.6 and 4.7 one can conclude that neither active neutrino oscillations nor a fourth sterile neutrino family can alter the nucleosynthesis-relevant conditions, nor can they create a neutron-rich site ($Y_e < 0.5$) to activate the r-process in the adopted ECSN model (without nucleon potential corrections; see Sect. 4.7).

4.7 Neutrino oscillations in a neutron-rich wind

In the previous sections, we considered the neutrino emission properties in the proton-rich environment obtained in the ECSN model of Hüdepohl et al. (2010). As mentioned in Sect. 4.1, however, re-

Table 4.2. Toy model parameters emulating mean-field nucleon potential corrections on the neutrino opacities[a]

Toy mod.	t_0[b] [s]	L_{ν_e}[c] [B/s][p]	$L_{\bar{\nu}_e}$[d] [B/s]	L_{ν_x}[e] [B/s]	$L_{\nu_e}/\langle E_{\nu_e}\rangle$[f] [B/s]	$L_{\bar{\nu}_e}/\langle E_{\bar{\nu}_e}\rangle$[g] [B/s]	$L_{\nu_x}/\langle E_{\nu_x}\rangle$[h] [B/s]	$\langle E_{\nu_e}\rangle$[i] [MeV]	$\langle E_{\bar{\nu}_e}\rangle$[j] [MeV]	$\langle E_{\nu_x}\rangle$[k] [MeV]	$Y_{e,a}$[l]	$Y_{e,a}^{X_\alpha=0}$[m]	$Y_{e,a}^{act}$[n]	$Y_{e,a}^{ste}$[o]
T1	2.9	**3.30**	**3.40**	**3.70**	3.268	1.099	**1.471**	6.3	19.3	**15.7**	0.422	0.403	0.422	0.430
T1	6.5	**1.00**	**0.99**	**1.04**	1.248	0.325	**0.549**	5.0	19.0	**11.8**	0.428	0.368	0.428	0.510
T2	2.9	1.670	2.899	**3.70**	**1.303**	**1.302**	**1.471**	8.0	13.9	**15.7**	0.420	0.405	0.421	0.440
T2	6.5	0.645	1.165	**1.04**	**0.499**	**0.518**	**0.549**	8.0	14.0	**11.8**	0.431	0.380	0.431	0.486
T3	2.9	**3.30**	**3.40**	**3.70**	3.268	1.099	1.196	6.3	19.3	19.3	0.422	0.403	0.422	0.407
T3	6.5	**1.00**	**0.99**	**1.04**	1.248	0.325	0.342	5.0	19.0	19.0	0.428	0.368	0.428	0.465

[a]In the first two cases (T1), we keep the neutrinospheric luminosities of ν_e and $\bar{\nu}_e$ as given by the hydrodynamical simulation, and do not change the luminosity and mean energy of ν_x (see Table 4.1). In the third and fourth cases (T2), we keep the neutrinospheric number fluxes of ν_e and $\bar{\nu}_e$ as given by the hydrodynamical simulation, and do not change the corresponding values of ν_x. In the last two cases (T3), we keep the neutrinospheric luminosities of ν_e, $\bar{\nu}_e$ and ν_x as given by the hydrodynamical simulation, and assume the same neutrinospheric mean energies for $\bar{\nu}_e$ and ν_x. Notice that in all cases we mark in boldface the unchanged hydrodynamical neutrinospheric parameters of ν_e, $\bar{\nu}_e$ and ν_x.

[b]Postbounce time.

[c,d,e]Neutrinospheric luminosities of ν_e, $\bar{\nu}_e$ and ν_x, respectively.

[f,g,h]Neutrinospheric number fluxes of ν_e, $\bar{\nu}_e$ and ν_x, respectively.

[i,j,k]Neutrinospheric mean energies of ν_e, $\bar{\nu}_e$ and ν_x, respectively.

[l]Asymptotic wind electron fraction taking into account the α-effect.

[m]Asymptotic wind electron fraction without taking into account the α-effect ($X_\alpha = 0$).

[n]Asymptotic wind electron fraction taking into account neutrino oscillations in the active sector and α-effect.

[o]Asymptotic wind electron fraction taking into account neutrino oscillations in the active and sterile sectors as well as α-effect.

[p]1 Bethe = 1 B = 10^{51} erg.

cent work suggests that these conditions might be valid only in the early ($t_{\rm pb} \lesssim 1$ s) and late ($t_{\rm pb} \gtrsim 3$ s) wind phases. Including mean-field nucleon potential corrections for charged-current neutrino opacities in the dense medium of the proto-neutron star (Reddy et al. 1998) can cause Y_e of the wind material to become neutron-rich (possibly down to $Y_e \simeq 0.42$–0.45, see e.g. Roberts 2012; Martínez-Pinedo et al. 2012; Roberts et al. 2012) during an intermediate evolution period, although the result is sensitively dependent on the employed nuclear equation of state. To explore the role of neutrino oscillations in such a neutron-rich environment, we construct three toy models to emulate mean-field corrections of the neutrino opacities in their effect on lowering $\langle E_{\nu_e}\rangle$ and increasing $\langle E_{\bar{\nu}_e}\rangle$. Each toy model case will be discussed for an intermediate postbounce time ($t_0 = 2.9$ s) and a late one ($t_0 = 6.5$ s).

4.7.1 Toy model inputs

In all toy models, we artificially prescribe the ν_e and $\bar{\nu}_e$ spectra by fixing the shape factors[7]: $\alpha_{\nu_e} = \alpha_{\bar{\nu}_e} = 4$; The neutrino spectral properties not mentioned in the following are assumed as in Table 1.

In the first toy model (T1), we choose $\langle E_{\nu_e}\rangle$ and $\langle E_{\bar{\nu}_e}\rangle$ in order to obtain an asymptotic electron fraction

---

[7]We assume the shape factors of a moderately degenerate Fermi-Dirac distribution, for which $\langle E_\nu^2\rangle/\langle E_\nu\rangle^2 \simeq 1.2$ (Horowitz & Li 1999).

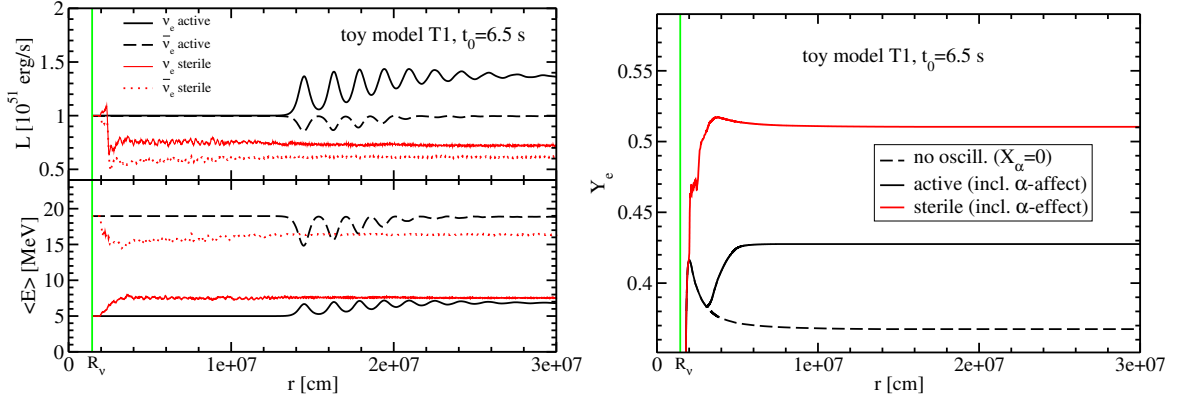Figure 4.9 Same as Fig. 4.8, but for toy model 1 at $t_0 = 6.5$ s (see text for details). (The red lines here are running averages over $\Delta r \simeq 1.1 \cdot 10^5$ cm.)

[8] including the α-effect ($Y_{e,a}$), or neglecting it ($Y_{e,a}^{X_\alpha=0}$), lower than 0.5 (see T1 in Table 4.2). We then adopt the neutrino energy spectra and the electron fraction constructed in this way as initial conditions to study the neutrino flavor evolution and its impact on the wind Y_e. The ν_x and $\bar{\nu}_x$ spectral properties are unchanged (see Tab. 4.1).

Luminosities and mean energies simultaneously affect Y_e. In order to prove the robustness of the T1 results, we consider another test case (toy model 2, T2), keeping the neutrinospheric number fluxes of ν_e and $\bar{\nu}_e$ (i.e., the $L_\nu/\langle E_\nu \rangle$ ratios) fixed as from the hydrodynamic simulation (Hüdepohl et al. 2010) and varying both the luminosities and mean energies of ν_e and $\bar{\nu}_e$ in order to reproduce a neutron-rich environment in the absence of oscillations. The new initial conditions are reported in Table 4.2 (case T2). The third toy model (T3) is similar to T1, except that we assume $\langle E_{\nu_x} \rangle = \langle E_{\bar{\nu}_e} \rangle$ while leaving L_{ν_x} and α_{ν_x} as in Table 4.1, in order to recover the usual hierarchy among the different neutrino flavors.

4.7.2 Neutrino oscillations

Figures 4.8 and 4.9 (left panels) show the luminosities and mean energies of ν_e and $\bar{\nu}_e$ in the active and sterile cases as functions of radius for toy model 1.

In the active case, the initial conditions for neutrinos are different from the ones discussed in Sect. 4.5 at the same t_0 (i.e., here we have $L_{\nu_e}/\langle E_{\nu_e} \rangle - L_{\nu_x}/\langle E_{\nu_x} \rangle > 0$). Moreover, the new spectral parameters also prescribe larger differences between the ν_e ($\bar{\nu}_e$) and ν_x spectra and spectral crossings which are different from the previous cases. Bipolar oscillations due to ν-ν interactions (Fogli et al. 2008, 2009b) are then triggered at $r \simeq 2.2 \times 10^7$ cm at $t_0 = 2.9$ s and $r \simeq 1.35 \times 10^7$ cm at $t_0 = 6.5$ s. The neutrino and antineutrino luminosities and mean energies are correspondingly modified, as shown in Figs. 4.8 and 4.9 (left panels).

In the sterile case, at $t_0 = 2.9$ s (see left panel of Fig. 4.8), the inner active-sterile MSW resonance converts both ν_e and $\bar{\nu}_e$ to sterile states. As expected, ν_e's are converted slightly more abundantly to sterile states than $\bar{\nu}_e$'s. Soon after, the ratio $L_{\nu_e}/\langle E_{\nu_e} \rangle$ increases, and the outer active-sterile MSW

---

[8]Note that Roberts et al. (2012) employed the approximate formula $Y_e \simeq 1/(1 + \lambda_{\bar{\nu}_e}/\lambda_{\nu_e})$ of Qian & Fuller (1995) for estimating the electron fraction in the wind. This formula does not account for the α-effect on Y_e.
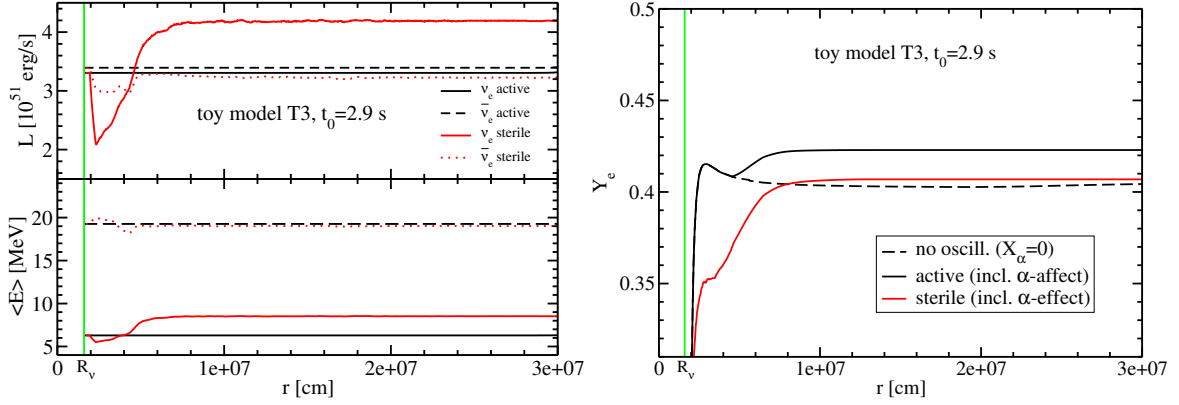
Figure 4.10 Same as Fig. 4.8, but for toy model 3 (see text for details). (The red lines here are running averages over $\Delta r \simeq 4.5 \cdot 10^5$ cm.)

resonance occurs together with neutrino self-interactions. Note that due to the feedback effect on Y_e and due to the initially lower value of Y_e compared to the corresponding standard case, the outer MSW resonance is more adiabatic and it is expected to occur at smaller radii ($r_{OR} \simeq 4 \cdot 10^6$ cm) than in the standard case. Moreover, due to the hierarchy of the active neutrino fluxes and due to the lower matter potential, neutrino self-interactions mix ν_e and $\bar{\nu}_e$ with the heavy lepton flavors, increasing the ν_e survival probability, differently from what is shown in Fig. 4.4.

In the sterile case, at $t_0 = 6.5$ s (see left panel of Fig. 4.9), the inner MSW resonance is visible as a small drop of $L_{\nu_e}/\langle E_{\nu_e}\rangle$ (and even smaller for the $\bar{\nu}_e$) at $r_{IR} \simeq 2 \cdot 10^6$ cm. Slightly farther outside, at $r_{OR} \simeq 2.5 \cdot 10^6$ cm, the outer MSW resonance occurs (similarly to the standard case). Sterile neutrinos and antineutrinos are both abundantly produced through flavor conversions due to an interplay between the outer MSW resonance and collective oscillations, before α particles start forming at $r \simeq 3 \cdot 10^6$ cm. As a consequence, both ν_e and $\bar{\nu}_e$ fluxes decrease, causing an increase of Y_e above 0.5 before the onset of the α-effect. Toy model 2 is very similar to toy model 1 concerning the oscillation phenomenology, therefore we do not show our results here and only report the corresponding neutrino emission properties and the asymptotic Y_e values in Table 4.1.

Toy model 3 is shown in Figs. 4.10 and 4.11. In this case, the active flavors show a hierarchy of the mean energies more similar to the one reported in Table 4.1, although we have $L_{\nu_e}/\langle E_{\nu_e}\rangle - L_{\nu_x}/\langle E_{\nu_x}\rangle > 0$, similar to toy model T1. Therefore, in the active case, bipolar oscillations occur at $r > 3 \times 10^7$ cm at $t_0 = 2.9$ s , while they start at $r \simeq 2.4 \times 10^7$ cm at $t_0 = 6.5$ s. In the sterile case, the inner resonance is visible at $r_{IR} \simeq 2 \times 10^6$ cm at $t_0 = 2.9$ s. Soon afterwards ν-ν interactions are triggered and the ν_e survival probability starts to increase already before the region where the outer MSW resonance is expected to take place ($r_{OR} \simeq 4 \times 10^6$ cm). In the sterile case, at $t_0 = 6.5$ s, the regions of the inner and outer MSW resonances almost overlap with each other, similarly to the standard case (Fig. 4.5). This is responsible for an overall drop of $L_{\nu_e}/\langle E_{\nu_e}\rangle$ and $L_{\bar{\nu}_e}/\langle E_{\bar{\nu}_e}\rangle$.

4.7.3 Feedback on the electron fraction

In this section, we discuss the evolution of the electron fraction for toy models T1, T2, and T3 considered in the previous section in order to disentangle between the impact of neutrino oscillations and
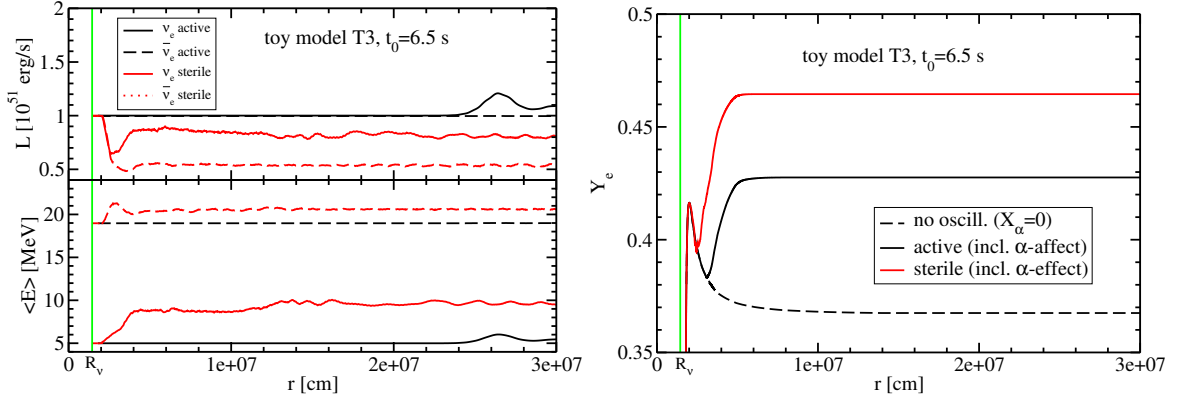
Figure 4.11 Same as Fig. 4.9, but for toy model 3 (see text for details). (The red lines here are running averages over $\Delta r \simeq 4.5 \cdot 10^5$ cm.)

α-effect on Y_e in a neutron-rich neutrino-driven wind environment.

In Figs. 4.8 and 4.9 (right panels), we show the evolution of Y_e, at intermediate ($t_0 = 2.9$ s) and late ($t_0 = 6.5$ s) evolution phases of the neutrino-driven wind in the T1 model (see Table 4.2). The dashed lines refer to Y_e in the case where neither neutrino oscillations nor α-effect are taken into account, while the solid lines display Y_e radial evolutions, including the α-effect in the active (solid black lines) and sterile (solid red lines) cases. Since active oscillations take place at $r > 1.2 \times 10^7$ cm in both cases (i.e., after Y_e has reached its asymptotic value), the difference between $Y_{e,a}^{\rm act}$ and $Y_{e,a}^{X_\alpha=0}$ is just caused by α-effect (see Table 4.2), which pushes Y_e towards 0.5 as expected. Also for these toy models, the impact of the α-effect on Y_e is larger at late times, for the reasons we already discussed in Sect. 4.6.

In the sterile case, neutrino oscillations raise the asymptotic value of the electron fraction compared to the active case, therefore the matter becomes *more proton-rich* compared to the case where oscillations are not considered or where they occur in the active sector only.

In particular, at $t_0 = 2.9$ s, the inner and outer MSW resonances in the sterile case cause Y_e to be lower than in the active case, already before α particles start forming. Then, the ν-ν interactions, which repopulate the ν_e sector, drive Y_e towards 0.5 and even above the value of Y_e in the active case, even without the α-effect, which remove free nucleons and thus moderate the impact of neutrino oscillations on Y_e, as discussed in detail in Sect. 4.6.

At $t_0 = 6.5$ s, neutrino oscillations occur very close to the neutrinosphere and push Y_e in the sterile case to a much higher value (> 0.5) than in the active case, already before α particles start forming at $r \sim 4.0 \times 10^6$ cm. Therefore, the formation of α particles impacts the evolution of Y_e in the usual way, namely towards more symmetric conditions ($Y_e \longrightarrow 0.5$).

In order to prove the robustness of our conclusions about the interplay between neutrino oscillations and α-effect, we also calculate Y_e for the toy models T2 and T3. We don't show the evolution of Y_e for T2, because the discussion is very similar to T1, but we report the corresponding Y_e results in Table 4.2.

In the T3 active case (see black solid lines in Figs. 4.10 and 4.11), the discussion about the impact of α-effect and neutrino oscillations on the evolution of Y_e at $t_0 = 2.9$ s and $t_0 = 6.5$ s is very similar to what we already discussed in the T1 case.

In the T3 sterile case, instead, at $t_0 = 2.9$ s, we observe an interesting interplay between neutrino oscillations and α-effect, because Y_e in the sterile case (solid red line) is lower than in the active case (solid black line), different from case T1 and T2 at $t_0 = 2.9$ s. This is due to the fact that the MSW resonances initially deplete the number flux of ν_e in favor of ν_s much more than in cases T1 and T2, for the reasons discussed in the previous subsection. Therefore, Y_e in the sterile case is already much lower than in the active case, before α-particles start forming. In the following evolution, different from cases T1 and T2, the α-effect damps the efficiency of ν-ν interactions in raising Y_e, which remains lower than in the active case. However, the difference between Y_e in the active case and in the sterile case is not sufficiently large to conclude that neutrino oscillations in the sterile case make the environment significantly more neutron-rich than in the case without neutrino oscillations.

At $t_0 = 6.5$ s, we basically observe the same trend as in the T1 and T2 cases, namely Y_e in the sterile case is higher than in the active case. The reasons are very similar to what was already discussed for the T1 model.

In conclusion, neutrino oscillations (with or without sterile neutrinos) combined with the α-effect do not support very neutron-rich conditions in the neutrino-driven wind for the considered SN model. Therefore, conditions for a strong r-process in this SN progenitor are disfavored, because Y_e tends to be pushed close to 0.5 and thus the formation of a highly neutron-rich environment is prevented.

4.8 Discussion

In this work, we studied the nucleosynthesis outcome of an ECSN with $8.8\,M_\odot$, by adopting the SN model presented in Hüdepohl et al. (2010). The same SN simulation was adopted in Tamborra et al. (2012b) to study the impact of neutrino oscillations on the electron fraction in the presence of light sterile states. However, due to the complications induced by the numerical solution of a large number of non-linear, coupled equations with three neutrino families and the oscillation feedback on Y_e, the inner MSW resonance was not included in Tamborra et al. (2012b), assuming that its impact on the electron fraction was negligible during the neutrino-driven wind phase due to the steepness of the matter potential in that region. It was found that neutrino conversions to a sterile flavor and neutrino self-interactions influence the radial variation and time-dependent asymptotic value of Y_e in the neutrino-driven wind in complicated and time-dependent ways. These conclusions motivated us to investigate in detail the effect of oscillations on a larger variety of wind conditions and on the nucleosynthetic abundances. In this work, the neutrino evolution is followed from the neutrinosphere outward. We also develop a more detailed treatment of the Y_e evolution than in Tamborra et al. (2012b), by accounting for the α-effect as well as recoil and weak magnetism corrections in the β processes. We find that the inner active-sterile MSW resonance has a negligible impact on Y_e during the intermediate and late cooling phases, although it modifies the ν and $\bar{\nu}$ spectra. In particular, as discussed in Appendix A, when ν-ν interactions are included, the flavor instability induced by the active-sterile MSW resonance triggers neutrino self-interactions modifying the flavor evolution history compared to the case where only interactions with the matter background are considered. On the other hand, the inner MSW resonance induces non-negligible modifications of the electron fraction during the accretion phase, as pointed out in Wu et al. (2014), and in the early proto-NS cooling phase; It is responsible for the formation of a plateau in Y_e that drives the asymptotic value of Y_e towards smaller values.

The early cooling phase (i.e., at $t_0 = 0.5$ s and 1 s) was also discussed in Wu et al. (2014) for the same ECSN progenitor, but adopting the simulation of Fischer et al. (2010). With sterile neutrino oscillations Wu et al. (2014) obtain a neutron-rich environment ($Y_e^a[0.5s] = 0.38$) different from us ($Y_e^a[0.5s] = 0.53$, see Figs. 4.3 and 4.6). Such a discrepancy might be due to the different supernova models adopted as inputs in Wu et al. (2014) (i.e., Fischer et al. 2010) and in our work (i.e., Hüdepohl et al. 2010). In fact, the electron fraction without oscillations is $Y_e[0.5s] = 0.49$ in Fig. 3 (red curve) of Wu et al. (2014), while in our case it is $Y_e[0.5s] = 0.56$ as shown in Fig. 4.3. Our work also adopts an approach to study the electron fraction evolution different from the one employed in Wu et al. (2014) (i.e., our Eq. 3.4 vs. Eq. 4 of Wu et al. 2014). The static approach of Wu et al. (2014) carries "memory" of the large modifications of the neutrino fluxes and of the electron fraction due to the inner MSW resonance at $t < 0.5$ s, while our sampling is sparse, because 90% of the ejecta of the early cooling are combined into one trajectory ejected at 0.5 s. Even adopting a denser grid in t_0, our dynamic approach should not be accurate during the accretion phase where the steady-state approximation is not applicable. Other differences on Y_e might be due to a different treatment of the neutrino oscillations. In Wu et al. (2014), a 1(active) + 1(sterile) approximation is adopted and ν-ν interactions are neglected assuming that they are suppressed due to the high matter potential during the accretion phase (Sarikas et al. 2012), while we include the ν_e-ν_x flavor mixing as well as neutrino self-interactions in our computations.

Given the complex and nonlinear nature of neutrino self-interactions, all existing numerical studies with neutrino-neutrino refraction use simplifying assumptions. In our treatment of the neutrino evolution, we averaged the angular dependence of ν-ν interactions (the so-called "single-angle approximation," Duan et al. 2006). Because of the similarity between the ν_e and $\bar{\nu}_e$ fluxes and those of the corresponding heavy-lepton neutrinos in our hydrodynamical simulations, and because of the observed strength of the α-effect in pushing Y_e close to 0.5, even a possible relevance of multi-angle effects due to a small asymmetry among the neutrino fluxes of different flavors (Esteban-Pretel et al. 2007) is unlikely to play any important role for Y_e. In the "sterile" case, the asymmetry between ν_e and ν_x becomes even larger than in the active case due to the ν_s production, therefore we expect that a full-multi-angle treatment would only induce a smearing of the neutrino fluxes (Fogli et al. 2007), without a dramatic impact on Y_e. If the matter potential is high enough, neutrino multi-angle effects could also be responsible for a matter suppression of collective effects, and therefore produce results which are different from the ones obtained within the "single-angle" approximation (Esteban-Pretel et al. 2008). A multi-angle study was developed by Chakraborty et al. (2011) for one energy mode and for the 8.8 $M_\odot$ progenitor presented in Fischer et al. (2010): A complete matter suppression of the collective effects due to multi-angle matter effects was never achieved for this progenitor, because of the low-density matter profile. We therefore suspect that also the triggering of the collective effects induced by the inner MSW resonance instability should not be suppressed by a multi-angle treatment of the neutrino flavor oscillations during the cooling phase. However, more accurate studies including multi-angle effects are mandatory and should be conducted for a larger sample of supernova progenitors and nuclear equations of state, especially because, according to the modeling presented in Duan et al. (2011b), it was concluded that multi-angle effects among active flavors may affect the nucleosynthetic outcome under certain conditions.

Concerning the nucleosynthesis outcome, in the case without sterile neutrino and neutrino oscillations, all relevant results can be found in Fig. 3 of Wanajo et al. (2011): There are nucleosynthetic yields for a 1D model (to be directly compared with Wu et al. 2014) and of a more realistic 2D model as well. The 2D model yields major and important differences compared to the 1D case, as in all

details discussed in Wanajo et al. (2011). The differences between the the 1D nucleosynthesis result of Wanajo et al. (2011) and Wu et al. (2014) are most probably due to differences in the mass-versus-Y_e distribution, which are caused by the different neutrino interaction processes adopted in our models and in that of Fischer et al. (2010). Since the mass-versus-Y_e distribution is not provided in Wu et al. (2014), a detailed comparison between our and their nucleosynthesis results is impossible.

4.9 Conclusions

We presented neutrino oscillations and nucleosynthesis calculations for the neutrino-cooling phase of the proto-neutron star born in an 8.8 $M_\odot$ electron-capture supernova, using trajectories for the ν-driven wind from 1D hydrodynamic simulations, in which a sophisticated treatment of neutrino transport was applied (Hüdepohl et al. 2010). In particular, we studied the consequences of neutrino oscillations of two active flavors driven by the atmospheric mass difference and θ_{13} and, motivated by hints on the possible existence of light sterile neutrinos, we also discussed the role of flavor oscillations with 1 sterile + 2 active flavors. In our study neutrino-neutrino refraction effects were included, too. We chose ν_e-ν_s mixing parameters as suggested by the reactor anomaly (Mention et al. 2011). However, our conclusions remain valid also for moderate variations of the sterile mass-mixing parameters.

Our results demonstrate that the α-effect plays a crucial role in discussing the consequences of neutrino oscillations on the Y_e evolution in neutrino-driven winds. It can damp as well as enhance the Y_e-reducing impact of ν_e-ν_s conversions, depending on the radial position of the active-sterile MSW region relative to the radius where α-particles form from nucleon recombination. In the late proto-neutron star cooling phase the production of sterile neutrinos via an MSW resonance takes place very close to the neutrinosphere, while a significant abundance of α-particles in the wind appears only at larger distances. The Y_e reduction in the ejecta associated with the transformation of ν_e to ν_s is therefore amplified by the subsequent α-effect, driving Y_e from initial values considerably above 0.5 to an asymptotic value closer to 0.5. In the early wind phase the effect is different. Here the outer ν_e-ν_s MSW conversions occur farther away from the neutron star and exterior to (or coincident with) the formation region of α-particles. The α-effect then moderates the Y_e reduction caused by the presence of sterile neutrinos. Because of this dominance of the α-effect, the asymptotic neutron-to-proton ratio in the early wind becomes very similar in the cases with and without sterile neutrinos (whereas without α-effect sterile neutrinos always cause a significant reduction of Y_e).

While the neutrino-driven wind of our ECSN model is well on the proton-rich side (Hüdepohl et al. 2010), equation-of-state dependent nucleon mean-field potentials in the neutrinospheric region might lead to a considerably lower Y_e in the wind outflow (Roberts et al. 2012; Martínez-Pinedo et al. 2011). For this reason we constructed six toy model cases for the intermediate and late wind phases, in which the (unoscillated) neutrino spectra were chosen such that the neutrino-driven wind became neutron-rich with an asymptotic wind-Y_e (including the α-effect) of about 0.42–0.43, which is on the extreme side of the theoretical estimates. Including active-sterile flavor oscillations, the outflow turns, in some cases, *more proton-rich*, despite the conversion of ν_e to ν_s. This counterintuitive Y_e increase is caused by neutrino oscillations, which modify the neutrino emission properties such that either the ν_e absorption is more strongly increased than the competing $\bar{\nu}_e$ absorption or the $\bar{\nu}_e$ absorption is more strongly reduced than the competing ν_e absorption. Our conclusion that sterile neutrinos are unlikely to help enforcing neutron-rich conditions in the wind ejecta therefore seems to remain valid even when nucleon-potential effects are taken into account in future neutron-star cooling simulations.

If oscillations are disregarded, the wind ejecta in our ECSN model develop a proton excess and therefore only iron-group and some *p*-rich isotopes are created with small production factors (below 10), not adding any significant production of interesting isotopes to the nucleosynthesis yields computed for the early ejecta of 2D explosion models of such ECSNe (Wanajo et al. 2011, 2013a,b). When neutrino oscillations are taken into account by our simplified neutrino-mixing scheme, the feedback of oscillations on Y_e is time-dependent, since it is sensitive to the detailed matter profile and neutrino fluxes. In the early *v*-driven wind, the asymptotic Y_e value in the presence of a sterile family is lower than the Y_e value obtained without oscillations, although always > 0.5. In the intermediate phase of the *v*-driven wind Y_e in the presence of sterile neutrinos is even a bit higher than the one without oscillations.

In the late *v*-driven wind the asymptotic Y_e in the presence of sterile neutrinos is slightly lowered compared to the case without oscillations or to the case where oscillations in the active sector are considered. However, in our model of the neutrino cooling of the proto-neutron star born in an ECSN, the corresponding effects do not lead to any neutron excess. The changes of the nucleosynthetic output for models with (active or sterile) neutrino oscillations compared to the no oscillations case are insignificant. It appears unlikely that in the studied progenitor viable conditions for strong r-processing can be established.

Our conclusions concern the *v*-driven wind of an $8.8\ M_\odot$ progenitor. More studies of the impact of neutrino oscillations on the early-time ejecta including multi-dimensional effects arising in hydrodynamic simulations (Wanajo et al. 2011, 2013a) and including the effects of nucleon mean-field potentials in the neutrino opacities, are needed in order to shed light on the consequences of neutrino oscillations for the explosion mechanism and nucleosynthetic abundances (cf. Wu et al. 2014, who considered only a 1D model). Studies of a broader range of progenitor models, in particular also iron-core SNe with more massive proto-neutron stars, applying state-of-the-art neutrino-oscillation physics, are also desirable to identify possible cases where favorable conditions for an r-process may be produced.

5 Hints on the Explosion Mechanism of Core-Collapse Supernovae from the Study of the Production of ^{44}Ti and ^{56}Ni

We investigate the production of the radioactive isotopes ^{44}Ti and ^{56}Ni in 3D as well as 1D core-collapse supernovae (CCSNe) of 15 $M_\odot$ and 20 $M_\odot$ progenitors, whose explosions are simulated using the light-bulb neutrino approach with the PROMETHEUS code. We see a general spatial correlation between the production of ^{44}Ti and ^{56}Ni, although ^{44}Ti can even be found in regions where almost no ^{56}Ni is produced. The asymmetries which arise at the onset of the explosion play a crucial role in determining the spatial distribution of these isotopes. The produced amount, instead, depends sensitively on the SN explosion energy and on the shock wave propagation. Taking into account some uncertainties in key nuclear reaction rates involving ^{44}Ti and in the electron fraction of the matter which interacts with neutrinos, we get (within the error bars) a good agreement between the amounts of ^{44}Ti and ^{56}Ni produced in our models and the ones given by observations. We conclude that the delayed neutrino-driven explosion mechanism of CCSNe can be an explanation for the spatial distribution and the synthesized amounts of ^{44}Ti and ^{56}Ni observed in supernovae remnants.

5.1 Introduction

Understanding the mechanism which gives birth to core-collapse supernovae (CCSNe) explosions is still a challenging question. For an overview on the supernovae theory as well as the multi-dimensional effects on the explosion of massive stars see Janka (2012), Burrows (2013), and Foglizzo et al. (2015). With the exception of the lowest mass progenitor ($M \simeq 8\ M_\odot$) of CCSNe (Hüdepohl et al. 2010, Fischer et al. 2010), all models fail to explode in 1D including detailed neutrino transport. In 2D the situation becomes more optimistic. In fact, hydrodynamic instabilities and non-radial motions, e.g. convection in the neutrino-heated post- shock layer, and the so-called standing accretion shock instability (SASI, Blondin et al. 2003) can help the explosion, since they enhance the neutrino-heating conditions behind the shock (e.g., see Janka & Mueller 1996). In 3D, namely without any symmetry restriction on the fluid motion, the optimistic scenario of 2D explosions with detailed neutrino transport becomes questionable. In 3D the explosion condition is found to be less favourable than in 2D (Hanke et al. 2012). Until now, there is only one successful example of a 3D neutrino-driven SN explosion of a 9.6 iron-core star which is computed fully self-consistently with the neutrino-hydrodynamics code Prometheus-Vertex (Melson et al. 2015). Furthermore, Melson et al. (2015) identify, for the first time, the impact of 3D turbulence in the convective gain layer that increases the explosion energy and accelerate the shock expansion in 3D relative to 2D.

It is generally accepted that asymmetries play a crucial role in launching successful CCSNe explosions. However, the details of the explosion, which are needed to produce robust explosions for a

broad range of progenitors, are not yet fully understood. In order to shed light on the mechanism which drives the SNe explosions, one can have some hints from the observations of the energy and material which are injected into the interstellar medium from CCNSe explosions. Some of this material, which is the result of nucleosynthesis processes occurring during the explosion, is made of radioactive isotopes, and therefore allow us to infer the CCSNe physical conditions which are needed in order to produce them. For example, the observations of ^{44}Ti and ^{56}Ni in CCSNe events, such as the well known SN 1987A and CasA, can significantly help us to better understand the explosion mechanism of SNe, since the production of these two isotopes strongly depends on the temperature, density and electron fraction, which, on their turn, depend on the details of the explosion. Furthermore, the spatial distribution of these isotopes is strongly connected to the asymmetries which arise at the onset of the explosion.

Therefore, by comparing the outcome (e.g., nucleosynthesis material) from the SNe modelling with the observations, we can test our theory. To this aim, we need long-term CCSNe explosions which, depending on the degree of complexity and completeness of the physical processes which are used in modelling the explosion, can be, computationally speaking, extremely expensive, especially for the aforementioned models which use detailed neutrino transport. Besides the neutrino heating, other methods are used to explode the star, among them there are the piston (e.g., Woosley & Weaver 1995, Limongi & Chieffi 2006) and the thermal bomb models (e.g., Thielemann et al. 1996). In these models, some additional energy is artificially added to the system in order to trigger the explosion. Besides the explosion energy, the mass cut, namely the boundary between the ejecta and the proto-neutron star (PNS), has to be taken as a free parameter which is chosen in order to produce the observed mass of ^{56}Ni ejecta. These models are appropriate to predict the outcome of the nucleosynthesis in the outer layers of the star, since it mainly depends on the strength of the shock wave which passes through the different layers, but they fail to accurately predict the nucleosynthesis in the innermost layer of the star. Recently, Perego et al. (2015) proposed a new method, called PUSH, to explode the massive stars in spherical symmetry. In PUSH, a fraction of the luminosity of the heavy flavor neutrinos emitted by the PNS is deposited in the gain region, in order to mimic the effects seen in multi-dimensional supernovae simulations. The artificially increased heating is calibrated in order to reproduce the observational properties of SN 1987A (for details see Perego et al. 2015).

In order to have some more hints on the explosion mechanism of CCSNe, in this work, we perform nucleosynthesis calculation, focusing on the production of ^{44}Ti and ^{56}Ni in *long-term simulations* of a set of 15 $M_\odot$ and 20 $M_\odot$ progenitor stars (Wongwathanarat et al. 2010b, Wongwathanarat et al. 2013, Wongwathanarat et al. 2014). In these simulations the so-called light-bulb neutrino transport is adopted in order to trigger the SNe explosions. Namely, the core of the PNS is replaced by a representative point mass and a grid boundary is placed at the surface of the excised PNS core. A boundary condition is set at the grid boundary such that it radiates suitable amounts of neutrinos to trigger the explosion (for details see Wongwathanarat et al. 2010b, Wongwathanarat et al. 2013, Wongwathanarat et al. 2014). In this way, the detailed neutrino transport is replaced by a simplified version of neutrino absorption and emission terms in optically thin conditions. Furthermore, the non-radial instabilities in SN core of the 3D models are triggered by small random perturbations on the grid scale (for details, see Wongwathanarat et al. 2014). The chosen set of the CCSNe models allows us to discuss the dependence of the production of ^{44}Ti and ^{56}Ni on different aspects: progenitor, dimensionality, explosion energy, and asymmetry. We structure our work as follows: in Sect. 5.2, we shortly present our input supernovae models as well as our nuclear reaction network. In Sect. 5.3, we discuss our post-processing method. In Sect. 5.4, we show the first part of our results concerning the progenitor dependence of the production of ^{44}Ti and ^{56}Ni. In Sect. 5.5, we investigate the difference between the production of ^{44}Ti and ^{56}Ni in 3D and 1D supernovae simulations. In Sect. 5.7, we compare our

Table 5.1 For each of the considered models in 3D or 1D, we report some presupernova and explosion properties: type (RSG or BSG), ZAMS mass (M), radius ($R_\star$), postbounce time of the explosion (t_{exp}), and the explosion energy (E_{exp}) (Wongwathanarat et al. 2013, Wongwathanarat et al. 2014).

Model [1]	Progenitor Type	M $M_\odot$	$R_\star$ [10^6 km]	t_{exp} [s]	E_{exp} [B][2]
W15-1-3D	RSG	15	339	0.24	1.12
W15-2-3D	RSG	15	339	0.25	1.13
N20-2-3D	BSG	20	33.8	0.28	3.12
N20-4-3D	BSG	20	33.8	0.33	1.35
N20-4-1D	BSG	20	33.8	0.55	0.45
N20-8-1D	BSG	20	33.8	0.36	~ 1.5

results with other theoretical works and observations and, finally, in Sect. 5.8, we present our main conclusions and perspectives.

5.2 Neutrino-driven explosion simulations of supernovae and nuclear reaction network

The simulations of our SN explosions in 3D and 1D are performed with the PROMETHEUS code (Fryxell et al. 1991, Müller et al. 1991), which is an explicit finite-volume, Eulerian, multi-fluid hydrodynamics code. It solves the multidimensional hydrodynamic equations using dimensional splitting (Strang 1968), piecewise parabolic reconstruction (Colella & Woodward 1984), and a Riemann solver for real gases (Colella & Glaz 1984). The advection of nuclear species in the code is treated using the consistent multifluid advection scheme of Plewa & Müller (1999). An axis-free overlapping "Yin-Yang" grid (Kageyama & Sato 2004) in spherical coordinates is employed in PROMETHEUS (Wongwathanarat et al. 2010a). The "Yin-Yang" grid has, among others, the advantage of avoiding numerical artifacts near the polar axis (for details see Wongwathanarat et al. 2010a).

The neutrino transport and the neutrino-matter interactions are treated using the so-called light-bulb neutrino transport method similar to what was done in Scheck et al. (2006). Suitable choices of the neutrino parameters trigger SNe explosions. The equation of state (EoS) of Janka & Mueller (1996) is used to describe the matter. In our simulations, the inner core of the proto-neutron star (PNS) is excised and replaced by a point mass at the origin of the coordinate system and the cooling of the excised part of the PNS due to neutrino emission is taken into account by setting the neutrino properties (luminosities and mean energies) as time-dependent boundary conditions (see Wongwathanarat et al. 2013, Wongwathanarat et al. 2014). After the supernova explosion has been launched and the explosion energy is almost saturated, which happens at about $1.1 - 1.3$ s postbounce time, the outer boundary of the grid is extended to a radius $r = 10^{14}$ cm. This allows us to follow the propagation

---

[1]The 1D models have not yet been published (private communication of Annop Wongwathanarat).
[2]1B = 1Bethe = 10^{51}erg

of the shock wave through the different layers of the progenitor and to take into account mixing processes during the late-time evolution of the explosion until the shock wave breaks out from the stellar surface. In these long term simulations the aforementioned neutrino transport and interactions with matter are not taken into account. Furthermore, the EoS of Janka & Mueller (1996) is switched to the one of Timmes & Swesty (2000). These long term simulations are stopped at $\sim 35000 - 61000$ seconds after the bounce of the core. While performing the supernovae simulations, a small α-chain reaction network is solved in order to take into account, although very approximately, the explosive nucleosynthesis (for more details see Wongwathanarat et al. 2014).

Therefore, in order to be able to predict as accurately as possible the amount of nuclear species which are produced during the explosive nucleosynthesis of the SN, and in particular of our isotopes of interest ^{44}Ti and ^{56}Ni, an accurate post-processing of the matter using a full reaction network is necessary.

5.2.1 Input stellar models

In order to perform our study concerning the production of ^{44}Ti and ^{56}Ni in explosive nucleosynthesis we choose a set of six non-rotating presupernova models having a Zero Age Main Sequence mass (ZAMS) $M = 15\ M_\odot$ (see model s15s7b2 in Woosley & Weaver 1995) and $M = 20\ M_\odot$ (Shigeyama & Nomoto 1990), respectively. Noticed that, the mass of the N20 models reduces to a values of $16.3\ M_\odot$ when the collapse occurs, because of the mass loss. In Table 5.1, we report some of the main presupernova as well as explosion properties of our models which are relevant for our investigation: ZAMS mass, radius of the star, explosion energy E_{exp}[3], and explosion time[4] (Wongwathanarat et al. 2013, Wongwathanarat et al. 2014). The first part of the name we choose for our models (e.g., W15-1) refers to the model used as input for our neutrino-driven explosion simulations, while the second part refers to the dimensionality of the simulation either 3D or 1D (e.g., W15-1-3D). The W15-1-3D and W15-2-3D models are two Red-Super-Giant (RSG) stars and they differ in the initial perturbation configuration which was imposed to break the spherical symmetry of the 1D collapse model at 15 ms postbounce time (see details in Wongwathanarat et al. 2013). These models have almost the same explosion energies, but, due to the chaotic nature of non-radial hydrodynamic instabilities, the ejecta asymmetries develop in a different way in these models during the shock revival phase. Therefore, the comparison between the nucleosynthesis results of the W15-1-3D and W15-2-3D models allows us to investigate the impact of these asymmetries on the ejecta distribution, in particular of ^{44}Ti and ^{56}Ni. Summarizing, we choose the aforementioned set of models (see Tab. 5.1) in order to investigate different aspects of the production of ^{44}Ti and ^{56}Ni in the supernova explosive nucleosynthesis:

- The *progenitor* dependence by comparing models W15-1-3D and W15-2-3D ($M = 15 M_\odot$) with models N20-2-3D and N20-4-3D ($M = 20\ M_\odot$);

- The *asymmetry* influence of the ejecta by comparing the spatial distribution of model W15-1-3D and model W15-2-3D;

- The *explosion energy* dependence by comparing model N20-2-3D and model N20-4-3D, the latter having an almost double E_{exp} as the former;

---

[3]The explosion energy is defined as the sum of the total (internal+kinetic+gravitational) energy over all grid zones where the total energy is positive.

[4]The explosion time is defined as the moment when $E_{\mathrm{exp}} \gtrsim 10^{48}$ erg, which approximately happens at the same time when the average shock radius (see Eq. 5.5) exceeds a value of 400-500 km.

- The *dimensionality* importance by comparing model N20-4-3D with N20-4-1D and N20-8-1D models;

Furthermore, our choice of the progenitor models and their explosion properties, in particular of the explosion energy, is due to the fact that SN 1987A is thought to have a ZAMS mass progenitor in the range $18 - 20$ $M_\odot$ (Shigeyama & Nomoto 1990, Woosley 1988) and an explosion energy of the about $(1.1 \pm 0.3) \cdot 10^{51}$ B (Blinnikov et al. 2000), while CasA has an estimated mass around 16 $M_\odot$ (Grefenstette et al. 2014).

5.2.2 Nuclear reaction network

We use a nuclear reaction network in which 6300 nuclear species are taken into account between the proton-drip line and neutron-drip line, up to the $Z = 110$ isotopes, for more details see Wanajo (2006). All the important reactions such as (n, γ), (p, γ), (α, γ), (p, n), (α, n), (α, p), and their inverse ones are taken into account (see also chapters 3 and 4). In the following, besides the 3α reaction which influences the outcome of nucleosynthesis globally, we list some of the most important reactions which are relevant for the production of ^{44}Ti: ^{44}Ti$(\alpha, p)^{47}$V, ^{40}Ca$(\alpha, \gamma)^{44}$Ti, ^{47}V$(p, \gamma)^{46}$Cr, ^{40}Ca$(\alpha, p)^{53}$Sc, ^{17}F$(\alpha, p)^{20}$Ne, ^{21}Na$(\alpha, p)^{24}$Mg, ^{41}Sc$(p, \gamma)^{42}$Ti, ^{43}Sc$(p, \gamma)^{44}$Ti, ^{44}Ti$(p, \gamma)^{54}$V, and ^{57}Ni$(p, \gamma)^{58}$Cu. For a detailed discussion on the impact of the different reaction rates on the production of ^{44}Ti see The et al. (2006) and Magkotsios et al. (2010). These rates are either know experimentally or inferred theoretically. The rates which we use are taken from Cyburt et al. (2010). In particular, the rate of the reaction ^{44}Ti$(\alpha, p)^{47}$V, which is still not very well constrained experimentally (Margerin et al. 2014), plays a crucial role in determining the final amount of the produced ^{44}Ti. We will come back to this question in Sect 5.6. The outcome of the nucleosynthesis in general crucially depends also on the electron fraction Y_e, which is determined by the β-reactions: $p(e^-, \nu_e)n$ and $n(e^+, \bar{\nu}_e)p$, as widely discussed in chapters 3 and 4. However, since the treatment of neutrinos in our supernova simulations is done only approximately (in our light-bulb neutrino approach we do not fully take into account all the reactions of neutrinos with matter), we do not consider the above reactions involving neutrinos in our nucleosynthesis calculations. Therefore, we have to make certain assumptions (as it will be specified in the following) about the Y_e evolution in the matter which is heated by neutrinos. We will come back to this question in Sect. 5.4.2.

5.3 Post-processing and methodology

In order to perform our nucleosynthesis calculations we use for each model a set of tracer particles (see Tab. 5.2), whose density and temperature profiles where simulated for at least 10 s, which is enough to perform nucleosynthesis calculations without making any extrapolation of the hydrodynamical trajectories. We choose a mass resolution of the particles (a few 10^{-6} $M_\odot$), which is lower than the estimated or observed amount of ^{44}Ti in SN explosions SN 1987A and CasA, namely a few $(10^{-5} - 10^{-4})M_\odot$ (Grefenstette et al. 2014, Seitenzahl et al. 2014). The production of ^{44}Ti and ^{56}Ni takes mainly place in the silicon and oxygen layers above the PNS and if the matter goes enough close to the PNS, let say at radii $r \lesssim 250$ km, then the interactions with neutrinos become important. Therefore, due to the limitation of our neutrino transport, we distinguish our particles, and nucleosynthesis calculations, into two different sets:

Table 5.2 For each of the considered supernova models, we report the rough number of tracer particles which we use in the post-processing nucleosynthesis calculations as well as their mass resolution in $M_\odot$.

Model	Number Tracers	M_{part} $10^{-6} M_\odot$
W15-1-3D	~ 84000	3.49
W15-2-3D	~ 76000	3.49
N20-2-3D	~ 48000	1.87
N20-4-3D	~ 32000	1.79
N20-4-1D	~ 8000	5.00
N20-8-1D	~ 18000	5.00

- *shock-heated* matter, namely we take into account only the hydrodynamical trajectories of particles whose highest temperature is $T_{\text{peak}} \lesssim 9$ GK and whose radius is $r \gtrsim 250$ km, because we want to avoid neutrino interactions with matter;

- *neutrino-heated* (ν-heated) matter, corresponding to the remaining particles which are heated by neutrinos at $T_{\text{peak}} > 9$ GK and, therefore, can go very close to the PNS.

In the shock-heated matter case, we use the nuclear composition of the pre-supernova model as initial condition for the nuclear abundances, which is taken from Woosley & Weaver (1995) for the W15-1-3D and W15-2-3D model, while it is taken from Shigeyama & Nomoto (1990) for all the other models. In the ν-heated case, we make two different assumptions about the initial abundances of the matter which is in NSE (see chapter 1), and therefore is only made of free protons Y_p and neutrons Y_n due to the very high temperatures:
(i) We take the initial Y_e as it is given by our models with the *approximate* neutrino-transport at a temperature $T \simeq 5$ GK (the lowest temperature at which the matter is still in NSE), and then perform our nucleosynthesis calculations with initial abundances $Y_p = Y_e$ (charge neutrality) and $Y_n = 1 - Y_e$;
(ii) We take as initial Y_e the one of the progenitor and then by setting again the initial composition $Y_p = Y_e$ and $Y_n = 1 - Y_e$, we perform our nucleosynthesis calculations. By considering the cases (i) and (ii) we can have an idea about the amounts of ^{44}Ti and ^{56}Ni which are produced in the ν-heated matter, although, for the aforementioned reasons, our predictions have to taken with a "caveat", since they will be significantly affected by the uncertainties related to the non accurate knowledge of Y_e. After taking into account all of the above assumptions, we summarize in Tab. 5.2, for each of the considered models, the rough number of tracer particles which we use for our calculations as well as their mass resolutions.

5.4 Results I: Progenitor dependence of ^{44}Ti and ^{56}Ni production

In this section, we examine the production of ^{44}Ti and ^{56}Ni with respect to the progenitor dependence by taking into account a 15 $M_\odot$ and a 20 $M_\odot$ ZAMS star (see Tab. 5.1). We will first present general

considerations about the dependence of ^{44}Ti and ^{56}Ni on the hydrodynamic properties, such as temperature and density profiles, and then we will focus on each of the considered supernova explosion models.

5.4.1 Trends in the peak density – temperature plane

Together with the expansion time scale, which decides how fast reactions occur, the entropy and the initial composition, the explosive nucleosynthesis of ^{44}Ti and ^{56}Ni is mainly determined by the peak density and by the peak temperature reached by the matter due to the passage of the SN shock through the different layers of the star or due to the neutrino heating of the matter.

Magkotsios et al. (2010) explored in detail the sensitivity of the ^{44}Ti and ^{56}Ni production to the variations in reaction rates, electron fraction, and nuclear network size by using simple hydrodynamic trajectories which scale exponentially or as a power low with time. In particular, they identify six main regions in the peak temperature-density (peak T-D) plane which are characterized by different nuclear burning patterns. They control the production of ^{44}Ti, independently from which kind of evolution profile they choose for the temperature and density. The only difference caused by the shape of the trajectories, or the expansion time scale, is the extension of these regions in the peak T-D plane. This means that the expansion time scale is not the reason for their formation. Instead, the reason is related to the amount of entropy during the expansion which affects the strength of the key reactions and therefore of the outcome of the nucleosynthesis. Consequently, the phase transitions occur among different burning processes for certain densities and temperatures. On the other hand, the expansion time scale of the matter influences the actual location of the separation between the different burning regions in the peak T-D plane. In fact, for larger expansion time scales the matter spends more time in a certain burning regime. Therefore, the value of the density can be different when the temperature at which the burning transition occurs is reached. This translates into a shifting of the borders of the different burning processes in the peak T-D plane. Following the work of Magkotsios et al. (2010) and the general considerations about the explosive nucleosynthesis in SN which we made in chapter 1, we summarize the main features of the different regions in the peak T-D plane which characterize the production of ^{44}Ti and ^{56}Ni, assuming $Y_e \sim 0.5$:

- Region 1, called "normal freeze-out" (Woosley et al. 1973), is a freeze-out from nuclear statistical equilibrium (NSE), and the abundances are mostly determined by the Q values. If the threshold temperature for NSE ($T \sim 5$ GK) is reached at relatively high densities ($\rho \simeq 10^9$ g/cm^3), then the NSE freeze out distribution is dominated by ^{56}Ni, Si and Fe group nuclei and a small amount of α particles ($X_\alpha \sim 10^{-3}$);

- Region 2, called "QSE-leakage", is formed when the temperature decreases to $T \sim 5$ GK at a density about $\rho \simeq 10^8$ g/cm^3. At this density, the matter composition is dominated by Si and Fe group nuclei, and there are very few α-particles. Differently from the normal freeze-out region, in this case the efficiency of the capture reactions is different. This results in the formation of two quasi-statistical-equilibrium (QSE, see chapter 1) clusters in the region of Si-Ca nuclei and Fe-group nuclei, with ^{44}Ti being located in the upper limit of the intermediate mass cluster and ^{56}Ni in the center of the Fe-group cluster. Since there is a continuous flow transfer from the Si-Ca cluster to the Fe-group cluster, the amount of ^{44}Ti which is synthesized will be decreased a lot, while the one of ^{56}Ni will be favored. Consequently, a ^{44}Ti chasm region is formed due to the phase transition from one QSE cluster configuration to two QSE cluster configurations and to the subsequent flow leakage which depletes ^{44}Ti and enhances ^{56}Ni;

- Region 3, called "α-rich freeze out" (Woosley et al. 1973), which spans, at $T \simeq 5$ GK, over $10^4 \text{g/cm}^3 \lesssim \rho \lesssim 10^7 \text{g/cm}^3$. As the matter expands and cools some Si-group and Fe-group, as well as ^{44}Ti mass fractions in QSE have the shape of an "arc", starting from low values at high temperature, going to a local maximum and then back to a local minimum as the temperature decreases. In particular, after this "arc", the mass fraction of Si-group nuclei, of some Fe-group nuclei and of ^{44}Ti increases again (see the detailed discussion in Magkotsios et al. 2010). After the freeze out, the most important nucleosynthesis yield include a very large amount of ^{56}Ni, a relatively high mass fraction of ^{44}Ti and α particles ($X_\alpha \sim 10^{-2}$);

- Region 4, called "αp-rich freeze-out", is a particular case of the α-rich freeze out. In this region, the β-processes p(e$^-$, ν_e)n and n(e$^+$, $\bar{\nu}_e$)p play a crucial role compared to the other regions. The β-processes cause the matter to be slightly more proton-rich at high densities and temperatures. This increase of the proton number in an α-rich environment is the reason for the name αp-rich freeze-out;

- Region 5, called "photodisintegration", corresponds to temperatures high enough to establish equilibrium conditions (NSE or QSE), but the densities are so low that the photodisintegration dominates over the capture reactions, and after freeze-out, the matter is mainly made of protons and α particles;

- Region 6, is the "incomplete Si burning" (see chapter 1). The peak temperatures and densities are such that the expansion timescale is comparable to the time to reach a single QSE cluster state and several small-scale QSE clusters are formed in these conditions. The mass fractions of the produced elements freeze out from the QSE states without undergoing any transition phase. The trends of the mass fraction in region 6 are similar to the ones of region 1. However, in region 6, the matter freezes out from different equilibrium states depending on the number and shape of QSE clusters and, thus, on the initial composition of the burning process.

Magkotsios et al. (2010) identify a border between regions 6 and 3 (between Si-rich and α-rich freeze out) which appears as a thin chasm line in the peak T-D plane. It encloses an angle of $\sim 70°$ with the temperature axis (see Fig. 4 of Magkotsios et al. 2010). The behavior of the mass fraction of ^{56}Ni in the peak temperature-density plane is simpler to interpret, because ^{56}Ni does not go through different phase transitions as ^{44}Ti does. This is due to the fact that, differently from ^{44}Ti, ^{56}Ni remains in equilibrium with its neighborhood. In region 1, a single QSE cluster which includes ^{56}Ni stays intact until freeze out. In region 2, two QSE clusters are formed. One of them includes ^{56}Ni. In region 3, the QSE cluster remains centralized in the Fe-group nuclei, including ^{56}Ni. In general, the trend of ^{56}Ni, at $Y_e = 0.5$, can be simply explained by global equilibrium considerations. The above considerations made about the behavior of the ^{44}Ti and ^{56}Ni yields in the peak T-D plane using parametrized trajectories can only be taken as a general guidance in interpreting the nucleosynthesis results of the post-processed hydrodynamic trajectories of SNe simulations for several reasons. For example, our hydrodynamic trajectories, in particular the density and temperature profiles, obtained with sophisticated numerical simulations do not simply have an exponential or power low dependence with time, as the ones used in the study of Magkotsios et al. (2010). Nevertheless, we expect to reproduce the general trends and features of ^{44}Ti and ^{56}Ni mass fractions in the peak T-D plane mentioned above, in the regions which overlap with the peak temperature and density values from our hydrodynamic simulations (in 3D or 1D).
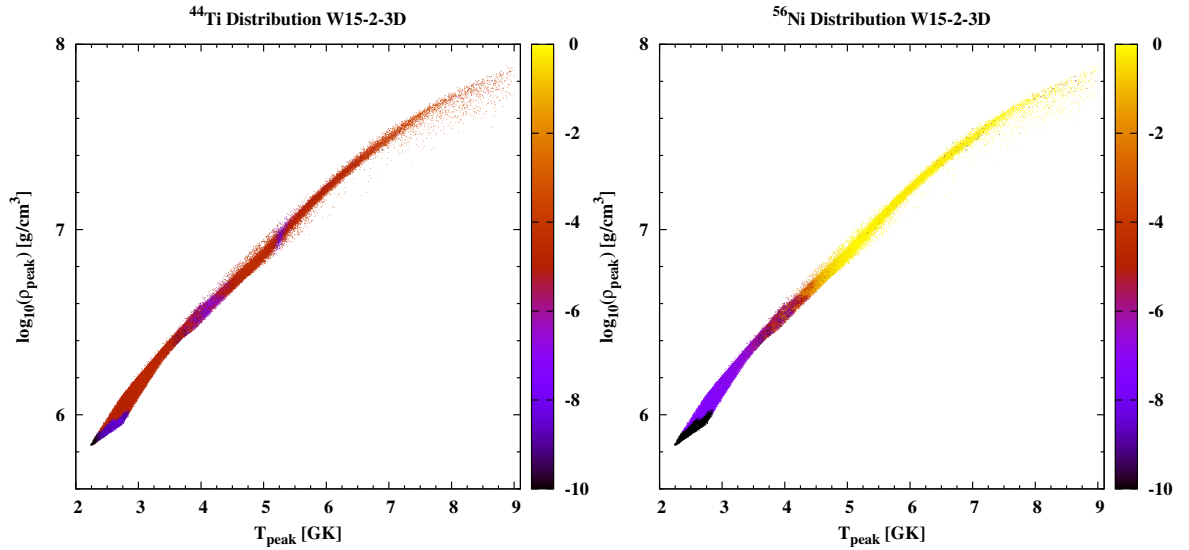
Figure 5.1 Left: For each of the post-processed particles of model W15-2-3D (Wongwathanarat et al. 2014), we show the logarithm of the mass fraction of ^{44}Ti as function of the peak density and peak temperature reached by the matter due to the passage of the shock wave during the supernova explosion. The thin blue line at $T_{\text{peak}} \sim 5.2$ GK corresponds to the chasm which separates the α-rich from the Si-rich region. Right: Same as left, but for ^{56}Ni.

5.4.2 Production of ^{44}Ti and ^{56}Ni in 3D 15 $M_\odot$ models
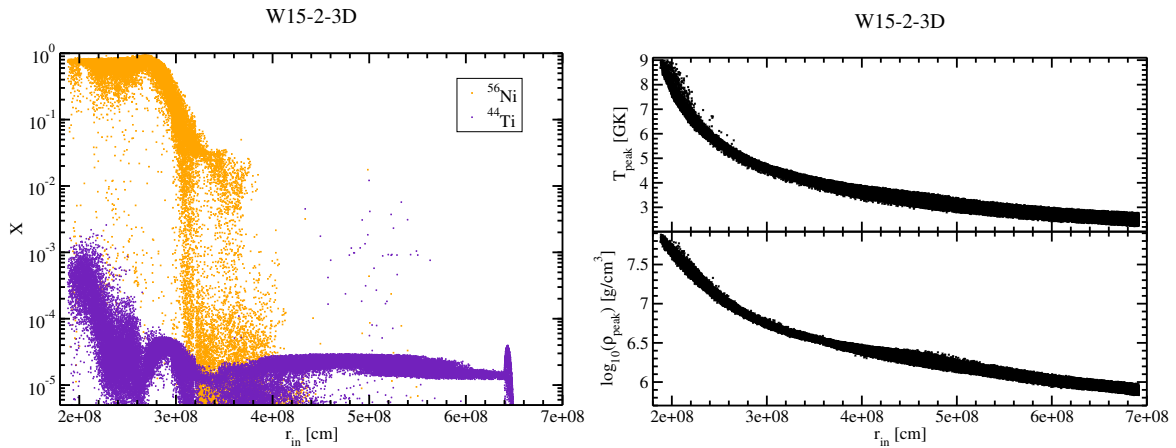
Figure 5.2 Left: Mass fraction X of ^{44}Ti and ^{56}Ni of the post-processed trajectories of model W15-2-3D from Wongwathanarat et al. (2014) as function of the initial radius r_{in}. Right: Peak temperature T_{peak} in GK (upper panel) and logarithm of peak density in g/cm^3 (lower panel) reached by the post-processed trajectories as function of the initial radius.

After the above general considerations about the expected behavior of ^{44}Ti and ^{56}Ni mass fractions in the peak-temperature density plane, we start by examining our nucleosynthesis results of model W15-2-3D (see Tables 5.1 and 5.2) in the *shock-heated* ejecta only (see Sect. 5.3) which have an initial

$Y_e \sim 0.5$. In Fig. 5.1, we show for each of the post-processed trajectories of the shock-heated matter the color scale of the logarithm of $X(^{44}\text{Ti})$ (left) and $X(^{56}\text{Ni})$ (right) as functions of the logarithm of the peak density ($\log_{10}(\rho_{\text{peak}})$, ρ_{peak} in g/cm^3) and peak temperature (T_{peak}, in GK) for the model W15-2-3D. The relevant values of ρ_{peak} and T_{peak} in our simulations span in the ranges $\rho_{\text{peak}} \simeq (10^6 - 10^8)$ g/cm^3 and $T_{\text{peak}} \simeq (2-9)$ GK. Thus, from the above six considered regions in peak T-D plane in which ^{44}Ti and ^{56}Ni can be produced explosively, we are only dealing with the α-rich and the Si-rich freeze out ones. From Fig. 5.1 (left), we notice that ^{44}Ti seems to be produced with an average mass fraction of $\sim (10^{-4} - 10^{-5})$ with the exception of some regions (bluish), in which a depletion in the production of ^{44}Ti takes place. The first depletion region of ^{44}Ti appears as a very thin band at about $T_{\text{peak}} \simeq 5.2$ GK and corresponds to the phase transition from the α-rich to the Si-rich freeze out. Its orientation with respect to the temperature axis is about $80°$, which is quite similar to what Magkotsios et al. (2010) identify in their study. The second blue band (low mass fraction of ^{44}Ti) appears at $T \simeq 4.2$ and is broader than the first one and is mixed to other higher values of $X(^{44}\text{Ti})$. At temperatures lower than 4.2 GK, the yield of ^{44}Ti generally starts decreasing in a monotonic way. Since the amount of ^{44}Ti produced in the Si-rich freeze out sensitively depends also on the matter composition, it can happen that ^{44}Ti is still significantly produced even for $T \lesssim 4$GK, especially if the peak density of the matter is high enough at these temperature. The blue band at $T_{\text{peak}} \lesssim 3.8$ GK shows the boundary at which ^{44}Ti is not further significantly produced in the model W15-2-3D.

From Fig. 5.1 (right), as expected from the above discussion, we notice a simpler behavior of the mass fraction of ^{56}Ni compared to ^{44}Ti. In fact, there is no evident phase transition in the peak T-D plane for ^{56}Ni, as we can see from the color coding of $X(^{56}\text{Ni})$ which spans quite smoothly from very high values at high T_{peak} and ρ_{peak}, corresponding to α-rich freeze out region, to gradually lower and lower values as T_{peak} and ρ_{peak} decrease towards the Si-rich freeze out regime. Finally, at $T_{\text{peak}} \lesssim 4$ GK, ^{56}Ni is not significantly produced anymore.

In Fig. 5.2 (left), we even show $X(^{44}\text{Ti})$ and $X(^{56}\text{Ni})$ for each of the post-processed trajectories as functions of the initial distance from the center of the star (r_{in}), while, on the right, we show the corresponding T_{peak} (upper panel) and ρ_{peak} (lower panel) as functions of r_{in}. On the left, we notice that up to $r_{\text{in}} \lesssim 2.6 \cdot 10^8$ cm, there is a significant amount of ^{44}Ti which is produced during the α-rich freeze out. At about $r_{\text{in}} \simeq 2.6 \cdot 10^8$ cm $X(^{44}\text{Ti})$ drops abruptly due to the transition phase from α-rich to Si-rich freeze out. The downward spike of $X(^{44}\text{Ti})$ does not occur exactly at the same position for all of the trajectories, since the traverse of the thin chasm line depends on the exact value of T_{peak} and ρ_{peak} of the matter and on the location of the thin chasm itself in the peak T-D plane which depends on the expansion timescale (see also the corresponding T_{peak} and ρ_{peak} on the right). Therefore, one of the effects of 3D simulations is to produce different amounts of ^{44}Ti for the same initial radius, because, in 3D, the shock hits the matter with an angular dependence, even if the particles have the same r_{in}. This can also be seen from the "width" of T_{peak} and ρ_{peak} as functions of r_{in}. After the passage of the thin chasm, with increasing r_{in}, the production of ^{44}Ti occurs in the Si-rich freeze out region. In particular, its mass fraction increases and then decreases again at $T_{\text{peak}} \simeq 4$ GK, which corresponds to $r_{\text{in}} \simeq 3.2 \cdot 10^8$ cm, assuming a typical "arc" shape. For larger radii, although T_{peak} is relatively low ($T_{\text{peak}} \simeq (3-4)$ GK), ^{44}Ti is still produced in non negligible amounts, because ρ_{peak} is relatively high ($\rho_{\text{peak}} \sim 10^6$g/cm^3), so that some ^{28}Si can still be converted to ^{44}Ti. Furthermore, in the Si-rich region the exact amount of produced ^{44}Ti sensitively depends on the initial composition of the fuel, as mentioned above. The production of ^{56}Ni is, as already seen in the peak T-D plane in Fig. 5.1, very high in the α-rich region, namely at $r_{\text{in}} \lesssim 2.6 \cdot 10^8$ cm, while it starts decreasing in the Si-rich region, and at $T_{\text{peak}} \simeq 4$ GK there is again a dramatic decrease of $X(^{56}\text{Ni})$, although there are a lot of "raining" points mainly due to the explosion asymmetries of our 3D model.

After having seen how $X(^{44}\text{Ti})$ and $X(^{56}\text{Ni})$ depend on the peak temperature and density reached

by the matter during the explosion, one may ask which is the correlation, if there is any, between the produced amounts of ^{44}Ti and ^{56}Ni themselves. The answer to this question is very important, because it tells us whether we should expect to detect ^{56}Ni each time ^{44}Ti is detected in observations of SNe remnants (we will come back to this point in Sect. 5.7). An attempt to answer this question, at least theoretically speaking, leads us to the next subsection, in which we simply show X(^{44}Ti) as a function of X(^{56}Ni) for our SN model W15-2-3D.

Trends in the Ti – Ni plane

In Fig. 5.3, we show the logarithm of X(^{44}Ti) as function of X(^{56}Ni) for the post-processed matter of model W15-2-3D of Wongwathanarat et al. (2014) which is heated by the shock wave during the SN explosion. This allows us to see if there is any correlation between the amount of ^{44}Ti and ^{56}Ni which is produced during the SN shock wave passage through the different layers above the proto-neutron star. Indeed, we notice certain correlations between X(^{44}Ti) and X(^{56}Ni), since X(^{44}Ti) is not scattered in a completely random way as a function of X(^{56}Ni), as it would happen in the absence of correlations. Furthermore, at least from a phenomenological point of view, we can identify what we call the four "components" which are shown with different colors:
1) The *first component* (1st comp., black color) corresponds to a relatively high amount of ^{44}Ti, but very little ^{56}Ni (X(^{56}Ni)$\lesssim$ 0.02);
2) The *second component* (2nd comp., red color) corresponds to the band with the "arc" shape which extends over the whole range of X(^{56}Ni) values, but to a quite narrow range of X(^{44}Ti) values, (X(^{44}Ti) $\propto 10^{-5}$);
3) We call *third component* (3rd comp., green color) the big patch in the range of X(^{56}Ni)~(0.4-0.8) and, besides this patch, some randomly scattered values over the whole X(^{56}Ni) and X(^{44}Ti) ranges;
4) The *fourth component* (4th comp., blue color) corresponds to the quite narrow band which extends over a small range of X(^{56}Ni) values (X(^{56}Ni)$\sim$ 0.6 − 0.92) but to a very large interval of X(^{44}Ti) values (X(^{44}Ti) $\sim 10^{-6} - 10^{-3}$).
In order to understand the reasons behind the formation of these components or correlations between the ^{44}Ti and ^{56}Ni distributions, we refer once again to Fig 5.2. It shows, on the left, for each of the post-processed trajectories X(^{44}Ti) and X(^{56}Ni) (as already discussed in detail in the previous section) as well as the corresponding T_{peak} in GK and $\log_{10}(\rho_{peak})$ (ρ_{peak} in g/cm^3), on the right, as a function of the initial distance r_{in} of the matter from the center of the star. For the reasons reported in the previous section, at the T_{peak} and ρ_{peak} of our simulation, the distribution of ^{44}Ti has two depletion regions: one corresponding to the traverse of the thin chasm in the peak T-D plane, and the other one at $T_{peak} \sim 4$ GK. On the other hand, X(^{56}Ni) is very high at low r_{in} (at high T_{peak} and ρ_{peak}), and then, at large radii (at low T_{peak} and ρ_{peak}), it starts gradually decreasing up to $T_{peak} \sim 4$ GK. Afterwards, it decreases even much faster to very low values. All these features which we identified in Fig. 5.2 can also be seen in Fig. 5.3. In fact, at large X(^{56}Ni) (at low r_{in}) in average a lot of ^{44}Ti is produced (3rd component), then, at still very high X(^{56}Ni), while approaching the thin chasm of ^{44}Ti, X(^{44}Ti) decreases very steeply (4th component). After the thin chasm, X(^{56}Ni) decreases gradually, while X(^{44}Ti) assumes the typical "arc" shape (2rd component). Finally, at the lowest T_{peak}, X(^{56}Ni) is almost zero, while ^{44}Ti is still being produced in the Si-rich burning regime. In summary, we can generally say that:

- The 1st component corresponds to the Si-rich freeze out region, at $T_{peak} \simeq (2.2 - 4)$ GK, where, depending on ρ_{peak}, some Si can still convert to ^{44}Ti, while there is almost no production of
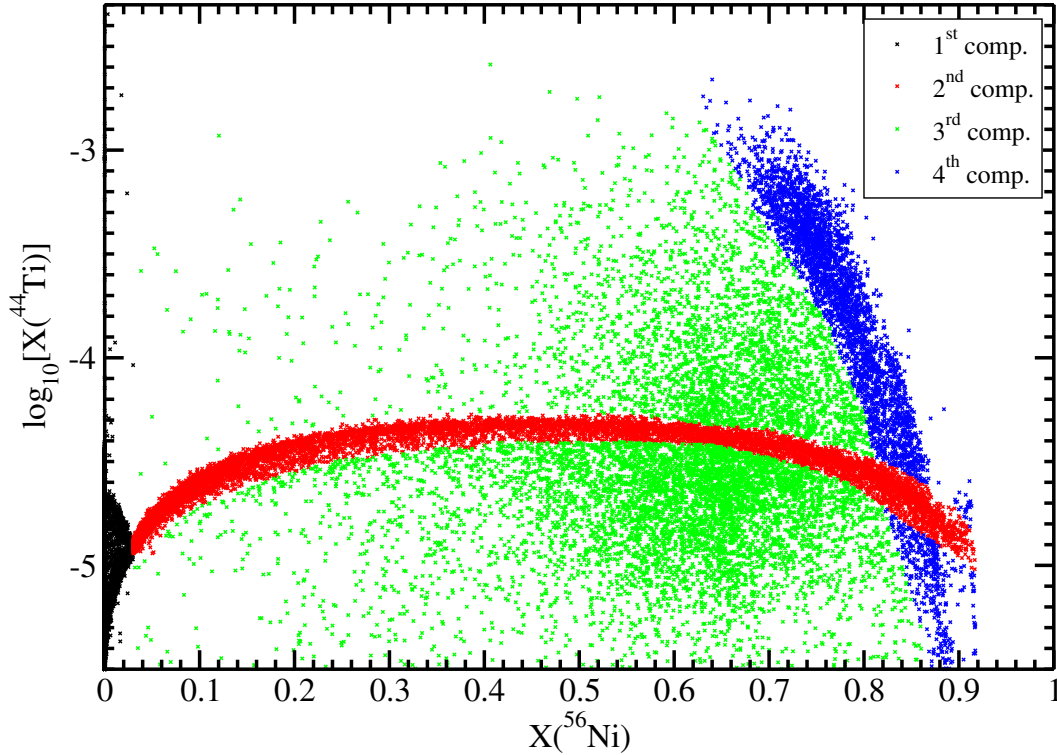
W15-2-3D

Figure 5.3 Logarithm of the mass fraction of ^{44}Ti ($X(^{44}$Ti)) produced in the shock-heated ejecta of the 3D model W15-2-3D as function of the mass fraction of ^{56}Ni ($X(^{56}$Ni)).

^{56}Ni;

- The 2nd component extends from the thin chasm in the peak T-D plane up to $T_{peak} \simeq 4$ GK, where $X(^{44}$Ti) assumes the typical "arc" shape, while $X(^{56}$Ni) decreases gradually;

- The 3rd component corresponds to the production of ^{44}Ti and ^{56}Ni in the α-rich freeze out region, where a lot of ^{44}Ti and a lot of ^{56}Ni are produced. The "patch" and the scattering pattern are due to the asymmetries of the 3D modeling;

- The 4th component corresponds to the region where the chasm is approached from the α-rich freeze out side in the peak T-D plane. Therefore, $X(^{56}$Ni) is always high (^{56}Ni does not go through any transition phase), while $X(^{44}$Ti) is very high in the α-rich region and significantly decreases as the thin chasm is approached.

After the above considerations about the general trends of the post-processed amounts of $X(^{44}$Ti) and $X(^{56}$Ni) in the peak T-D and Ti-Ni planes, in Figs. 5.4 and 5.5, we show, for each of the above considered four components of model W15-2-3D, $X(^{44}$Ti) and $X(^{56}$Ni) in the peak T-D plane. The first components (upper panel in Fig. 5.4) are mainly concentrated in the low region of the peak T-D plane, with a significant amount of ^{44}Ti and a negligible amount of ^{56}Ni. The second components (lower panel in Fig. 5.4), are mainly located in the central region of the peak T-D plane, as expected, since they represent the production of ^{44}Ti and ^{56}Ni in the Si-rich region of the peak T-D plane. The
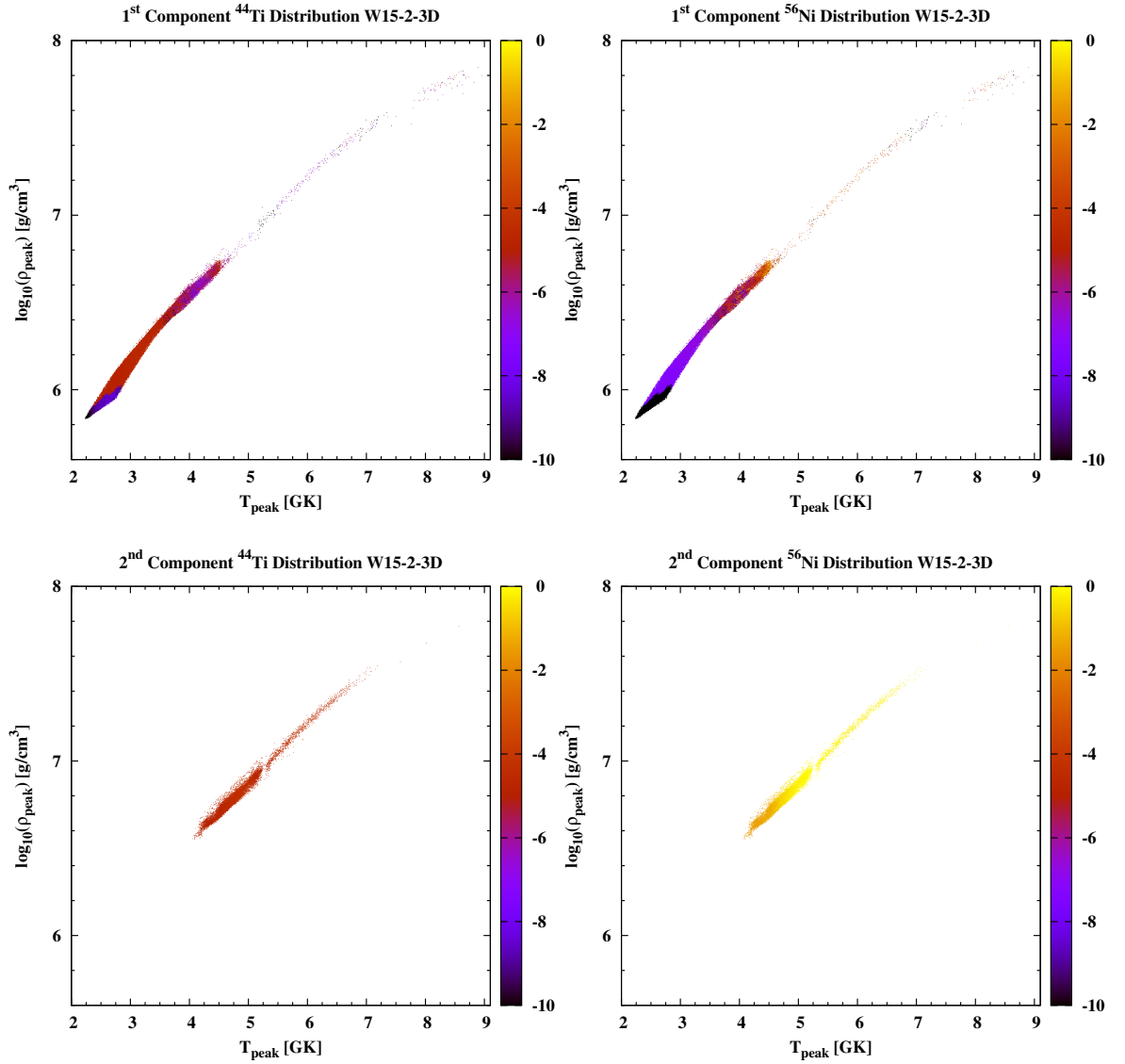
Figure 5.4 In each panel we show the logarithm of the mass fraction of ^{44}Ti ($\log_{10}[X(^{44}\text{Ti})]$) and ^{56}Ni for each of the considered 1st (upper panels) and 2nd (lower panels) components (see Fig. 5.3 and text for details) of model W15-2-3D as functions of the logarithm of peak density $\log_{10}(\rho_{\text{peak}})$ (ρ_{peak} in g/cm^3) and peak temperature T_{peak} in GK reached by the matter because of the shock wave heating. The panels on the left refer to ^{44}Ti, while the ones on the right to ^{56}Ni.
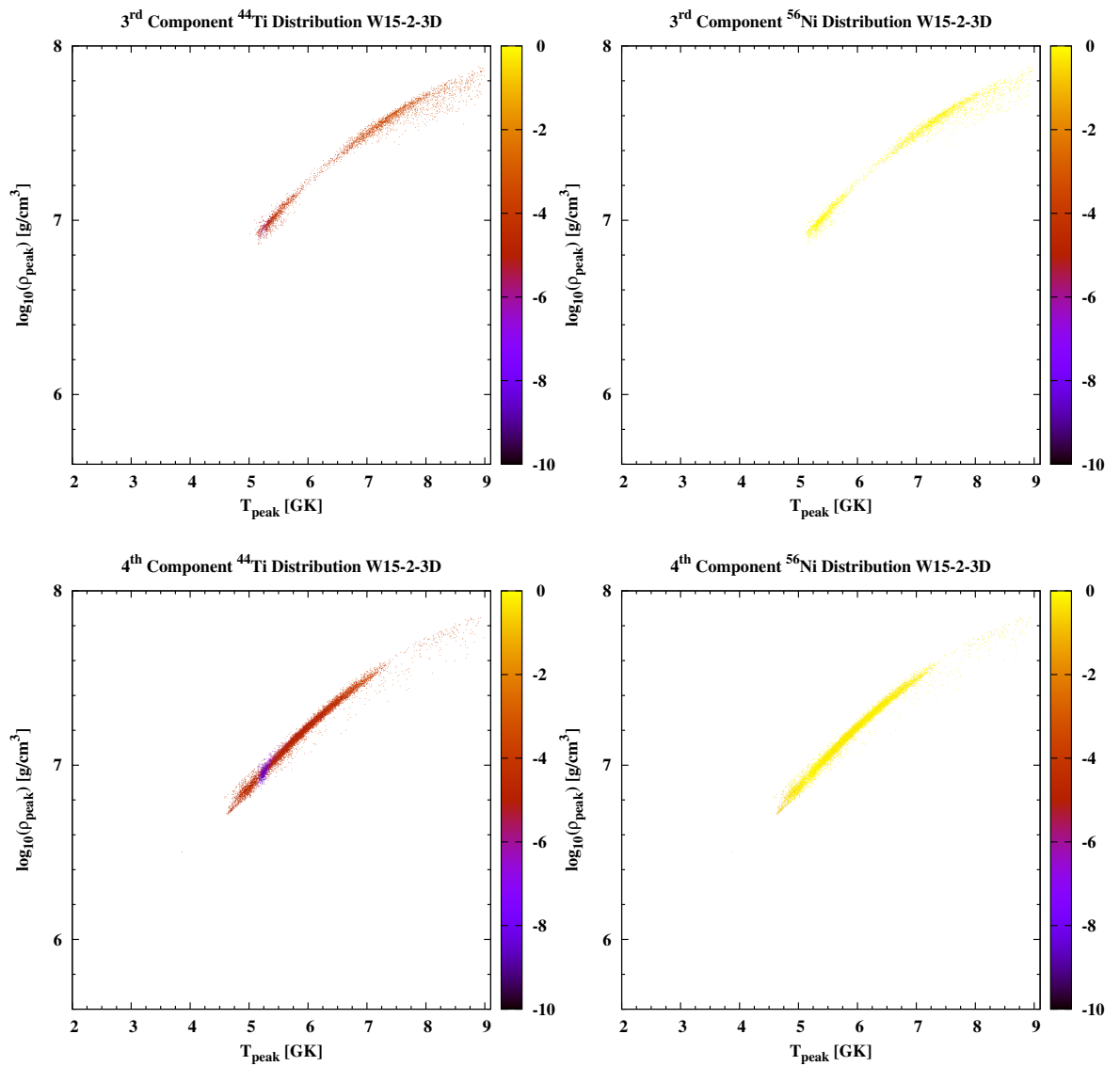
Figure 5.5 Same as Fig. 5.4, but for the 3rd and 4th components of the model W15-2-3D (see Fig. 5.3 and text for more details).
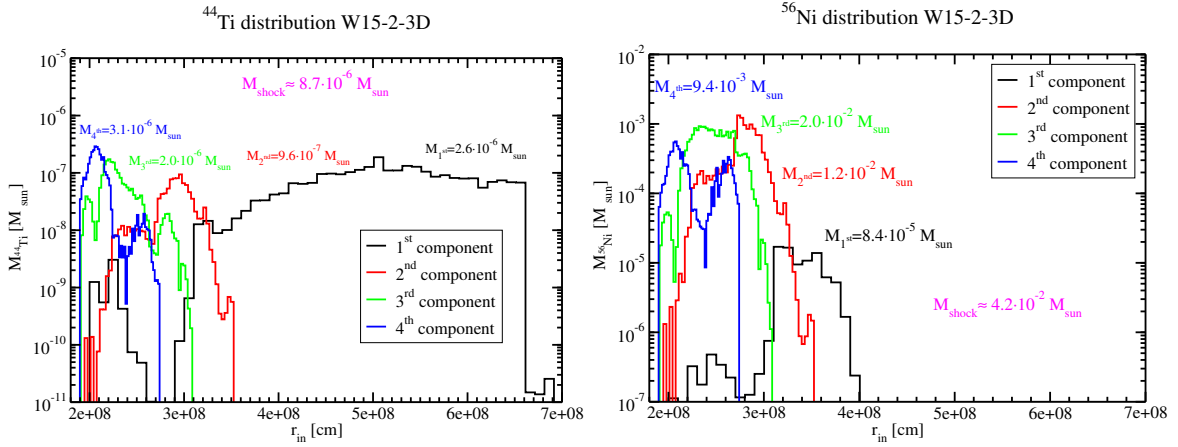
Figure 5.6 Left: Histogram of the mass distribution in $M_\odot$ of ^{44}Ti produced in the shock-heated ejecta as a function of the initial radius r_{in} for each of the considered "components" (see Fig. 5.3) of the 3D model W15-2-3D. Right: Same as left, but for ^{56}Ni.

third and the fourth components in Fig. 5.5 are centered in the right upper part of the peak T-D plane, and they both overlap with the α-rich freeze out region. In particular, we notice the presence of the thin chasm in the fourth component, which appears as a thin blue line in the X(^{44}Ti) distribution, while there is nothing for ^{56}Ni in the corresponding location in the peak T-D plane, because ^{56}Ni does not go through any transition phase while passing from the α-rich to the Si-rich freeze out regions.

In Fig. 5.6 we show the histograms of the produced mass distributions in $M_\odot$ of ^{44}Ti (left) and ^{56}Ni (right) as functions of the initial radius r_{in} for each of the four identified components (see Fig. 5.3), in order to have a quantitative idea about the amounts of these isotopes which are produced in each of them. As we expect, the most part of ^{44}Ti and ^{56}Ni is produced in the third and fourth components, because they correspond to the α-rich freeze out regime. Quite surprisingly, in the first component of ^{44}Ti distribution, there is about 30% of the total amount of ^{44}Ti which is produced thanks to the shock heating of the matter in the SN explosion: $M_{shock}(^{44}\text{Ti}) \simeq 8.7 \cdot 10^{-6} \, M_\odot$. Analogously, the total amount of synthesized ^{56}Ni in our analysis of the shock-heated ejecta is $M_{shock}(^{56}\text{Ni}) \simeq 4.2 \cdot 10^{-2} \, M_\odot$. These amounts of ^{44}Ti and ^{56}Ni which we obtain in the shock-heated ejecta are only a *lower limit* of the actual amounts which can be synthesized in our models, since the yields which can be produced in the matter heated by neutrinos (ν-heated ejecta) have not yet been considered, due to the approximate knowledge of Y_e in whose ejecta, as discussed in Sect. 5.3. Therefore, one of the open questions which we want to address now is: Which is the contribution of the ν-heated ejecta to the total amount of the produced ^{44}Ti and ^{56}Ni in CCSNe? This brings us to the next discussion.

Production of ^{44}Ti and ^{56}Ni in the neutrino-heated ejecta

If the matter interacts with neutrinos, then the electron fraction can change significantly due to the β-processes (as discussed in chapters 3 and 4) and the synthesis of ^{44}Ti and ^{56}Ni sensitively depends on Y_e. The electron fraction of the matter corresponds to the weighted average, with a probability X_i, of the proton/nucleon ratio of the nuclear species, each of them having a mass fraction X_i. In general, the most abundant nuclei which are produced during nucleosynthesis calculations have a proton/nucleon ratio close to the current value of Y_e, although a certain spread exists due to different nuclear structure

and reaction rate effects (Arnett 1977). This means that the production of ^{44}Ti and ^{56}Ni (symmetric nuclei, $Z/A = 0.5$) is maximized if $Y_e = 0.5$. For lower Y_e values, both ^{44}Ti and ^{56}Ni tend to be underproduced compared to the symmetric case (Woosley & Hoffman 1992), while at slightly higher Y_e, the production of ^{56}Ni is still comparable to the $Y_e = 0.5$ case (Magkotsios et al. 2008). Since Y_e in our ν-heated ejecta is not very well constrained, we make two different assumptions in order to perform our nucleosynthesis calculations:

(1) We take Y_e (at $T = 5$ GK, threshold temperature for NSE) as it is given by the hydrodynamic simulations ($Y_{e,\text{sim}}$);

(2) We simply take Y_e from the progenitor ($Y_{e,\text{prog}}$).

These assumptions allow us to give different limits about the produced yields of ^{44}Ti and ^{56}Ni. For model W15-2-3D, in the $Y_{e,\text{sim}}$ case, we get $M_\nu(^{44}\text{Ti}) \simeq 7.16 \cdot 10^{-6} \ M_\odot$ and $M_\nu(^{56}\text{Ni}) \simeq 0.1 \cdot 10^{-2} \ M_\odot$, while in the $Y_{e,\text{prog}}$ case, we have $M_\nu(^{44}\text{Ti}) \simeq 1.49 \cdot 10^{-4} \ M_\odot$ and $M_\nu(^{56}\text{Ni}) \simeq 5.38 \cdot 10^{-2} \ M_\odot$. In these approximations, we can give an estimate of the total amounts $M_{\text{TOT}} = M_{\text{shock}} + M_\nu$ of ^{44}Ti and ^{56}Ni yields produced in our model.

Using $Y_{e,\text{sim}}$ to determine the initial composition of our network calculations, we get:

$$M_{\text{TOT}}(^{44}\text{Ti}) \simeq 1.6 \cdot 10^{-5} \ M_\odot, \tag{5.1}$$

$$M_{\text{TOT}}(^{56}\text{Ni}) \simeq 4.3 \cdot 10^{-2} \ M_\odot. \tag{5.2}$$

Using $Y_{e,\text{prog}}$ as boundary condition for the nuclear species, we obtain:

$$M_{\text{TOT}}(^{44}\text{Ti}) \simeq 1.6 \cdot 10^{-4} \ M_\odot, \tag{5.3}$$

$$M_{\text{TOT}}(^{56}\text{Ni}) \simeq 9.6 \cdot 10^{-2} \ M_\odot. \tag{5.4}$$

The produced yields of both ^{44}Ti and ^{56}Ni using $Y_{e,\text{prog}}$ are much higher than the ones using $Y_{e,\text{sim}}$, because $Y_{e,\text{prog}} \simeq 0.5$, differently from $Y_{e,\text{sim}}$ which, in average, is far from the symmetric value, because of the neutrino interactions with matter. In this way, the efficiency of the synthesis of our isotopes of interest is dramatically damped. Within the limitations of our model, we can consider the yields in $Y_{e,\text{sim}}$ case as a lower limit for the produced amounts of ^{44}Ti and ^{56}Ni, while the ones in $Y_{e,\text{prog}}$ case as an upper limit (we will come back to this question in Sect. 5.7). We notice that while the total amounts of ^{44}Ti and ^{56}Ni sensitively depend on Y_e, their correlations (see Fig. 5.3 and related discussion) are not affected, because the most efficient production of ^{56}Ni and and ^{44}Ti happens for the same conditions in the peak T-D plane, i.e., in the α-rich freeze out regime.

Besides the uncertainties related to Y_e, the production of ^{44}Ti and ^{56}Ni depends also sensitively on the explosion energy of the SN and on the nuclear reaction rates. We will address the first question in Sect. 5.4.4 and the second one in Sect. 5.6.

Furthermore, together with the amounts of produced ^{44}Ti and ^{56}Ni, another observable, which directly gives us important hints about the explosion mechanism of the SN and the role played by the asymmetries, is their spatial distribution. This leads us to the next topic.

Explosion asymmetry dependence and spatial distribution

The model W15-1-3D is very similar to model W15-2-3D in what concerns the relevant physical conditions for the amount of produced ^{44}Ti and ^{56}Ni, since they have the same mass and explosion energy (see Tab. 5.1), but the spatial distribution of ^{44}Ti and ^{56}Ni can be different, because the explosion perturbations are set in a different way (see Wongwathanarat et al. 2014). Therefore, we refer to the

previous sections for the detailed discussion of the formation of the different components in the Ni-Ti plane and their location in the peak T-D plane. We only report the amounts of produced ^{44}Ti and ^{56}Ni obtained in the post-processing of the shock-heated trajectories: $M_{\text{shock}}(^{44}\text{Ti}) \sim 8.3 \cdot 10^{-6}$ $M_\odot$ and $M_{\text{shock}}(^{56}\text{Ni}) \sim 4.1 \cdot 10^{-2}$ $M_\odot$. The very small difference between these values and the corresponding ones of model W15-2-3D is just due to statistical fluctuation. We can estimate that the total amount of produced ^{44}Ti and ^{56}Ni and the uncertainties related to Y_e are similar to what already discussed for model W15-2-3D. On the contrary, a big difference between these two models is the spatial distribution of ^{44}Ti and ^{56}Ni, as shown in Fig. 5.7, in which we display the maps of the surface densities of ^{44}Ti and ^{56}Ni obtained by projecting (integrating) 3D distributions onto a (rotated) meridian plane (these images are courtesy of Annop Wongwathanarat). The white arrows show the kick direction of the compact remnant[5]. The lengths of the arrows do not correspond to the kick magnitudes. The red "+" sign marks the center of the explosion (coordinate origin), while the white "x" marks the current position of the NS[6]. The maps show the distributions at time $t = 37562.3$ s and $t = 50321.6$ s for model W15-1-3D (upper panel: ^{44}Ti on the left and ^{56}Ni on the right) and model W15-2-3D (lower panel: ^{44}Ti on the left and ^{56}Ni on the right), respectively. There is a clear difference between the spatial distribution of the ejecta of the two models: in model W15-1-3D, both ^{44}Ti and ^{56}Ni are distributed in a more "spherical" way than in model W15-2-3D, where they have a much more elongated shape. The detailed reasons behind the spatial distributions of the nucleosynthesis ejecta in these models are explained in Wongwathanarat et al. (2013). In particular, Wongwathanarat et al. (2013) see a clear correlation between the anisotropic production and distribution of elements produced during the explosive nucleosynthesis and the size of the NS kick. In the case of large NS kicks, as it happens for our models W15-1-3D and W15-2-3D, the explosion is significantly stronger in the direction opposite to the kick, and therefore the elements which are explosively produced are ejected in directions opposite to the NS kick. As we may expect from our previous study of the correlations between ^{44}Ti and ^{56}Ni in the Ni-Ti plane, these isotopes are produced together. This is also confirmed in Fig. 5.7, where, in general, we find ^{44}Ti in the same place where we find ^{56}Ni, as we can see by comparing the left and the right sides of each panel. Therefore, theoretically speaking, we expect strong correlations between the spatial distributions of ^{44}Ti and ^{56}Ni produced in a SN, while from the observational side (e.g., CasA), there is not yet an unambiguous answer to this question (e.g., Grefenstette et al. 2014, Milisavljevic & Fesen 2015). We will come back to this point in Sect. 5.7, where we will put our theoretical results in a more general context by comparing them with other theoretical works and observations.

Now that we have a general idea about what to expect in the ^{44}Ti and ^{56}Ni distributions of a $M = 15$ $M_\odot$ progenitor, let us see what happens if we consider a $M = 20$ $M_\odot$ progenitor. This allows us to investigate the progenitor dependence of the production of our isotopes of interest.

5.4.3 Production of ^{44}Ti and ^{56}Ni in 3D 20 $M_\odot$ models

In this section, we consider the production of ^{44}Ti and ^{56}Ni in a 20 $M_\odot$ progenitor, whose SN explosion was simulated in 3D (Wongwathanarat et al. 2013, Wongwathanarat et al. 2014). This model has an explosion energy similar to W15-2-3D and W15-1-3D, but a different mass (Tab. 5.1). This allows us to focus only on the progenitor dependence of the production of ^{44}Ti and ^{56}Ni. Analogously to what we have done for model W15-2-3D in Sect. 5.4.2, we will start by discussing the outcome of the SN explosive nucleosynthesis only in the *shock-heated* ejecta. In Fig. 5.8, we show, similarly to

---

[5]We refer to Wongwathanarat et al. (2010b) and Wongwathanarat et al. (2014) for a detailed discussion about the definition and the mechanism which forms the kick of the NS in these simulations, since it goes beyond the aims of this work.

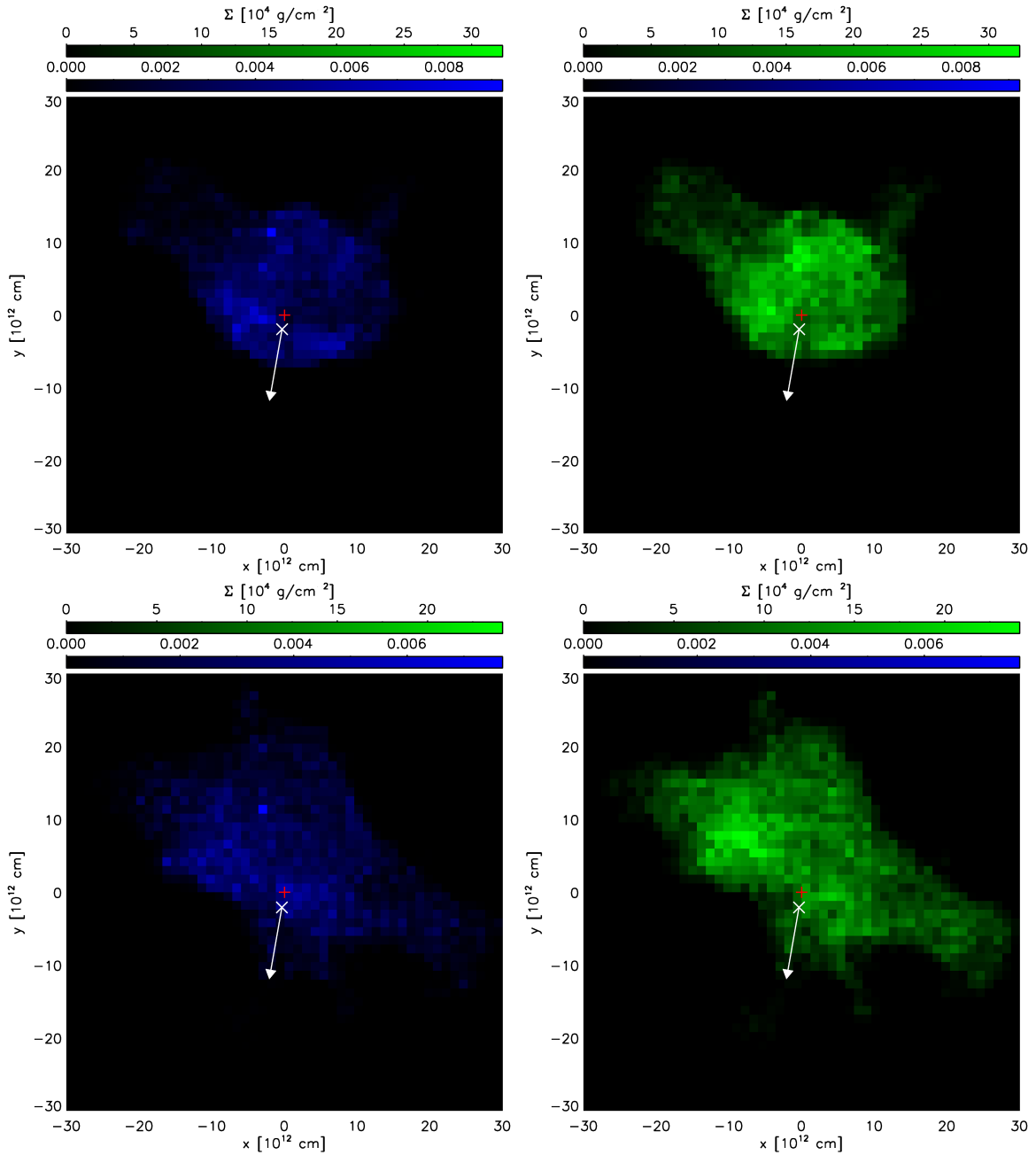[6] The position is obtained simply by $v_{\text{NS}}(3.3s) \cdot t$, where v_{NS} is the velocity of the NS.

Figure 5.7 Upper panels: Surface densities Σ in g/cm^2 of the distribution of ^{44}Ti (left) and ^{56}Ni (right) in model W15-1-3D. The white arrows show the kick direction of the compact remnant. The length of the arrows doesn't correspond to the kick magnitude. The red "+" sign marks the center of the explosion (coordinate origin), while the white "x" marks the current position of the NS. Lower panels: Same as upper panel, but for model W15-2-3D. The maps show the distributions at time $t = 37562.3$ s and $t = 50321.6$ s for W15-1-3D and W15-2-3D, respectively. (Images are courtesy of Annop Wongwathanarat.)

Fig. 5.1, the logarithm of the mass fraction of ^{44}Ti (left) and ^{56}Ni (right) as functions of T_{peak} and ρ_{peak} reached by the matter in the Si and O layers when the SN shock wave passes through it. In this case as well, we can recognize some general features in the peak T-D plane, as we already did in the W15-2-3D case. At $T_{\text{peak}} \simeq 5.2$ GK in Fig. 5.8 (left), we notice the presence of the thin chasm which appears as a thin blue line in the distribution of ^{44}Ti and separates the region where nucleosynthesis happens in the α-rich freeze out (at $T_{\text{peak}} \gtrsim 5.2$ GK) and the region where it happens in the Si-rich freeze out (at $T_{\text{peak}} \lesssim 5.2$ GK). As expected, in the distribution of ^{56}Ni in the peak T-D plane, there is no feature appearing, while passing from the α-rich to the Si-rich freeze out regime (see discussions in Sect. 5.4.1). At $T_{\text{peak}} \lesssim 4$ GK both X(^{44}Ti) and X(^{56}Ni) decrease significantly. Differently from the W15-2-3D model, in the N20-4-3D case the production of ^{44}Ti in the Si-rich region stops at $T_{\text{peak}} \sim 4$ GK and does not continue at lower temperatures. This is due to the difference in the progenitor structure, in particular in the density profile (plots not shown here), which is reflected in the post explosion structure as well.

In fact, by comparing Figs. 5.1 and 5.8, we notice that at the same T_{peak} the corresponding ρ_{peak} in the N20-4-3D case is lower than in the W15-2-3D case. Therefore, while in the W15-2-3D model even at relatively low T_{peak}, ρ_{peak} is high enough so that some Si can still be converted to ^{44}Ti, this does not happen in the N20-4-3D model. Another difference between these models is the width of the "diagonal bands" of the mass distributions of ^{44}Ti and ^{56}Ni, namely the ones of N20-4-3D are broader than those of model W15-2-3D.

In order to better understand this difference, we show in Fig. 5.9, analogously to Fig. 5.2, X(^{44}Ti) and X(^{56}Ni) (left) and T_{peak} and ρ_{peak} (right) of model N20-4-3D as functions of the initial radius r_{in} for each of the post-processed trajectories. We notice that the range of T_{peak} and ρ_{peak}, especially at $r_{\text{in}} \lesssim 3.4 \cdot 10^8$ cm, is broader than the corresponding one of model W15-2-3D, which has an almost uniform narrow width as function of r_{in}. The reason for this is, once again, related to the density structure of the progenitors, which shows up in a different propagation of the SN shock wave, since in 3D, the way the SN shock wave hits the matter depends not only on r_{in}, but also on the inclination with respect to it. On the contrary, at $r_{\text{in}} \gtrsim 3.4 \cdot 10^8$ cm, the values of T_{peak} and ρ_{peak} of model N20-4-3D are confined in a narrower range, at fixed r_{in}, than the corresponding ones of model W15-2-3D. This is the reason why, at $T_{\text{peak}} \gtrsim 4$ GK ($r_{\text{in}} \lesssim 3.4 \cdot 10^8$ cm), the mass distribution of ^{44}Ti and ^{56}Ni in the peak T-D plane looks broader in the N20-4-3D case than in the W15-2-3D case. On the other hand, at $T_{\text{peak}} \lesssim 4$ GK ($r_{\text{in}} \gtrsim 3.4 \cdot 10^8$ cm), the mass distribution of ^{44}Ti and ^{56}Ni in the peak T-D plane in the N20-4-3D case is narrower than in the W15-2-3D case.

In Fig. 5.9 (left), we can identify in the X(^{44}Ti) and X(^{56}Ni) distributions all the features which we already discussed in the peak T-D plane. In fact, up to $r_{\text{in}} \simeq 3 \cdot 10^8$ cm, ^{44}Ti and ^{56}Ni are produced in the α-rich freeze out regime and, at $r_{\text{in}} \simeq 3 \cdot 10^8$ cm, the transition to the Si-rich regime takes place, as we can see from the drop of both X(^{44}Ti) and X(^{56}Ni). In the range $r_{\text{in}} \sim (3 - 3.5) \cdot 10^8$ cm, ^{44}Ti and ^{56}Ni are synthesized in the Si-rich region, where X(^{44}Ti) assumes the typical "arc" shape. Finally, at $T_{\text{peak}} \gtrsim 4$ GK, the production of ^{44}Ti and ^{56}Ni is basically finished. In particular, the production of ^{44}Ti does not continue further, for the reasons explained above.

In Fig. 5.10, analogously to Fig. 5.3, we show the logarithm of X(^{44}Ti) as a function of X(^{56}Ni). In analogy to Fig. 5.3, we can identify four "components" in the X(^{44}Ti) distribution. In this case as well, the "1$^{\text{st}}$ component" (black color) and "2$^{\text{nd}}$ component" (red color) correspond to the synthesis of ^{44}Ti and ^{56}Ni in Si-rich freeze out, the "3$^{\text{rd}}$ component" (green color) results from the α-rich freeze out region. The "4$^{\text{th}}$ component" (blue color) contains the thin chasm of ^{44}Ti and corresponds to the transition between the α-rich and Si-rich freeze out regions.

In Figs. 5.11 and 5.12, analogously to Figs. 5.4 and 5.5, we display the location of X(^{44}Ti) and X(^{56}Ni) in the peak T-D plane for each of the identified components. As we expect from the above

discussions, we find the 1st component in the lower region of the peak T-D plane. Then, as T_{peak} and ρ_{peak} increase, we identify the 2nd component. Finally, the 3rd and 4th components appear, together with the thin chasm in the ^{44}Ti distribution, as soon as T_{peak} and ρ_{peak} which characterize the α-rich freeze out are reached.   In order to have a precise idea about the amounts of ^{44}Ti and ^{56}Ni which are
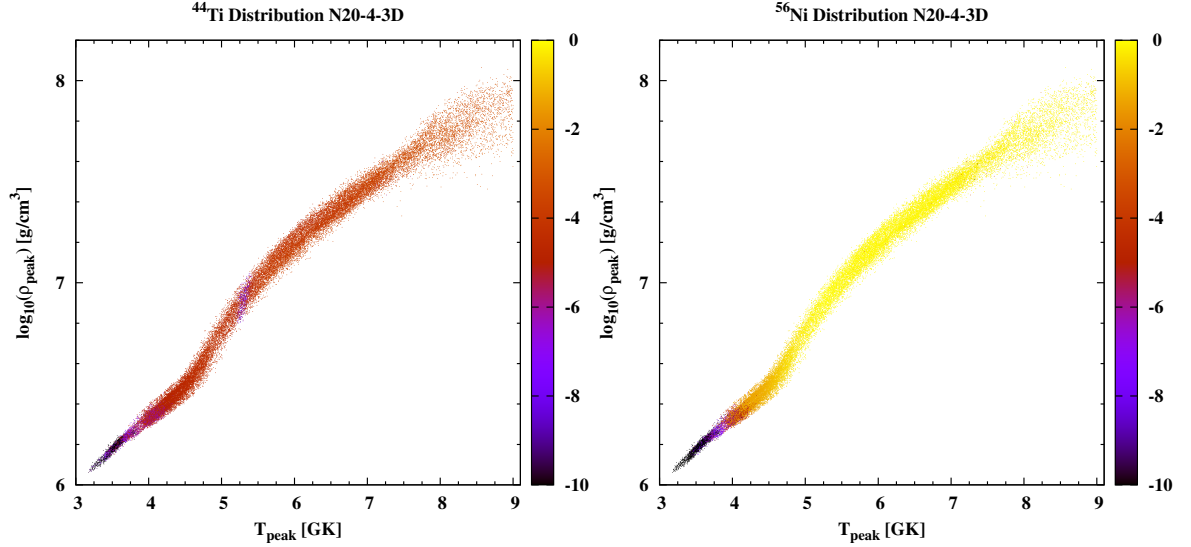

Figure 5.8 Left: Logarithm of the mass fraction of ^{44}Ti as a function of the peak density and of the peak temperature reached by the matter during the passage of the shock wave during the supernova explosion of the 3D model N20-4-3D. Right: Same as left, but for ^{56}Ni.
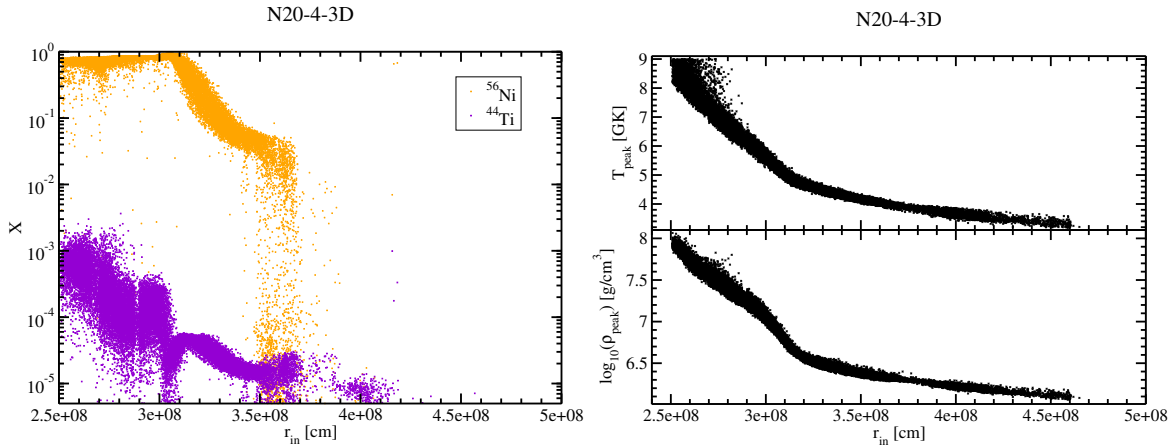
Figure 5.9 Left: Mass fraction X of ^{44}Ti and ^{56}Ni of the post-processed trajectories of model N20-4-3D from Wongwathanarat et al. (2014) as a function of the initial radius r_{in}. Right: Peak temperature T_{peak} in GK (upper panel) and logarithm of the peak density in g/cm^3 (lower panel) reached by the post-processed trajectories as a function of the initial radius.

produced in each of the identified components in the shock-heated ejecta, we show in Fig. 5.13, the histograms for each component of ^{44}Ti (left) and ^{56}Ni (right) as function of the initial radius r_{in}. The total amount of ^{44}Ti produced during the SN shock wave heating is about $8.6 \cdot 10^{-6}$ $M_\odot$, while the
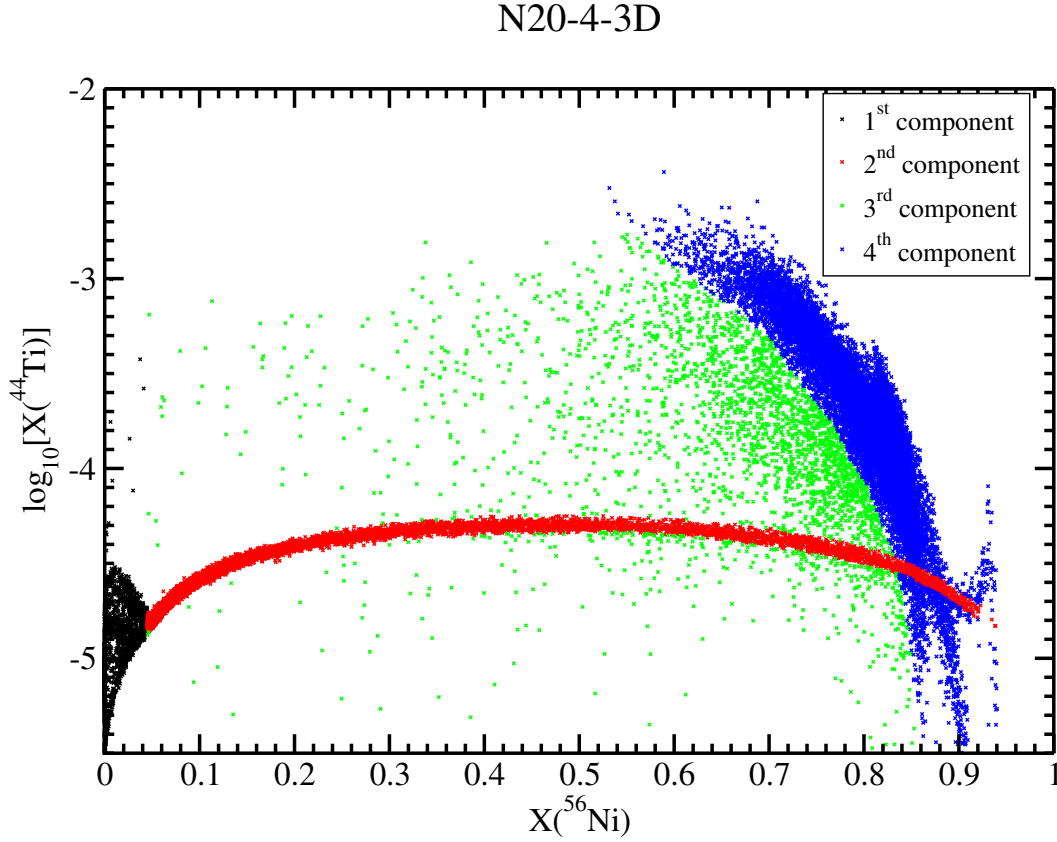
N20-4-3D

Figure 5.10 Mass fraction of ^{44}Ti produced in the explosion of the 3D model N20-4-3D as a function of the mass fraction of ^{56}Ni.The different colors are used to distinct the different correlations between X(^{44}Ti) and X(^{56}Ni), which we call "components".

amount of produced ^{56}Ni is $3 \cdot 10^{-2}$ $M_\odot$. In particular, the shock-heated amount of ^{44}Ti produced in the N20-4-3D model is very similar to the one synthesized in the models W15-2-3D and W15-1-3D. Therefore, it seems that there is no big impact of the different progenitor structure on the production of ^{44}Ti, while there is a bigger impact on the production of ^{56}Ni, since in the heavier progenitor (N20-4-3D) less ^{56}Ni is synthesized as in the lighter ones (W15-2-3D and W15-1-3D). However, we have not yet considered the yields which are produced in the ν-heated ejecta which dramatically depend on Y_e, as already discussed for model W15-2-3D. Therefore, the amounts which we find can only be taken as a lower limit in our model.

After having seen the progenitor difference in the production of ^{44}Ti and ^{56}Ni, we have now to face the next question of our investigations, namely how does the production of our isotopes of interest depends on the explosion energy of the supernova?

5.4.4 Impact of the explosion energy on the production of ^{44}Ti and ^{56}Ni

In this section, we discuss the dependence of the production of ^{44}Ti and ^{56}Ni on the supernova explosion energy. To this aim, we consider a 3D model, called N20-2-3D, which has the same progenitor mass as the N20-4-3D model, but an almost double explosion energy (see Tab. 5.1). Since the be-
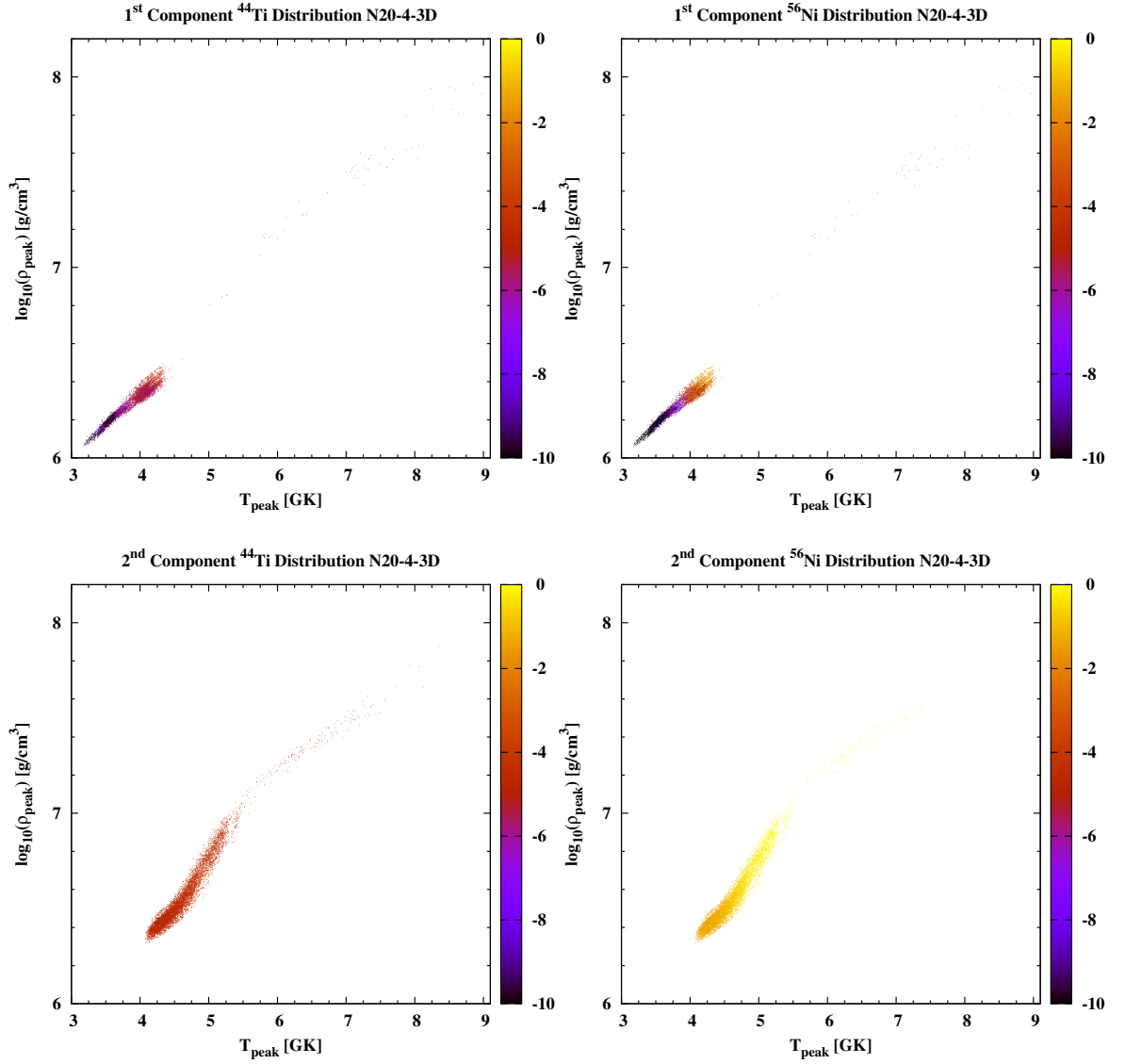
Figure 5.11 In each panel we show the logarithm of the mass fraction of ^{44}Ti ($\log_{10}[X(^{44}\text{Ti})]$) and ^{56}Ni for each of the considered "first 1st and second 2nd components" (see Fig. 5.10 and text) of model N20-4-3D as functions of the logarithm of the peak density $\log_{10}(\rho)$ in g/cm^3 and of the peak temperature in GK. The panels on the left refer to ^{44}Ti, while the ones on the right to ^{56}Ni.
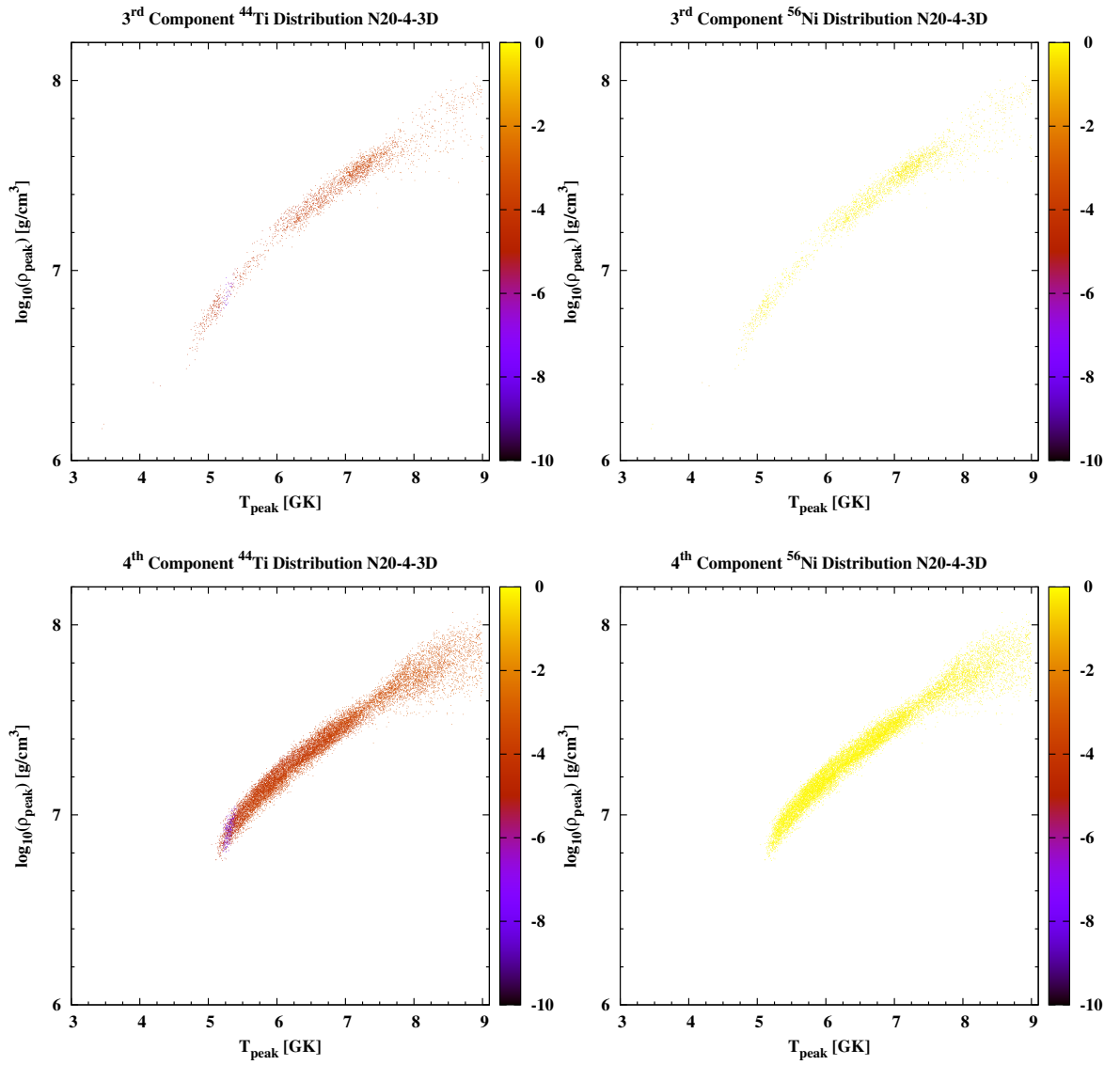
Figure 5.12 Same as Fig. 5.11, but for the third (3rd) and fourth (4th) components of model N20-4-3D (see Fig. 5.10 and text).
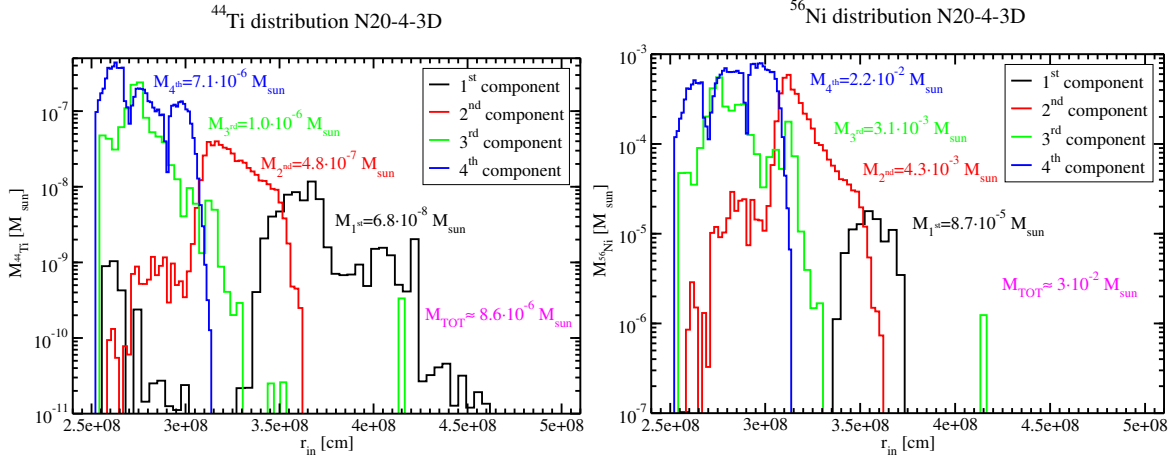
Figure 5.13 Left: Histogram of the mass distribution in $M_\odot$ of ^{44}Ti as a function of the initial radius for each of the considered "components" (see Fig. 5.10) of the 3D model N20-4-3D. Right: Same as left, but for ^{56}Ni.

havior of X(^{44}Ti) and X(^{56}Ni) in the Ni-Ti and peak T-D planes is very similar to the ones of models W15-2-3D and N20-4-3D, we only report here the total amounts of ^{44}Ti and ^{56}Ni which are produced in model N20-2-3D due to the shock-heating of the ejecta: $M_{shock}(^{44}\text{Ti}) \simeq 20.1 \cdot 10^{-6} \, M_\odot$ and $M_{shock}(^{56}\text{Ni}) \simeq 4.9 \cdot 10^{-2} \, M_\odot$. By comparing these amounts with the corresponding ones which are produced in the models N20-4-3D and N20-2-3D, we can say that there is a linear dependence between the synthesized ^{44}Ti and the explosion energy of the SN, since in model N20-2-3D the amount of ^{44}Ti is almost twice as in model N20-4-3D, the latter having half of the explosion energy of the former. The production of ^{56}Ni, instead, is about 1.6 higher in the N20-2-3D case than in the N20-4-3D case.

After having seen the progenitor and explosion energy impacts on the production of ^{44}Ti and ^{56}Ni in the SN shock processed matter, we investigate, in the next section, the dependence of the production of these isotopes on the dimensionality of the simulations, namely we want to investigate the difference between 3D and 1D models.

5.5 Results II: dimensionality dependence of the production of ^{44}Ti and ^{56}Ni

In this section, we consider the production of ^{44}Ti and ^{56}Ni in supernova simulations performed in 1D for the same 20 $M_\odot$ mass progenitor considered in the previous section. This allows us to investigate the difference between the nucleosynthesis yields produced in 1D and 3D thanks to the comparison between model N20-4-3D and the 1D models N20-4-1D and N20-8-1D (see Tab. 5.1). In Fig. 5.14, we show the logarithm of X(^{44}Ti) (left) and of X(^{56}Ni) (right) in the peak T-D plane. By comparing this figure with the 3D counterpart in Fig. 5.8, we notice that the range of values of ρ_{peak} in the 1D case is lower than in the 3D case, while the T_{peak} values are similar. Furthermore, the width of the band in which the values of X(^{44}Ti) and X(^{56}Ni) are confined is much narrower than in the 3D case, as expected from the asymmetries of the 3D model. In the 1D case as well, we can distinguish the different burning regimes in the peak T-D plane, namely at higher T_{peak} and ρ_{peak} we can identify the

α-rich freeze out region, while at $T_{\text{peak}} \simeq 5.2$ GK, the thin chasm appears in the X(^{44}Ti) distribution, while nothing similar appears for X(^{56}Ni) (see discussion in Sect. 5.4.3). Similarly to the 3D case, for model N20-4-1D as well, the significant production of ^{44}Ti and ^{56}Ni ends at $T_{\text{peak}} \simeq 4$ GK. Once again, the reason for this can be seen in Fig. 5.15, where we show X(^{44}Ti) and X(^{56}Ni) (left) and T_{peak} and ρ_{peak} (right) as functions of the initial radius r_{in}. The "raining" points in the X(^{44}Ti) and X(^{56}Ni) distribution are due to the fact that at very similar values of r_{in}, T_{peak} and ρ_{peak} can have very different values (e.g., at $r_{\text{in}} \simeq 3.2 \cdot 10^8$ cm). If T_{peak} and ρ_{peak} had a strict monotonic behavior as a function of r_{in}, then we would expect the ^{44}Ti and ^{56}Ni distributions to be very narrow (almost constant) up to the region where the thin chasm (at $r_{\text{in}} \simeq 3.5 \cdot 10^8$ cm) is approached, and afterwards both X(^{44}Ti) and X(^{56}Ni) decrease significantly.

In Fig. 5.16, we depict the logarithm of X(^{44}Ti) as a function of X(^{56}Ni) for model N20-4-1D. Similarly to the 3D model N20-4-3D, in this case as well, we can distinguish the "four components" in X(^{44}Ti) which describe the passage through different transition phases in the production of ^{44}Ti in the peak T-D plane, namely from α-rich freeze out (3$^{\text{rd}}$ and 4$^{\text{th}}$ components) to Si-rich freeze out (1$^{\text{st}}$ and 2$^{\text{nd}}$). For a detailed discussion of the formation of the different components, we refer to Sect. 5.4.1 and 5.4.2. The main difference between Figs. 5.16 and 5.10 is the width of the components, which is much larger in 3D than in 1D. This is a natural consequence of the fact that in 3D, at the same initial radius, the matter can experience very different T_{peak} and ρ_{peak} depending on the angle at which the shock wave hits the matter (see Sect. 5.4.3), differently from 1D where, by construction, this cannot happen (only radial dependence). In Tab. 5.1, we point out the different mass resolution used for our tracer particles in 3D and 1D, which can also make a small difference in the distributions of ^{44}Ti as a function of ^{56}Ni. In Figs. 5.17 and 5.18, we display, analogously to Figs. 5.11 and 5.12, the location of each component of ^{44}Ti and ^{56}Ni in the peak T-D plane. Similar to the 3D cases, we can distinguish the regions of the α-rich freeze out (3$^{\text{rd}}$ and 4$^{\text{th}}$ components), the Si-rich regime (1$^{\text{st}}$ and 2$^{\text{nd}}$ components), and, as expected, the thin chasm at $T_{\text{peak}} \simeq 5.2$ GK. In Fig. 5.19, we show the histogram of the mass of ^{44}Ti (left) and ^{56}Ni (right) in $M_\odot$ produced in the shock-heated ejecta of each of the four components. As expected, the most of the mass contribution comes from the 4$^{\text{th}}$ and 3$^{\text{rd}}$ components. In total, for model N20-4-1D, we get $M_{\text{shock}}(^{44}\text{Ti}) \simeq 5.2 \cdot 10^{-6} M_\odot$ and $M_{\text{shock}}(^{56}\text{Ni}) \simeq 1.4 \cdot 10^{-2} M_\odot$. In particular, the amount of ^{44}Ti produced in 1D is about a factor of 1.6 lower than in 3D. In fact, the model N20-4-1D has a much lower explosion energy than the N20-4-3D model (see Tab. 5.1). This is due to the fact that in 1D the explosion sets in much later than in 3D (see Fig. 5.20), because in 3D convective motions and instabilities support the explosion, while in 1D this is not possible due to the symmetry restrictions (e.g., Hanke et al. 2012). This can also be seen in the r_{in} range in which nucleosynthesis occurs, namely for the 1D model the nucleosynthesis due to the SN shock wave propagation starts at $r_{\text{in}} \simeq 3.2 \cdot 10^8$ cm (see Fig. 5.15), while in the 3D case it starts at smaller radii, $r_{\text{in}} \simeq 2.5 \cdot 10^8$ cm, as it can see in Fig. 5.9. In order to better constrain the differences between the amount of ^{44}Ti and ^{56}Ni produced in 1D and 3D, we even construct a 1D model which is similar to the 3D model as much as possible, as discussed in the next paragraph.

Impact of the shock propagation on the production of ^{44}Ti and ^{56}Ni

In this paragraph, we discuss the production of ^{44}Ti and ^{56}Ni in the SN explosion of the 1D model N20-8-1D. This model is set up in such a way that the evolution of the shock radius is similar to the one of model N20-4-3D and the explosion sets in more or less at the same time as for the model N20-4-3D. In Fig. 5.20, together with the explosion energy (left), we show the average shock radius (right) for all the considered models with a mass M of 20 $M_\odot$. The average SN shock radius is defined
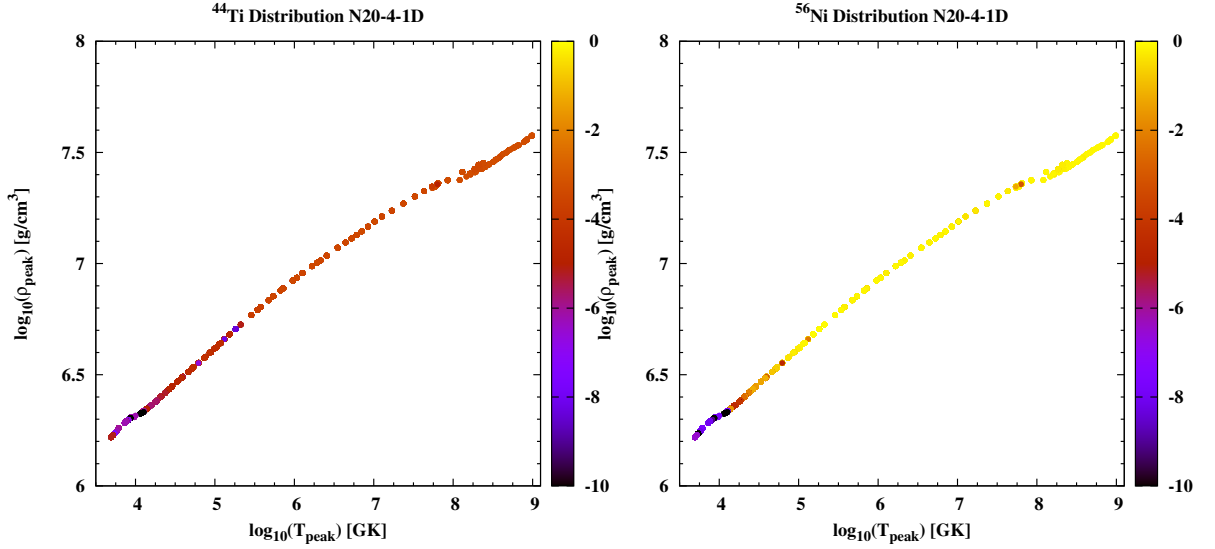
Figure 5.14 Left: Logarithm of mass fraction of ^{44}Ti as a function of the peak density and peak temperature reached by the matter due to the passage of the shock wave during the supernova explosion of the 1D model N20-4-1D. Right: Same as left, but for ^{56}Ni.

as:

$$\langle R_s \rangle \equiv \frac{1}{4\pi} \int R_s(\theta, \phi) d\Omega, \tag{5.5}$$

where $d\Omega = \sin\theta d\theta d\phi$, and $R_s(\theta, \phi)$ is the angle-dependent value of the SN shock radius. In the blue and green boxes we outline the relevant values of radii and postbounce times at which the explosive nucleosynthesis happens, as we can see by comparing with the r_{in} values in the histograms of Figs. 5.13 and 5.19. In Fig. 5.20, we notice that, at the postbounce time which is relevant for explosive nucleosynthesis ($t \sim 0.5 - 0.6$ s), the model N20-8-1D has an explosion energy similar to the one of model N20-4-3D ($E_{\text{exp}} \simeq 1.5$), therefore we expect the amounts of ^{44}Ti and ^{56}Ni produced in model N20-8-1D to be similar to the ones of model N20-4-3D. The amounts of ^{44}Ti and ^{56}Ni produced in the shock-heated ejecta of model N20-8-1D are: $M_{\text{shock}}(^{44}\text{Ti}) \simeq 8.3 \cdot 10^{-6} M_{\odot}$ and $M_{\text{shock}}(^{56}\text{Ni}) \simeq 3.5 \cdot 10^{-2} M_{\odot}$. These values are similar to those obtained for the model N20-4-3D, suggesting that the explosion energy and the propagation of the shock radius, more than the dimensionality, play the leading role in the production of ^{44}Ti and ^{56}Ni.

In Tab. 5.3, we summarize the amounts of ^{44}Ti and ^{56}Ni determined by post-processing the shock-heated ejecta of each of the corresponding models.

Before comparing our results with the observations and discussing them in a more general context, we have to wonder how accurate are the amounts of ^{44}Ti and ^{56}Ni which we predict with our nuclear reaction network. One of the main uncertainties is related to the not very precise knowledge of some reaction rates which play a crucial role in determining the nucleosynthesis yields. In particular, the amount of synthesized ^{44}Ti depends mainly on the following reactions (see The et al. 2006, Magkotsios et al. 2010): $^{40}\text{Ca}(\alpha,\gamma)^{44}\text{Ti}$ and $^{44}\text{Ti}(\alpha,\text{p})^{47}\text{V}$, the former being responsible for its creation, the latter for its destruction.
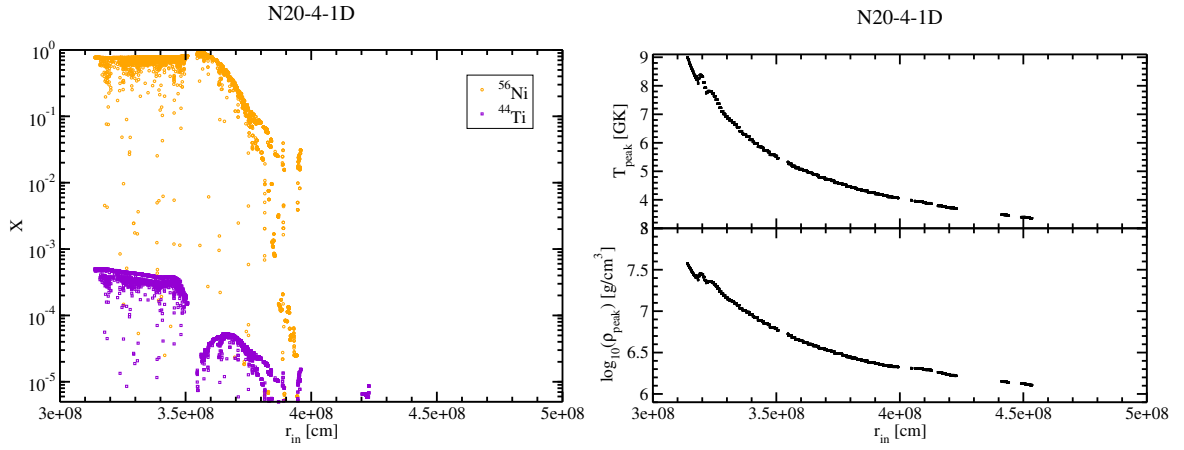
Figure 5.15 Left: Mass fraction X of ^{44}Ti and ^{56}Ni of the post-processed trajectories of model N20-4-1D from Wongwathanarat et al. (2014) as a function of the initial radius r_{in}. Right: Peak temperature T_{peak} in GK (upper panel) and logarithm of peak density in g/cm^3 (lower panel) reached by the post-processed trajectories as a function of initial radius.

Table 5.3 For each of the considered models, we report the amounts of ^{44}Ti and ^{56}Ni synthesized in the shock-heated ejecta.

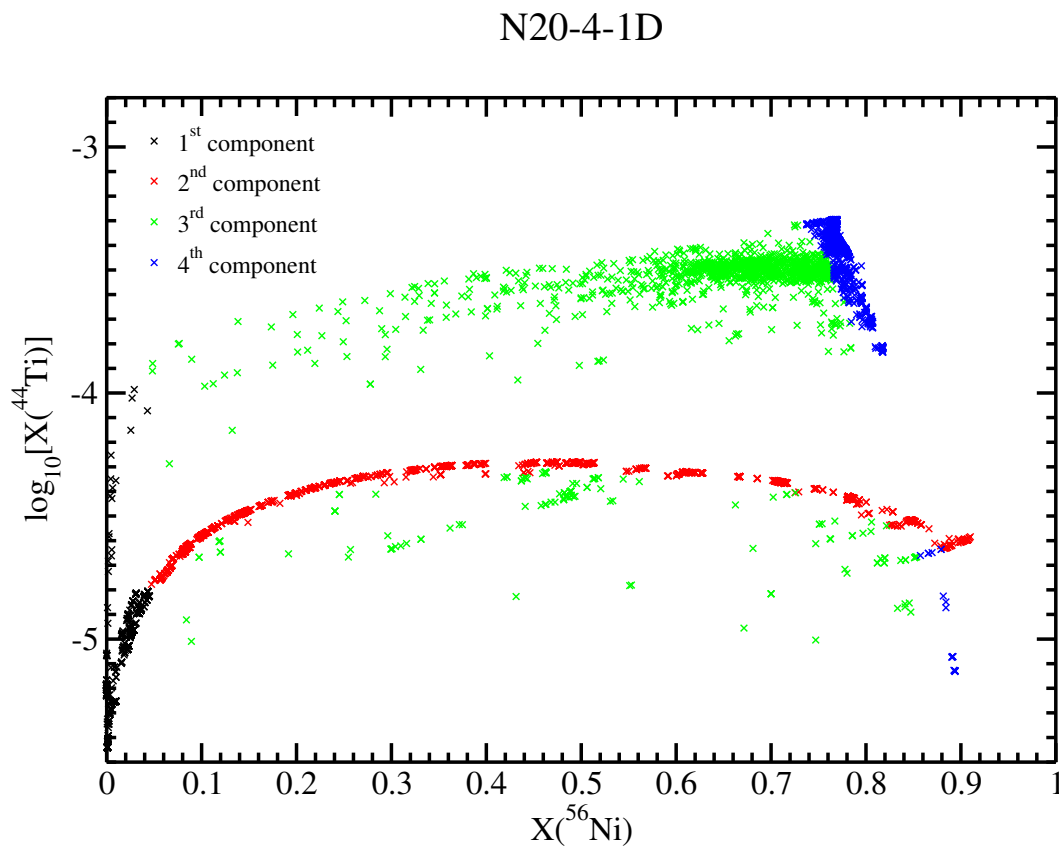| Model	$M_{\text{shock}}(^{44}\text{Ti})$ $10^{-6}M_\odot$	$M_{\text{shock}}(^{56}\text{Ni})$ $10^{-2}M_\odot$
W15-1-3D	8.3	4.1
W15-2-3D	8.7	4.2
N20-2-3D	20.1	4.9
N20-4-3D	8.6	3.0
N20-4-1D	5.2	1.4
N20-8-1D	8.3	3.5

N20-4-1D

Figure 5.16 Same as Fig. 5.10, but for the 1D model N20-4-1D.
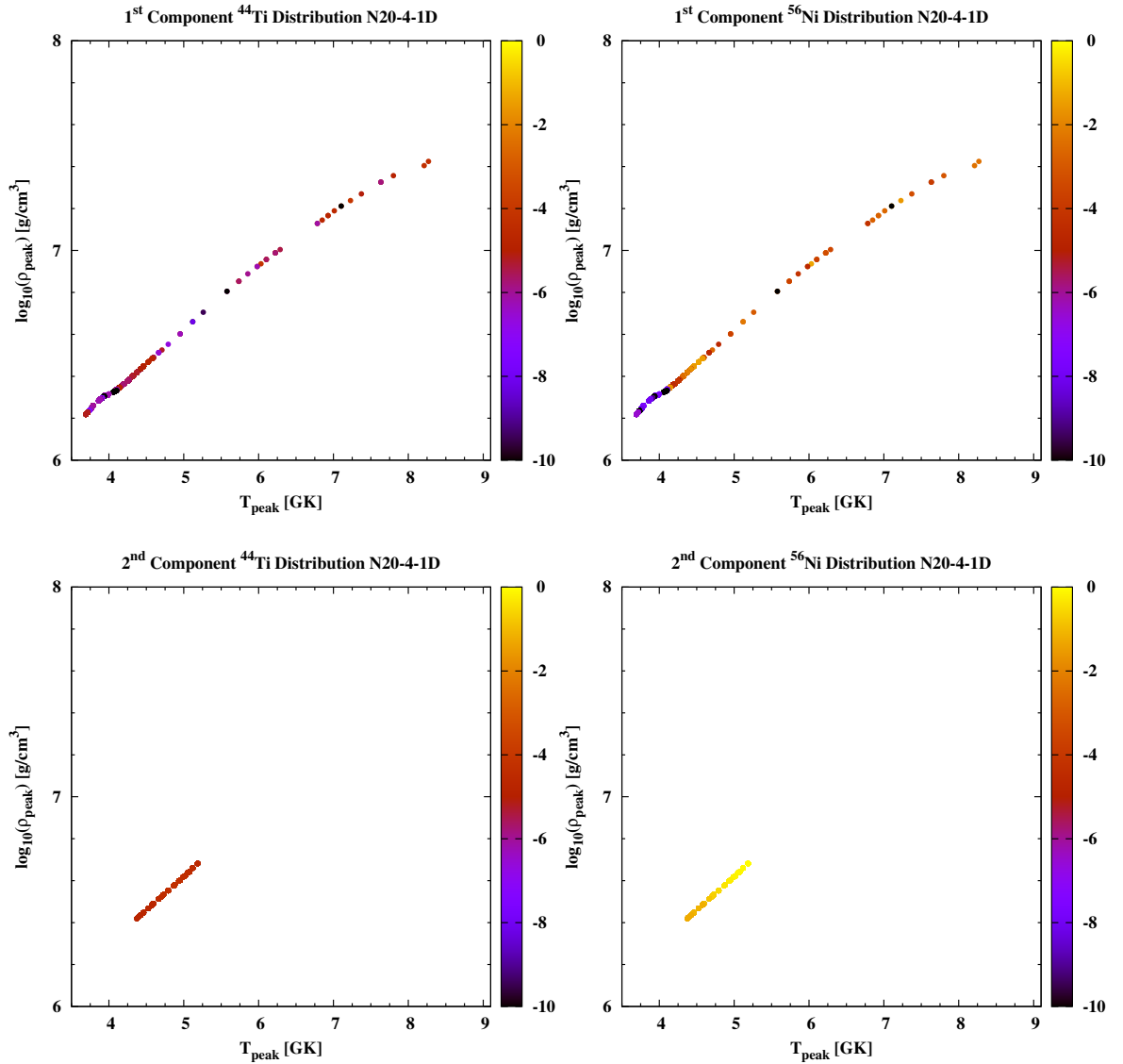
Figure 5.17 In each panel, we show the logarithm of the mass fraction of ^{44}Ti ($\log_{10}[X(^{44}\text{Ti})]$) and ^{56}Ni for each of the considered "1st and 2nd components" (see Fig. 5.16 and text) of model N20-4-1D as functions of the logarithm of the peak density $\log_{10}(\rho)$ in g/cm^3 and of the peak temperature in GK. The panels on the left refer to ^{44}Ti, while the ones on the right to ^{56}Ni.
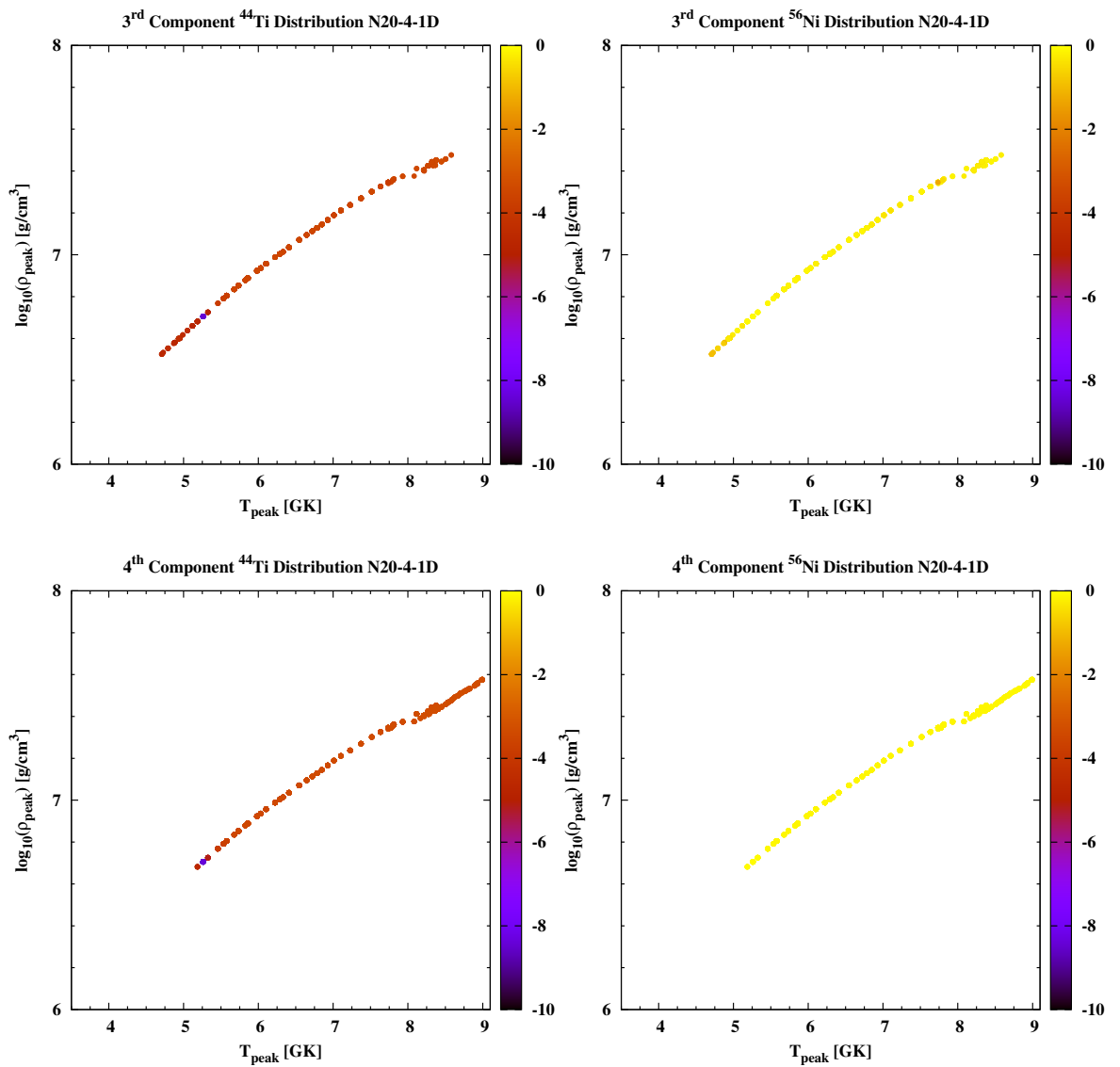
Figure 5.18 Same as Fig. 5.17, but for the third (3rd) and fourth (4th) components of model N20-4-1D (see Fig. 5.16 and text).
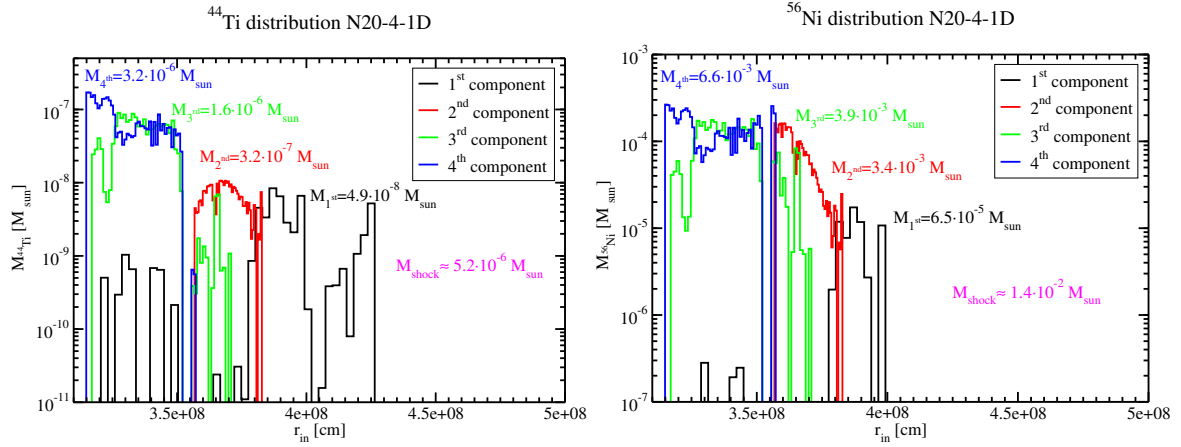
Figure 5.19 Left: Histogram of the mass distribution in M$_\odot$ of ^{44}Ti as function of the initial radius for each of the considered "components" (see Fig. 5.16) of the 1D model N20-4-1D. Right: Same as left, but for ^{56}Ni.
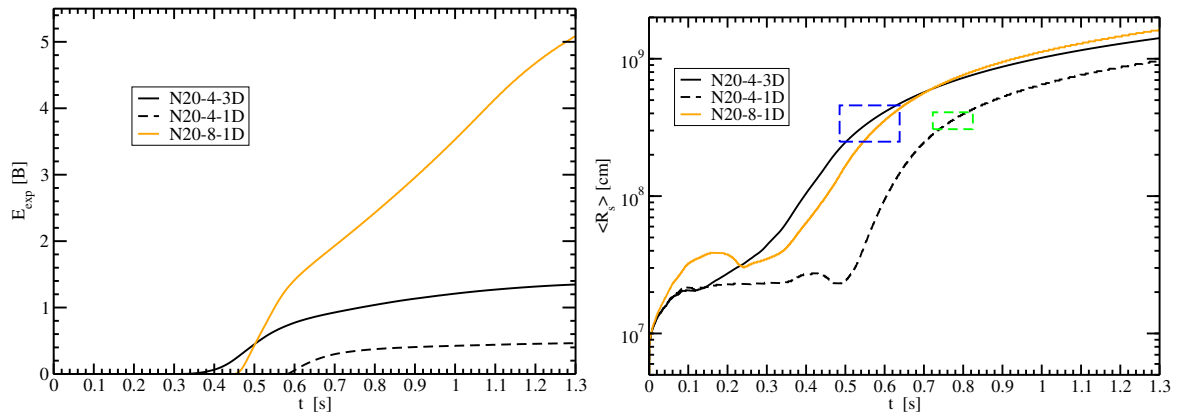

Figure 5.20 Left: Explosion energy E_{exp} in Bethe as a function of the postbounce time for each of the considered models with $M = 20\,M_\odot$. Right: Similar to the left, but for the average shock radius $\langle R_s \rangle$. The blue and green boxes indicate approximately the relevant radii and postbounce times at which the explosive nucleosynthesis occurs (compare with r_{in} in histograms in Figs. 5.13 and 5.19).

5.6 Sensitivity study of the production rates of ^{44}Ti

In this section, we discuss the impact of the reaction ^{44}Ti$(\alpha,\text{p})^{47}$V on the production of ^{44}Ti, since it deeply impacts the yields of ^{44}Ti (The et al. 2006) and since we only have upper limit values of its rate λ_0. Recently, Margerin et al. (2014), performing measurements of λ_0 within the Gamow window, have concluded that its value may be smaller than estimated by previous theoretical predictions (as the one which we use, taken from Cyburt et al. 2010), at least by a factor of about 2.2. In order to test its impact on the produced amount of ^{44}Ti in the shock-heated ejecta, we randomly choose 20 particles from the 3$^\text{rd}$ and 4$^\text{th}$ components[7] of ^{44}Ti of model N20-4-3D. Then, we change by hand the rate λ_0 of the reaction ^{44}Ti$(\alpha,\text{p})^{47}$V and of its inverse reaction in order to fulfill the detailed balance theorem. We explore the consequences of three different possible values of the aforementioned reaction rate: $\lambda_1 = 1/2 \cdot \lambda_0$, $\lambda_2 = 1/100 \cdot \lambda_0$ and $\lambda_3 = 0 \cdot \lambda_0$. Then, we calculate the average value of $\langle \text{X}(^{44}\text{Ti})\rangle_{j,k}$, for the 3$^\text{rd}$ and 4$^\text{th}$ components over the 20 chosen representative trajectories:

$$\langle \text{X}(^{44}\text{Ti})\rangle_{j,k} = \sum_{i=1}^{20} \text{X}_{i,j,k}(^{44}\text{Ti}), \tag{5.6}$$

where $k = 3^\text{rd}, 4^\text{th}$ and λ_j, $j = 0, 1, 2, 3$. In order to get a rough idea about the impact of each λ_j on the produced mass of ^{44}Ti in the 3$^\text{rd}$ and 4$^\text{th}$ components ($\overline{M}_{j,k}$), we use the following relation:

$$\overline{M}_{j,k} = M_{0,k} \cdot \frac{\langle \text{X}(^{44}\text{Ti})\rangle_{j,k}}{\langle \text{X}(^{44}\text{Ti})\rangle_{0,k}}, \tag{5.7}$$

where $M_{0,k}$ is the mass of ^{44}Ti produced in the 20 representative post-processed trajectories corresponding to the rate λ_0 (second column in Tab. 5.4). In Tab. 5.4, we report the mass of ^{44}Ti (in units of $10^{-6} M_\odot$) which is produced in the 3$^\text{rd}$ and 4$^\text{th}$ components for $\lambda_1 = 1/2 \cdot \lambda_0$, $\lambda_2 = 1/100 \cdot \lambda_0$, $\lambda_3 = 0 \cdot \lambda_0$. We also show the total amount of ^{44}Ti which is produced in each of the considered cases: $\overline{M}_j = \sum_k \overline{M}_{j,k}$.

In particular, from the ratio $\overline{M}_1/\overline{M}_0 \simeq 1.5$, we deduce that the amount of ^{44}Ti produced in the shock-heated ejecta is underestimated in our calculations (see Tab. 5.3) by, at least, a factor of about 1.5.

We will take into account its implications in the next section, where we will compare our results with other theoretical works and observations.

5.7 Comparison with observations and other theoretical works

Several theoretical and observational efforts have been made in order to estimate the amount of ^{44}Ti and ^{56}Ni which are produced in SN 1987A and Cas A. The proximity of SN 1987A, which exploded in the Large Magellanic Cloud, allowed the very first detection of γ-ray lines from the radioactive process ^{56}Ni$\longrightarrow^{56}$Co$\longrightarrow^{56}$Fe (Matz et al. 1988). This discovery made also clear how ^{56}Fe is produced. The appearance of the γ-ray lines of ^{56}Co six months earlier than expected from spherical SN models suggested that the ejecta of the SN were asymmetric, and ^{56}Co was driven close to the surface by

---

[7]We choose only the 3$^\text{rd}$ and 4$^\text{th}$ components, since they contain about 94% of the total produced ^{44}Ti. Therefore, the estimate of the contribution from the 1$^\text{st}$ and 2$^\text{rd}$ components to the production of ^{44}Ti is not very relevant in this sensitivity study.

Table 5.4 Mass fraction of ^{44}Ti produced in the 3rd and 4th components of model N20-4-3D, obtained by changing the reaction rate (λ_0) of ^{44}Ti(α,p)^{47}V by a factor of 1/2, 1/100, and 0 which correspond to the rates λ_1, λ_2 and λ_3, respectively. Notice that we only consider the 3rd and 4th components, since they contain 94% of the total amount of produced ^{44}Ti.

$M_{shock}(^{44}Ti)$ $10^{-6}M_\odot$	λ_0	λ_1	λ_2	λ_3
$\overline{M}_{j,3}$	1.00	1.64	9.21	21.40
$\overline{M}_{j,4}$	7.10	10.65	48.47	102.12
$\overline{M}_j$	8.10	12.29	57.68	123.52
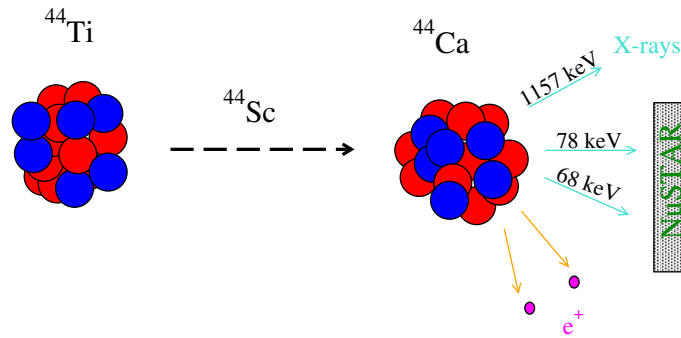
Figure 5.21 Schematic representation of the decay of ^{44}Ti (^{44}Ti→^{44}Sc→^{44}Ca) which results in the emission of three lines of a similar intensity at about 68, 78, and 1157 keV. Recently, the space-based high-energy X-ray telescope *NuSTAR*, which operates in the band 3-79 keV, has detected the lines at 68 and 78 keV in Cas A (Grefenstette et al. 2014).
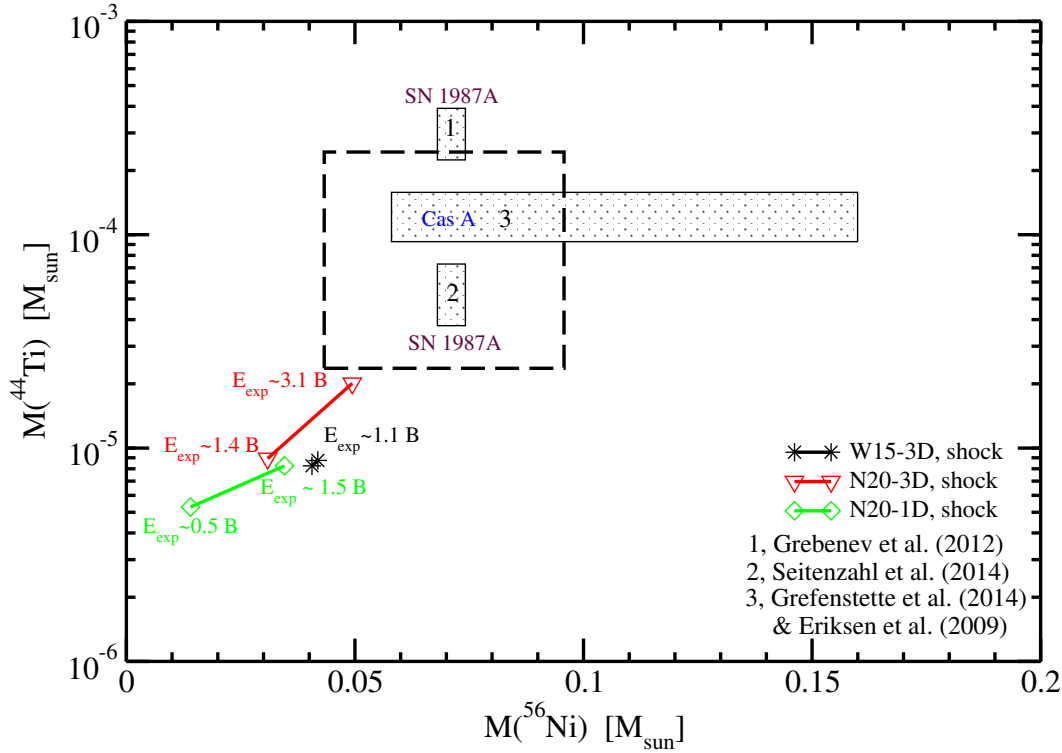
Figure 5.22 Total mass of ^{44}Ti produced in our models as a function of the corresponding amount of synthesized ^{56}Ni. The black line refers to the models W15-3D, the red line to the models N-20-3D, while the green line to the models N-20-1D. We also indicate next to each model the corresponding explosion energy E_{exp}. The black dashed rectangle refers to the yields produced in the shock-heated ejecta plus the ones produced in the ν-heated ejecta of model W15-2-3D, and then corrected by a factor of about 1.5 due to the uncertainties of the reaction rate of ^{44}Ti$(\alpha,p)^{47}$V (see text for details).

hydrodynamic instabilities (see Prantzos 2010 and references therein). The amount of produced ^{56}Ni of SN 1987A is inferred from lightcurves. The standard value is ^{56}Ni~ 0.07 $M_{\odot}$ (e.g, Seitenzahl et al. 2014). Up to now, ^{44}Ti has not yet been directly detected in SN 1987A. From modeling of the UVOIR light curves, different values of the amount of produced ^{44}Ti have been predicted, which do not always agree with each other, neither within the respective uncertainties. For example, from analysis of X-ray data taken from *INTEGRAL*, Grebenev et al. (2012) suggest a value of $(3.1 \pm 0.8) \cdot 10^{-4}$ $M_{\odot}$, while UVOIR light curves analysis of Seitenzahl et al. (2014) indicate a value $(0.55 \pm 0.17) \cdot 10^{-4}$ $M_{\odot}$. Another well known example of SN explosion is the ~ 340 yr old Cas A, which is located at a distance of about 3.4 kpc from Earth (Prantzos 2010). By estimates of the extinction towards Cas A and the Fe mass from X-ray observations, Eriksen et al. (2009) predict the mass of ^{56}Ni to be in the range $(0.58 - 0.16)$ $M_{\odot}$. In 2012 and 2013, the space-based Nuclear Spectroscopic Telescope ARray (*NuSTAR*), which operates at high-energy X-ray (3-79 keV), observed Cas A. Grefenstette et al. (2014) suggest for the produced amount of ^{44}Ti a value of $(1.25 - 0.3) \cdot 10^{-4}$ $M_{\odot}$, by measuring the flux of decay lines of ^{44}Ti at about 78 and 68 keV (see a schematic representation of this process in Fig. 5.21).

Summarizing, from direct or indirect observational data, we have:

$$M_{\mathrm{obs}}(^{44}\mathrm{Ti}) \simeq (0.55 - 3.1) \cdot 10^{-4} \ M_{\odot}, \tag{5.8}$$

$$M_{\mathrm{obs}}(^{56}\mathrm{Ni}) \simeq (5.8 - 16.0) \cdot 10^{-2} \ M_{\odot}. \tag{5.9}$$

Theoretically speaking, different predictions have been made for the amounts of ^{56}Ni and ^{44}Ti synthesized in SNe. Spherically symmetric (1D) models of SN 1987A produce, in general, a few $10^{-5} \ M_{\odot}$ ^{44}Ti (Seitenzahl et al. 2014). For example, Perego et al. (2015) using the method PUSH to produce a 1D SN explosion, which better fits to the produced amounts of ^{56}Ni in SN 1987A, predict an amount of $3.99 \cdot 10^{-4} \ M_{\odot}$ for ^{44}Ti. Concerning Cas A, Magkotsios et al. (2010) post-processed the trajectories of a 1D SN model from Young et al. (2008), whose progenitor was designed to match Cas A, and got a value of $1.04 \cdot 10^{-4} \ M_{\odot}$ for ^{44}Ti and of $2.46 \cdot 10^{-1} \ M_{\odot}$ for ^{56}Ni. While using a two-dimensional rotating 15 $M_{\odot}$ model of Fryer & Heger (2000), they obtain a higher value for ^{44}Ti, namely $6.98 \cdot 10^{-4} \ M_{\odot}$, and a value of $3.89 \cdot 10^{-1} \ M_{\odot}$ for ^{56}Ni. As we can see from these examples, different models predict very different amounts of ^{56}Ni and ^{44}Ti in CCSNe. All the above examples have to face the problem of mass cut and the simulations do not follow the SN shock long enough, and therefore hydrodynamic trajectories have to be extrapolated in order to be able to perform nucleosynthesis calculations.

On the other hand, our models do not suffer the problem related to the mass cut and are simulated long enough, but still our simplified neutrino transport does not allow us to accurately determine Y_e, which has a big impact in determining the amount of ^{56}Ni and ^{44}Ti, as we showed in Sect. 5.4.2. In Fig. 5.22, we show a summary of the amounts of ^{56}Ni and ^{44}Ti, which we obtain for each model, in 1D or 3D, in the shock-heated ejecta. The black dashed rectangle refers to the yields produced in the shock-heated ejecta plus the ones produced in the ν-heated ejecta of model W15-2-3D and then corrected by a factor of about 1.5 due to the uncertainties of the rate of the reaction $^{44}\mathrm{Ti}(\alpha,\mathrm{p})^{47}\mathrm{V}$ (see Sect. 5.6):

$$M_{\mathrm{theo}}(^{44}\mathrm{Ti}) \simeq (0.24 - 2.40) \cdot 10^{-4} \ M_{\odot}, \tag{5.10}$$

$$M_{\mathrm{theo}}(^{56}\mathrm{Ni}) \simeq (4.30 - 9.60) \cdot 10^{-2} \ M_{\odot}. \tag{5.11}$$

The filled rectangles correspond to the above mentioned observational values concerning SN 1987A and Cas A. As we can see, after taking into account the uncertainties related to our model, especially the huge ones of Y_e in the ν-heated ejecta, the yields of ^{56}Ni and ^{44}Ti which we predict match quite well with the ones suggested from observations. Of course, our theoretical amounts suggested for ^{56}Ni and ^{44}Ti have to be taken with the necessary caveat, since a better neutrino transport is mandatory in order to be able to accurately predict the value of Y_e in the ν-heated ejecta and, therefore the amount of synthesized nuclei as well.

However, due to the fact that most of the amounts of ^{56}Ni and ^{44}Ti are produced in the same conditions, namely in the α-rich freeze out regime with $Y_e \simeq 0.5$, their spatial distribution is not affected by the uncertainties related to the exact amount which is produced. In Fig. 5.23 (upper panel) we show the combined spatial distributions of ^{44}Ti (blue) and ^{56}Ni (green) for model W15-1-3D (left) and model W15-2-3D (right), see also Sect. 5.4.2 for more details. In both models we see, as expected, that, in general in regions where there is a lot of ^{44}Ti, there is also a lot of ^{56}Ni. Additionally, in Fig. 5.23 (lower panel), we show the spatial distribution of Cas A done using data from *Chandra* and *NuSTAR* (Grefenstette et al. 2014): ^{44}Ti is depicted in blue, while ^{56}Fe is shown in red (decay product of ^{56}Ni). From the spatial distributions of these isotopes, symmetric explosions for Cas A, as well as highly asymmetric bipolar explosions resulting from a very fast progenitor are ruled out. Instead,

they provide strong evidence for the development of low-mode convective instabilities in CCSNe explosions (Grefenstette et al. 2014). By comparing the spatial distribution of ^{56}Ni and ^{44}Ti of model W15-2-3D (right) with the image of Cas A, we can say that the asymmetries used to set up the SNe explosion match quite well to what is observed. Inspecting the image of Grefenstette et al. (2014) it looks like there is no correlation between the spatial distribution of ^{44}Ti, which is observed in the unshocked interior of the remnant, and ^{56}Fe, contrary to what we would expect from all our models. Grefenstette et al. (2014) suggest that maybe the unexpected correlation is due to the fact that, in the unshocked ejecta, we cannot see the X-ray emission lines of ^{56}Fe. Furthermore, recently, Milisavljevic & Fesen (2015) did a near-infrared imaging of Cas A and a 3D map of its interior unshocked ejecta. They suggest that the interior of Cas A has a bubble-like morphology and that a lot of ^{56}Fe could be still in these cavities, which would confirm our theoretical results concerning the correlation between ^{56}Ni and ^{44}Ti.

5.8 Conclusions

In this chapter, we investigated the production of the radioactive isotopes ^{44}Ti and ^{56}Ni in core-collapse supernovae (CCSNe). These isotopes can help us in shedding light on the mechanism which is behind CCSNe explosions. In fact, their spatial distributions and produced amounts are strictly connected to the asymmetries, explosion energy, peak temperatures and densities which are reached during the explosion.

We examine the production of ^{44}Ti and ^{56}Ni in a set of 15 $M_\odot$ and 20 $M_\odot$ progenitors, whose SN explosion is performed in 3D and 1D (Wongwathanarat et al. 2013, 2014). The SN explosion is performed using the so-called light-bulb neutrino approach (Wongwathanarat et al. 2013). The choice of our models allows us to investigate different aspects of the production of ^{44}Ti and ^{56}Ni: progenitor, explosion energy, explosion asymmetry and dimensionality dependence. Our main results can be summarized as follows:

- Independently from the progenitor structure and the explosion conditions, we always see a strong correlation between the production of ^{44}Ti and ^{56}Ni. The correlations are a natural consequence of the different nuclear burning regimes where ^{44}Ti and ^{56}Ni are produced (especially α-rich freeze out and Si-rich freeze out). However, the detailed features of these correlations are dimensionality and explosion model dependent;

- The amount of the produced ^{44}Ti does not depend on the progenitor, as much as ^{56}Ni does. We get the same amount of synthesized ^{44}Ti in both models, but a smaller amount of produced ^{56}Ni in the 20 $M_\odot$ progenitor than in the 15 $M_\odot$ progenitor;

- There is an almost linear relation between the explosion energy (E_{exp}) and the produced amount of ^{44}Ti and ^{56}Ni;

- The asymmetries at the onset of the explosion play a crucial role in determining the spatial distribution of ^{44}Ti and ^{56}Ni, while the produced amounts depend mainly on the explosion energy;

- By comparing the 3D and 1D models, we conclude that the explosion energy as well as the propagation of the shock radius play a crucial role in determining the synthesized amounts of ^{44}Ti and ^{56}Ni;

- Due to the limitations of the light-bulb neutrino approach in determining the neutrino properties, which deeply impact the electron fraction of the matter, and therefore the nucleosynthesis outcome, we made different assumptions about Y_e in the matter heated by neutrinos. On the one hand, we simply took Y_e from the simulations and then performed nucleosynthesis calculations. On the other hand, we took Y_e from the progenitor. The contribution of the ν-heated matter to the total amount of produced ^{44}Ti and ^{56}Ni can be very important;

- The production of ^{44}Ti sensitively depends on the reaction rate of ^{44}Ti$(\alpha,p)^{47}$V (The et al. 2006). Following the recent results of Margerin et al. (2014), we get a production factor for ^{44}Ti of about 1.5 greater than the one obtained using the reaction rates of Cyburt et al. (2010);

- Taking into account the uncertainties related to Y_e in the matter heated by neutrinos and those related to the not well constrained reaction rate of ^{44}Ti$(\alpha,p)^{47}$V, the produced amounts of ^{44}Ti and ^{56}Ni in our models are consistent with whose given by direct or indirect SN observations;

- By comparing the spatial distribution of ^{44}Ti and ^{56}Ni produced in one of our models with the one of Cas A (Grefenstette et al. 2014; Milisavljevic & Fesen 2015), we see a general good agreement, confirming the robustness of the neutrino-driven explosion mechanism.

However, our results are affected by the fact that the SN explosion is done in an approximate way, since neutrinos are not treated self-consistently. In particular, the exact amounts of the produced isotopes ^{44}Ti and ^{56}Ni sensitively depend on the electron-fraction, which is influenced by the β-reaction. Therefore, if the interaction of the matter with neutrinos becomes important, then we cannot accurately predict the amount of ^{44}Ti and ^{56}Ni which are produced in SN explosions, but can only give upper/lower limits according to our assumptions about Y_e.
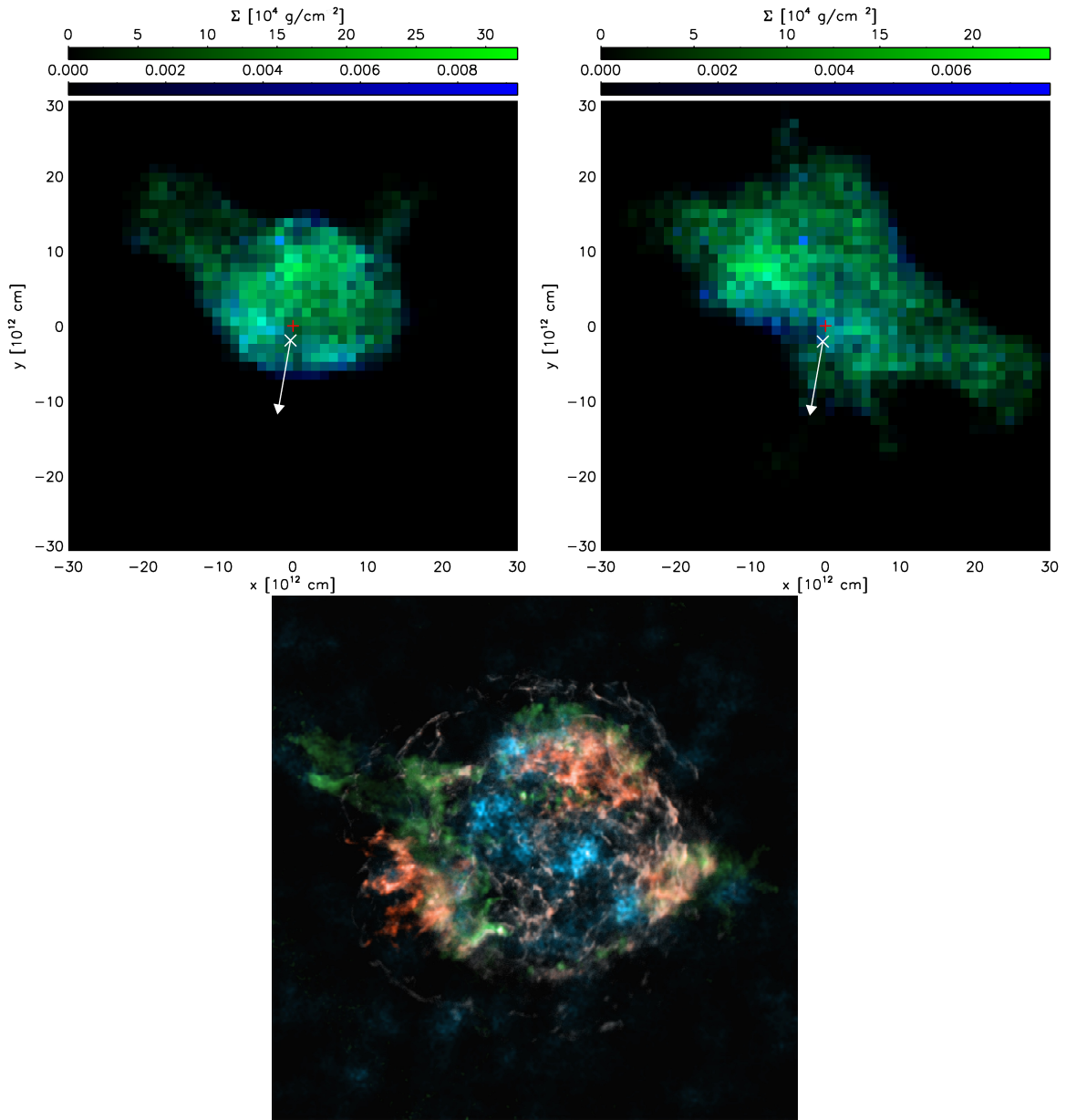
Figure 5.23 Upper panel: Surface densities Σ of the distribution of ^{44}Ti (blue color) and ^{56}Ni (green color) of model W15-1-3D (left), and of model W15-2-3D (right). The white arrows show the kick direction of the compact remnant. The length of the arrows doesn't correspond to the kick magnitude. The red "+" sign marks the center of the explosion (coordinate origin), while the white "x" marks the current position of the NS. The maps show the distributions at time $t = 37562.3$ s and $t = 50321.6$ s for W15-1-3D and W15-2-3D, respectively. (Images are courtesy of Annop Wongwathanarat). Lower panel: Fig. 3 of Grefenstette et al. (2014) showing comparison of the spatial distribution of ^{44}Ti with known Fe K emission in Cas A. The ^{44}Ti observed by *NuSTAR* is shown in blue. The ^{44}Ti is resolved into distinct knots and is non-uniformly distributed and almost entirely contained within the central 100 arcsec. In green is shown the *Chandra* ratio image of Si/Mg band, which highlights the jet/contour-jet structure. In white is shown the continuum emission band 4 to 6 keV and the spatial distribution of X-ray bright Fe (red) seen by *Chandra*.

6 Summary and Conclusions

In this work, we have investigated different aspects of the nucleosynthesis in core-collapse supernovae (CCSNe). After giving a brief summary of the reasons why CCSNe are interesting sites for the production of the chemical elements in chapter 1, we presented the tools which we use to perform nucleosynthesis calculations in chapter 2.

In chapter 3, we have investigated the impact of the nucleon potential correction on the neutrino spectra, and therefore on the electron fraction (Y_e) in the neutrino-driven wind (ν-driven wind) of an 8.8 $M_\odot$ progenitor electron-capture supernova (ECSN) (Hüdepohl et al. 2010). The aforementioned corrections can have important consequences for the nucleosynthesis in the ν-driven wind (Martínez-Pinedo et al. 2012; Roberts et al. 2012).

In order to perform our study, we have parametrized the electron neutrino and antineutrino spectra using different prescriptions, while adopting the hydrodynamic trajectories of the sophisticated simulation of Hüdepohl et al. (2010). We have also made different assumptions about the physics involved in the electron neutrino and antineutrino opacities, namely we have included or omitted the weak magnetism and recoil corrections (Horowitz & Li 1999). Furthermore, we have investigated different assumptions about the evolution of Y_e in the ν-driven wind. In one case, we have performed full network calculations which have allowed us to properly take into account all dynamical effects (e.g., α-effect, see McLaughlin et al. 1996). In another case, we have made some assumptions about the nuclear composition or simply assumed that an equilibrium configuration applies to Y_e.

Since the evolution of Y_e in the ν-driven wind is time dependent, we have explored three different trajectories representing the different phases of the ν-driven wind evolution. One at a postbounce time $t_0 = 0.5$ s (early phase), one at $t_0 = 2.9$ s (intermediate phase) and one at $t_0 = 6.5$ s (late phase). The main results of this project can be summarized as follows:

- The weak magnetism and recoil corrections can deeply impact Y_e. They can increase its value (especially in the late phases of the ν-driven wind) compared to the case where they are not included or decrease it (mostly in the early phases of the ν-driven wind);

- The α-effect tends to push the value of Y_e towards 0.5. This effect is very evident in the late phases of the ν-driven wind;

- The equilibrium assumptions about Y_e are fulfilled in the intermediate and late phases of the ν-driven wind. In the early phases of the ν-driven wind, full network calculations are needed for an accurate knowledge of the value of Y_e;

- For electron neutrino and antineutrino parameters (luminosities and mean energies) not very far from the ones given by the hydrodynamic simulations, the matter in the ν-driven wind is proton-rich rather than neutron-rich.

However, a proper inclusion of the nucleon potential corrections in the hydrodynamic simulations is necessary in order to accurately predict Y_e, and therefore the outcome of the nucleosynthesis.

In chapter 4, using the aforementioned ECSN of Hüdepohl et al. (2010), we have investigated another aspect of the neutrino properties. Namely, the impact of neutrino flavor oscillations, with or without the inclusion of an eV-mass sterile neutrino, on the nucleosynthesis in the ν-driven wind. On the one hand, we have considered the oscillations among two active neutrino flavors driven by the atmospheric mass difference and the mixing angle θ_{13}. On the other hand, motivated by hints about the possible existence of eV-mass sterile neutrinos, we have considered the oscillations between two active neutrinos and one sterile neutrino. The mixing parameters are suggested by the so-called reactor anomaly (Mention et al. 2011). In this case as well, we have investigated three trajectories which are representative of the different evolution phases of the ν-driven wind (early, intermediate and late).

The main results concerning our model (without inclusion of the nucleon potential corrections) are:

- Neutrino oscillations among active flavors do not play any important role in the outcome of the nucleosynthesis, since they take place too far away from the proto-neutron star, where Y_e has already reached its asymptotic value;

- The competition between the α-effect and neutrino oscillations with sterile neutrinos plays a significant role in setting the value of Y_e. The α-effect can enhance as well as reduce the impact of MSW ν_e-ν_s conversions on Y_e, depending on the radial position where the inner and outer MSW resonances take place relative to the formation of the α particles;

- In the early phase of the ν-driven wind, both MSW resonances occur before the α-effect takes place and Y_e remains above 0.5. At intermediate times, there is an overlap between the outer MSW resonance and the α-effect. In this case, the efficiency of ν_e-ν_s oscillations in lowering Y_e is damped and $Y_e > 0.5$. At late times, the outer MSW resonance occurs before the α-effect, which further enhances the impact of ν_e-ν_s oscillations in lowering Y_e. However, Y_e is always greater than 0.5;

- If neutrino oscillations are not taken into account, then Y_e is greater than 0.5 in the ν-driven wind and only Fe-group and some proton-rich nuclei are produced, but with very small production factors. The contribution to the total amount of the nucleosynthesis yields of this ECSN is negligible, especially compared to the yields of the same ECSN produced in the early ejecta of 2D explosion models (Wanajo et al. 2011, 2013a,b);

- Due to the strong competition between the α-effect and neutrino flavor oscillations, Y_e in the ν-driven wind of our ECSN does never become lower than 0.5, excluding the possibility for the r-process to occur. The nucleosynthesis yields with neutrino oscillations, even including a sterile flavor, are very similar to the ones without neutrino oscillations. This is always due to the α-effect which dominates over neutrino oscillations.

Furthermore, we have constructed different toy models to mimic the effects of nucleon potential corrections on Y_e in our ν-driven wind model (using some prescriptions similar to whose in chapter 3), such that the matter becomes neutron-rich. Then, in these neutron-rich conditions, we have taken into account neutrino flavor oscillations, similarly to what discussed above. In some cases, the neutrino oscillations to sterile flavors can make the matter more proton-rich than without neutrino oscillations.

In general, we conclude that neutrino oscillations with or without sterile neutrinos are unlikely to help in making the matter significantly neutron-rich so that the r-process can occur.

However, more investigations with other progenitors (especially heavier ones) are needed in order to shed light on the impact of neutrino flavor oscillations on the nucleosynthesis in CCSNe.

In chapter 5, we have examined the production of ^{44}Ti and ^{56}Ni during the explosion of CCSNe. The produced amounts and spatial distributions of these radioactive isotopes can give us hints about the explosion mechanism behind CCSNe (e.g., Grefenstette et al. 2014; Milisavljevic & Fesen 2015). In particular, we have examined a set of 15 $M_\odot$ and 20 $M_\odot$ progenitors, whose SN explosions were simulated using the light-bulb neutrino approach (Wongwathanarat et al. 2013, 2014). The choice of our models has allowed us to investigate the dependence of the production of ^{44}Ti and ^{56}Ni on different aspects: progenitor, explosion energy, explosion asymmetry and dimensionality (3D and 1D). Due to the limitations of our neutrino transport we have separated our ejecta in two different sets. On the one hand, we have considered only the matter which is heated up by the passage of the SN shock wave. On the other hand, we have considered the matter which interacts with neutrinos and made some assumptions about Y_e. In one case, we have adopted Y_e given by our limited neutrino transport. In another case, we have simply taken the pre-collapse progenitor Y_e. Since the amount of ^{44}Ti is extremely sensitive to the reaction rate of ^{44}Ti$(\alpha,$p$)^{47}$V, which is not well constrained experimentally (Margerin et al. 2014), we have also made some tests about its impact on the production of ^{44}Ti. The main results of this project are summarized in the following:

- In each model, we find strong correlations between the production of ^{44}Ti and ^{56}Ni. These correlations are intrinsic to the nuclear burning regimes in which these isotopes are produced (e.g., the α-rich and Si-rich freeze out regimes);

- We do not see a clear progenitor dependence of the production of ^{44}Ti and ^{56}Ni. In fact, the amount of ^{44}Ti which is synthesized in the models with a 15 $M_\odot$ mass is similar to the corresponding one produced in the models with a 20 $M_\odot$ mass. In the heaviest models, less ^{56}Ni is produced than in the lightest ones;

- By comparing the SN models with the same mass, but different explosion energies, we see an almost linear dependence between the production of ^{44}Ti (^{56}Ni) and the SN explosion energy;

- By comparing models with the same mass and explosion energy, but different asymmetries at the onset of the SN explosion, we notice that the amounts of the produced ^{44}Ti and ^{56}Ni are very similar. On the contrary, their spatial distributions can be completely different, depending on the adopted asymmetries;

- From the investigation of 3D and 1D models, we conclude that the explosion energy as well as the propagation of the SN shock wave play an important role in the production of our isotopes of interest;

- The amount of ^{44}Ti and ^{56}Ni synthesized in the neutrino-heated ejecta can be extremely significant, depending on Y_e. The production of these symmetric nuclei is maximized if $Y_e = 0.5$, which is similar to the one of the pre-collapse model;

- Using the experimental limit of the reaction rate of ^{44}Ti$(\alpha,$p$)^{47}$V (Margerin et al. 2014), we get a production factor for ^{44}Ti of about 1.5 higher than the one we obtain using the reaction rates of Cyburt et al. (2010);

- Taking into account all the above mentioned uncertainties, the amounts of the produced ^{44}Ti and ^{56}Ni in our models are consistent with the observational data, within the error bars. Furthermore, the spatial distributions of ^{44}Ti and ^{56}Ni, which are not affected by the above mentioned uncertainties, are also consistent with the observations. In particular, the puzzling uncorrelation

between the ^{44}Ti and ^{56}Ni distributions in Cas A shown in Grefenstette et al. (2014), seems to be solved by Milisavljevic & Fesen (2015). The latter suggests that a lot of ^{56}Ni should be "hidden" where ^{44}Ti is observed. In fact, we cannot observe it, because it has not yet been shocked. This would confirm our results, in which there is always a strong correlation between the production of ^{44}Ti and of ^{56}Ni.

Our results are affected, among others, by the uncertainties of the SN explosion models which we use, for example the light-bulb neutrino approach. In particular, the amounts of the produced ^{44}Ti and ^{56}Ni cannot be well constrained until the self-consistent SN explosions in 3D will tell us the accurate value of Y_e in the matter which interacts with neutrinos.

The aim of this thesis was to give some hints on the answers to certain open questions in CCSNe nucleosynthesis. In particular, we focused on the role played by neutrinos and the radioactive isotopes ^{44}Ti and ^{56}Ni. The latter can give us precious indications about the asymmetries arising from the SN explosion, and therefore about the explosion mechanism itself.

However, this thesis is only a drop in the ocean and, of course, a lot of work remains to be done in order to understand the origin of the elements...

A Feedback of Neutrino Self-Interactions on the Electron Fraction

Given the non-linear nature of neutrino self-interactions, in this appendix we discuss the oscillation physics at the selected postbounce times $t_0 = 2.9$ and 6.5 s where ν-ν interactions significantly affect the neutrino spectral properties. In order to disentangle between the role played by ν-ν interactions and the MSW resonances, we also discuss a simpler case obtained by switching off the neutrino self-interaction term (i.e., including matter effects only). Here, we discuss the "sterile" case with the prescription (ii) in Sect. 3 for α particles, namely without taking into account the α-effect.

A simple quantity that can be introduced in order to have an idea about the locations of the active-sterile MSW resonances is the refractive energy difference between ν_e and ν_s caused by matter and neutrino refraction (see Sect. 4.4):

$$V_{es} = \mathsf{H}_{ee}^{\mathrm{m}+\nu\nu} - \mathsf{H}_{ss}^{\mathrm{m}+\nu\nu} \quad = \quad \sqrt{2}G_{\mathrm{F}}\left[N_b\left(\frac{3}{2}Y_e - \frac{1}{2}\right) + 2(N_{\nu_e} - N_{\bar{\nu}_e}) + (N_{\nu_x} - N_{\bar{\nu}_x})\right]. \quad (A.1)$$

We show V_{es} (Eq. A.1) as a function of radius at $t_0 = 2.9$ s in the top left panel of Fig. A.1. This profile already includes a self-consistent solution of Y_e. The regions where we should expect the inner and outer active-sterile MSW resonances are defined by the intersection of the V_{es} profile with the $\pm\omega_S$ lines (corresponding to the typical oscillation frequency of 15 MeV ν and $\bar{\nu}$, see Eq. 22): The MSW resonances should occur at $r_{\mathrm{IR}} \simeq 2 \times 10^6$ cm for ν and $\bar{\nu}$ and at $r_{\mathrm{OR}} \simeq 4.5 \times 10^6$ cm for neutrinos only.

In the "matter background" case, the $\nu_e \rightarrow \nu_s$ conversions are more abundant than the antineutrino ones, as already discussed in Sect. 4.5. Correspondingly, the electron fraction (fourth panel of Fig. A.1 on the left) is lower than the one in the case without oscillations. The outer resonance occurs at $r_{\mathrm{OR}} \simeq 50 \times 10^5$ cm only for neutrinos and it favors an even lower value of the electron fraction.

In the "matter+ν background" case, the inner MSW resonance takes place at the same radius as in the "matter background" case (see second and third panels on the left of Fig. A.1), but a slightly lower fraction of the ν_e are converted to ν_s because of $\mathsf{H}^{\nu\nu} \neq 0$. Moreover, it is clear by comparing the second and the third panels of Fig. A.1, that the ν-ν interaction term is responsible for replenishing the ν_e flux before the outer active-sterile MSW resonance occurs at $r_{\mathrm{OR}} \simeq 5 \times 10^6$ cm. Correspondingly, the electron fraction increases compared to the case without oscillations close to the neutrinosphere and decreases afterwards because of the outer MSW resonance. Comparing the Y_e profiles in the "matter+ν background" and "matter background" cases, we find that $Y_e(\mathrm{matter} + \nu) - Y_e(\mathrm{matter}) \simeq 0.025$.

The right side of Fig. A.1 shows the same quantities discussed at $t_0 = 2.9$ s, but at $t_0 = 6.5$ s. In the "matter background" case, the inner MSW resonance occurs at $r_{\mathrm{IR}} \simeq 1.8 \times 10^6$ cm as shown by the

$L_{\nu_e}/\langle E_{\nu_e}\rangle$ and $L_{\bar{\nu}_e}/\langle E_{\bar{\nu}_e}\rangle$ behavior in the second panel of Fig. A.1 and by the top panel of the same figure. In this case, almost the same amount of ν_e and $\bar{\nu}_e$ is converted to sterile states (due to the steepness of the matter potential as discussed in Sect. 4.5). The outer MSW resonance occurs closer to the inner one than at $t_0 = 2.9$ s (at $r_{OR} \simeq 2.5 \times 10^6$ cm) and it is responsible for depleting the ν_e flux in favor of sterile state production. Therefore, the electron fraction, plotted in the fourth right panel of Fig. A.1, becomes lower than in the case without oscillations.

In the "matter+ν background" case, the role played by the neutrino self-interactions is evident already close to the inner resonance. In fact, the difference between the $\nu_e \rightarrow \nu_s$ and $\bar{\nu}_e \rightarrow \bar{\nu}_s$ flavor conversions is responsible for lowering Y_e compared to the case without oscillations and with "matter background" only. Soon afterwards, and in correspondence to the outer resonance, the interplay between the matter and neutrino background and the non-linear effects due to ν-ν interactions is responsible for partially repopulating the ν_e and the $\bar{\nu}_e$ sectors and, as a consequence, Y_e does not decrease further as it happens in the case at $t_0 = 2.9$ s. Comparing the Y_e profiles in the "matter+ν background" and "matter background" cases, we find that $Y_e(\text{matter} + \nu) - Y_e(\text{matter}) \simeq 0.02$. For both the discussed profiles, ν-ν interactions are triggered at smaller radii than usually expected in the "active" case by the presence of non-zero off-diagonal terms in the density matrices of neutrinos and antineutrinos, similar to what was discussed in Dasgupta et al. (2010) for three active flavors. The role played by the neutrino self-interactions becomes particularly evident at late postbounce times t_0, because the matter background is lower and, therefore, the effective mixing angle θ_{13} (Esteban-Pretel et al. 2008; Duan et al. 2008) is larger than in the early cooling phase.
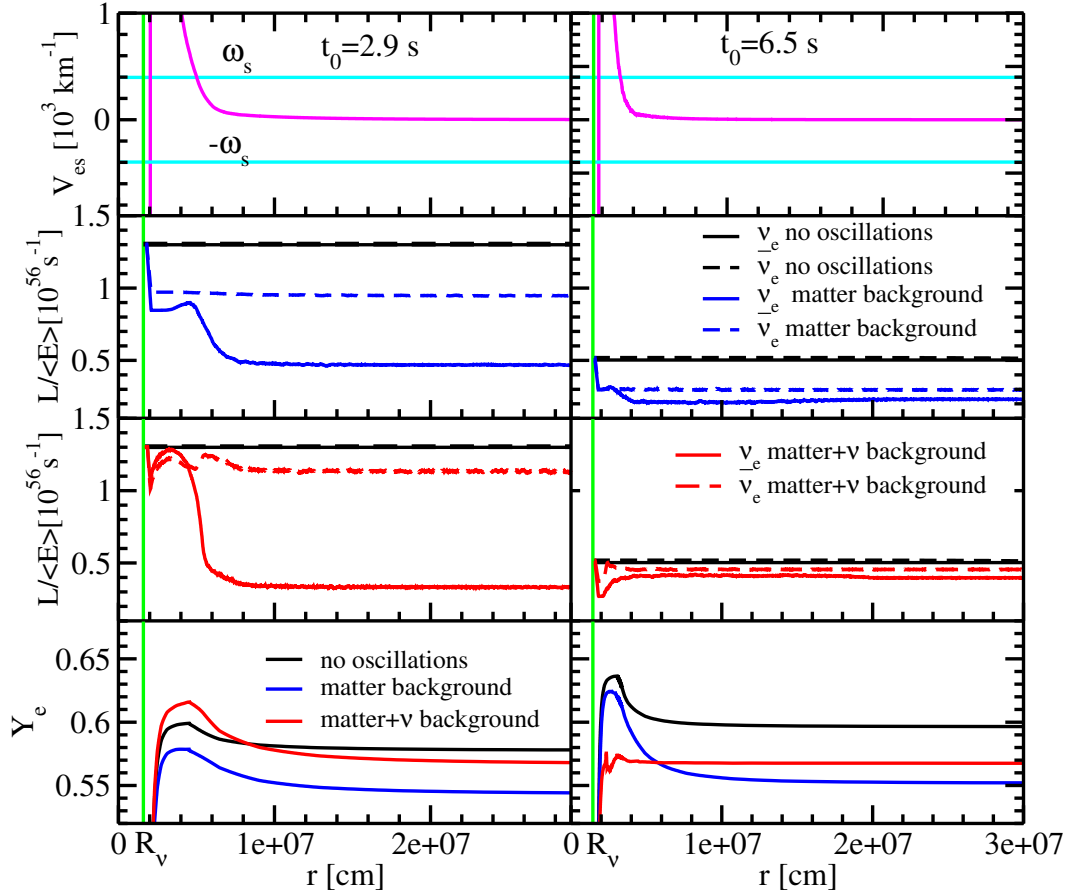
Figure A.1 *Top panel:* Refractive energy difference between ν_e and ν_s (V_{es}) in the "sterile" case. The horizontal lines ($\pm\omega_S$) mark the oscillation frequency of a typical energy mode of 15 MeV for neutrinos and antineutrinos. *Second panel:* $L_{\nu_e}/\langle E_{\nu_e}\rangle$ and $L_{\bar{\nu}_e}/\langle E_{\bar{\nu}_e}\rangle$ in units of 10^{51} erg/(MeV s) as functions of distance (r) from the center of the PNS in the "sterile" case with "matter background" and the case without oscillations for comparison. *Third panel:* $L_{\nu_e}/\langle E_{\nu_e}\rangle$ and $L_{\bar{\nu}_e}/\langle E_{\bar{\nu}_e}\rangle$ in the "sterile" case with "matter+ν background" and the case without oscillations for comparison. *Fourth panel:* Electron fraction Y_e as a function of distance r from the center of the PNS in the "matter background," "matter +ν background" and "no oscillation" cases, without including the α-effect. The panels on the left side refer to $t_0 = 2.9$ s postbounce time, while the ones on the right to $t_0 = 6.5$ s. The vertical line marks the neutrinosphere radius R_ν.

Bibliography

Abazajian, K. N., Acero, M. A., Agarwalla, S. K., et al. 2012, ArXiv:1204.5379

Aguilar, A., Auerbach, L. B., Burman, R. L., et al. 2001, Phys. Rev. D, 64, 112007

Aguilar-Arevalo, A. A., Anderson, C. E., Bazarko, A. O., et al. 2009a, Phys. Rev. Lett., 102, 101802

Aguilar-Arevalo, A. A., Anderson, C. E., Brice, S. J., et al. 2009b, Phys. Rev. Lett., 103, 111801

Archidiacono, M., Fornengo, N., Giunti, C., Hannestad, S., & Melchiorri, A. 2013, Phys. Rev. D, 87, 125034

Arcones, A. & Montes, F. 2011, ApJ, 731, 5

Arcones, A. & Thielemann, F.-K. 2013, Journal of Physics G Nuclear Physics, 40, 013201

Arnett, W. D. 1977, ApJS, 35, 145

Arnett, W. D., Bahcall, J. N., Kirshner, R. P., & Woosley, S. E. 1989, ARA&A, 27, 629

Arnould, M., Goriely, S., & Takahashi, K. 2007, Phys. Rep., 450, 97

Aver, E., Olive, K. A., & Skillman, E. D. 2012, JCAP, 4, 4

Bauswein, A., Goriely, S., & Janka, H.-T. 2013, ApJ, 773, 78

Bethe, H. A. 1990, Reviews of Modern Physics, 62, 801

Beun, J., McLaughlin, G. C., Surman, R., & Hix, W. R. 2006, Phys. Rev. D, 73, 093007

Blatt, J. M. & Weisskopf, V. F. 1952, Joh Wiley & Sons, Inc., New York

Blinnikov, S., Lundqvist, P., Bartunov, O., Nomoto, K., & Iwamoto, K. 2000, ApJ, 532, 1132

Blondin, J. M. & Mezzacappa, A. 2007, Nature, 445, 58

Blondin, J. M., Mezzacappa, A., & DeMarino, C. 2003, ApJ, 584, 971

Bruenn, S. W. 1985, ApJS, 58, 771

Burbidge, E. M., Burbidge, G. R., Fowler, W. A., & Hoyle, F. 1957, Reviews of Modern Physics, 29, 547

Burrows, A. 2013, Reviews of Modern Physics, 85, 245

Capozzi, F., Fogli, G. L., Lisi, E., et al. 2013, ArXiv e-prints:1312.2878

Chakraborty, S., Fischer, T., Mirizzi, A., Saviano, N., & Tomas, R. 2011, Phys.Rev., D84, 025002

Colella, P. & Glaz, H. 1984, Journal on Computational Physics, 59, 264

Colella, P. & Woodward, P. 1984, Journal on Computational Physics, 54, 174

Cyburt, R. H., Amthor, A. M., Ferguson, R., et al. 2010, ApJS, 189, 240

Dasgupta, B. & Dighe, A. 2008, Phys. Rev. D, 77, 113002

Dasgupta, B., Mirizzi, A., Tamborra, I., & Tomàs, R. 2010, Phys. Rev. D, 81, 093008

Dasgupta, B., Raffelt, G. G., & Tamborra, I. 2010, Phys.Rev., D81, 073004

Donini, A., Hernández, P., López-Pavón, J., Maltoni, M., & Schwetz, T. 2012, Journal of High Energy Physics, 7, 161

Duan, H., Friedland, A., McLaughlin, G. C., & Surman, R. 2011a, Journal of Physics G Nuclear Physics, 38, 035201

Duan, H., Friedland, A., McLaughlin, G. C., & Surman, R. 2011b, Journal of Physics G Nuclear Physics, 38, 035201

Duan, H., Fuller, G. M., Carlson, J., & Qian, Y.-Z. 2006, Phys. Rev. D, 74, 105014

Duan, H., Fuller, G. M., & Qian, Y.-Z. 2008, Phys.Rev., D77, 085016

Duan, H., Fuller, G. M., & Qian, Y.-Z. 2010, Annual Review of Nuclear and Particle Science, 60, 569

Eriksen, K. A., Arnett, D., McCarthy, D. W., & Young, P. 2009, ApJ, 697, 29

Esteban-Pretel, A., Mirizzi, A., Pastor, S., et al. 2008, Phys.Rev., D78, 085012

Esteban-Pretel, A., Pastor, S., Tomàs, R., Raffelt, G. G., & Sigl, G. 2007, Phys. Rev. D, 76, 125018

Fetter, J., McLaughlin, G. C., Balantekin, A. B., & Fuller, G. M. 2003, Astroparticle Physics, 18, 433

Fetter, J. M. 2000, PhD thesis, THE UNIVERSITY OF WISCONSIN - MADISON

Fischer, T., Whitehouse, S. C., Mezzacappa, A., Thielemann, F.-K., & Liebendörfer, M. 2010, A&A, 517, A80

Fogli, G., Lisi, E., Marrone, A., & Mirizzi, A. 2007, JCAP, 12, 10

Fogli, G., Lisi, E., Marrone, A., & Tamborra, I. 2009a, JCAP, 4, 30

Fogli, G., Lisi, E., Marrone, A., & Tamborra, I. 2009b, JCAP, 10, 2

Fogli, G. L., Lisi, E., Marrone, A., Mirizzi, A., & Tamborra, I. 2008, Phys. Rev. D, 78, 097301

Fogli, G. L., Lisi, E., Marrone, A., & Palazzo, A. 2006, Progress in Particle and Nuclear Physics, 57, 742

Foglizzo, T., Kazeroni, R., Guilet, J., et al. 2015, PASA, 32, 9

Fröhlich, C., Hauser, P., Liebendörfer, M., et al. 2006a, ApJ, 637, 415

Fröhlich, C., Martínez-Pinedo, G., Liebendörfer, M., et al. 2006b, Phys. Rev. Lett., 96, 142502

Fryer, C. L. & Heger, A. 2000, ApJ, 541, 1033

Fryxell, B., Arnett, D., & Mueller, E. 1991, ApJ, 367, 619

Giunti, C. & Laveder, M. 2011a, Physics Letters B, 706, 200

Giunti, C. & Laveder, M. 2011b, Phys. Rev. D, 84, 093006

Giunti, C., Laveder, M., Li, Y. F., Liu, Q. Y., & Long, H. W. 2012, Phys. Rev. D, 86, 113014

Giunti, C., Laveder, M., Li, Y. F., & Long, H. W. 2013, Phys. Rev. D, 88, 073008

Giusarma, E., Di Valentino, E., Lattanzi, M., Melchiorri, A., & Mena, O. 2014, ArXiv e-prints:1403.4852

Gonzalez-Garcia, M. C. & Maltoni, M. 2008, Phys. Rep., 460, 1

Goriely, S., Sida, J.-L., Lemaître, J.-F., et al. 2013, Physical Review Letters, 111, 242502

Grebenev, S. A., Lutovinov, A. A., Tsygankov, S. S., & Winkler, C. 2012, Nature, 490, 373

Grefenstette, B. W., Harrison, F. A., Boggs, S. E., et al. 2014, Nature, 506, 339

Hamann, J., Hannestad, S., Raffelt, G. G., Tamborra, I., & Wong, Y. Y. Y. 2010, Phys. Rev. Lett., 105, 181301

Hammer, N. J., Janka, H.-T., & Müller, E. 2010, ApJ, 714, 1371

Hanke, F., Marek, A., Müller, B., & Janka, H.-T. 2012, ApJ, 755, 138

Hannestad, S., Raffelt, G. G., Sigl, G., & Wong, Y. Y. Y. 2006, Phys. Rev. D, 74, 105010

Hashimoto, M., Nomoto, K., Arai, K., & Kaminishi, K. 1985, Phys. Rep. Kumamoto Univ., 7, 47

Herant, M., Benz, W., & Colgate, S. 1992, ApJ, 395, 642

Hidaka, J. & Fuller, G. M. 2007, Phys. Rev. D, 76, 083516

Hillebrandt, W., Höflich, P., Janka, H.-T., & Mönchmeyer, R. 1989, in Big Bang, Active Galactic Nuclei and Supernovae, ed. S. Hayakawa & K. Sato, 441

Hinshaw, G., Larson, D., Komatsu, E., et al. 2013, ApJS, 208, 19

Hoffman, R. D., Woosley, S. E., & Qian, Y.-Z. 1997, ApJ, 482, 951

Horowitz, C. J. & Li, G. 1999, Phys. Rev. Lett., 82, 5198

Hou, Z., Keisler, R., Knox, L., Millea, M., & Reichardt, C. 2013, Phys. Rev. D, 87, 083008

Hoyle, F., Fowler, W. A., Burbidge, G. R., & Burbidge, E. M. 1956, Science, 124, 611

Hüdepohl, L., Müller, B., Janka, H.-T., Marek, A., & Raffelt, G. G. 2010, Phys. Rev. Lett., 104, 251101

Ishimaru, Y. & Wanajo, S. 1999, ApJ, 511, L33

Itoh, N., Totsuji, H., Ichimaru, S., & Dewitt, H. E. 1979, ApJ, 234, 1079

Janka, H.-T. 2012, Annual Review of Nuclear and Particle Science, 62, 407

Janka, H.-T., Hanke, F., Hüdepohl, L., et al. 2012, Progress of Theoretical and Experimental Physics, 2012, 010000

Janka, H.-T. & Mueller, E. 1996, A&A, 306, 167

José, J. & Iliadis, C. 2011, Reports on Progress in Physics, 74, 096901

Just, O., Bauswein, A., Pulpillo, R. A., Goriely, S., & Janka, H.-T. 2015, MNRAS, 448, 541

Kageyama, A. & Sato, T. 2004, Geochemistry, Geophysics, Geosystems, 5, 9005

Karagiorgi, G., Djurcic, Z., Conrad, J. M., Shaevitz, M. H., & Sorel, M. 2009, Phys. Rev. D, 80, 073001

Keil, M. T., Raffelt, G. G., & Janka, H.-T. 2003, ApJ, 590, 971

Keränen, P., Maalampi, J., Myyryläinen, M., & Riittinen, J. 2007, Phys. Rev. D, 76, 125026

Kifonidis, K., Plewa, T., Scheck, L., Janka, H.-T., & Müller, E. 2006, A&A, 453, 661

Kopp, J., Maltoni, M., & Schwetz, T. 2011, Phys. Rev. Lett., 107, 091801

Lattimer, J. M. 2014, Nuclear Physics A, 928, 276

Liebendörfer, M., Messer, O. E. B., Mezzacappa, A., & Hix, W. R. 2001, in American Institute of Physics Conference Series, Vol. 586, 20th Texas Symposium on relativistic astrophysics, ed. J. C. Wheeler & H. Martel, 472–477

Limongi, M. & Chieffi, A. 2006, ApJ, 647, 483

Lodders, K. 2003, ApJ, 591, 1220

Magkotsios, G., Timmes, F. X., Hungerford, A. L., et al. 2010, ApJS, 191, 66

Magkotsios, G., Timmes, F. X., Wiescher, M., et al. 2008, in Nuclei in the Cosmos (NIC X), 112

Margerin, V., Murphy, A., Davinson, T., & Dressler, R. 2014, Physics Letters B, 731, 358

Martínez-Pinedo, G. 2008, European Physical Journal Special Topics, 156, 123

Martínez-Pinedo, G., Fischer, T., Lohs, A., & Huther, L. 2012, Phys. Rev. Lett., 109, 251104

Martínez-Pinedo, G., Ziebarth, B., Fischer, T., & Langanke, K. 2011, European Physical Journal A, 47, 98

Matz, S. M., Share, G. H., Leising, M. D., Chupp, E. L., & Vestrand, W. T. 1988, Nature, 331, 416

McLaughlin, G. C., Fetter, J. M., Balantekin, A. B., & Fuller, G. M. 1999, Phys. Rev. C, 59, 2873

McLaughlin, G. C., Fuller, G. M., & Wilson, J. R. 1996, ApJ, 472, 440

Melson, T., Janka, H.-T., & Marek, A. 2015, ApJ, 801, L24

Mention, G., Fechner, M., Lasserre, T., et al. 2011, Phys. Rev. D, 83, 073006

Meyer, B. S., Mathews, G. J., Howard, W. M., Woosley, S. E., & Hoffman, R. D. 1992, ApJ, 399, 656

Meyer, B. S., McLaughlin, G. C., & Fuller, G. M. 1998, Phys. Rev. C, 58, 3696

Mikheyev, S. P. & Smirnov, A. Y. 1985, Yadernaya Fizika, 42, 1441

Milisavljevic, D. & Fesen, R. A. 2015, Science, 347, 526

MiniBooNE Collaboration, Aguilar-Arevalo, A. A., Brown, B. C., et al. 2012, ArXiv:1207.4809

Mueller, E., Fryxell, B., & Arnett, D. 1991, A&A, 251, 505

Mueller, E. & Janka, H.-T. 1997, A&A, 317, 140

Müller, E. 1998, in Saas-Fee Advanced Course 27: Computational Methods for Astrophysical Fluid Flow., ed. O. Steiner & A. Gautschy, 343

Müller, E., Fryxell, B., & Arnett, D. 1991, in European Southern Observatory Conference and Workshop Proceedings, Vol. 37, European Southern Observatory Conference and Workshop Proceedings, ed. I. J. Danziger & K. Kjaer, 99

Nishimura, N., Takiwaki, T., & Thielemann, F.-K. 2015, ArXiv e-prints

Nunokawa, H., Peltoniemi, J. T., Rossi, A., & Valle, J. W. F. 1997, Phys. Rev. D, 56, 1704

Palazzo, A. 2013, Modern Physics Letters A, 28, 30004

Perego, A., Hempel, M., Fröhlich, C., et al. 2015, ArXiv e-prints

Pettini, M. & Cooke, R. 2012, MNRAS, 425, 2477

Planck Collaboration, Ade, P. A. R., Aghanim, N., et al. 2013, ArXiv:1303.5076

Plewa, T. & Müller, E. 1999, A&A, 342, 179

Pllumbi, E., Tamborra, I., Wanajo, S., Janka, H.-T., & Hüdepohl, L. 2015, ApJ, 808, 188

Prantzos, N. 2010, in Eighth Integral Workshop. The Restless Gamma-ray Universe (INTEGRAL 2010), 18

Pruet, J., Hoffman, R. D., Woosley, S. E., Janka, H.-T., & Buras, R. 2006, ApJ, 644, 1028

Qian, Y.-Z. & Fuller, G. M. 1995, Phys. Rev. D, 52, 656

Qian, Y.-Z. & Woosley, S. E. 1996, ApJ, 471, 331

Rampp, M. & Janka, H.-T. 2000, ApJ, 539, L33

Reddy, S., Prakash, M., & Lattimer, J. M. 1998, Phys. Rev. D, 58, 013009

Reid, B. A., Verde, L., Jimenez, R., & Mena, O. 2010, JCAP, 1, 3

Roberts, L. F. 2012, ApJ, 755, 126

Roberts, L. F., Reddy, S., & Shen, G. 2012, Phys. Rev. C, 86, 065803

Sarikas, S., Raffelt, G. G., Hüdepohl, L., & Janka, H.-T. 2012, Phys. Rev. Lett., 108, 061101

Scheck, L., Kifonidis, K., Janka, H.-T., & Müller, E. 2006, A&A, 457, 963

Seitenzahl, I. R., Timmes, F. X., & Magkotsios, G. 2014, ApJ, 792, 10

Shen, H., Toki, H., Oyamatsu, K., & Sumiyoshi, K. 1998, Nuclear Physics A, 637, 435

Shigeyama, T. & Nomoto, K. 1990, ApJ, 360, 242

Sigl, G. & Raffelt, G. 1993, Nuclear Physics B, 406, 423

Strang, G. 1968, SIAM Journal on Numerical Analysis, 5, 506

Strumia, A. 2002, Physics Letters B, 539, 91

Takahashi, K., Witti, J., & Janka, H.-T. 1994, A&A, 286, 857

Tamborra, I., Müller, B., Hüdepohl, L., Janka, H.-T., & Raffelt, G. 2012a, Phys. Rev. D, 86, 125031

Tamborra, I., Raffelt, G. G., Hüdepohl, L., & Janka, H.-T. 2012b, JCAP, 1, 13

The, L.-S., Clayton, D. D., Diehl, R., et al. 2006, A&A, 450, 1037

Thielemann, F.-K., Nomoto, K., & Hashimoto, M.-A. 1996, ApJ, 460, 408

Timmes, F. X. 1999, ApJS, 124, 241

Timmes, F. X. & Swesty, F. D. 2000, ApJS, 126, 501

Tubbs, D. L. & Koonin, S. E. 1979, ApJ, 232, L59

Wanajo, S. 2006, ApJ, 647, 1323

Wanajo, S., Janka, H.-T., & Müller, B. 2011, ApJ, 726, L15

Wanajo, S., Janka, H.-T., & Müller, B. 2013a, ApJ, 767, L26

Wanajo, S., Janka, H.-T., & Müller, B. 2013b, ApJ, 774, L6

Wanajo, S., Kajino, T., Mathews, G. J., & Otsuki, K. 2001, ApJ, 554, 578

Witti, J., Janka, H.-T., & Takahashi, K. 1994, A&A, 286, 841

Wolfenstein, L. 1978, Phys. Rev. D, 17, 2369

Wongwathanarat, A., Hammer, N. J., & Müller, E. 2010a, A&A, 514, A48

Wongwathanarat, A., Janka, H.-T., & Müller, E. 2010b, ApJ, 725, L106

Wongwathanarat, A., Janka, H.-T., & Müller, E. 2013, A&A, 552, A126

Wongwathanarat, A., Mueller, E., & Janka, H.-T. 2014, ArXiv e-prints

Woosley, S. E. 1988, ApJ, 330, 218

Woosley, S. E., Arnett, W. D., & Clayton, D. D. 1973, ApJS, 26, 231

Woosley, S. E., Heger, A., & Weaver, T. A. 2002, Rev. Mod. Phys., 74, 1015

Woosley, S. E. & Hoffman, R. D. 1992, ApJ, 395, 202

Woosley, S. E. & Weaver, T. A. 1995, ApJS, 101, 181

Woosley, S. E., Wilson, J. R., Mathews, G. J., Hoffman, R. D., & Meyer, B. S. 1994, ApJ, 433, 229

Wu, M.-R., Fischer, T., Huther, L., Martínez-Pinedo, G., & Qian, Y.-Z. 2014, Phys. Rev. D, 89, 061303

Young, P., Ellinger, C., Arnett, D., Fryer, C., & Rockefeller, G. 2008, in Nuclei in the Cosmos (NIC X), 20

Acknowledgments

After these three and a half years passed preparing my PhD thesis, it is time for me to make some conclusions about this experience which has given so much to me, and not only from the academic point of view.

I would like to thank all the people who have accompanied me during this "journey" and, for a reason or another, have contributed in making me achieve this moment.

First of all, I would like to thank Thomas Janka and Shinya Wanajo for giving me the opportunity to work with my favorite subjects, namely astrophysics and nuclear physics. Thanks for your supervision, your availability and your patience. Thanks Shinya for providing me with your code and your precious explanations. Thanks Thomas for having helped me a lot to improve my method to approach the problems in physics and the way to go towards the solutions.

Thanks so much to my collaborators Irene Tamborra, Lorenz Hüdepohl and Annop Wongwathanarat for providing me with their data and for their availability.

I would like to thank all the people I met at MPA, who contributed in making the "tough" PhD life easier and more enjoyable.

Thanks to all the secretaries for always being available and so helpful with all the bureaucratic procedures: Dankeschön an Cornelia, Gabi, Kate, Maria und Sonja.

Thanks to all present and former people in Thomas' group for the nice working environment: Dankeschön an Alexander, Alexandra, Andi B., Andi M., Andreas V., Annop, Bernhard (danke auch für die Tabellen), Christoph, Florian, Georg, Janina, Jérôme, Lorenz, Marcella, Maxime, Michael, Nicole und Elisa, Oliver (danke für deine Zeit, um meine Einleitung zu lesen), Pedro, Ricard, Robert, klein Thomas, mini Tom und Tobi. Ich möchte mich auch bei euch bedanken für jedes deutsches Wort, das ihr mir beigebracht habt. Danke für euer Verständnis und eure Geduld, insbesondere wenn, naja, mein Deutsch ein bisschen komischer war als jetzt!!

Thanks to all the "ladies" for their encouragement and support, especially during the last months of my PhD: Anabele, Mei-Ling, Monika, Nitya and Valentina. Ein herzliches Dankeschön an Irina for her delicious "PhD survivor packets!" and for her support. A special faleminderit shumë goes to my friends of more or less forever Ana and Marsela. Thanks so much to Francesca for being there, doesn't matter how far (grazie Frà per saper esserci sempre nel modo in cui solo tu ne sei capace).

I desire to thank them who have been and are a constant source of immense love and support in each step of my life: faleminderit me gjithë zemër to my parents and to my brothers Anton and David. Thanks Mum and Dad for all the efforts that you have gone through to give me possibility to fulfill my wishes. Thanks for being an example for me, thanks for always having encouraged me to never give up and to try to follow my inspirations, doesn't matter how difficult the way can be. I will never be able to do for you as much as you have done for me, but I would like, at least, to dedicate to you this thesis and all the passion and work which I have put to achieve this moment.

Now, I wish to thank the one who more than anybody else stood by me during these years of PhD. Danke Florian für immer da sein, für deine Geduld, für deine Hilfe und dein Verständnis, insbesondere in den letzten Zeiten. Danke für deine ständige und liebevolle Unterstützung bei der Doktorarbeit und nicht nur.